

# Quantitative Biaxial Texture Analysis with Reflection High-Energy Electron Diffraction for Ion Beam-Assisted Deposition of MgO and Heteroepitaxy of Perovskite Ferroelectrics

Thesis by

Rhett Ty Brewer

In Partial Fulfillment of the Requirements

For the Degree of

Doctor of Philosophy

California Institute of Technology

Pasadena, California

2004

(Defended July 10, 2003)

© 2004

Rhett T. Brewer

All Rights Reserved

## Acknowledgements

Once our group took a chartered flight and the pilot, before the flight, asked us a question: what makes an airplane fly? After the pilot sat patiently through an awkward minute of half explanations about fluid flow, the Bernoulli effect, and drag, he said, “You are all wrong. Money makes the airplane fly.” Well, money makes research happen. Despite its shortcomings, our government has shown reasonable commitment to funding scientific research. I owe almost all of the financial support for my thesis work directly to the federal government. I received money from DARPA through the VIP III program, the Army Research Office through the Caltech MURI program, the Department of Energy through synchrotron time, and the National Science Foundation through a graduate student research fellowship. In addition to government support, I received a fellowship from the Intel Foundation (including a laptop whose hard drive is cluttered with iterations of this thesis).

I cannot look back now that I am at the end of the road (or the beginning, depending on which road you are talking about) without considering the contributions and efforts of all who went before me making this possible. The ephemeral lives of individuals, passing like phantoms, have left behind the creation that is our world today. Conquerors crushed other civilizations, slaves built monuments and overthrew oppressors, philosophers noticed we have consciousness, religions organized individuals into great tides, and scientists turned telescopes to the sky, microscopes to cells, lasers on atoms, and atoms on themselves. Truly I stand on the shoulders of giants.

The giant who I stand most directly on is John Hartman, the postdoctoral fellow who started the RHEED computation business in our group. Whenever I thought he was wrong, it turned out he was right. Thanks John for starting this thing right.

I will always feel a special affinity to my Atwater groupies (not Harry's "groupies," but my fellow members of the Atwater group). With the Atwater group, bad karaoke was good fun and technical conferences were like a big party (except for the small issue of spending eight hours a day in talks and a few hours at night sifting through posters). I must confess that the 2001 Gordon conference was actually more party than conference (mostly because both parts lasted until 3 – the conference until 3 p.m. and the party until 3 a.m.). I think every graduate student should have the opportunity to "accidentally" capsize their thesis advisor's canoe. Each groupie has meant something to me. Kyu Sung Min set the tone with his competence, training, and most importantly showing me that it was possible to graduate from this group. Liz Boer was the quiet light of XPS knowledge, occupying the office window seat, providing laughter and solid fashion advice. She always wore a sweater, but for some reason it took me three years of freezing my keister off in the lab to understand her deep wisdom and to adopt her example (although I never went for the striped look). Claudine taught me how to store food in the lab – an important skill for one who lives at work – and how to boogie in Hollywood night clubs. Regina was a great friend and ally, possessing sound advice and an open ear when all I could talk about was J. Maribeth served up pounds of haggis and encouraged me to try out for "Survivor." She is the real survivor though; anyone who can spend 5 years working with silane and a Thermionics heater deserves to be on the show more than I. Jason (not J) with his quick wit, funny faces (riiiightttt – coupled with

the OK sign), and genuine friendship made bars worth frequenting. He changed more than anyone else I knew during graduate school (except myself) without becoming a different person. Julie was the best friend I did not know I had. Diva of the dance floor, Caltech heartbreaker, and a smile I could always count on. Stefan demonstrated that Germanic efficiency could overcome plasmon inefficiency by 5:00 p.m. Jimmy was the best and worst conference roommate I had (even his engaging interlocution wore thin at somewhere between 4 and 5 a.m.). His keen social insights and persistence showed me the errors of my conservative ways at least once, maybe twice, OK once. Pieter introduced us to mobile karaoke with his drunken guitar antics. His English is so filled with colloquial expression that you would never guess he is Dutch. Cecily helped drive Goth clubbing night and was the only other Linux geek in the lab. Tao corrected some of my views concerning the Chinese cultural revolution (apparently Nien Chiang's autobiography, "Life and Death in Shanghai," is not consistent with the official history of the Chinese Communist Revolution). He also proved that his moving/packing skills were second to none. Beth reactivated my workout swimming habits with her compulsive exercise habits. She is the only person I know who runs 20 km, swims 4000 meters or bikes 50 km (science is metric isn't it?) because "it is, like, so fun." Biteen was a founding member of the Atwater Dragons, our short-lived, unofficial masters swim team. Robb demonstrated what it means to be a team player. With his penchant for solving other groupies' research problems, he is a postdoc stuck in a graduate student's body. Luke and Jen's return from death (Harvard) breathed new life into group fun. I will always be jealous of Brendan because he comes from Middle Earth. Youngbae provided

much needed help at the very end with expertise on ferroelectric domain mapping and polarization hysteresis loops.

Several collaborations were necessary to finish this work and I am indebted to a number of people for their efforts. Jay Whitacre and Paul Zsack trained me on synchrotron x-ray diffraction measurements. Carol Garland performed key TEM work. Paul Arendt, Bob Hammond, and James (Randy) Groves taught me everything I know about IBAD MgO, well almost. On more than one occasion, Randy provided helpful advice, equipment, and samples. I received e-mails from L. M. Peng and J. M. Cowley about electron diffraction. Yu Chen taught me about dynamical electron scattering. Channing Ahn was a valuable resource for diffraction questions. Darrell Schlom steered me clear of oxide MBE hazards and gave helpful advice for ferroelectric growth. My ferroelectric research benefited from oversight by Kaushik Bhattacharya, sol-gel PBT sample growth and x-ray measurements by Stacey Boland, MOCVD PBT growth and Raman measurements made by David Boyd and Mohamed El-Naggar.

I would like to express my appreciation to my advisor and mentor Harry Atwater. He inspired me to do my best with his implicit confidence in my abilities. He provided me opportunities to develop within the scientific community as a whole by sending me to countless conferences and supporting my travel to visit collaborators around the country. He provided crucial guidance and oversight for my research. More than anyone else, I could not have finished the thesis without his guidance. As I develop my own career, I hope to live his “light a candle instead of cursing at the darkness” philosophy.

Finally I would like to thank the Keith Meister, Das Mutter, Krissy, Lance, Roy Boy, and Kiwi for their undying love and support.

## Abstract

To facilitate ferroelectric-based actuator integration with silicon electronics fabrication technology, we have developed a route to produce biaxially textured ferroelectrics on amorphous layers by using biaxially textured MgO templates. For optimization of MgO biaxial texturing and fast analysis of MgO and ferroelectric biaxial texture, we developed reflection high-energy electron diffraction (RHEED) as an *in situ* biaxial texture measurement technique.

Using a kinematical electron scattering model, we show that the RHEED pattern from a biaxially textured polycrystalline film can be calculated from an analytic solution to the electron scattering probability. We found that diffraction spot shapes are sensitive to out-of-plane orientation distributions, but not to in-plane orientation distributions, requiring the use of in-plane RHEED rocking curves to fully experimentally determine biaxial texture. Using information from the simulation, a RHEED-based experimental technique was developed for *in situ* measurement of MgO biaxial texture. The accuracy of this technique was confirmed by comparing RHEED measurements of in-plane and out-of-plane orientation distribution with synchrotron x-ray rocking curve measurements. An offset between the RHEED-based and x-ray measurements (the RHEED measured slightly narrower orientation distributions than x-ray analysis), coupled with evidence that the biaxial texture narrows during ion beam-assisted deposition, indicates that RHEED-based measurements are a more sensitive technique for probing surface biaxial texture than x-ray measurements.

Biaxially textured MgO is grown on amorphous  $\text{Si}_3\text{N}_4$  by ion beam-assisted deposition (IBAD). MgO is e-beam evaporated onto the amorphous substrate with a

simultaneous 750-1200 eV Ar<sup>+</sup> ion bombardment at 45° from normal incidence and ion/MgO flux ratios ranging from 0.3 to 0.6. The MgO biaxial texture is optimized within the first 8 nm of MgO growth. We observed a previously unseen, dramatic texture evolution in IBAD MgO using TEM and RHEED-based quantitative texture measurements of MgO films thinner than 4 nm. We find specifically that the first layers of IBAD MgO are diffraction amorphous until the film is about 3.5 nm thick. During the next 1 nm (~ 5 monolayers) of additional growth, a sudden and striking development of biaxial texture evolution is observed. From the diffraction amorphous film, (001) fiber oriented grains with random in-plane orientations first emerge, but biaxially textured grains quickly dominate the film microstructure due to selection from the ion bombardment. The link between MgO crystalline fraction and in-plane orientation distribution, coupled with the rapid biaxial texture development, indicates that ion damage of misaligned MgO grains is responsible for ion mediated texturing. The biaxially textured MgO film results from a solid phase crystallization of biaxially textured MgO crystals in an amorphous matrix, which is corroborated by plan view transmission electron microscopy (TEM).

We have investigated the limitations of MgO biaxial texturing by varying the ion/MgO flux ratio and have measured the optimal ratio to be 0.47 for 750 eV IBAD. The in-plane orientation distribution optimal alignment is limited by the out-of-plane orientation distribution. Our results indicate that if the MgO grains can uniformly be oriented perpendicular to the substrate (out-of-plane orientation distribution approaching 0° full width at half maximum (FWHM)), IBAD could create MgO films with in-plane orientation distributions as narrow as 2° (FWHM).

Finally, we investigated the growth of perovskite ferroelectrics on biaxially textured MgO templates. Sol-gel and metallorganic chemical vapor deposition (MOCVD) were used to grow  $\text{Ba}_x\text{Pb}_{1-x}\text{TiO}_3$  (PBT) and molecular beam epitaxy (MBE) was used to grow  $\text{Ba}_{0.67}\text{Sr}_{0.03}\text{Ti}_{1.3}\text{O}_3$  (BST). PBT grown directly on IBAD MgO surfaces was not biaxially textured, where as if the IBAD MgO layer was capped with an additional 25 nm of homoepitaxial MgO before heteroepitaxy, the PBT would inherit the biaxial texture from the MgO template. Through RHEED-based biaxial texture analysis we observed that the in-plane orientation distribution of PBT, deposited using *ex situ* techniques (not performed in the same high vacuum growth environment where the MgO was deposited), narrowed significantly with respect to the in-plane orientation distribution of its MgO template (from  $11^\circ$  to  $6^\circ$  FWHM). We also observed that the in-plane orientation distribution of *in situ* MBE BST on biaxially textured MgO resulted in a BST film whose in-plane orientation distribution was within  $1.5^\circ$  FWHM of the MgO template in-plane orientation distribution. Evidence from cross section (TEM) and RHEED suggest that atmospheric moisture degrades the crystallinity of highly defective, misaligned MgO grains and that heteroepitaxially grown PBT preferentially nucleates on well-aligned grains and over grows misaligned regions of MgO.

The ferroelectric domain structure of biaxially textured PBT and BST was mapped using dynamic contact mode electrostatic force microscopy (DC-EFM). C-axis domains were observed to be associated with large grains. Polarization hysteresis loops obtained with the DC-EFM at several locations on each film indicate that the entire film is ferroelectric on the scale of the AFM tip size.

## List of Publications

### Refereed Publications

1. "Reflection High-Energy Electron Diffraction Experimental Analysis of Polycrystalline MgO Films with Grain Size and Orientation Distributions", **R. T. Brewer**, J. R. Groves, P. N. Arendt, and Harry A. Atwater, J. Appl. Phys. **93**, 205 (2003).
2. "Reflection High-Energy Electron Diffraction Analysis of Polycrystalline Films With Grain Size and Orientation Distributions", J. W. Hartman, **R. T. Brewer**, and Harry A. Atwater, J. Appl. Phys. **92**, 5133 (2002).
3. "Rapid Biaxial Texture Development During Nucleation of MgO Thin Films During Ion Beam-Assisted Deposition", **R. T. Brewer** and H. A. Atwater, Appl. Phys. Lett. **80**, 3388 (2002).
4. "RHEED In-Plane Rocking Curve Analysis of Biaxially-Textured Polycrystalline MgO Films on Amorphous Substrates Grown by Ion Beam-Assisted Deposition", **R. T. Brewer**, J. W. Hartman, J. R. Groves, P. N. Arendt, P. C. Yashar, H. A. Atwater, Appl. Surf. Sci. **175-176**, 691 (2001).

### Proceedings Articles

1. "*In Situ* Biaxial-Texture Analysis of MgO Films on Amorphous Substrates During Ion Beam-Assisted Deposition", **R. T. Brewer**, J. R. Groves, P. N. Arendt, H. A. Atwater, Mat. Res. Soc. Symp. Proc. **672**, O6.2 (2001).
2. "Quantitative RHEED Analysis of Biaxially-Textured Polycrystalline MgO Films on Amorphous Substrates Grown by Ion Beam-Assisted Deposition", **R. T. Brewer**, J. W. Hartman, and H. A. Atwater, Mat. Res. Soc. Symp. Proc. **585**, 75 (2000).

## Table of Contents

ACKNOWLEDGEMENTS.....	III
ABSTRACT.....	VII
LIST OF PUBLICATIONS.....	X
TABLE OF CONTENTS .....	XI
TABLE OF FIGURES.....	XX
CHAPTER 1 INTRODUCTION .....	1
1.1 Ferroelectrics and Si integration .....	2
1.1.1 Ion beam-assisted deposition .....	7
1.1.2 Biaxially textured ferroelectrics.....	8
1.2 Reflection high-energy electron diffraction (RHEED).....	10
1.3 Thesis outline .....	12
1.3.1 RHEED-based biaxial texture measurements.....	13
1.3.2 Biaxial texture development in IBAD MgO.....	14
1.3.3 Biaxially textured ferroelectric films .....	15

CHAPTER 2 RHEED-BASED MEASUREMENT OF BIAXIAL TEXTURE.....	18
2.1 Introduction.....	18
2.2 RHEED pattern computations.....	20
2.2.1 Kinematic electron scattering model .....	23
2.2.2 Dependence of RHEED pattern on thin film microstructure.....	26
2.2.2.1 Diffraction spot shape.....	26
2.2.2.2 In-plane rocking curve calculations.....	31
2.2.2.3 Generalization to all cubic crystals.....	33
2.3 Experimental method for measuring biaxial texture of RHEED on MgO.....	36
2.3.1 Single-image RHEED analysis.....	36
2.3.1.1 Background subtraction .....	37
2.3.1.2 Lookup tables.....	41
2.3.2 RHEED in-plane rocking curves .....	43
2.4 RHEED measurement reliability .....	44
2.4.1 Experimental setup.....	44
2.4.2 Standard texture measurement methods .....	46
2.4.3 RHEED-based measurement validation: in-plane orientation distribution .	48
2.4.4 RHEED-based measurement validation: out-of-plane orientation distribution	
52	
2.5 Conclusions.....	54

## CHAPTER 3 BIAXIAL TEXTURE DEVELOPMENT OF IBAD MGO.57

3.1	Introduction.....	57
3.1.1	Texture formation using IBAD.....	58
3.1.2	Theories of IBAD biaxial texturing mechanisms .....	61
3.1.2.1	Anisotropic ion damage .....	62
3.1.3	MgO texture development .....	66
3.1.4	Chapter overview .....	69
3.2	IBAD MgO biaxial texture during nucleation .....	70
3.2.1	Experiment.....	70
3.2.2	Results.....	72
3.2.3	Biaxial texture nucleation mechanism.....	75
3.3	Biaxial texture improvement as a function of film thickness .....	77
3.4	Biaxial texture development during homoepitaxy .....	80
3.5	Dependence of biaxial texture on growth conditions .....	81
3.6	Conclusion .....	85

## CHAPTER 4 FERROELECTRIC PROPERTIES OF $BA_xPB_{1-x}TiO_3$ ON BIAXIALLY TEXTURED MGO .....91

4.1	Introduction.....	91
4.1.1	Ferroelectric actuator .....	91

4.1.2	Ferroelectric thin film characterization.....	93
4.1.3	Polarization hysteresis loops.....	94
4.1.3.1	Dynamic contact mode electrostatic force microscopy .....	95
4.2	Chapter summary .....	96
4.3	Biaxially textured ferroelectrics on biaxially textured MgO .....	96
4.3.1	Growth methods.....	96
4.3.1.1	Sol-gel.....	97
4.3.1.2	MOCVD.....	98
4.3.1.3	MBE.....	99
4.3.2	Crystallographic orientation.....	105
4.3.2.1	Composition and c/a ratio .....	107
4.3.2.2	Biaxially textured MgO substrate effects .....	109
4.3.3	Biaxial texture.....	111
4.3.4	TEM analysis .....	113
4.3.4.1	MOCVD PBT on MgO.....	114
4.3.4.2	Sol-gel PBT on MgO .....	118
4.3.4.3	MBE BST on biaxially textured MgO .....	120
4.3.5	Effect of deposition method on the biaxially textured MgO template.....	122
4.4	Ferroelectric properties.....	124
4.4.1	DC-EFM and polarization hysteresis loops .....	125
4.4.1.1	Sol-gel PBT.....	126
4.4.1.2	MOCVD PBT .....	128

4.4.1.3	MBE BST.....	130
4.4.1.4	Further ferroelectric characterization.....	131
4.5	Conclusion .....	132
CHAPTER 5 CONCLUSION.....		135
5.1	RHEED-based biaxial texture measurements.....	135
5.2	Biaxial texture development in IBAD MgO.....	136
5.3	Biaxially textured ferroelectric films .....	137
5.4	The next step.....	139
APPENDIX A DERIVATION OF KINEMATIC ELECTRON SCATTERING MODEL FOR BIAXIALY TEXTURED POLYCRYSTALLINE FILMS.....		140
A.1	Electron scattering from a periodic potential.....	140
A.2	Polycrystalline potential construction.....	145
APPENDIX B DIRECTIONS FOR USING RHEED-BASED BIAXIAL TEXTURE ANALYSIS SOFTWARE.....		154
B.1	Procedure outline .....	154
B.1.1	RHEED settings .....	155

B.1.2 Imaging settings .....	155
B.2 Layer by layer growth RHEED analysis.....	156
B.2.1 Experimental procedure .....	157
B.2.1.1 Creating a background image .....	157
B.2.2 Input file .....	158
B.2.2.1 Header line .....	160
B.2.2.2 Spot separation.....	160
B.2.2.3 Image size (Pixels).....	161
B.2.2.4 Threshold for Gaussian fit .....	161
B.2.2.5 Background subtraction method .....	162
B.2.2.6 Adjust.....	162
B.2.2.7 Make the background file .....	162
B.2.2.8 Reduce the array size .....	163
B.2.2.9 Print out intensity file.....	163
B.2.2.10 Make movie .....	164
B.2.2.11 Shift background position .....	164
B.2.2.12 Manual shift .....	165
B.2.2.13 Taylor expand background .....	166
B.2.2.14 Set (004) position.....	167
B.2.2.15 Through spot location .....	167
B.2.2.16 Spot positions (2-6).....	168
B.2.2.17 Background locations.....	168
B.2.2.18 Z extension of the background.....	169

B.2.2.19	Spot number for background matching.....	169
B.2.2.20	No spots .....	170
B.2.2.21	Low coverage analysis.....	170
B.2.2.22	Number of low coverage files.....	170
B.2.2.23	Fraction above (004).....	170
B.2.2.24	Calculate d-spacing.....	171
B.2.2.25	Calibration file .....	171
B.2.2.26	Look at calibrated file only.....	171
B.2.2.27	Number of IBAD files .....	172
B.2.2.28	Time per file.....	172
B.2.2.29	File names .....	173
B.2.3	Output files.....	173
B.2.4	Look up table comparisons .....	174
B.2.5	Making new lookup tables .....	178
B.2.5.1	Unused inputs.....	179
B.2.5.2	Nominal orientation .....	180
B.2.5.3	Distance between peaks .....	180
B.2.5.4	Angle of incidence .....	180
B.2.5.5	Energy.....	181
B.2.5.6	Placement.....	181
B.2.5.7	Test run .....	181
B.2.5.8	Parameter space settings .....	181
B.2.5.9	Specifying spot locations .....	182

B.2.5.10	Building the crystal potential .....	183
B.2.5.11	Lookup table making conclusion .....	185
B.3	In-plane RHEED rocking curves .....	185
B.3.1	Experimental setup and procedure .....	185
B.3.2	Input file .....	186
B.3.2.1	Spot separation guess .....	188
B.3.2.2	Image size (pixels) .....	189
B.3.2.3	Background subtraction settings .....	189
B.3.2.4	Reduce array size by 2 .....	194
B.3.2.5	Diffraction spot locations .....	194
B.3.2.6	Calibration file .....	195
B.3.2.7	Make movie? .....	195
B.3.2.8	Rocking curve range .....	196
B.3.2.9	Input files .....	197
B.3.3	Output files .....	197
B.3.3.1	Rocking curve verification .....	198
B.3.3.2	Inlookup.dat – the lookup table file .....	203
B.3.4	Look up table comparisons .....	205
B.3.5	Making new lookup tables .....	207
B.3.5.1	Input file infastrock.dat .....	208
B.3.5.2	Unused inputs .....	208
B.3.5.3	Nominal orientation .....	209
B.3.5.4	Distance between peaks .....	209

B.3.5.5	Angle of incidence .....	209
B.3.5.6	Energy .....	210
B.3.5.7	Placement .....	210
B.3.5.8	Rocking curve settings .....	210
B.3.5.9	Test run .....	211
B.3.5.10	Parameter space settings .....	211
B.3.5.11	Diffraction spot size .....	212
B.3.5.12	Specifying spot locations .....	214
B.3.5.13	Building the crystal potential .....	214
B.3.5.14	Rockfast.c output files .....	216
B.3.5.15	Rockout.c – making the file lookup tables.....	216
B.4	Final results .....	216
APPENDIX C OXIDE MBE GROWTH CHAMBER.....		218
C.1	Overview .....	218
C.1	Parts List .....	223
C.2	Chamber Design.....	223

## Table of Figures

Figure 1.1: The crystal structure of the ferroelectric perovskite  $\text{BaTiO}_3$ . At temperatures above the Curie temperature ( $120^\circ\text{C}$ ) the crystal is cubic (a). When the crystal cools below the Curie temperature there is a tetragonal distortion (b) creating a long c-axis and two short a-axes. The c/a ratio is 1.01. The lattice distortion results in a spatial off-set between positively and negatively charged ions, causing a spontaneous electric dipole along the c-axis. 3

Figure 1.2: Actuator material figures of merit. Adopted by K. Bhattacharya from Krulevitch et al. (SMA: Shape-memory alloy, ES: Electrostatic, EM: Electromagnetic, PZT: Piezoelectric Lead-Zirconate-Titanate). 4

Figure 1.3: Schematic of a ferroelectric membrane linear actuator using stress and electrical fields. a) With zero electric field the stress orients the c-axis in plane, elongating the membrane, and causing the center of the membrane to sink. b) With the application of an electric field perpendicular to the membrane, the ferroelectric dipole moment aligns with the electric field and the shorter a-axes are aligned in-plane, shrinking the membrane and lifting the center up a distance  $\Delta x$ , which is the linear translation attainable from this structure. 5

Figure 1.4: (a) Randomly oriented polycrystalline film. (b) Biaxially textured polycrystalline film. Biaxially textured films have a preferred out-of-plane orientation (side view) and a preferred in-plane orientation (top view). 7

Figure 1.5: Schematic of an ion beam-assisted deposition system. For  $\text{MgO}$  the optimal angle  $\theta$  is  $45^\circ$  8

Figure 1.6: Reflection high-energy electron diffraction (RHEED) schematic. High-energy electrons (15-50 keV) impinge on a crystal at grazing incidence, diffract, and are detected by taking an image of the electron pattern created on a phosphorescent screen. 10

Figure 1.7: Ewald sphere construction of electron diffraction. The incident electron wave vector is  $\mathbf{k}$ , the scattered electron wave vector is  $\mathbf{p}$ , and  $\Delta\mathbf{k}$  is the change in the electron wave vector, which must be equal to an inverse lattice vector. 11

Figure 2.1: Schematic representation of the variables used to create a polycrystalline scattering potential. Each grain is addressed individually and given an envelope function,  $\Theta_g$ , which is one on the inside and zero outside the grain. Each grain is also given an orientation using  $B_g$ , which rotates the crystal axis of the grain around the x, y, and z-axis by the angle  $\omega_x$ ,  $\omega_y$ , and  $\phi$ , respectively. 24

Figure 2.2: Simulated  $\text{MgO}$  RHEED patterns, 25 keV at  $2.6^\circ$  incidence angle, as the parameters for grain size (L), effective electron penetration depth (h), and out-of-plane

orientation distribution ( $\Delta\omega$ ) are changed. Images a-c have  $h = 5$  nm,  $\Delta\omega = 0^\circ$  and a)  $L = 5$  nm, b)  $L = 10$  nm, and c)  $L = 25$  nm. Images d-f have  $L = 10$  nm,  $\Delta\omega = 0^\circ$ , and d)  $h = 5$  nm, e)  $h = 10$  nm, and f)  $h = 25$  nm. Images g-I have  $h = 5$  nm,  $L = 10$  nm, and g)  $\Delta\omega = 4^\circ$ , h)  $\Delta\omega = 8^\circ$ , and i)  $\Delta\omega = 12^\circ$ . 26

Figure 2.3: Simulated RHEED pattern of 20 keV electrons at  $1.2^\circ$  grazing incidence along [100] from well-textured polycrystalline MgO with effective lateral grain size  $L = 4$  nm, electron penetration depth  $h = 1$  nm, out-of-plane grain orientation distribution  $\Delta\omega = 7^\circ$ , and in-plane orientation distribution  $\Delta\phi = 14^\circ$ . The qualitative effects of these parameters upon the RHEED spot shapes and relative intensities are indicated. 27

Figure 2.4: Calculated horizontal MgO (044) diffraction spot width as a fraction of the distance between the (004) and (024) diffraction spots. 28

Figure 2.5: Simulated width of the (044) MgO diffraction spot in the direction perpendicular to the non-diffracted beam. The width is normalized to the distance between the (004) and (024). In a) the effective electron penetration depth ( $h$ ) is set to 5 nm, while in b) the grain size ( $L$ ) is set to 10 nm. 29

Figure 2.6: Schematic of a RHEED in-plane rocking curve experiment. Incident electrons  $k$  from the electron gun are diffracted by the polycrystalline film into wave vectors  $p$ , which are collected on a phosphorous screen and imaged (the RHEED pattern). The substrate is rotated about its vertical axis and the intensity of several diffraction spots are recorded as a function of the rotation angle  $\phi$ . The rocking curves are characterized by the FWHM from a Gaussian fit. 30

Figure 2.7: Simulated in-plane rocking curve FWHM ( $\Delta\phi$  degrees) for the MgO a) (024) and b) (044) diffraction spots, where the out-of-plane orientation distribution is equal to  $5^\circ$  FWHM ( $\Delta\omega$ ). The in-plane rocking curve displays an inverse relationship to grain size ( $L$ ) for grain sizes smaller than 20 nm. 31

Figure 2.8: Simulated in-plane rocking curve FWHM ( $\Delta\phi$  degrees) for the MgO a) (024) and b) (044) diffraction spots and grain size set to 10 nm. The in-plane rocking curve displays a direct dependence on out-of-plane orientation distribution ( $\Delta\omega$ ). 32

Figure 2.9: Comparison of the simulated RHEED dependence of MgO and BaTiO<sub>3</sub> on biaxial texture. a) For grain size ( $L = 10$  nm) and effective electron penetration depth ( $h = 6$  nm) the (024) diffraction spot width in the direction perpendicular to the non-diffracted spot, as a fraction of the separation between the (004) and (024) diffraction spots, is measured as a function of the out-of-plane orientation distribution ( $\Delta\omega$ ). b) The (024) in-plane rocking curve FWHM is measured as a function of the in-plane orientation distribution ( $\Delta\phi$ ) with  $\Delta\omega = 5^\circ$  FWHM and  $L = 10$  nm. 34

Figure 2.10: Experimental MgO RHEED image at 25 keV and  $2.6^\circ$  incidence angle. The diffraction spots shown are those which are used for RHEED-based biaxial texture

analysis. The cuts across the diffraction spots show the directions across which the computer program measures the FWHM of the diffraction spots. 35

Figure 2.11 Experimental IBAD MgO RHEED images taken at 25 keV and  $2.6^\circ$  incidence. a) Top view. b) Side view. The diffuse background is significant fraction of the diffraction spot intensity. 37

Figure 2.12: RHEED image of amorphous  $\text{Si}_3\text{N}_4$  taken at 25 keV and  $2.6^\circ$  incidence angle before IBAD MgO growth. 38

Figure 2.13: Background subtracted experimental RHEED images of IBAD MgO taken at 25 keV and  $2.6^\circ$  incidence angle. These are the background subtract images of Figure 2.11. a) Top view. b) Side view. 39

Figure 2.14: TEM image of IBAD MgO on amorphous  $\text{Si}_3\text{N}_4$ . The four fold symmetric arcs indicate that the MgO has a preferred in-plane orientation and the angular width of the arcs is a measurement of the in-plane orientation distribution ( $\Delta\phi$ ). 45

Figure 2.15: In-plane and out-of-plane x-ray rocking curves of IBAD MgO (002) with in-plane orientation distribution  $\Delta\phi = 10.6^\circ$  and out-of-plane orientation distribution  $\Delta\omega = 6.5^\circ$  FWHM. The rocking curve was taken at APS. 46

Figure 2.16: In-plane orientation distribution ( $\Delta\phi$ ) measured by RHEED analysis versus TEM or X-ray diffraction measurements. X-ray rocking curves collected using either a rotating anode source at Los Alamos or synchrotron radiation from the advanced photon source (APS). The error bars originate from limitations in deconvoluting the effects of out-of-plane orientation distribution and grain size measurements using RHEED. 49

Figure 2.17: In-plane ( $\Delta\phi$ ) and out-of-plane ( $\Delta\omega$ ) orientation distribution for IBAD MgO growth as a function of film thickness measured using RHEED. The lines are a fit to the data. 50

Figure 2.18: RHEED intensity of two separate Si Bragg rods as amorphous MgO was deposited on the Si (001) substrate. RHEED was performed at 25 keV at  $2.6^\circ$  incidence angle. 51

Figure 2.19: Out-of-plane orientation distribution ( $\Delta\omega$ ) measured using RHEED and synchrotron x-ray out-of-plane rocking curves. The line is a linear fit to the data. 53

Figure 3.1: Schematic of an ion beam-assisted deposition (IBAD) apparatus. The ion source is typically a Kaufmann ion gun and the growth material is deposited using physical vapor deposition (PVD). The optimal incidence angle of the ion bombardment ( $\theta$ ) depends on the film,  $45^\circ$  is optimal for MgO<sub>33</sub> and  $55.4^\circ$  is optimal for yttrium stabilized zirconia. 59

Figure 3.2: Biaxially textured film. The side view shows the MgO grains growing out of amorphous Si<sub>3</sub>N<sub>4</sub> with a preferred out-of-plane direction (the arrows indicate the (001) direction). On the right, the in-plane (001) planes, represented by the arrows, nominally align around the direction of the Ar<sup>+</sup> bombardment. 60

Figure 3.3: Molecular dynamics simulation of FCC crystals after twenty 100 eV, perpendicular Ar ion impacts. The top crystal has a (110) c-axis orientation and the bottom crystal has a (111) c-axis orientation. Crystal damage depends on the crystal direction oriented toward the ion flux. 63

Figure 3.4: In-plane alignment direction for IBAD YSZ as a function of r (ion/atom flux ratio) and ion bombardment angle. The different symbols represent that the films were grown by different deposition methods, e.g., sputter deposition and e-beam evaporation, and substrate temperatures, e.g., room temperature to 600° C. 64

Figure 3.5: Cross section TEM of IBAD MgO (deposited at 300 C) in which the ion beam was incident at roughly 45 degrees with respect to the normal of the substrate and image planes. 68

Figure 3.6: *In situ* RHEED images from a continuous IBAD MgO growth experiment where the film thickness is equal to: 2.5 nm (a), 3.1 nm (b), 3.6 nm (c), and 4.2 nm (d). The field of view contains diffraction spots from (0 $\bar{2}$ 4), in the upper left corner, to (046) in the lower right corner. 71

Figure 3.7: RHEED images from different IBAD MgO films grown to: 1.9 nm (a), 3.7 nm (b), 4.6 nm (c), and 4.8 nm (d). The field of view contains diffraction spots from (0 $\bar{2}$ 4), in the upper left corner, to (046) in the lower right corner. 72

Figure 3.8: TEM dark field images and diffraction patterns for IBAD MgO films with thicknesses equal to: 1.9 nm (a) (top image), 3.7 nm (b) (second image), 4.6 nm (c) (third image), and 4.8 nm (d) (bottom image). 74

Figure 3.9: Fraction of crystalline material observed for IBAD MgO with dark field TEM as a function of film thickness. In-plane orientation distribution ( $\Delta\phi$ ) measured as a function of film thickness. 75

Figure 3.10 In-plane ( $\Delta\phi$ ) and out-of-plane ( $\Delta\omega$ ) orientation distribution for IBAD MgO growth as a function of film thickness measured using RHEED. The lines are a fit to the data. In-plane orientation distribution ( $\Delta\phi$ ) measured using grazing incidence x-ray diffraction by Groves et al. are included for comparison. 77

Figure 3.11: *In situ* RHEED measurements of out-of-plane orientation distribution ( $\Delta\omega$ ) as a function of film thickness for ion/MgO flux ratios from 0.37 to 0.52. 78

Figure 3.12: Out-of-plane orientation distribution ( $\Delta\omega$ ) for IBAD MgO growth and MgO homoepitaxy. From 0-8 nm the growth is performed by IBAD, while subsequent growth is done using homoepitaxy at 600° C. 80

Figure 3.13: Optimal in-plane ( $\Delta\phi$ ) and out-of-plane ( $\Delta\omega$ ) orientation distributions for IBAD MgO growth with 750 eV Ar<sup>+</sup> ions as a function of ion/MgO molecule flux ratio. Measurements were performed using RHEED-based analysis and the lines are fits to the data. 82

Figure 4.1: Schematic of a ferroelectric membrane linear actuator using stress and electrical fields. a) With zero electric field the stress orients the c-axis in plane, elongating the membrane, and causing the center of the membrane to sink. b) With the application of an electric field perpendicular to the membrane, the ferroelectric dipole moment aligns with the electric field and the shorter a-axes are aligned in-plane, shrinking the membrane and lifting the center up a distance  $\Delta x$ , which is the linear translation attainable from this structure. 92

Figure 4.2: A polarization hysteresis loop plots the dielectric polarization as a function of applied voltage. Points C and E are the positive and negative remnant polarizations ( $P_r$ ), respectively. The coercive field ( $E_c$ ) must be calculated from the voltage drop across the ferroelectric material when the net polarization goes to zero. 93

Figure 4.3: Schematic of a dynamic contact mode electrostatic force microscopy (DC-EFM) system. 95

Figure 4.4: Schematic of the IBAD MgO and oxide MBE chamber. 100

Figure 4.5: Side view of the IBAD MGO and oxide MBE chamber. 101

Figure 4.6: Front view of the IBAD MgO and oxide MBE chamber. 102

Figure 4.7: Top view of the IBAD MgO and oxide MBE chamber. 103

Figure 4.8: X-ray  $\theta$ - $2\theta$  curves from PBT deposited by MOCVD and sol-gel on single-crystal MgO (001) and biaxially textured MgO. An x-ray  $\theta$ - $2\theta$  curve from MBE BST is also included. 106

Figure 4.9: C/a ratio of  $Ba_xPb_{1-x}TiO_3$  as a function of Ba composition (x). 108

Figure 4.10: RHEED images of PBT grown on biaxially textured MgO. Sol-gel PBT (a) and MOCVD (c) PBT RHEED images from films deposited on MgO templates made from 8 nm of IBAD MgO and an additional 20 nm of homoepitaxial MgO grown at 600° C. Sol-gel (b) and MOCVD (d) PBT RHEED images from films deposited on MgO templates made from 8 nm of IBAD MgO. 109

Figure 4.11: RHEED image of BST grown heteroepitaxially on biaxially textured MgO made from 8 nm of IBAD MgO and 20 nm of homoepitaxial MgO grown at 600° C. 110

Figure 4.12: Out-of-plane ( $\Delta\omega$ ) and in-plane ( $\Delta\phi$ ) orientation distributions of biaxially textured MgO templates and the heteroepitaxial perovskite (BST or PBT) deposited by MBE, MOCVD, or sol-gel. 112

Figure 4.13: Cross section TEM images of MOCVD PBT grown on single-crystal MgO (001). b) is a high-resolution image of one of the 45° defects in (a). 114

Figure 4.14: Diffraction patterns from MOCVD PBT grown on (a) single-crystal MgO (001) and (b) biaxially textured MgO. 115

Figure 4.15: MOCVD PBT grown on biaxially textured MgO. In some areas the MgO layer appears crystalline (a), while in other areas it does not appear to be crystalline (b). 116

Figure 4.16: a) High-resolution TEM image of the interface between biaxially textured MgO and MOCVD PBT. b) Plan view diffraction pattern of MOCVD PBT on biaxially textured MgO. 117

Figure 4.17: Cross section TEM high-resolution image of sol-gel PBT on biaxially textured MgO. b) Close up of a small interface region from image (a). 119

Figure 4.18: Cross section TEM high-resolution image of BST on biaxially textured MgO. (b) Diffraction pattern from image (a). The diffraction pattern is a super position of diffraction spots from MgO, a BST perovskite structure, and Si. 121

Figure 4.19: Dark field TEM image of the BST/ biaxially textured MgO/ amorphous Si<sub>3</sub>N<sub>4</sub>/Si film stack. MgO grain orientation propagates into the BST layer. 122

Figure 4.20: (a) Contact AFM topographic image of sol-gel PBT deposited on biaxially textured MgO. (b) Dynamic contact mode electrostatic force microscopy image of the film in (a). (c) Polarization hysteresis loops taken with the dynamic contact mode electrostatic force microscopy system from sol-gel PBT films deposited on different substrates. The biaxially textured and broad texture PBT films are 50 nm thick and the PBT on single-crystal MgO is 150 nm thick. 126

Figure 4.21: (a) Contact mode AFM topographical image of sol-gel PBT deposited on single-crystal MgO (001). (b) DC-EFM image of the film in (a). (c) A smaller DC-EFM scan of the image in (a). Decreasing the DC-EFM scan size increases sensitivity. 128

Figure 4.22: (a) Contact mode AFM image of MOCVD PBT deposited on biaxially textured MgO. (b) DC-EFM ferroelectric domain image of the topographical image (a). (c) Contact mode AFM image of MOCVD PBT deposited on single-crystal MgO (001).

(d) DC-EFM ferroelectric domain image of the topographical image (c). (e) Polarization hysteresis loops of MOCVD deposited on different MgO substrates. 129

Figure 4.23: (a) Contact mode AFM topographical image of MBE BST deposited on biaxially texture MgO. (b) DC-EFM ferroelectric domain image of the BST in image (a). (c) Polarization hysteresis loops taken with the DC-EFM system from sol-gel and MOCVD PBT films deposited on biaxially textured MgO. A polarization hysteresis loop from MBE BST on biaxially textured MgO is also included. 131

## Chapter 1 Introduction

Billions of dollars in semiconductor foundries and fifty years of technological development provide enormous momentum for the continued dominance of silicon-based electronics and systems for the foreseeable future. There is also wide-spread enthusiasm for micro- and nano-electrical mechanical systems (MEMs and NEMs) which have the potential to enable new technologies and create smaller, more highly integrated versions of today's mechanical device technologies. Silicon is also the dominant material for MEMs device fabrication partially due to the vast technology base developed from years of working with silicon MOS electronics and partly to facilitate MEMs integration with silicon-based electronics.

Though preferred for processing and integration reasons, silicon is not the ideal material for all MEMs applications. To realize miniaturized systems that can perform multiple tasks like biochemical sensing, communications, computational processing, and actuation requires the integration of ceramics, organics, metals, semiconductors, ferroelectrics, and other active materials with silicon electronics. Vertical integration of MEMs/NEMs with silicon electronics is important for device miniaturization, as well as for device functionality. The speed would increase and the complexity would decrease for communication between the active devices and control electronics for vertically integrated systems compared with separate chip device solutions. Unfortunately, silicon electronics devices are sensitive to contamination, greatly restricting the possibilities for introducing new materials into semiconductor foundries.

The most practical integration processes will allow new materials to be used for MEMs fabrication while still enabling the use of current silicon electronics fabrication

technology. One simple way to enable use of the current silicon electronics fabrication process and introduce new materials into MEMs devices is to fabricate the active structures during backend processing, i.e., after the silicon electronics have been fabricated and protected from contamination. One of the main challenges with this approach is that any subsequent processing must be performed at relatively low temperatures ( $< 450^{\circ}\text{C}$ ) to preserve the integrity of the silicon devices. Another major challenge is that the surface available for growth (metal layers and low-k dielectric materials) is not single-crystalline and not suitable for heteroepitaxy.

## 1.1 Ferroelectrics and Si integration

Ferroelectric materials contain components not easily compatible with silicon-based electronics fabrication, but could increase functionality of silicon-based MEMs/NEMs. Ferroelectric materials exhibit a spontaneous electric dipole moment without the application of an external electric field. Perovskite ferroelectrics produce a spontaneous dipole moment as the result of a tetragonal crystal lattice distortion which offsets the center of the positively charged ions from the center of the negatively charged ions in the crystal. For example, in its paraelectric state at elevated temperatures,  $\text{BaTiO}_3$  possesses a cubic structure (Figure 1.1a). Once  $\text{BaTiO}_3$  cools below its Curie temperature at  $120^{\circ}\text{C}$ , the unit cell experiences a tetragonal distortion along the (001) lattice plane creating a spontaneous dipole (Figure 1.1b). The tetragonal distortion of perovskite ferroelectrics ranges from a  $c/a$  (axis) ratio of 1.01 for  $\text{BaTiO}_3$  to 1.06 for  $\text{PbTiO}_3$ .

Krulevitch et al. identified frequency response and work/volume as important figures of merit for MEMs actuator materials. A plot illustrating how various actuator

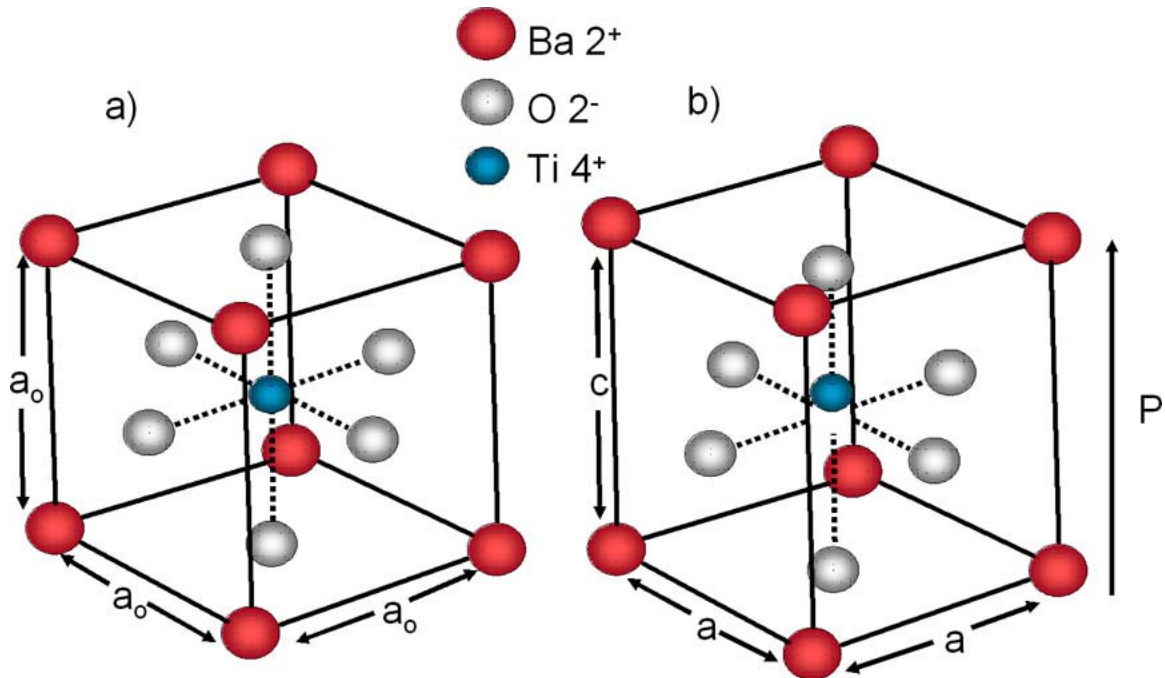


Figure 1.1 The crystal structure of the ferroelectric perovskite BaTiO<sub>3</sub>. At temperatures above the Curie temperature (120° C) the crystal is cubic (a). When the crystal cools below the Curie temperature there is a tetragonal distortion (b) creating a long  $c$ -axis and two short  $a$ -axes. The  $c/a$  ratio is 1.01. The lattice distortion results in a spatial off-set between positively and negatively charged ions, causing a spontaneous electric dipole along the  $c$ -axis.

candidate materials compare is included as Figure 1.2<sup>1</sup>. Theoretically, high-strain ferroelectrics (like BaTiO<sub>3</sub> and PbTiO<sub>3</sub>) are desirable actuator materials because they combine high work/volume with high-frequency response.

The orientation of the tetragonal distortion can be switched by either the application of an electric field or strain. One can imagine linear actuator structures fabricated out of a ferroelectric membrane or bridge structure which uses a combination of electric fields and stress to accomplish linear actuation. Linear actuation from a stress/electric field actuator is depicted pictorially in Figure 1.3. The force applied normal to the ferroelectric thin film could be pressure from a trapped gas or it could be from a rod attached to the structure to be moved by the actuator. In Figure 1.3a, no electric field is applied across the ferroelectric membrane so the tensile stress causes the

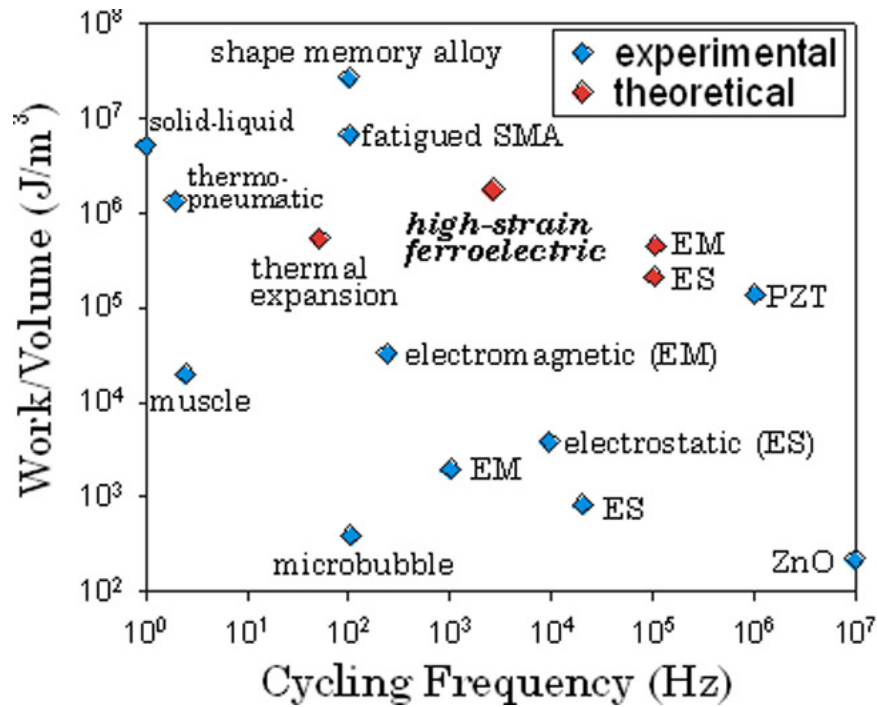


Figure 1.2 Actuator material figures of merit. Adopted by K. Bhattacharya from Krulevitch et al.<sup>1</sup> (SMA: Shape-memory alloy, ES: Electrostatic, EM: Electromagnetic, PZT: Piezoelectric Lead-Zirconate-Titanate).

c-axes to rotate into the plane of the film. As a result the overall membrane lateral length is elongated and the center of the membrane depresses. In Figure 1.3b, an electric field is applied perpendicular to the membrane, inducing the electric dipoles to orient along the direction of the applied electric field. If the electric field imposed across the thin plane of the film exceeds a minimum coercive field, then the electric dipole, and therefore the c-axis, is forced to orient in the direction of the electric field, despite the tensile stress which tends to orient the c-axis in the plane of the ferroelectric membrane. If all crystals have their c-axes oriented out-of-plane, the shorter a-axes are oriented in the plane of the ferroelectric membrane, making the ferroelectric membrane as short and flat as possible, lifting the center of the membrane. Releasing the electric field would allow the membrane to revert to the state shown in Figure 1.3a. The translation distance for this

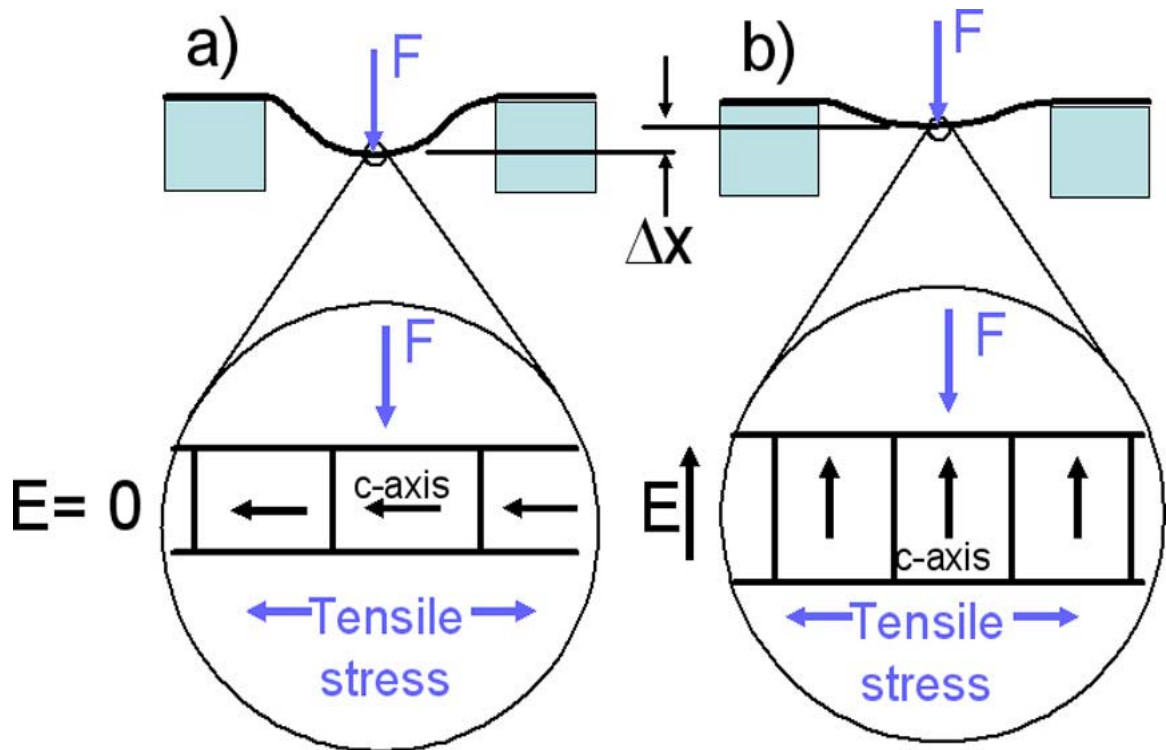


Figure 1.3 Schematic of a ferroelectric membrane linear actuator using stress and electrical fields. a) With zero electric field the stress orients the  $c$ -axis in plane, elongating the membrane, and causing the center of the membrane to sink. b) With the application of an electric field perpendicular to the membrane, the ferroelectric dipole moment aligns with the electric field and the shorter  $a$ -axes are aligned in-plane, shrinking the membrane and lifting the center up a distance  $\Delta x$ , which is the linear translation attainable from this structure.

linear actuator structure,  $\Delta x$  in Figure 1.3, is proportional to the length of the membrane and the  $c/a$  ratio. This type of actuator could either exploit the changing size of the cavity beneath the membrane to form a micropump or exploit the vertical displacement of the rod by attaching it to a mirror for optical switching.

There has been considerable success in efforts to grow high-quality single-crystalline perovskites on silicon. Molecular beam epitaxy (MBE) was used to grow  $\text{SrTiO}_3$  on (001) Si with “perfect registry”<sup>2</sup>. While essentially defect free perovskite ferroelectrics can be grown epitaxially on Si, for use as high  $K$  gate dielectrics, this does

not solve the silicon/ferroelectric-based MEMs integration problem. Once the integrated circuits are fabricated, the Si (001) surface is not accessible for heteroepitaxy. With layers of oxides, metallization, and low-k dielectrics, any candidate techniques for building actuators on top of transistors must start with an amorphous layer.

Wafer bonding is a promising technique that could integrate single-crystal ferroelectrics with amorphous layers. Wafer bonding is accomplished by pressing a ferroelectric single-crystal wafer against a flat amorphous surface (Si, SiO<sub>2</sub>, Si<sub>3</sub>N<sub>4</sub>), which could be used to cap the silicon integrated circuits. If the surfaces are sufficiently smooth and contaminate free, the Van der Waals forces will bring the surfaces into atomic contact. A high-temperature annealing step changes these bonds to covalent bonds, resulting in single-crystalline films on amorphous substrates. Unfortunately, this simplistic explanation of the wafer bonding process masks the technological difficulties of this technique. Surface contamination is often a barrier to successful wafer bonding. Excessive stress caused by coefficient of thermal expansion mismatches can also introduce difficulties. Finally, the desired ferroelectric layer thickness is much thinner than an entire wafer. Polishing a layer to the correct thickness is impractical, but layer transfer methods like crystal ion slicing<sup>3</sup> or some version of the Smart Cut process<sup>4</sup> provide hope for this alternative in the future.

Another route for ferroelectric/silicon integration is to create biaxially textured ferroelectrics using a buffer layer as a heteroepitaxial template. As previously stated, the only substrate reliably available during back end silicon processing for ferroelectric deposition will be amorphous; however, biaxially textured films can be grown on amorphous layers using ion beam-assisted deposition.

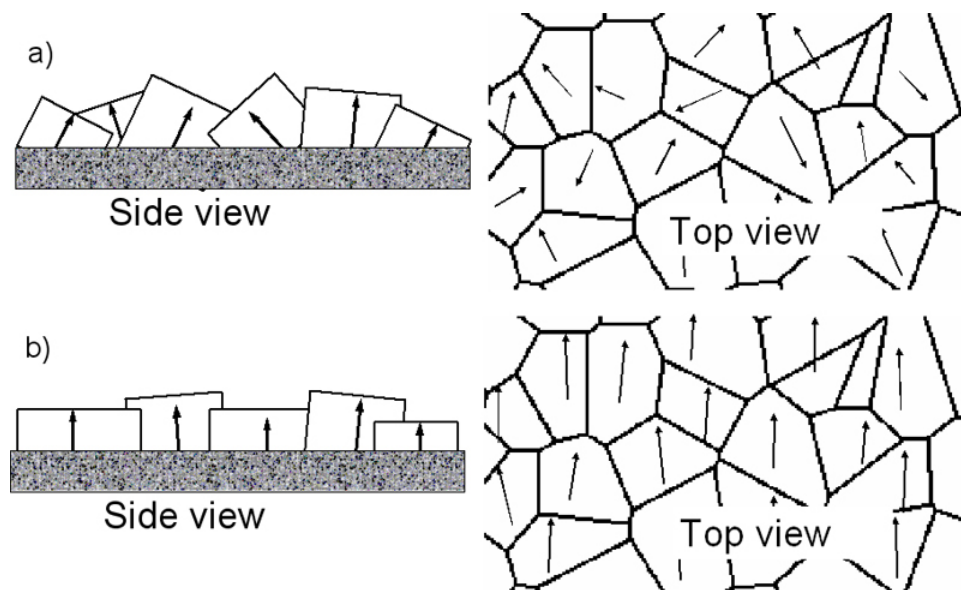


Figure 1.4 (a) Randomly oriented polycrystalline film. (b) Biaxially textured polycrystalline film. Biaxially textured films have a preferred out-of-plane orientation (side view) and a preferred in-plane orientation (top view).

### 1.1.1 Ion beam-assisted deposition

In 1985, Yu et al. were the first to demonstrate that niobium thin films with preferred in-plane and out-of-plane crystal axis orientations, i.e., biaxially textured (see Figure 1.4), could be grown on amorphous substrates using ion beam-assisted deposition (IBAD)<sup>5</sup>. A standard IBAD system schematic is included as Figure 1.5. IBAD consists of physical vapor deposition on an amorphous substrate with simultaneous ion bombardment of the substrate (ion bombardment energy is on the order of 1 keV).

Wang et al. recently showed that IBAD could be used to create highly aligned, biaxially textured MgO on amorphous  $\text{Si}_3\text{N}_4$ . The in-plane orientation distribution full width at half maximum (FWHM) was  $< 7^\circ$  and the out-of-plane orientation distribution FWHM was  $< 4^\circ$ <sup>6</sup>. MgO is a well-known heteroepitaxial template for ferroelectrics like  $\text{BaTiO}_3$ <sup>7</sup> and  $\text{PbTiO}_3$ <sup>8</sup>. Therefore, it is expected that biaxially textured ferroelectrics on ultimately amorphous substrates can be constructed by using IBAD MgO as a template.

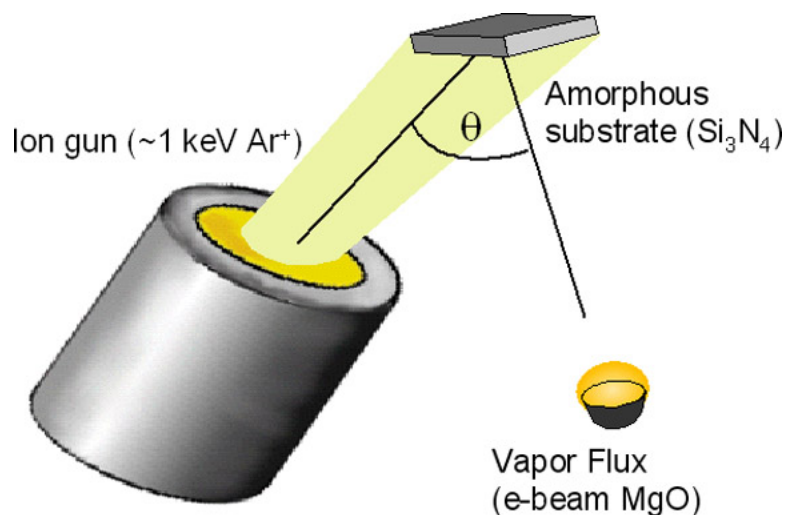


Figure 1.5 Schematic of an ion beam-assisted deposition system. For MgO the optimal angle  $\theta$  is  $45^\circ$ .

### 1.1.2 Biaxially textured ferroelectrics

The literature is silent on the properties of biaxially textured ferroelectric thin films, even though theoretically their properties should approach those of a single-crystalline film. Biaxial texture is important for polycrystalline actuator performance because the film elongation is directed and switchable only along the (001) crystal planes. A randomly oriented polycrystalline film performs less than half of the actuation that a single-crystal film produces, while a biaxially textured ferroelectric film (with the previously mentioned out-of-plane and in-plane orientation distributions of  $3^\circ$  FWHM and  $7^\circ$  FWHM, respectively, for MgO) can produce over 90% of the single-crystal actuation.

Biaxial texture can also be expected to play an important role in ferroelectric domain structure and ferroelectric domain boundary migration kinetics. Ferroelectric materials exhibit ferroelectric domain structure and domain switching similar to those observed in ferromagnetic materials. However, the ferroelectric dipole moments are tied

to the crystallographic directions. Randomly oriented polycrystalline films will have neighboring grains with very different orientations, forcing the crystal grain boundaries to be ferroelectric domain boundaries as well. A highly aligned biaxially textured ferroelectric will have neighboring grains with only slight misalignment between the crystallographic orientations. Subsequently, neighboring grains may have very similar ferroelectric dipole orientations, potentially enabling ferroelectric domain boundaries to span several grains. The energetic interaction between the well-aligned grains will be very different from the randomly oriented neighbors. This difference should be especially important when a field or stress is applied in an effort to reorient the ferroelectric domains. Grain boundaries have been implicated in domain wall motion pinning on the grounds that trapped charge at the domain boundaries inhibits domain wall motion<sup>9</sup>. High-angle grain boundaries offer greater disruption in the crystal potential than do low-angle grain boundaries, as attested by the ability of electrons to superconduct across low-angle grain boundaries in  $\text{YBa}_2\text{C}_3\text{O}_{7-x}$  but not in randomly oriented polycrystalline films<sup>10</sup>. Therefore, it is reasonable to expect that ferroelectric domain walls should migrate more easily across low-angle grain boundaries than across high-angle grain boundaries. Experiments and theoretical computations comparing domain switching speeds as a function of biaxial texture could yield insight into ferroelectric domain switching across grain boundaries and crystal defects. While still untested, biaxially textured ferroelectrics have the potential to perform like single-crystal films with the added advantage of facile integration with silicon electronics.

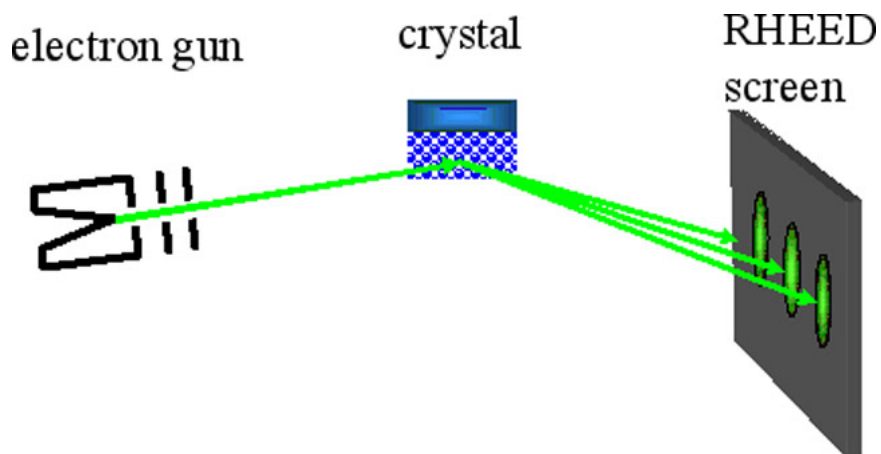


Figure 1.6 Reflection high-energy electron diffraction (RHEED) schematic. High-energy electrons (15-50 keV) impinge on a crystal at grazing incidence, diffract, and are detected by taking an image of the electron pattern created on a phosphorescent screen.

## 1.2 Reflection high-energy electron diffraction (RHEED)

The performance of biaxially textured ferroelectric MEMs is likely to depend on the biaxial texture inherited from the MgO substrate. Previous efforts to optimize the biaxial texture of IBAD MgO have been impeded by the *ex situ* nature of conventional biaxial texture analysis techniques (transmission electron microscopy (TEM) or x-ray diffraction). Because the biaxial texture develops within 11 nm of growth, x-ray diffraction cannot resolve biaxial texture unless the x-ray source has synchrotron brightness. For these same reasons, the IBAD biaxial texturing mechanisms are difficult to investigate. To circumvent these obstacles we have developed a reflection high-energy electron diffraction (RHEED) based method for quantitative *in situ* biaxial texture analysis of MgO.

A schematic of a RHEED system is included as Figure 1.6. A high-energy electron beam (15 – 50 keV) is incident on the sample at a grazing angle ( $1^\circ$  to  $5^\circ$ ). Electrons interact with the crystal potential and diffract into directions where the change

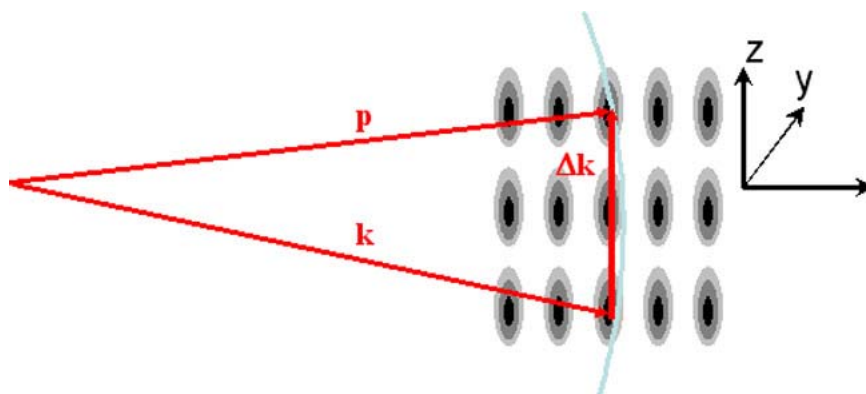


Figure 1.7 Ewald sphere construction of electron diffraction. The incident electron wave vector is  $\mathbf{k}$ , the scattered electron wave vector is  $\mathbf{p}$ , and  $\Delta\mathbf{k}$  is the change in the electron wave vector, which must be equal to an inverse lattice vector.

in the electron wave vector ( $\Delta\mathbf{k}$ ) is equal to an inverse lattice vector. This is the Laue condition. This process is demonstrated using the Ewald Sphere construction, illustrated in Figure 1.7. The incident electron wave vector is represented as  $\mathbf{k}$ , while all elastic scattering conditions are represented by a sphere (the intersection of the sphere with the page is drawn as a circle) centered on the origin of the  $\mathbf{k}$  vector. The head of the electron wave vector points to an inverse lattice position, which is also a point on the surface of the Ewald sphere. Where the Ewald sphere intersects inverse lattice positions a strong diffraction condition is created because the electrons can elastically scatter by exchanging energy with crystal phonons. The scattering vectors ( $\Delta\mathbf{k}$ ) are thus demonstrated to be equal to inverse lattice vectors. The radius of the Ewald sphere for high-energy electrons is large enough that it can be approximated as a flat sheet near the head of the incident electron wave vector  $\mathbf{k}$ . Because the Ewald sphere is so flat (the radius at 25 keV is  $82.02 \text{ \AA}^{-1}$ ), it intersects with many inverse lattice positions and RHEED makes a 2-D image of the inverse lattice, much like for transmission electron microscopy (TEM). The

RHEED pattern is obtained by collecting the diffracted electrons on a phosphorous screen and taking an image of the electron induced fluorescence.

RHEED is an ideal tool for measuring biaxial texture. Because it is an *in situ* measurement technique, biaxial texture can be measured during film growth. The strong coupling of electrons with the crystal lattice potential makes RHEED sensitive to films a few nanometers thick. Our experiments indicate that 90% of the diffracted intensity from 25 keV electrons at  $2.6^\circ$  incidence angle in MgO originates in the top 1 nm of film. By contrast, the weak interaction between x-rays and the crystal potential allows x-rays to penetrate into microns of film, making x-ray measurements reflective of bulk film properties. The weak interaction of x-rays with low Z (MgO) thin films is especially problematic for measuring biaxial texture which requires high-angles of incidence for out-of-plane orientation distribution measurements. Out-of-plane orientation distributions cannot be measured unless the x-ray source has synchrotron brightness. Even with a synchrotron, recording out-of-plane orientation distributions in <10 nm thick MgO films requires a half an hour. The speed (less than one second to collect a RHEED image), sensitivity ( $\sim 1$  nm of MgO), and *in situ* nature of RHEED experiments make it a powerful tool for biaxial texture measurement.

### 1.3 Thesis outline

Of the many possible routes for ferroelectric-based MEMs/NEMs integration with Si integrated circuits we have chosen to develop ion beam-assisted deposition as a heteroepitaxial template for biaxially textured ferroelectrics. This approach offers a specific set of challenges and advantages compared to other methods. The greatest advantage originates from the fabrication flexibility resulting from the ability to create

biaxially textured ferroelectrics on amorphous substrates. Before fabrication of MEMs/NEMs on a chip, the Si integrated circuits can be sealed off with diffusion barrier layers and protected from incompatible materials associated with ferroelectric deposition. Also, an amorphous layer can be deposited on any sacrificial or etch stop layer required for MEMs/NEMs structural fabrication. Because this fabrication would take place after Si integrated circuit fabrication, no new materials would need to be introduced into Si fabrication facilities, making this approach instantly compatible with current technology.

The outline of this thesis follows the development of our capability to grow highly aligned, biaxially textured perovskite ferroelectrics on amorphous substrates.

### **1.3.1 RHEED-based biaxial texture measurements**

Chapter 2 details the development of RHEED as an *in situ* biaxial texture measurement technique. Using a kinematical electron scattering model, we show that the RHEED pattern from a biaxially textured polycrystalline film can be calculated from an analytic solution to the electron scattering probability. We found that diffraction spot shapes are sensitive to out-of-plane orientation distributions, but not to in-plane orientation distributions, requiring the use of in-plane RHEED rocking curves to fully experimentally determine biaxial texture. Using information from the simulation, a RHEED-based experimental technique was developed for *in situ* measurement of MgO biaxial texture. The accuracy of this technique was confirmed by comparing RHEED measurements of in-plane and out-of-plane orientation distribution with synchrotron x-ray rocking curve measurements. An offset between the RHEED-based and x-ray measurements (the RHEED measured slightly narrower orientation distributions than x-ray analysis), coupled with evidence that the biaxial texture narrows during ion beam-

assisted deposition, indicates that RHEED-based measurements are more appropriate for probing surface biaxial texture than x-ray measurements.

RHEED-based biaxial texture measurement was essential to our efforts to produce biaxially textured ferroelectrics. Biaxially textured MgO has been used as a heteroepitaxial template for other perovskites, so optimization of the MgO biaxial texture is essential to optimizing the biaxial texture of ferroelectrics. RHEED measurements allow for fast optimization of MgO biaxial texture, fast analysis of MgO biaxial texture to determine if it is suitable for ferroelectric heteroepitaxy, and fast measurement of ferroelectric biaxial texture.

### **1.3.2 Biaxial texture development in IBAD MgO**

Our efforts to understand biaxial texture formation in ion beam-assisted deposition of MgO are discussed in Chapter 3. We discovered that biaxial textured MgO emerges after about 3 nm of growth. TEM and RHEED measurements were used to discover the initial deposition of an amorphous MgO layer, followed by an ion bombardment-mediated solid phase crystallization of a biaxially textured film. RHEED measurements were also used to show that once the biaxial textured film crystallized, the out-of-plane and in-plane orientation distributions narrowed as the film thickness increases. Finally, we optimized the IBAD MgO biaxial texture by measuring the biaxial texture for 750 eV Ar<sup>+</sup> ion bombardment as a function of the ion/MgO flux ratio. The most interesting result is that the in-plane orientation distribution is limited by the out-of-plane orientation distribution. Our experiments suggest that the minimum in-plane orientation distribution attainable by ion beam-assisted deposition is 2° FWHM and can

only be achieved if the (001) MgO planes are perfectly aligned perpendicular to the substrate (i.e., the out-of-plane orientation distribution goes to  $0^\circ$  FWHM).

Understanding the biaxial texture development of IBAD MgO is essential to optimizing and controlling it for ferroelectric heteroepitaxy. The quality of the IBAD MgO template greatly influences the ferroelectric film microstructure.

### 1.3.3 Biaxially textured ferroelectric films

In Chapter 4 we investigate the growth of perovskite ferroelectrics on biaxially textured MgO templates. Sol-gel and metallorganic chemical vapor deposition (MOCVD) were used to grow  $\text{Ba}_x\text{Pb}_{1-x}\text{TiO}_3$  (PBT) and molecular beam epitaxy (MBE) was used to grow  $\text{Ba}_{0.67}\text{Sr}_{0.03}\text{Ti}_{1.3}\text{O}_3$  (BST). PBT grown directly on IBAD MgO surfaces was not biaxially textured, whereas if the IBAD MgO layer was capped with an additional 25 nm of homoepitaxial MgO before heteroepitaxy, the PBT would inherit the biaxial texture from the MgO template. Through RHEED-based biaxial texture analysis we observed that the in-plane orientation distribution of PBT, deposited using *ex situ* techniques (not performed in the same high vacuum growth environment where the MgO was deposited), narrowed significantly with respect to the in-plane orientation distribution of its MgO template (from  $11^\circ$  to  $6^\circ$  FWHM). We also observed that the in-plane orientation distribution of *in situ* MBE BST on biaxially textured MgO resulted in a BST film whose in-plane orientation distribution was within  $1^\circ$  FWHM of the MgO template in-plane orientation distribution. Cross section transmission electron microscopy (TEM) was used to investigate the microstructure of the heteroepitaxial ferroelectric films. Films deposited on biaxially textured MgO using *ex situ* growth techniques (sol-gel and MOCVD) were found to have degraded MgO templates.

We speculate that moisture from the atmosphere degrades the MgO template by attacking the defects in the biaxially textured MgO substrate. PBT grown on IBAD MgO surfaces was not biaxially textured because the high defect density made the entire MgO template subject to hydroxylation and degradation from atmospheric moisture. By capping IBAD MgO with an MgO homoepitaxial layer, grown at 600° C, the MgO defect density was reduced and produced biaxially textured PBT on MgO using sol-gel synthesis and MOCVD. We also infer that PBT in-plane orientation distributions were narrower than the MgO template because misaligned MgO grains were more highly damaged during IBAD growth and were not fully healed by MgO homoepitaxy. These highly damaged, misaligned grains are preferentially degraded by atmospheric moisture, allowing PBT to preferentially nucleate on well-aligned MgO grains and to possess a narrower in-plane orientation distribution than the MgO template by over growing less well oriented MgO regions. The MBE BST more closely reflected the MgO template in-plane orientation distribution because the *in situ* BST growth did not subject the MgO to hydroxylation from the atmosphere, leaving all MgO grains crystalline and available for BST nucleation.

The ferroelectric domain structure of biaxially textured PBT (grown by sol-gel and MOCVD) and BST (grown by MBE) was mapped using dynamic contact mode electrostatic force microscopy (DC-EFM). C-axis domains were observed to be associated with large grains. Polarization hysteresis loops obtained with the DC-EFM at several locations on each film indicate that the entire film is ferroelectric on the scale of the AFM tip size.

- 
- <sup>1</sup> P. Krelevitch, A. P. Lee, P. B. Ramsey, J. C. Trevino, J. Hamilton and M. A. Northrup, *J. MEMS* **5**, 270 (1996).
- <sup>2</sup> R. A. McKee, F. J. Walker, and M. F. Chisholm, *Phys. Rev. Lett.* **81**, 3014 (1998).
- <sup>3</sup> M. Levy, R. M. Osgood, R. Liu, L. E. Cross, G. S. Cargill, A. Kumar, and H. Bakhru, *Appl. Phys. Lett.* **73**, 2293 (1998).
- <sup>4</sup> M. Bruel, B. Aspar, A. J. AubetonHerve, *Jap. J. Appl. Phys Part 1* **36**, 1636 (1997).
- <sup>5</sup> L. S. Yu, J. M. E. Harper, J. J. Cuomo, and D. A. Smith, *Appl. Phys. Lett.* **47**, 932 (1985).
- <sup>6</sup> C. P. Wang, K. B. Do, M. R. Beasley, T. H. Geballe, and R. H. Hammond, *Appl. Phys. Lett.* **71**, 2955 (1997).
- <sup>7</sup> Y. Yoneda, T. Okabe, K. Sakaue, and H. Terauchi, *Surface Science* **410**, 62 (1998).
- <sup>8</sup> S. Kim and S. Baik, *Thin Solid Film* **266**, 205 (1995).
- <sup>9</sup> F. Xu, S. Trolrier-McKinstry, W. Ren, B. M. Xu, Z. L. Xie, and K. J. Hemker, *J. Appl. Phys.* **89**, 1336 (2001).
- <sup>10</sup> X. D. Wu, S. R. Foltyn, P. N. Arendt, W. R. Blumenthal, I. H. Campbell, J. D. Cotton, J. Y. Coulter, W. L. Hulst, M. P. Maley, H. F. Safar, and J. L. Smith, *Appl. Phys. Lett.* **67**, 2397 (1995).

## Chapter 2 RHEED-Based Measurement of Biaxial Texture

### 2.1 Introduction

Monolithic integration of different materials is often desirable for creating novel device and system functionality. Unfortunately, materials integration can not always be achieved by heteroepitaxy on single-crystalline surfaces because of lattice size or crystal structure mismatch, as well as the lack of a suitable heteroepitaxial template layer because of previous materials processing steps. One integration option is growth of a polycrystalline film on an amorphous buffer layer. However, for many electronics applications the film functionality can strongly depend on both the out-of-plane grain orientation distribution (the full width at half maximum, FWHM, is designated as  $\Delta\omega$ ) and in-plane grain orientation distribution (FWHM is designated as  $\Delta\phi$ ). Some highly aligned biaxially textured oxide materials (oxide materials with a preferred out-of-plane and in-plane orientation) can exhibit similar functionality to single-crystalline films. For example, biaxially textured  $\text{YBa}_2\text{Cu}_3\text{O}_{7-x}$  superconducting thin films have been reported to have critical current densities approaching those of single-crystalline films, while randomly oriented polycrystalline films exhibit much lower critical current densities<sup>11</sup>. Biaxially textured ferroelectric films with  $90^\circ$  domain rotations are also expected to have actuation characteristics similar to those of single-crystalline ferroelectric films, while randomly oriented polycrystalline ferroelectric films experience significant degradation of translational range of motion. Incorporation of biaxially textured ferroelectric films with silicon integrated circuits would enable new types of ferroelectric actuators for

micro electromechanical systems (MEMs). Previous work has shown that ferroelectric materials like BaTiO<sub>3</sub> and Pb(Zr,Ti)O<sub>3</sub> can be deposited heteroepitaxially onto single-crystal MgO (001)<sup>12,13</sup> and even Si (001)<sup>14</sup>. However, conventional silicon integrated circuit processing employs extensive hydrogen passivation, which degrades ferroelectrics like Pb(Zr,Ti)O<sub>3</sub> and BaTiO<sub>3</sub>. It is therefore desirable to monolithically integrate ferroelectric materials following integrated circuit fabrication. Wang et al. demonstrated that IBAD MgO grown on amorphous Si<sub>3</sub>N<sub>4</sub> develops narrow biaxial texture in films only 11 nm thick<sup>15</sup>. By eliminating the requirement for a pre-existing heteroepitaxial template, IBAD provides an opportunity to incorporate ferroelectric materials on top of amorphous dielectric films in silicon integrated circuits during the backend processing.

The performance of ferroelectric MEMs is likely to depend on the biaxial texture inherited from the MgO substrate. Previous efforts to optimize the biaxial texture of IBAD MgO have been impeded by the *ex situ* nature of conventional biaxial texture analysis techniques, e.g. transmission electron microscopy (TEM) or x-ray diffraction. Because the biaxial texture develops within 11 nm of growth, x-ray diffraction cannot resolve crystallographic texture unless the x-ray source has synchrotron brightness. For these same reasons, the IBAD biaxial texturing mechanisms are difficult to investigate. To circumvent these obstacles we have developed a reflection high-energy electron diffraction (RHEED) based method for quantitative *in situ* biaxial texture analysis of MgO. RHEED has been previously used to analyze the out-of-plane texture for CoCr alloys, assuming the grains were not large enough to affect the RHEED pattern<sup>16</sup>. The small grain size of IBAD MgO films (as small as 10 nm) necessitates that we

deconvolute the effects of grain size from the effects of out-of-plane orientation distribution for accurate texture distribution measurements.

In this chapter, I will describe in general terms the calculation used to predict the effect of biaxial texture on the RHEED pattern. A complete derivation of the equation used to calculate the RHEED pattern, beginning with the time independent Schrödinger Equation is included in Appendix A and is based on work done by John W. Hartman<sup>17</sup>. This algorithm is then used to measure the biaxial texture from experimental RHEED data taken from MgO films. I will detail the methodology developed to properly acquire and analyze RHEED patterns to measure the biaxial texture. Finally, I will compare RHEED-based biaxial texture measurements with measurements taken using standard techniques like x-ray rocking curves and TEM analysis to demonstrate the accuracy of the RHEED-based method.

## **2.2 RHEED pattern computations**

RHEED is a viable analysis technique for films only a few monolayers thick because electrons strongly couple to the crystal lattice potential through electron-electron interactions. A result of this strong coupling is that electrons will undergo multiple scattering during their interaction with the lattice. This multiple scattering process, together with absorption, is called dynamical scattering. For a full physical treatment of electron scattering in a crystal lattice both multiple scattering events and the inelastic nature of individual electron scattering events must be considered. Inelastic scattering processes are dominated by surface and bulk plasmons, which normally induce electron energy losses of less than 100 eV<sup>18</sup>, which is negligible compared to the energy of RHEED electrons (~25 keV). Therefore, calculations of RHEED patterns can safely

ignore inelastic scattering events. However, multiple scattering events are still important for quantitative calculations of electron scattering in a single-crystal material.

Calculating the RHEED pattern for a single-crystalline film requires solving the time independent Schrödinger Equation

$$\nabla^2\Psi(\vec{r}) + (V(\vec{r}) + k^2)\Psi(\vec{r}) = 0, \quad (2.1)$$

where the potential  $V(\mathbf{r})$  is the semi-infinite electron scattering potential of the crystal.

Because of lattice periodicity, a numerical solution to this equation becomes tractable using a Bloch equation to represent the electrons wave function

$$\Psi(\vec{r}) = \sum_{\mathbf{k}} \psi_{\vec{k}}(\vec{r}) \exp[i\vec{k} \cdot \vec{r}]. \quad (2.2)$$

The Bloch expansion is taken over  $\mathbf{k}$  vectors equal to the inverse lattice vectors (the modes of the Bloch expansion are called “beams”) because the Laue condition must be satisfied for the electron to scatter into a different mode. The Laue condition is that the change in wave vector for a scattering electron must be equal to an inverse lattice vector. Physically this describes the scattering process as a transfer of momentum between the electron and crystal lattice through phonons that have wave vectors equal to the inverse lattice vectors. For computational purposes, the number of inverse lattice vectors that electrons are allowed to scatter into must be determined *a priori*, ignoring directions that have essentially zero probability of being scattered into. The periodic potential  $V(\mathbf{r})$  (bold faced variables in the text signify vectors) determines the strength of the coupling between the different beams. As the electron propagates through the potential, multiple scattering is represented by exchanging amplitude between coefficients  $\psi_{\mathbf{k}}(\mathbf{r})$  in the Bloch representation of the electron wave function. Solving the dynamical scattering simulation yields values for the amplitude coefficients  $\psi_{\mathbf{k}}(\mathbf{r})$  and thus calculates the absolute probability for electron scattering into the specified beams.

Because the coupling between beams is generally strong, an electron scattering model only allowing a single scattering event, or kinematical model, is not reliable for quantitative RHEED modeling. Even so, RHEED modeling with a kinematic electron scattering model is attractive because it is extremely efficient and could provide the capability for real-time thin film growth analysis and control in high vacuum deposition processes. Much of the electron scattering physics is contained in kinematical modeling and a kinematical model will yield correct diffraction spot shapes because that information is contained in the scattering potential  $V(\mathbf{r})$ , but the kinematic intensities will be wrong because dynamical scattering will renormalize the scattering amplitudes. This effect will be most important for inner reflections where the coupling between scattered electron beams is strongest. For example, in the two-beam case for a randomly oriented polycrystal, Cowley<sup>19</sup> reports that the ratio of intensities between dynamical and kinematical scattering could be well represented by the equation:

$$I_{\text{dynamical}} / I_{\text{kinematic}} = F_G^{-1} \int_0^{F_G} dx J_0(2x), \quad (2.3)$$

where  $F_G$  is  $v(G)\lambda h/4\pi$ ,  $v(G)$  is the electronic form factor for the reciprocal lattice vector  $G$ ,  $\lambda$  is the electron wave length, and  $h$  is the film thickness. Experiments by Horstmann and Meyer<sup>20</sup> on aluminum found good agreement between this equation and experimental intensities, except for strong inner reflections like (400) and (222). While the films we are interested in are not randomly oriented, the crystals are sufficiently small that multiple scattering will occur between separate crystals, causing the dynamical intensities to add incoherently, as for the case of the randomly oriented films. Consequently, to first order we expect that performing kinematical, instead of dynamical simulations will cause a systematic error in the calculated intensities of RHEED diffraction spots. However,

information about the RHEED spot shape is contained in the scattering potential  $V(\mathbf{r})$  and can be accurately predicted using a kinematical simulation.

We will demonstrate that biaxial texture can be determined quantitatively without requiring the capability to predict the absolute intensities of RHEED spots as a function of biaxial texture. Enough information is contained in the RHEED diffraction spot shapes and relative intensities to permit us to ignore absolute spot intensities. Therefore, for computational efficiency we decided to use a kinematic simulation to calculate the effects of biaxial texture on diffraction patterns. While this method ignores both inelastic scattering effects and dynamical or multiple scattering effects, we have been able to show experimentally that a kinematical description is sufficient for measuring biaxial texture.

### 2.2.1 Kinematic electron scattering model

We employed the kinematic electron diffraction approximation for our RHEED simulation because it contains much of the important electron scattering physics and yields a compact, analytic solution to the scattering probability. Equation (2.4) represents the kinematic electron scattering amplitude for an electron going from wave vector  $\mathbf{k}$  to  $\mathbf{p}$  in a crystal lattice with a potential  $V(\mathbf{r})$ <sup>19</sup>, while Eq. (2.5) represents a single-crystal potential, where  $\mathbf{G}$  is the inverse lattice vector and  $\mathbf{R}$  is the real lattice vector. We constructed the polycrystalline potential  $V(\mathbf{r})$ , Eq. (2.6), as an aggregate of individual single-crystalline grains, where each grain ( $g$ ) is assigned a lateral dimension using an envelope function,  $\Theta_g(\mathbf{r}-\mathbf{r}_g)$ , a lattice slip displacement from neighboring grains,  $\mathbf{a}_g$ , and

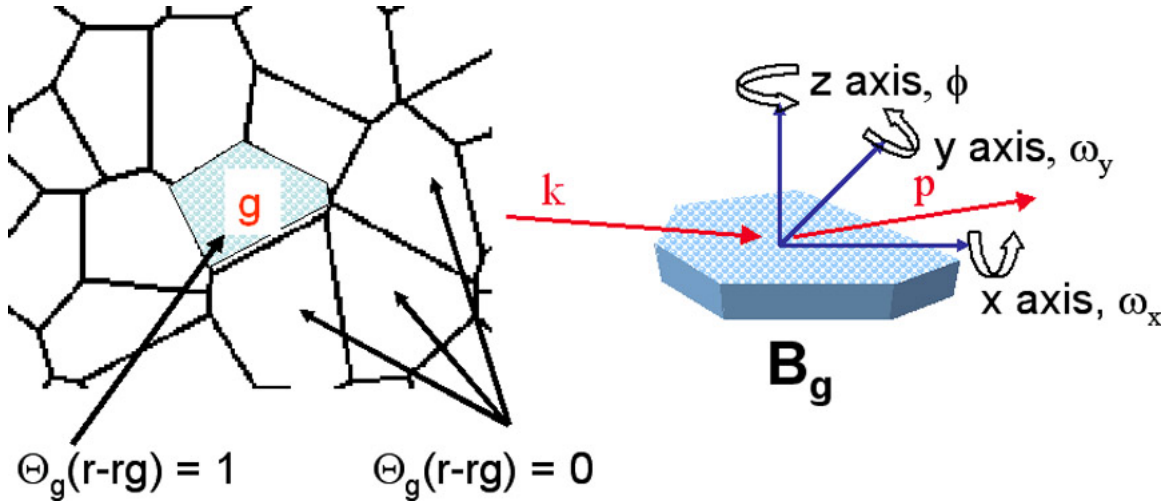


Figure 2.1 Schematic representation of the variables used to create a polycrystalline scattering potential. Each grain is addressed individually and given an envelope function,  $\Theta_g$ , which is one on the inside and zero outside the grain. Each grain is also given an orientation using  $\mathbf{B}_g$ , which rotates the crystal axis of the grain around the x, y, and z-axis by the angle  $\omega_x$ ,  $\omega_y$ , and  $\phi$ , respectively.

an orientation,  $\mathbf{B}_g$  (see Figure 2.1).

$$A_{\vec{k} \rightarrow \vec{p}} \propto -i \int d^3r \exp[-i(\vec{k} - \vec{p}) \cdot \vec{r}] V(\vec{r}) \quad (2.4)$$

$$V(\vec{r})_{\text{single crystal}} = \sum_{\vec{R}} v(\vec{r} - \vec{R}) = \sum_{\vec{G}} V_{\vec{G}} \exp(i\vec{G} \cdot \vec{r}) \quad (2.5)$$

$$V(\vec{r})_{\text{polycrystalline}} = \sum_g \Theta_g(\vec{r} - \vec{r}_g) \sum_{\vec{G}} V_{\vec{G}} \exp[i(\mathbf{B}_g \vec{G}) \cdot (\vec{r} - \vec{a}_g)] \quad (2.6)$$

The orientation  $\mathbf{B}_g$  is specified by a combination of rotation angles around the x-axis ( $\omega_x$ ), y-axis ( $\omega_y$ ), and the z-axis ( $\phi$ ), Eq. (2.7). Our construction of the polycrystalline scattering potential was also developed independently by Litvinov et al.<sup>21</sup>.

$$\mathbf{B}_g = \begin{pmatrix} 1 & 0 & 0 \\ 0 & 1 & 0 \\ 0 & 0 & 1 \end{pmatrix} + \omega_x \begin{pmatrix} 0 & 0 & 0 \\ 0 & 0 & -1 \\ 0 & 1 & 0 \end{pmatrix} + \omega_y \begin{pmatrix} 0 & 0 & 1 \\ 0 & 0 & 0 \\ -1 & 0 & 0 \end{pmatrix} + \phi \begin{pmatrix} 0 & -1 & 0 \\ 1 & 0 & 0 \\ 0 & 0 & 0 \end{pmatrix} \quad (2.7)$$

In order to create a compact and computationally efficient representation of the electron scattering probability into wave vector  $\mathbf{p}$ , we made the following assumptions: each grain is the same size, the grain displacement vector  $\mathbf{a}_g$  is random, and the orientation distribution of the grain rotations around each axis can be represented by a Gaussian with

a full width at half maximum (FWHM) represented by  $\Delta\omega_x$ ,  $\Delta\omega_y$ , and  $\Delta\phi$  for the x, y, and z axis rotations, respectively. It is important to note that in all cases, the x axis is in the plane of the sample and oriented along the axis of the incident electron beam, the y axis is in the plane of the sample and oriented perpendicular to the incoming electron beam, and the z axis is perpendicular to the substrate face. Using the previously mentioned assumptions, we are able to integrate the square of Eq. (2.4), instead of summing over individual grains, and produce an analytic solution for the kinematic scattering probability, shown as Eq. (2.8). The matrix  $\mathbf{A}_G$  contains the terms describing the lateral grain size ( $L_x$  and  $L_y$ ) and electron penetration depth ( $h$ ), as well as the terms which describe the in-plane and out of plane grain orientation distributions (Eq. (2.9)).

$$P_{\vec{k} \rightarrow \vec{p}} \propto \sum_{\vec{G}} |V_{\vec{G}}|^2 \sqrt{\det|\mathbf{A}_{\vec{G}}|} \exp[-\frac{1}{2}(\vec{G} + (\vec{k} - \vec{p}))\mathbf{A}_{\vec{G}}(\vec{G} + (\vec{k} - \vec{p}))] \quad (2.8)$$

$$\mathbf{A}_G^{-1} = \Sigma_g + \Delta\omega_x \begin{pmatrix} 0 & 0 & 0 \\ 0 & G_z^2 & -G_y G_z \\ 0 & -G_y G_z & G_y^2 \end{pmatrix} + \Delta\omega_y \begin{pmatrix} G_z^2 & 0 & -G_x G_z \\ 0 & 0 & 0 \\ -G_x G_z & 0 & G_x^2 \end{pmatrix} + \phi \begin{pmatrix} G_y^2 & -G_x G_y & 0 \\ -G_x G_y & G_x^2 & 0 \\ 0 & 0 & 0 \end{pmatrix} \quad (2.9)$$

$$\Sigma_g = \begin{pmatrix} 1/(\sigma L_g)^2 & 0 & 0 \\ 0 & 1/(\sigma L_g)^2 & 0 \\ 0 & 0 & 1/(\sigma h)^2 \end{pmatrix} \quad (2.10)$$

In Eq. (2.10),  $\sigma = .453$  (chosen to fit a Gaussian to the envelope function for convolved square grains) and  $G_x$ ,  $G_y$ , and  $G_z$  are the x, y, and z components of the inverse lattice vector. RHEED patterns are simulated by calculating the probability for scattering into the direction that corresponds to each pixel on the screen. Consequently, computational

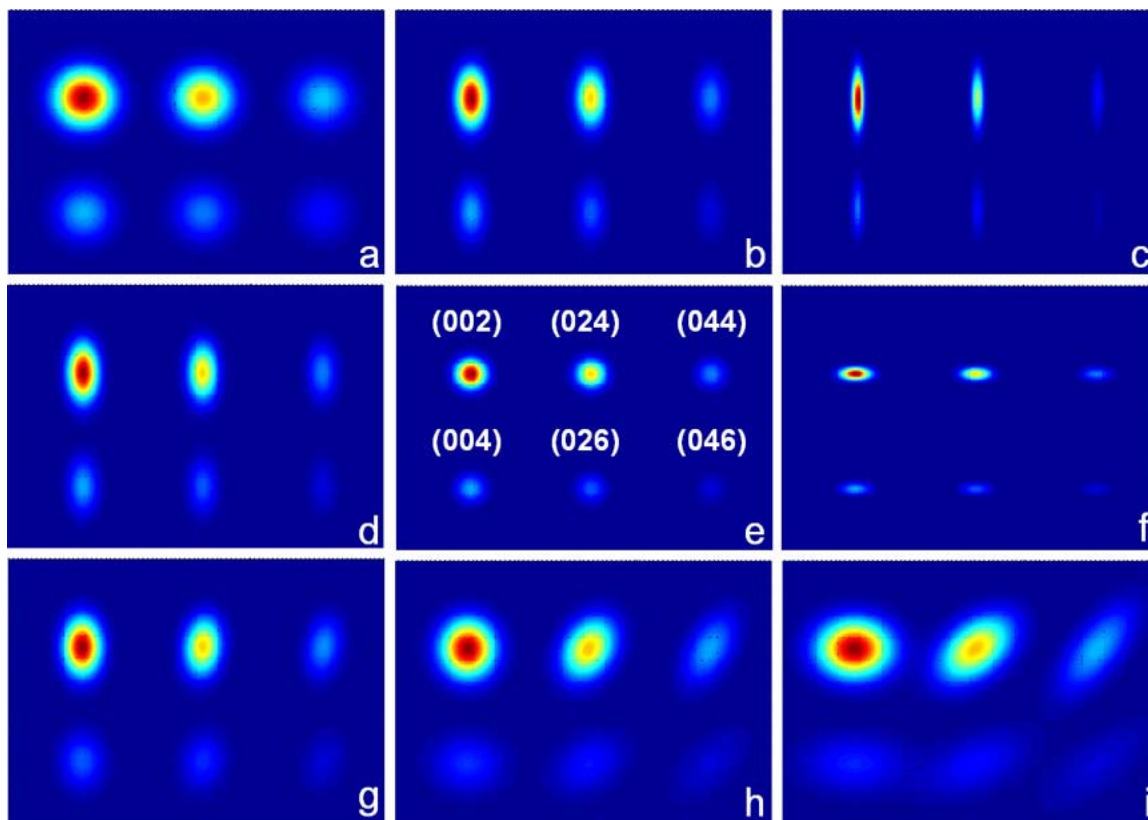


Figure 2.2 Simulated MgO RHEED patterns, 25 keV at  $2.6^\circ$  incidence angle, as the parameters for grain size ( $L$ ), effective electron penetration depth ( $h$ ), and out-of-plane orientation distribution ( $\Delta\omega$ ) are changed. Images a-c have  $h = 5$  nm,  $\Delta\omega = 0^\circ$  and a)  $L = 5$  nm, b)  $L = 10$  nm, and c)  $L = 25$  nm. Images d-f have  $L = 10$  nm,  $\Delta\omega = 0^\circ$ , and d)  $h = 5$  nm, e)  $h = 10$  nm, and f)  $h = 25$  nm. Images g-i have  $h = 5$  nm,  $L = 10$  nm, and g)  $\Delta\omega = 4^\circ$ , h)  $\Delta\omega = 8^\circ$ , and i)  $\Delta\omega = 12^\circ$ .

time scales directly with the number of pixels included in the simulated RHEED pattern, taking about 30 seconds for a 1000 by 750 pixel image on a 350 MHz processor.

## 2.2.2 Dependence of RHEED pattern on thin film microstructure

### 2.2.2.1 Diffraction spot shape

The kinematical simulation calculates a RHEED pattern using the following specified parameters: grain size  $L$ , effective electron penetration depth  $h$ , out-of-plane orientation distribution  $\Delta\omega$ , and in-plane orientation distribution  $\Delta\phi$ . Figure 2.2 shows



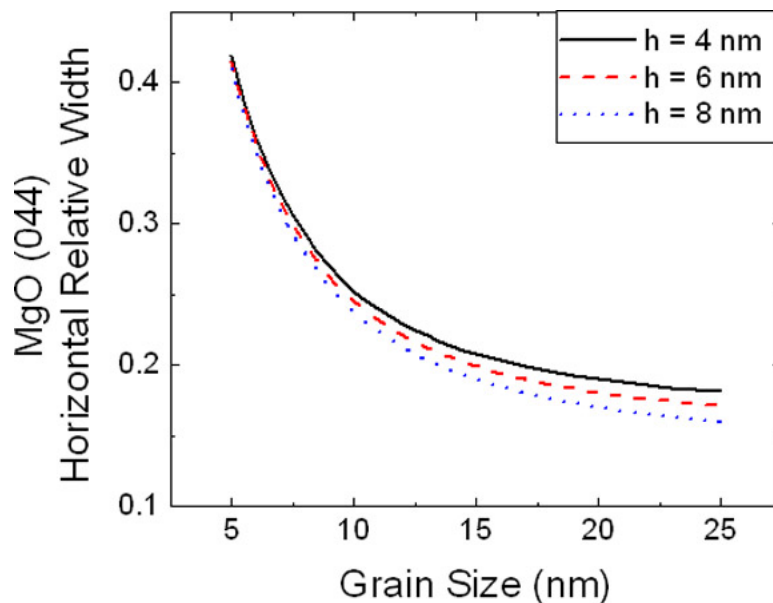


Figure 2.4 Calculated horizontal MgO (044) diffraction spot width as a fraction of the distance between the (004) and (024) diffraction spots.

the full width at half maximum (FWHM) of the Gaussian fit. Unfortunately, film microstructure can not be determined by looking at a single diffraction spot because the width of the diffraction spot in any direction results from a convolution of contributions from the different microstructure characteristics. The convolution mainly results from the broadening caused by the out-of-plane orientation distribution. Whereas finite electron penetration depth and grain size cause spot broadening in perpendicular directions, the broadening from the out-of-plane orientation distribution typically has components along both horizontal and vertical axes.

The effects of microstructure on RHEED spot shapes can be determined quantitatively using the RHEED simulation. Figure 2.4 plots the calculated MgO (044) diffraction spot lateral width as a function of grain size  $L$  and electron penetration depth  $h$  for a fixed out-of-plane orientation distribution  $\Delta\omega = 5^\circ$ . The ranges for  $h$  and  $L$  plotted represent the typical values observed for IBAD MgO. The lateral spot width is weakly

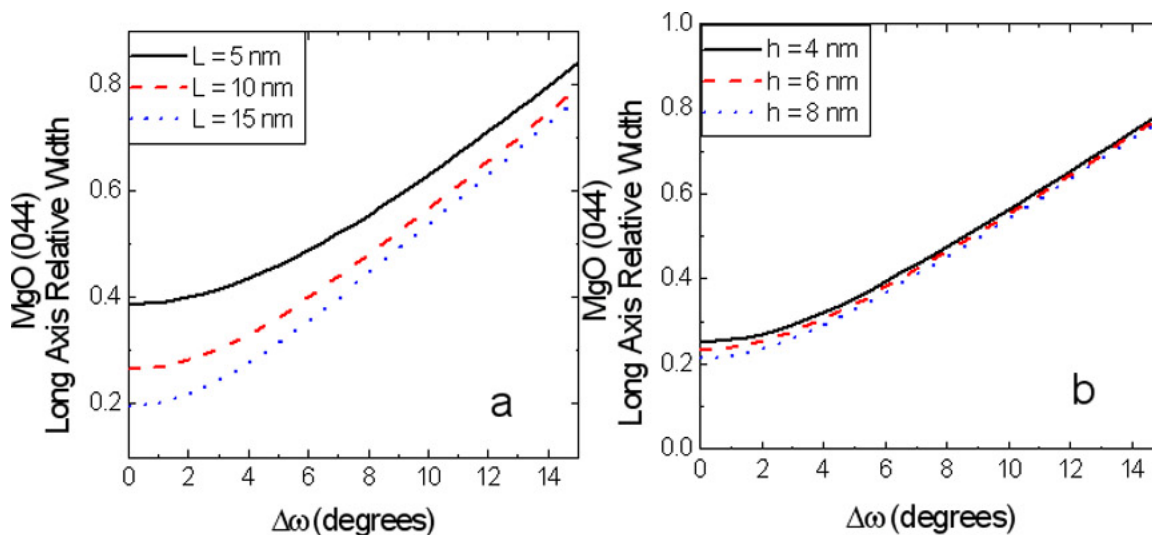


Figure 2.5 Simulated width of the (044) MgO diffraction spot in the direction perpendicular to the non-diffracted beam. The width is normalized to the distance between the (004) and (024). In a) the effective electron penetration depth ( $h$ ) is set to 5 nm, while in b) the grain size ( $L$ ) is set to 10 nm.

dependent on the electron penetration depth ( $h$ ) and strongly dependent on grain size.

The separation between these two parameters is maximized for spots along the (00) Bragg rod. RHEED simulations calculate that the lateral widths of the (004) and (006) diffraction spots do not change at all (to four significant figures) as  $h$  goes from 4 nm to 8 nm. From the Ewald Sphere construction we know that the out-of-plane orientation distribution will elongate the diffraction spot in the direction perpendicular to the non-diffracted beam. However, measuring the diffraction spot in this direction is not a direct measurement of out-of-plane orientation distribution because there are contributions from both finite grain size and electron penetration depth.

In Figure 2.5 the width of the MgO (044) diffraction spot in the direction perpendicular to the non-diffracted spot ( $45^\circ$  from vertical) is plotted as a function of out-of-plane orientation distribution ( $\Delta\omega$ ). A single diffraction spot width can result from several different values of  $\Delta\omega$  if the grain sizes and electron penetration depths are

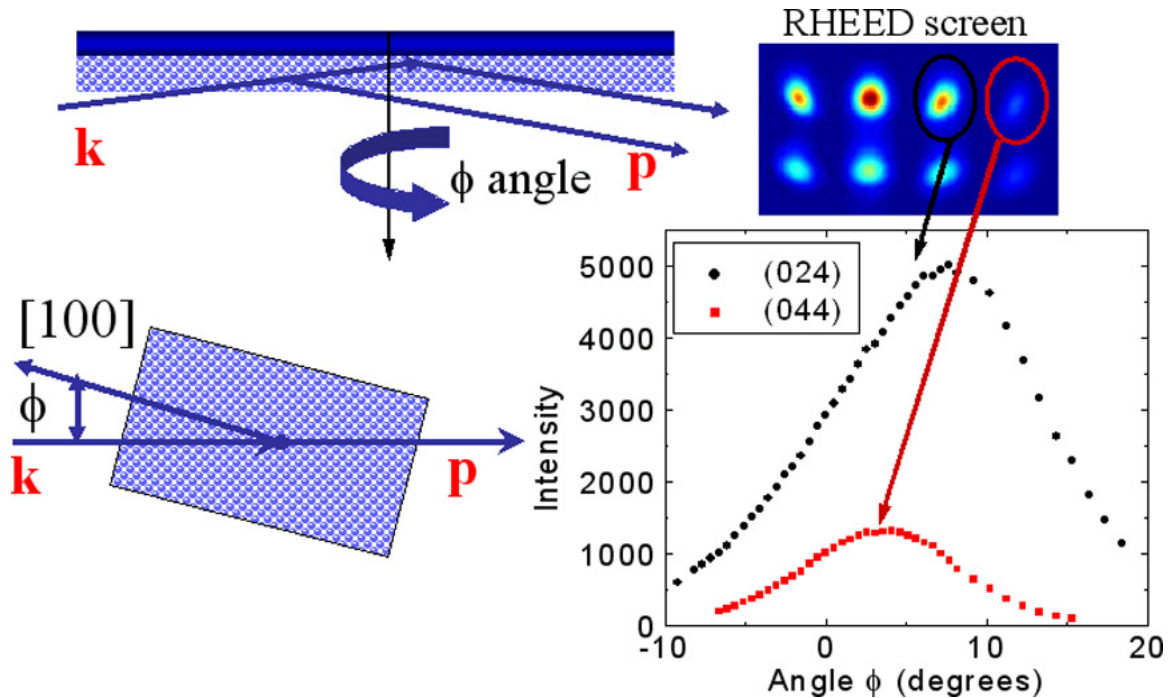


Figure 2.6 Schematic of a RHEED in-plane rocking curve experiment. Incident electrons  $\mathbf{k}$  from the electron gun are diffracted by the polycrystalline film into wave vectors  $\mathbf{p}$ , which are collected on a phosphorous screen and imaged (the RHEED pattern). The substrate is rotated about its vertical axis and the intensity of several diffraction spots are recorded as a function of the rotation angle  $\phi$ . The rocking curves are characterized by the FWHM from a Gaussian fit.

different. A similar effect is observed on the lateral and vertical spot widths, where the grain size and electron penetration depth, respectively, can not be determined if the out-of-plane orientation is unknown.

For any diffraction spot that we choose, there are three unknown parameters ( $h$ ,  $L$ , and  $\Delta\omega$ ) and there are three measurable parameters (the widths of the diffraction spots in the vertical, horizontal, and tilted along the axis perpendicular to the non-diffracted spot). From elementary algebra we know that we can uniquely determine  $h$ ,  $L$ , and  $\Delta\omega$  from the three measured widths because we have three equations and three unknowns.

The equations are  $f(h, \Delta\omega) =$  vertical width,  $f(L, \Delta\omega) =$  horizontal width, and  $f(h, L, \Delta\omega) =$  the width along the axis perpendicular to the non-diffracted spots.

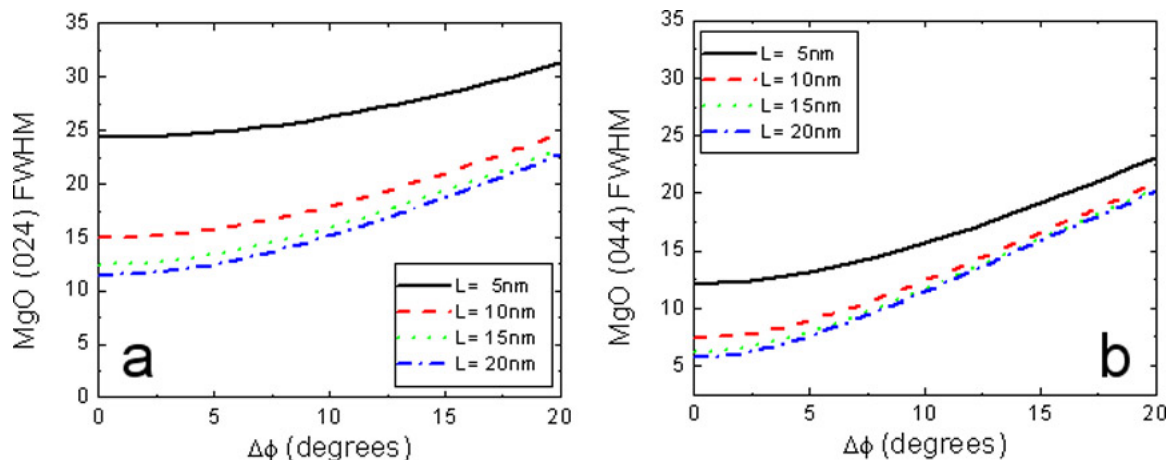


Figure 2.7 Simulated in-plane rocking curve FWHM ( $\Delta\phi$  degrees) for the MgO a) (024) and b) (044) diffraction spots, where the out-of-plane orientation distribution is equal to  $5^\circ$  FWHM ( $\Delta\omega$ ). The in-plane rocking curve displays an inverse relationship to grain size ( $L$ ) for grain sizes smaller than 20 nm.

Unfortunately the exact form of these equations is unknown so it can not be solved analytically. In section 2.3 I will discuss how we get around not knowing the form of the equations.

### 2.2.2.2 In-plane rocking curve calculations

The kinematical simulation predicts that the relative intensities of diffraction spots along the (00), (02), and (04) Bragg rods are correlated to the in-plane orientation distribution. Because the kinematic simulation does not reliably calculate absolute diffraction spot intensities, we can not quantitatively predict the effects of in-plane orientation distributions on a single RHEED pattern. In Section 2.2 we noted that kinematically calculated diffraction spot intensities will be renormalized by dynamical scattering. The constant of renormalization is unique to each diffraction spot, but does not change as the sample is rotated. We therefore expect that the kinematical simulation can be used to calculate a RHEED in-plane rocking curve because the measurements do not rely on knowing absolute intensities.

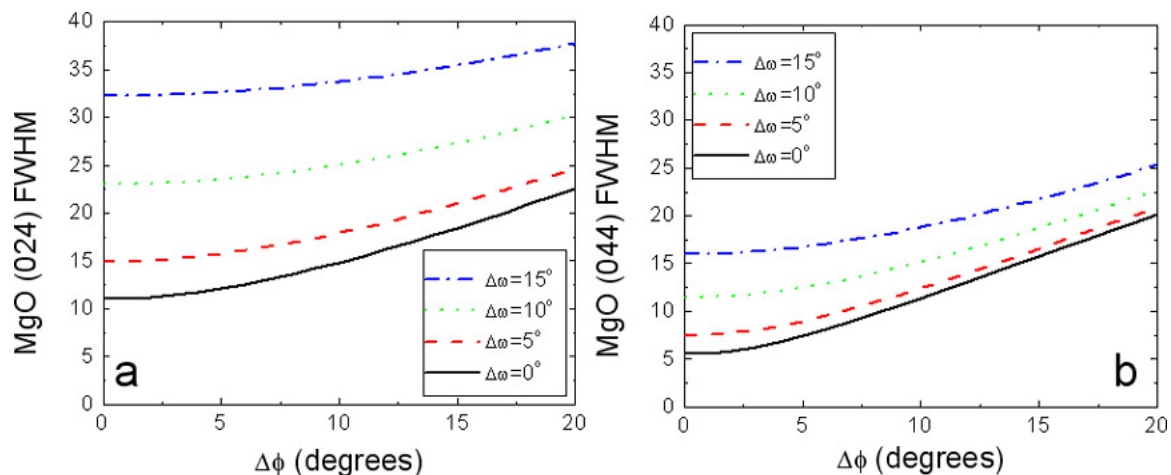


Figure 2.8 Simulated in-plane rocking curve FWHM ( $\Delta\phi$  degrees) for the MgO a) (024) and b) (044) diffraction spots and grain size set to 10 nm. The in-plane rocking curve displays a direct dependence on out-of-plane orientation distribution ( $\Delta\omega$ ).

RHEED in-plane rocking curves are constructed by rotating the sample around the surface normal and recording the maximum intensity for each diffraction spot for each angle  $\phi$  (the angle between the nominal [100] zone axis and the projection of the incident electron beam on the sample surface) (see Figure 2.6). The resulting intensity distributions are characterized by the FWHM. Dynamical renormalization of the diffraction spot intensities would only change the height of the rocking curves, not the FWHM.

Kinematical simulations predict that the RHEED in-plane rocking curve FWHM not only depends on the in-plane orientation distribution ( $\Delta\phi$ ), it also depends on the out-of-plane orientation distribution ( $\Delta\omega$ ), and lateral grain size ( $L$ ). Figure 1.7 illustrates the dependence of the RHEED in-plane rocking curve FWHM for the (024) and (044) diffraction spots as a function of  $\Delta\phi$  and  $L$  for  $\Delta\omega = 5^\circ$ . The simulation predicts that for small grain sizes ( $L$ ), the FWHM of the RHEED in-plane rocking curve is inversely proportional to  $L$ . As the grain size increases beyond 30 nm the dependence on  $L$  is

negligible, but for small grain sizes it is essential to know  $L$  to measure  $\Delta\phi$  using the RHEED in-plane rocking curve from a single diffraction spot.

Figure 2.8 illustrates the calculated dependence of the RHEED in-plane rocking curve FWHM for the (024) and (044) diffraction spots as a function of  $\Delta\phi$  and  $\Delta\omega$  for  $L = 10$  nm (a typical value for IBAD MgO). The RHEED in-plane rocking curve FWHM is directly proportional to the out-of-plane orientation distribution. The simulations show that the effect of the out-of-plane orientation distribution on the rocking curve varies for different diffraction spots, i.e., the farther away from (000) the diffraction spot is, the larger the effect of the out-of-plane orientation distribution on the in-plane rocking curve. Without *a priori* knowledge of out-of-plane orientation distribution and grain size, the in-plane orientation distribution cannot be determined from the in-plane rocking curve of a single diffraction spot. Because the out-of-plane orientation distribution and grain size contributions to the in-plane rocking curves depend on the diffraction spot it is possible to separate their contributions from the effects of the in-plane orientation distribution.

### 2.2.2.3 Generalization to all cubic crystals

The previous examples for the effects of biaxial texture, grain size, and electron penetration depth on RHEED patterns and in-plane RHEED rocking curves were done for small grained MgO. Other crystals can be calculated by changing the electron scattering potential  $V_G$  in Eq. (2.6) and choosing the proper inverse lattice vectors. The diffraction spot shapes are independent of dynamical scattering effects, therefore for other materials besides MgO quantitative effects of grain size, electron penetration depth, and out-of-plane orientation distribution can be calculated. We have calculated in-plane rocking curve dependence on in-plane orientation distribution ( $\Delta\phi$ ) and diffraction spot widths

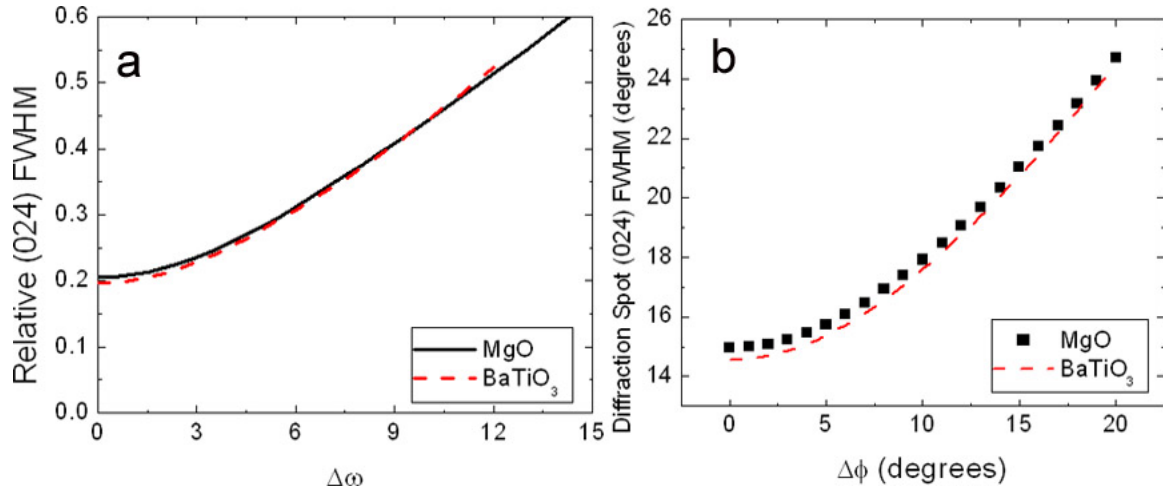


Figure 2.9 Comparison of the simulated RHEED dependence of MgO and BaTiO<sub>3</sub> on biaxial texture. a) For grain size ( $L = 10$  nm) and effective electron penetration depth ( $h = 6$  nm) the (024) diffraction spot width in the direction perpendicular to the non-diffracted spot, as a fraction of the separation between the (004) and (024) diffraction spots, is measured as a function of the out-of-plane orientation distribution ( $\Delta\omega$ ). b) The (024) in-plane rocking curve FWHM is measured as a function of the in-plane orientation distribution ( $\Delta\phi$ ) with  $\Delta\omega = 5^\circ$  FWHM and  $L = 10$  nm.

dependence on out-of-plane orientation distribution for BaTiO<sub>3</sub>, as well as for MgO. The dependence of the diffraction spot width on the out-of-plane orientation distribution for diffraction spot (024) for BaTiO<sub>3</sub> and MgO are plotted in Figure 2.9a. The functional dependence of the out-of-plane orientation distribution on diffraction spot is similar for both materials. The difference in length of the inverse lattice vectors, which is small, for the different sized crystals causes the difference in the magnitude of the diffraction spot elongation from crystal to crystal. For a fixed grain size ( $L = 10$  nm) and out-of-plane orientation distribution ( $\Delta\omega = 5^\circ$  FWHM), the (024) BaTiO<sub>3</sub> in-plane rocking curve very closely tracks the (024) MgO in-plane rocking curve (see Figure 2.9b). This example illustrates that other cubic crystals have RHEED pattern dependencies on biaxial texture that are similar to those observed for MgO, confirming the general applicability of the RHEED-based method of biaxial texture analysis for all cubic materials.

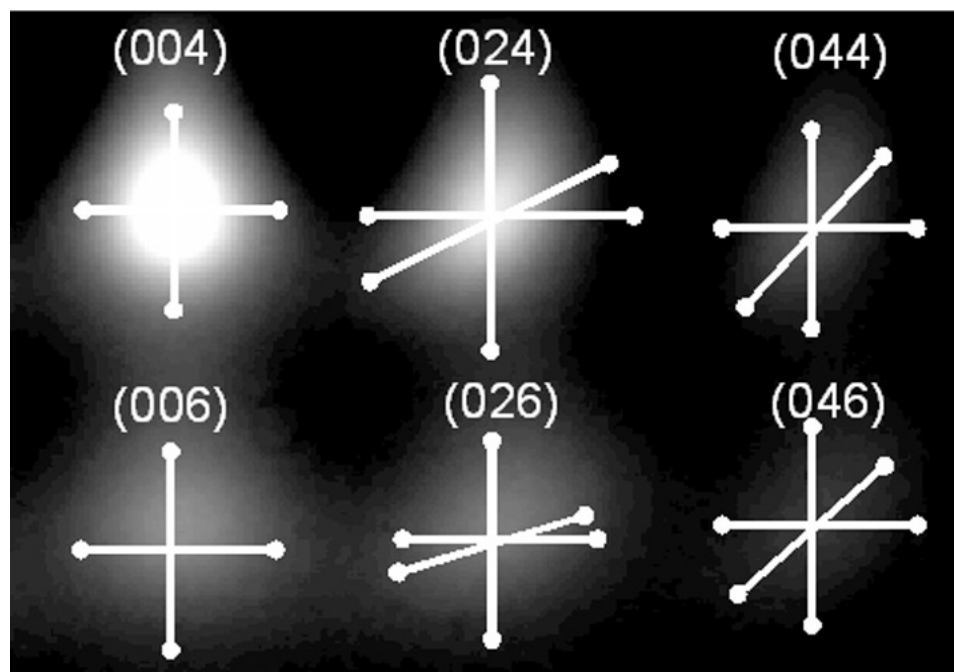


Figure 2.10 Experimental MgO RHEED image at 25 keV and  $2.6^\circ$  incidence angle. The diffraction spots shown are those which are used for RHEED-based biaxial texture analysis. The cuts across the diffraction spots show the directions across which the computer program measures the FWHM of the diffraction spots.

Using the kinematic RHEED simulations for in-plane RHEED rocking curves relies on the fact that the renormalization of diffraction spot intensity is constant for a single diffraction spot as the crystal is rotated about its z-axis. This assumption is especially good for a small grained material like MgO where multiple scatterings between grains guarantee that the multiple scattering effects will add incoherently like in a randomly oriented polycrystal. In the small grained limit we can expect Eq. (2.3) to be valid and the dynamical renormalization of the kinematic scattering intensity to stay constant. This assumption may not be valid for large grained materials. To determine the accuracy of the kinematic simulation for large grained materials, simulation results need to be compared with experimental RHEED in-plane rocking curves.

## 2.3 Experimental method for measuring biaxial texture of RHEED on MgO

### 2.3.1 Single-image RHEED analysis

Our RHEED-based biaxial texture analysis employs the previously described kinematical electron scattering model<sup>17</sup>. These calculations predict that spot shapes are sensitive to the film microstructure, as shown in Figure 2.3. Diffraction spot width and height are inversely proportional to the effective grain size and electron penetration depth, respectively. The width of the diffraction spot in the direction perpendicular to the location of the through spot, the non-diffracted electron beam, is directly proportional to the out-of-plane grain orientation distribution ( $\Delta\omega$ ). We therefore characterize RHEED patterns, whether calculated using a computer simulation or from an experiment, by cutting across the diffraction spots along the previously mentioned directions and measuring the FWHM of these cuts, as shown in Figure 2.10. We call this method “single-image analysis”. All diffraction spots shown in Figure 2.10 are analyzed simultaneously, and then compared to calculated RHEED pattern measurements using a lookup table. Earlier we said that analyzing a single diffraction spot should be sufficient for determining the grain size ( $L$ ), effective electron penetration depth ( $h$ ), and out-of-plane orientation distribution ( $\Delta\omega$ ). By simultaneously measuring several diffraction spots, we are getting redundant measurements and decreasing the experimental error.

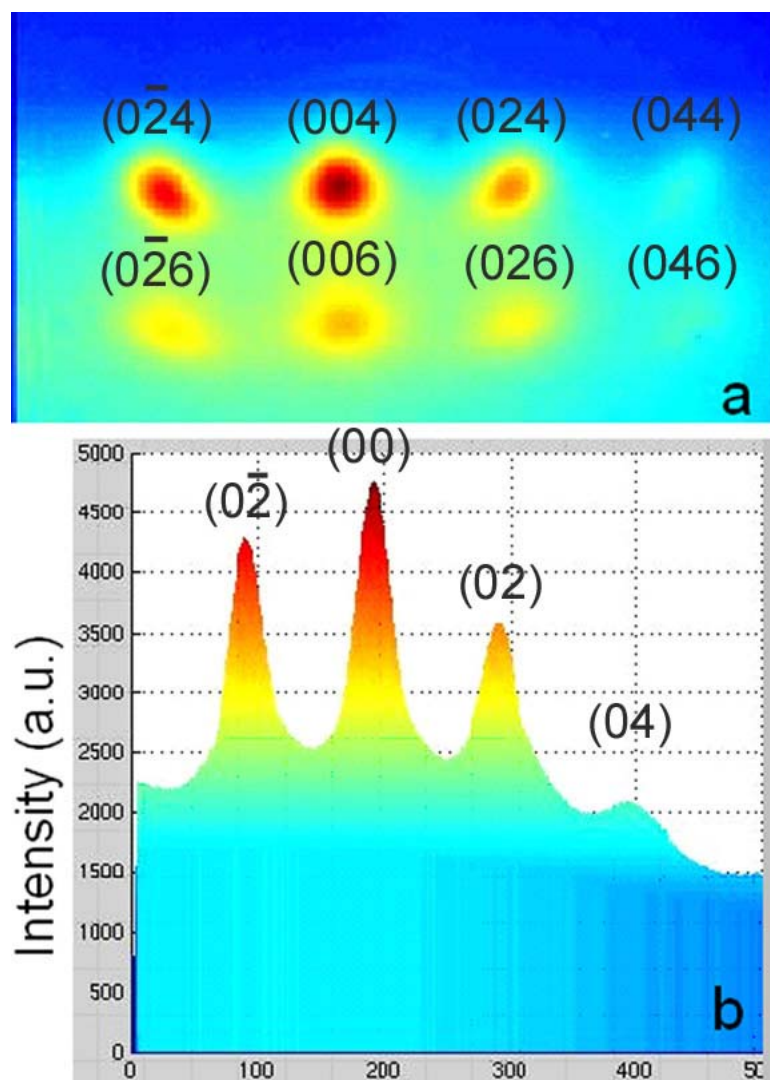


Figure 2.11 Experimental IBAD MgO RHEED images taken at 25 keV and  $2.6^\circ$  incidence. a) Top view. b) Side view. The diffuse background is significant fraction of the diffraction spot intensity.

### 2.3.1.1 Background subtraction

Experimental RHEED images contain diffuse background contributions to spot shape that are not accounted for in the kinematical simulation. It was therefore necessary to create an experimental method to deconvolute the diffuse background scattering from diffraction spots before they could be compared with simulation results. Both a planar and side view of an experimental RHEED pattern from an IBAD MgO sample with in-

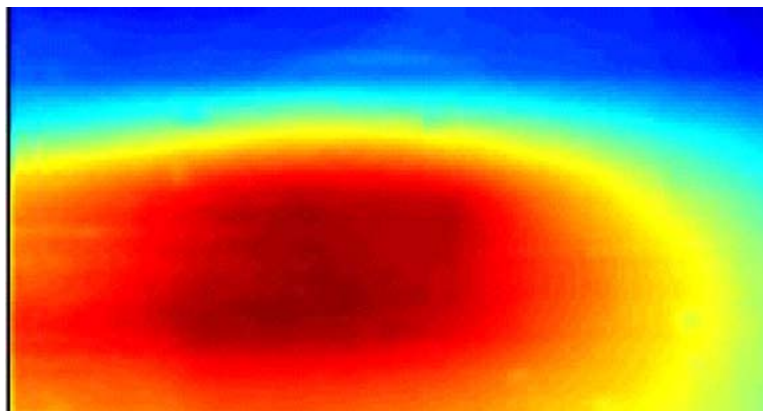


Figure 2.12 RHEED image of amorphous Si<sub>3</sub>N<sub>4</sub> taken at 25 keV and 2.6° incidence angle before IBAD MgO growth.

plane orientation distribution ( $\Delta\phi$ ) = 6.7° (one of the most highly in-plane aligned films we have grown) is shown in Figure 2.11. From the side view (Figure 2.11b), we can see that the diffuse background represents a significant fraction of the diffraction spot intensity and fitting a Gaussian to any spot requires knowing what the function of the background looks like underneath the diffraction spot.

Diffuse scattering results from random surface scattering off of the film surface (and other scattering processes not accounted for in the kinematic scattering model) and depends on the shape of the incident electron beam. From observation we discovered that the diffuse background from IBAD MgO was very similar to scattering from amorphous Si<sub>3</sub>N<sub>4</sub>. Therefore, before growing IBAD MgO on amorphous Si<sub>3</sub>N<sub>4</sub>, we take a RHEED image of the amorphous substrate (Figure 2.12) and then subtract this image from subsequent MgO RHEED images. This method of background subtraction has the advantage of accounting for the instrument effects on diffuse scattering and provides a measurement of the background that is unique for each experimental set up.

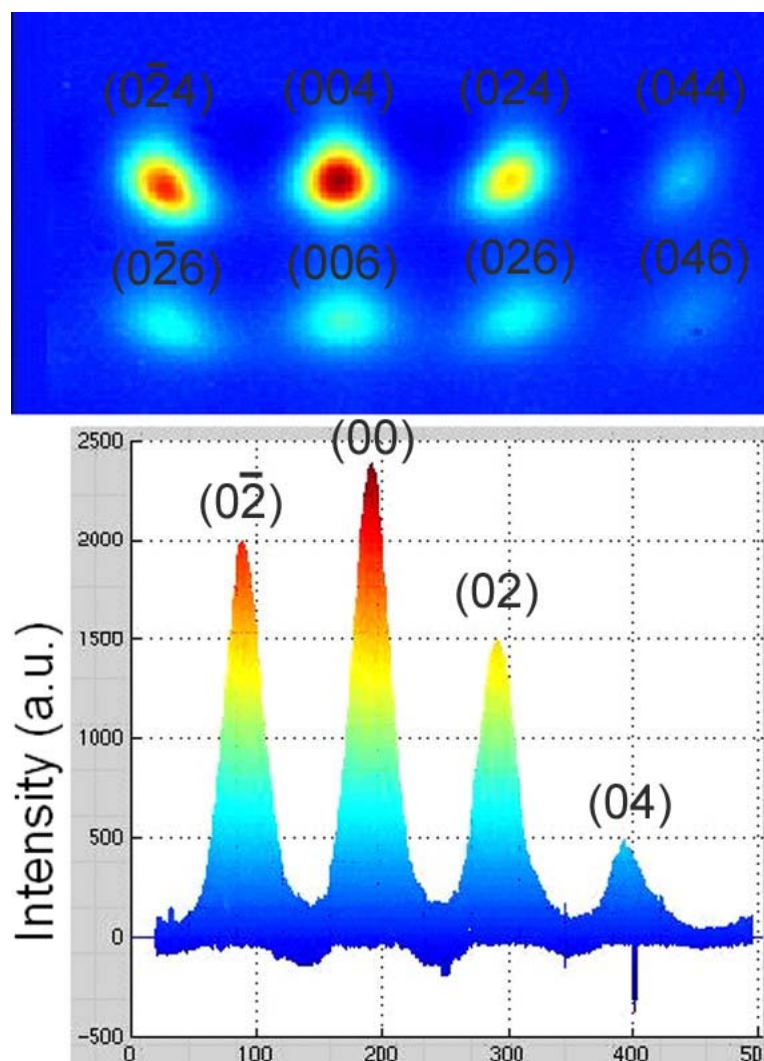


Figure 2.13 Background subtracted experimental RHEED images of IBAD MgO taken at 25 keV and  $2.6^\circ$  incidence angle. These are the background subtract images of Figure 2.11. a) Top view. b) Side view.

The background subtracted RHEED images from Figure 2.11 are shown in Figure 2.13. The electron beam current drifts slightly during a growth experiment, but this can be accounted for by rescaling the background image using a location on the RHEED pattern which should not include any contribution from diffraction, i.e. locations between the diffraction spots. The result is a greatly reduced contribution from the background to diffraction spot shape, allowing for measurement of the relevant diffraction spot widths.

This background subtraction process assumes that the functionality of the diffuse background scattering from the amorphous  $\text{Si}_3\text{N}_4$  substrate is valid for the diffuse scattering from the biaxially textured IBAD MgO film. After the first nanometer of IBAD MgO growth, the RHEED electrons no longer penetrate through to the amorphous  $\text{Si}_3\text{N}_4$ , so the contribution to the broad background from an amorphous layer does not exist. Even so, experiments have shown that the shape of the  $\text{Si}_3\text{N}_4$  amorphous electron scattering is approximately the same shape as the diffuse background for IBAD MgO (see Figure 2.13).

The background can also be subtracted by assuming that the area between the diffraction spots contains no contribution from diffraction and that by linearly interpolating between the diffuse electron scattering intensities on either side of the spot one can make a good approximation of the value of the diffuse electron scattering underneath the diffraction spot. This is done for in-plane RHEED rocking curves where the only important measurement is the absolute diffraction spot intensity. However, for single-image analysis the shape of the diffraction spot is critical and by forcing the background to go to zero at a user specified point could distort the spot shape and introduce user prejudice into the measurement. By blindly subtracting the amorphous  $\text{Si}_3\text{N}_4$  RHEED image from subsequent growth images, we avoid distorting the diffraction spots, we avoid user prejudice, and this method has been shown to work well for IBAD MgO. The appropriateness of this method needs to be evaluated when it is applied to other material systems because the functionality of the diffuse backgrounds may change from system to system. The section in the appendix, which addresses how to operate the RHEED analysis code, details several other background subtraction algorithms.

### 2.3.1.2 Lookup tables

The lookup table was generated by calculating the RHEED pattern for all relevant combinations of effective grain size (4-25 nm), electron penetration depth (2.5-10 nm), and out-of-plane orientation distribution (0-20 degrees FWHM) and measuring the FWHM of cuts across the six diffraction spots shown in Figure 2.10 in the directions where the RHEED pattern is sensitive to electron penetration depth ( $h$ ), grain size ( $L$ ), and out-of-plane orientation distribution ( $\Delta\omega$ ). An example of the lookup tables is included in the appendix. The effects of the in-plane orientation distribution on diffraction spot shapes are negligible, so the in-plane orientation distribution FWHM was set to  $10^\circ$  for lookup table calculations, which is a typical value for in-plane orientation distributions observed in IBAD MgO.

Lookup table entries exist for all combinations of effective grain size, electron penetration depth, and out-of-plane orientation distribution and contain the measurements of the FWHM of the cuts across each previously specified spot along the previously specified directions. The film effective grain size, electron penetration depth, and out-of-plane orientation distribution are determined by comparing the FWHM of experimental RHEED pattern diffraction spot cuts with the FWHM of the spot cuts in the lookup table. For each lookup table entry the experimentally measured FWHM of each spot cut is subtracted from the lookup table FWHM of the same spot in the same direction. The differences between the experimental and lookup table measurements are then individually squared before being added together to yield a total sum of the square errors measurement for that lookup table entry. Equation (2.11) describes how the sum of the

square error is calculated for each lookup table when comparing an experimental RHEED pattern with the lookup tables.

$$\begin{aligned}
yError(h, L, \Delta\omega) &= \sum_{i=1}^6 \left( yFWHM_{i,exp} - yFWHM_{i,lookup(h,L,\Delta\omega)} \right)^2 \\
zError(h, L, \Delta\omega) &= \sum_{i=1}^6 \left( zFWHM_{i,exp} - zFWHM_{i,lookup(h,L,\Delta\omega)} \right)^2 \\
lError(h, L, \Delta\omega) &= \sum_{i=1}^6 \left( lFWHM_{i,exp} - lFWHM_{i,lookup(h,L,\Delta\omega)} \right)^2 \\
sError(h, L, \Delta\omega) &= \sum_{i=1}^6 \left( sFWHM_{i,exp} - sFWHM_{i,lookup(h,L,\Delta\omega)} \right)^2 \\
Error(h, L, \Delta\omega) &= yError(h, L, \Delta\omega) + zError(h, L, \Delta\omega) \\
&\quad + lError(h, L, \Delta\omega) + sError(h, L, \Delta\omega)
\end{aligned} \tag{2.11}$$

In Equation (2.11) the summation over  $i$  from 1 to 6 represents summing over the six different diffraction spots analyzed: (004), (006), (024), (026), (044), and (046). The  $yFWHM$ ,  $zFWHM$ ,  $lFWHM$ , and  $sFWHM$  denote the FWHM of the width of the diffraction spot cut in the  $y$  direction (lateral),  $z$  direction (vertical), long axis direction of the diffraction spot (the direction perpendicular from the direction between the diffraction spot location and the location of the undiffracted RHEED beam), and the short axis direction of the diffraction spot (perpendicular to the long axis direction). The subscript  $exp$  denotes the value measured from the experimental RHEED pattern and  $lookup(h,L,\Delta\omega)$  denotes the value in the lookup table at the designated electron penetration depth ( $h$ ), grains size ( $L$ ), and out-of-plane orientation distribution ( $\Delta\omega$ ). The sum of the square errors is  $Error(h,L,\Delta\omega)$ .

The sum of the square errors is calculated for every lookup table entry and the microstructural parameters are determined as the simulated combination of electron penetration depth, effective grain size, and out-of-plane orientation distribution that yields the smallest sum of the square errors. Even though the kinematical electron

scattering calculations predict that the relative intensities of diffraction spots along the (00), (02), and (04) Bragg rods are correlated to the in-plane orientation distribution, it is not a very sensitive measurement. Besides the lack of sensitivity to relative spot intensities, kinematic simulations do not calculate absolute diffraction spot intensities accurately. Therefore, RHEED in-plane rocking curves are used to measure the in-plane orientation distribution.

### 2.3.2 RHEED in-plane rocking curves

RHEED in-plane rocking curves are constructed by rotating the sample around the surface normal and recording the maximum intensity for each diffraction spot, minus the average background intensity, for each angle  $\phi$  (the angle between the nominal [100] zone axis and the projection of the incident electron beam on the sample surface) (see Figure 2.6). The resulting intensity distributions are characterized by the FWHM. To experimentally measure in-plane grain orientation distribution ( $\Delta\phi$ ), the FWHM of RHEED in-plane rocking curves<sup>22</sup> from the (024), (026), (044), and (046) diffraction spots are measured simultaneously and compared to the FWHM of calculated in-plane rocking curves in another lookup table. As for the single-image analysis, a lookup table was generated by calculating the FWHM of diffraction spot in-plane RHEED rocking curves for all relevant film parameter combinations, i.e. effective grain size (4-25 nm), out-of-plane orientation distribution (0-20 degrees FWHM), and in-plane orientation distribution (0-30 degrees FWHM). In-plane rocking curve FWHM was calculated to be independent of the electron penetration depth so it was set to 5 nm, the value most often measured using single-image analysis at this electron energy and incidence angle. Each lookup table entry was indexed by its unique combination of the relevant film parameters

(grain size, out-of-plane orientation distribution, and in-plane orientation distribution) and contained the FWHM of the rocking curves from the (024), (026), (044), and (046) diffraction spots. The in-plane orientation distribution is determined by searching the lookup table for the simulation that has RHEED in-plane rocking curves that most closely match the experimental rocking curves for all four diffraction spots. The FWHM of the in-plane rocking curves are highly correlated with the in-plane orientation distribution, however, the rocking curve FWHM is also convoluted with the effective grain size and out-of-plane orientation distribution. Therefore, to accurately measure in-plane orientation distribution using in-plane rocking curves, the effective grain size and out-of-plane orientation distribution are first measured using single-image analysis as described above. The subsequent comparisons between the experimental and simulated FWHM of the RHEED in-plane rocking curves in the lookup tables are restricted to simulations with the effective grain size and out-of-plane orientation distribution measured using single-image analysis.

## **2.4 RHEED measurement reliability**

### **2.4.1 Experimental setup**

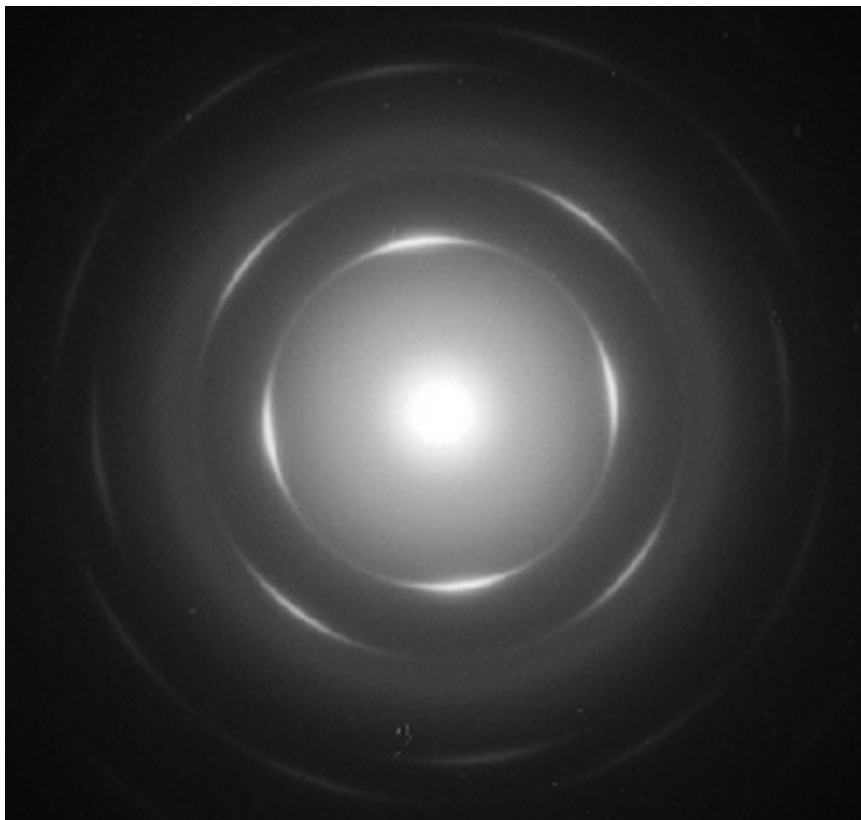


Figure 2.14 TEM image of IBAD MgO on amorphous  $\text{Si}_3\text{N}_4$ . The fourfold symmetric arcs indicate that the MgO has a preferred in-plane orientation and the angular width of the arcs is a measurement of the in-plane orientation distribution ( $\Delta\phi$ ).

Experimental RHEED in-plane rocking curves and single-image analyses were performed on 5 to 11 nm thick IBAD MgO films. MgO was deposited, at room temperature, on amorphous  $\text{Si}_3\text{N}_4$  by electron beam evaporation at deposition rates ranging from 1.7 to 3.1 Å/s, as measured by a quartz crystal monitor. Ion irradiation during MgO growth was carried out with 750 eV  $\text{Ar}^+$  ions at  $45^\circ$  incidence angle.

Ion/MgO flux ratios were varied between 0.33 and 0.58. A single-crystal of MgO was also analyzed for reference. Optimal film thickness was determined by monitoring the (004) diffraction peak intensity<sup>23</sup>. RHEED measurements were done at 25 keV and 2.6 degrees incidence angle. Bragg spots along the (00), (02), and (04) Bragg rods, as shown in Figure 2.10, were used in the RHEED analysis. A 16 bit, 1024 x 1024 pixels

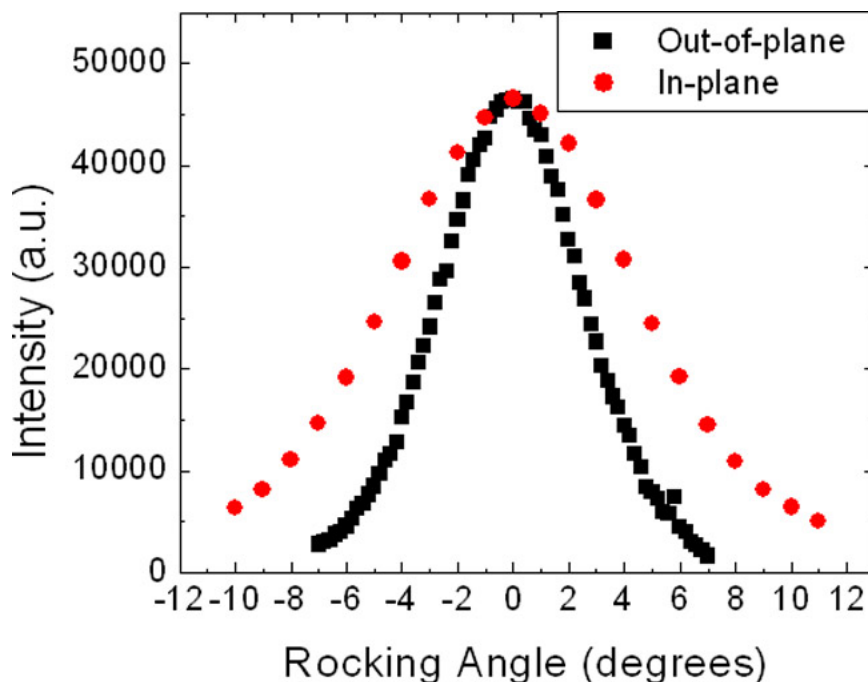


Figure 2.15 In-plane and out-of-plane x-ray rocking curves of IBAD MgO (002) with in-plane orientation distribution  $\Delta\phi = 10.6^\circ$  and out-of-plane orientation distribution  $\Delta\omega = 6.5^\circ$  FWHM. The rocking curve was taken at APS.

CCD camera provided adequate dynamic range to simultaneously observe all necessary diffraction spots and spatially resolve spot shapes for single-image analysis. Before attempting single-image analysis, the diffuse background was reduced by subtracting the  $\text{Si}_3\text{N}_4$  substrate RHEED image from the IBAD MgO RHEED pattern. This procedure was necessary to resolve weak diffraction spots and reduce spot shape distortion caused by the diffuse background.

## 2.4.2 Standard texture measurement methods

Biaxial texture was also measured with either transmission electron microscopy (TEM) or x-ray diffraction, taken at the advanced photon source (APS) synchrotron, to evaluate the accuracy of RHEED-based measurements. In-plane orientation distributions were measured using TEM by taking plan-view diffraction patterns and measuring the

angular width of the diffraction spot arcs. Figure 2.14 is a TEM diffraction pattern from an in-plane orientated IBAD MgO sample. A single-crystal of MgO would show four sharp diffraction spots, a randomly oriented film would exhibit rings at the correct d-spacing, whereas the in-plane oriented polycrystalline film has arcs whose angular FWHM is a direct measure of the sample in-plane orientation distribution FWHM.

X-ray diffraction was used to measure both the in-plane ( $\Delta\phi$ ) and the out-of-plane orientation distributions ( $\Delta\omega$ ) by performing rocking curves. Out-of-plane rocking curves are accomplished by setting the sample up in the  $\theta$ - $2\theta$  configuration for diffraction of the (002) or (004) diffraction peak. Both the incident x-ray beam and the detector are then fixed while the sample is rotated about the axis perpendicular to the incoming beam and the diffraction intensity is recorded as a function of the rotation angle ( $\omega$ ). The total x-ray scattering angle is always  $2\theta$ , but the incidence angle becomes  $(\theta+\omega)$  and the population of crystals with the (001) axis rotated off of the surface normal by the angle  $\omega$  will contribute strongly to the collected diffraction intensity, while those with other rotation angles will not. Therefore, the scattering intensity collected as a function of  $\omega$  is a direct measurement of the number of grains with the out-of-plane (001) direction rotated by the angle  $\omega$  from the surface normal and represents the out-of-plane orientation distribution. The resulting out-of-plane rocking curve is fit by a Gaussian and characterized by its FWHM. The same process was followed for in-plane rocking curves, with the exception that sample was rotated about  $\chi$  by  $90^\circ$ ,  $\theta$ - $2\theta$  was fixed for the (200) and (400) diffraction peaks in a grazing incidence geometry, and the sample was rotated about its normal axis and the diffraction intensity was collected as a function of the rotation angle  $\phi$ .

An example of rocking curves taken at APS, both in-plane and out-of-plane, for a sample with out-of-plane orientation distribution FWHM ( $\Delta\omega$ ) equal to  $6.5^\circ$  and in-plane distribution FWHM ( $\Delta\phi$ ) equal to  $10.4^\circ$  is included as Figure 2.15. The synchrotron x-ray energy was 12.4 keV, for a wave length  $\lambda = 0.1$  nm, and the (002) MgO diffraction peak was located at  $2\theta = 27.477^\circ$ . The angular and energy divergence of the synchrotron beam is negligible when analyzing the width of the rocking curves. The grazing incidence geometry of in-plane rocking curves enabled the use of either a rotating anode source or the Advanced Photon Source (APS) synchrotron to measure in-plane orientation distributions. However, out-of-plane orientation measurements of IBAD MgO layers required synchrotron radiation ( $3.0 \times 10^5$  counts per second) for the out-of-plane x-ray rocking curves. Even with the APS synchrotron radiation, the x-ray rocking curves did not provide reliable out-of-plane orientation distribution measurements for 8 nm thick MgO samples with the broadest out-of-plane distributions ( $> 11^\circ$ ).

### **2.4.3 RHEED-based measurement validation: in-plane orientation distribution**

The in-plane orientation distribution measured using RHEED-based analysis is compared to measurements from TEM or x-ray scattering in Figure 2.16. The data are well represented by a linear fit, demonstrating that the RHEED-based method successfully measures the in-plane orientation distribution. There are many possible sources of deviation from the straight line. The RHEED measurements require the deconvolution of the effective grain size and out-of-plane orientation distribution from the in-plane distribution. Errors in measurements of the effective grain size and out-of-

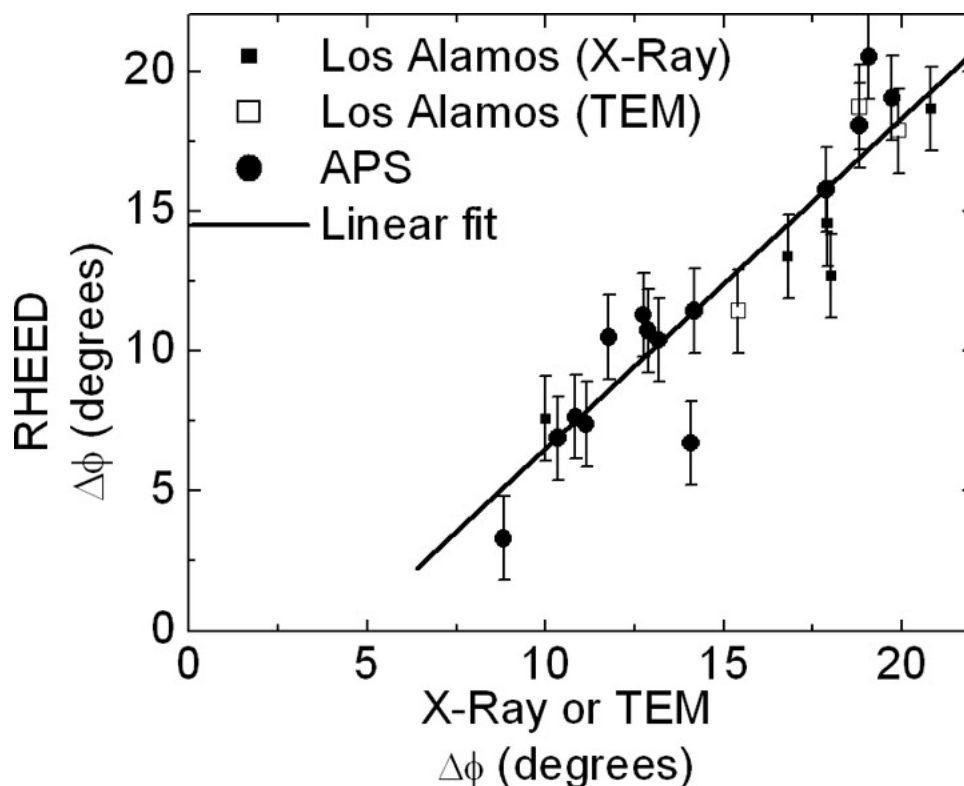


Figure 2.16 In-plane orientation distribution ( $\Delta\phi$ ) measured by RHEED analysis versus TEM or X-ray diffraction measurements. X-ray rocking curves collected using either a rotating anode source at Los Alamos or synchrotron radiation from the advanced photon source (APS). The error bars originate from limitations in deconvoluting the effects of out-of-plane orientation distribution and grain size measurements using RHEED.

plane orientation distribution therefore produce errors in the in-plane orientation distribution measurement. There is also a convolution between the measurement of effective grain size and out-of-plane orientation distribution such that an error in one measurement is compensated by an error in the other measurement. Reasonable errors for measurements of effective grain size and out-of-plane orientation distribution ( $\pm 1$  nm and  $\pm 1^\circ$  respectively) yield a total in-plane measurement error of  $\pm 1.5^\circ$ , represented by the error bars in Figure 2.16. Additional deviations from linear dependence originate in different sample to sample growth conditions which were used to produce films with in-plane orientation distributions ranging between  $6^\circ$  and  $22^\circ$  FWHM.

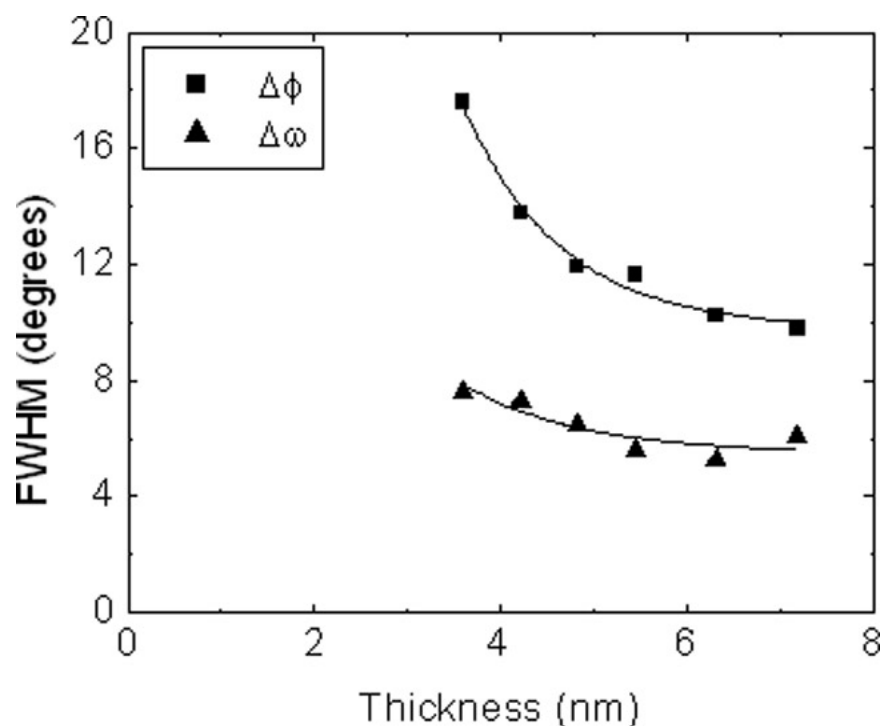


Figure 2.17 In-plane ( $\Delta\phi$ ) and out-of-plane ( $\Delta\omega$ ) orientation distribution for IBAD MgO growth as a function of film thickness measured using RHEED. The lines are a fit to the data.

RHEED-based measurements of IBAD MgO in-plane orientation distribution as a function of film thickness demonstrate that the in-plane orientation distribution decreases with increased film thickness, as illustrated in Figure 2.17. We have also observed that the rate at which the in-plane distribution decreases depends on the ion/MgO flux ratio. TEM and x-ray scattering techniques probe the biaxial texture in a scattering volume that spans the entire thin film, measuring the film's average orientation distribution, while RHEED measurements are more surface sensitive. To measure the surface sensitivity of 25 keV RHEED at  $2.6^\circ$  we grew MgO on (001) Si at room temperature and measured the intensity of the Si diffraction peaks as a function of MgO thickness. In Figure 2.18 90% of the Si diffraction intensity disappears within the first nanometer of MgO growth, emphasizing the surface sensitivity of RHEED. Therefore, the in-plane orientation

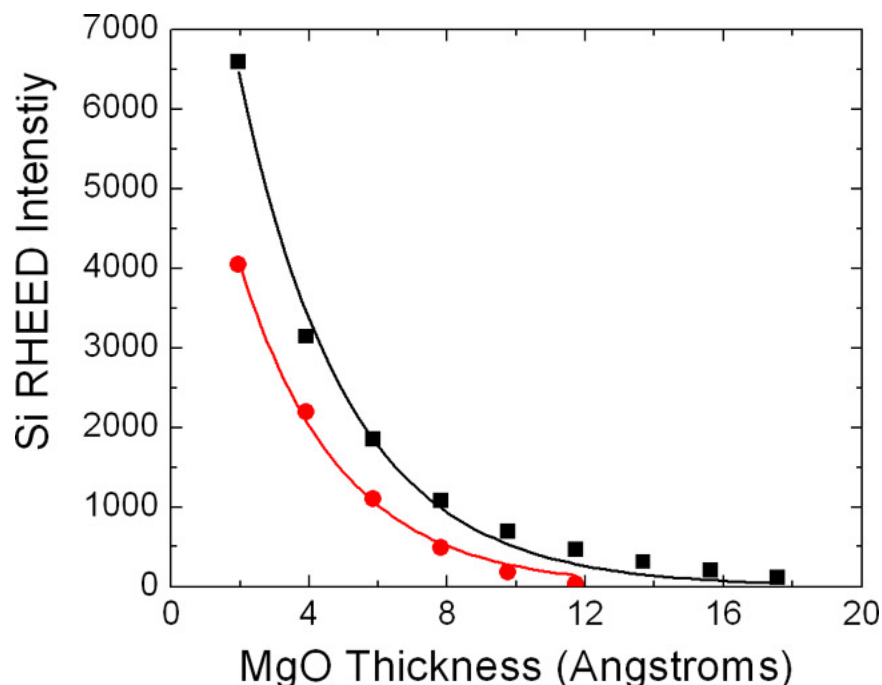


Figure 2.18 RHEED intensity of two separate Si Bragg rods as amorphous MgO was deposited on the Si (001) substrate. RHEED was performed at 25 keV at  $2.6^\circ$  incidence angle.

distribution measured by RHEED, a surface sensitive measurement, is not expected to directly correspond to the x-ray measurement, which probes the entire film thickness.

With 750 eV Ar<sup>+</sup> ion bombardment the first 3 nm of the IBAD MgO film is amorphous. However, this layer yields a biaxially textured film out of the amorphous matrix through solid phase crystallization<sup>24</sup>. The first measurable RHEED patterns reveal that the initial in-plane orientation distributions are very broad, but they narrow as the film thickens until reaching an optimal alignment. The difference between the initial and optimal in-plane orientation distribution measurements is typically on the order of  $10^\circ$  under these growth conditions. Depending on the thickness of the final film, the difference between the average and surface in-plane orientation distribution will be different, causing another possible source of deviation from the linear fit in Figure 2.16.

Optimal biaxial texture under specific growth conditions is achieved by growing the film until the (004) diffraction spot reaches its maximum intensity<sup>23</sup>. Integrating the measured in-plane orientation distribution in Figure 2.17 over the entire film thickness calculates an average film in-plane orientation distribution about  $2.5^\circ$  broader than the surface in-plane orientation distribution. This is consistent with the offset between the in-plane orientation distribution measurements based on RHEED analysis and the x-ray or TEM analysis. The magnitude of this offset depends on the thickness of the film when growth was stopped, as well as on growth conditions such as ion/MgO flux ratio.

Despite the expected differences between surface sensitive and bulk measurement methods, as well as the inherent limitations of the RHEED measurements because of convolution with effective grain size and out-of-plane distribution measurements, the comparison between RHEED and x-ray or TEM measurements is well represented by a linear fit. Not only does this analysis illustrate that RHEED can be used for *in situ*, quantitative in-plane orientation distribution measurements, it also highlights that the RHEED-based method yields more accurate estimates of surface biaxial textures than does x-ray diffraction.

#### **2.4.4 RHEED-based measurement validation: out-of-plane orientation distribution**

X-ray measurement of in-plane orientation distributions can be done with a rotating anode source because the grazing incidence geometry creates a relatively large scattering volume even for very thin films. Out-of-plane orientation distribution, measured with theta rocking curves, required synchrotron radiation to collect enough signal for reliable measurements. Even with the brightness of the 33ID-D undulator

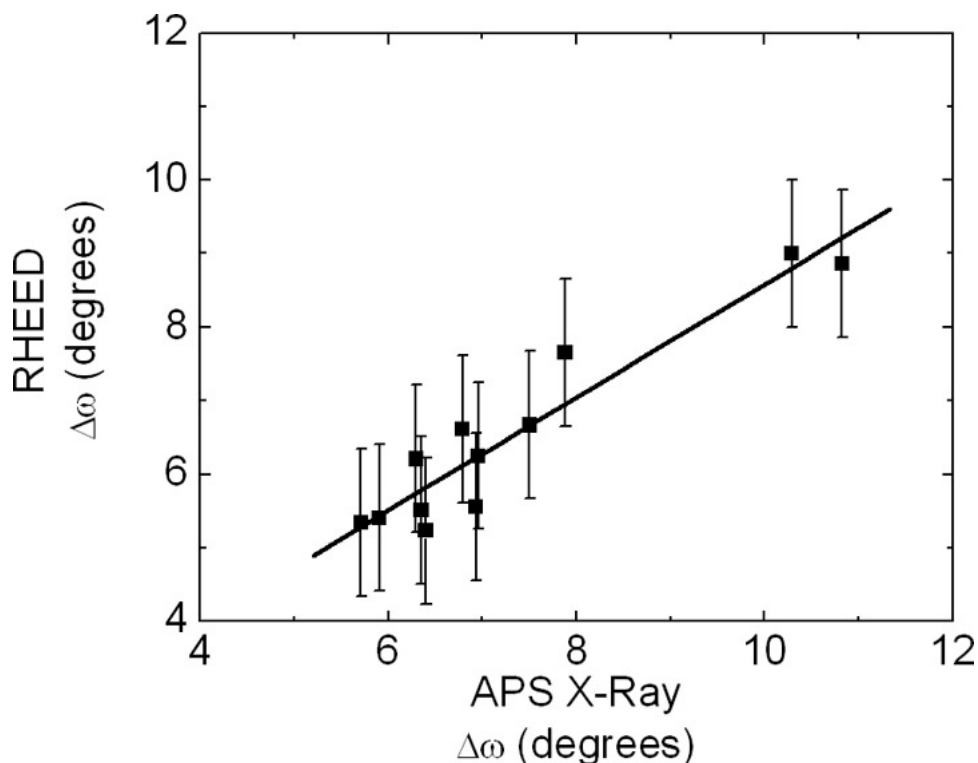


Figure 2.19 Out-of-plane orientation distribution ( $\Delta\omega$ ) measured using RHEED and synchrotron x-ray out-of-plane rocking curves. The line is a linear fit to the data. beam line at the Advanced Photon Source (APS), which produced  $3.0 \times 10^5$  counts per second (cps), some IBAD MgO films which yielded measurable in-plane rocking curves did not yield out-of-plane rocking curves with measurable peaks. RHEED measurements of out-of-plane orientation distribution are plotted in Figure 2.19 against measurements from the same samples made using x-ray rocking curves at APS. The error bars on the RHEED measurements result from expected uncertainties in the deconvolution of effects from grain size and electron penetration depth broadening of the RHEED pattern from effects caused by the out-of-plane orientation distribution. The clustering of the data points around the linear fit indicate that estimates for the measurement error may be too large. As with the in-plane measurements we expect a difference between surface sensitive RHEED measurements and bulk sensitive x-ray measurements. Figure 2.17 shows that *in situ* RHEED measurements of out-of-plane orientation distribution reveal

that the out-of-plane distribution improves as the film grows, similar to the narrowing of the in-plane orientation distribution with increasing film thickness. By integrating the RHEED out-of-plane distribution measurements over the film thickness, the average out-of-plane distribution is found to be approximately  $1^\circ$  broader than the surface measurement. This offset is consistent with the offset between the RHEED and x-ray measurements observed in Figure 2.19.

## 2.5 Conclusions

We have developed a RHEED-based method for quantitative biaxial texture measurement of MgO. RHEED patterns were calculated as a function of biaxial texture using a kinematical electron scattering model and then compared to experimental RHEED patterns using look-up tables. Comparison between biaxial texture measurements made using RHEED and synchrotron x-ray diffraction confirm that *in situ* RHEED analysis yields quantitative measurements of both in-plane and out-of-plane grain orientation distribution. The systematic offsets between RHEED analysis and x-ray measurements of biaxial texture, coupled with evidence that biaxial texture improves with increasing film thickness, indicate that RHEED is a superior technique for probing surface biaxial texture. RHEED simulations of other biaxially textured cubic materials like BaTiO<sub>3</sub> or CeO<sub>2</sub> demonstrate similar biaxial texture dependence to simulations for MgO, indicating that this method should be generally applicable to cubic materials. Weak scattering of MgO and rapid biaxial texture development make investigation of IBAD biaxial texture development difficult with *ex situ* x-ray diffraction. The surface sensitivity and *in situ* nature of RHEED provides novel information about biaxial texture

development and will facilitate rapid investigation of biaxial texturing mechanisms and biaxial texture optimization.

---

<sup>11</sup> X. D. Wu, S. R. Foltyn, P. N. Arendt, W. R. Blumenthal, I. H. Campbell, J. D. Cotton, J. Y. Coulter, W. L. Hulst, M. P. Maley, H. F. Safar, and J. L. Smith, *Appl. Phys. Lett.* **67**, 2397 (1995).

<sup>12</sup> W. J. Lin, T. Y. Tseng, H. B. Lu, S. L. Tu, S. J. Yang, and I. N. Lin, *J. Appl. Phys.* **77**, 6466 (1995).

<sup>13</sup> N. Wakiya, K. Kuroyanagi, Y. Xuan, K. Shinozaki, and N. Mizutani, *Thin Solid Films* **357**, 166 (1999).

<sup>14</sup> R. A. McKee, F. J. Walker, and M. F. Chisholm, *Phys. Rev. Lett.* **81**, 3014 (1998).

<sup>15</sup> C. P. Wang, K. B. Do, M. R. Beasley, T. H. Geballe, and R. H. Hammond, *Appl. Phys. Lett.* **71**, 2955 (1997).

<sup>16</sup> D. Litvinov, J. K. Howard, S. Khizroev, H. Gong, and D. Lambeth, *J. Appl. Phys.* **87**, 5693 (2000).

<sup>17</sup> J. W. Hartman, R. T. Brewer, and H. A. Atwater, *J. Appl. Phys.* **92**, 5133 (2002).

<sup>18</sup> S. Nikzad, C. C. Ahn, and H. A. Atwater, *J. Vac. Sci. Technol. B* **10**, 762 (1992).

<sup>19</sup> J. M. Cowley, *Diffraction Physics*, 3<sup>rd</sup> ed. (Elsevier Science, Amsterdam, 1995), pp. 113, 380-382.

<sup>20</sup> M. Horstmann and G. Meyer, *Z. Phys.* **182**, 380 (1965).

<sup>21</sup> D. Litvinov, T. O'Donnell, and R. Clarke, *J. Appl. Phys.* **85** (2151) 1999.

<sup>22</sup> R. T. Brewer, J. W. Hartman, J. R. Groves, P. N. Arendt, P. C. Yashar, and H. A. Atwater, *Appl. Surf. Sci.* **175**, 691 (2001).

<sup>23</sup> C. P. Wang, Ph.D. Thesis, Stanford University, (1999).

---

<sup>24</sup> R. T. Brewer and H. A. Atwater, Appl. Phys. Lett. **80**, 3388 (2002).

## Chapter 3      Biaxial Texture Development of IBAD

### MgO

#### 3.1 Introduction

Biaxially textured polycrystalline films can exhibit special single-crystal like properties not possessed by randomly oriented polycrystalline films. A biaxially textured film is one where the grains have a preferred out-of-plane and in-plane orientation, but also exhibits an orientation distribution of the grains around the preferred orientation. At the limit, a biaxial textured polycrystalline film would have orientation distributions resembling delta functions and the polycrystalline film would be a single-crystalline film with point or line defects instead of grain boundaries. Fortunately, even though functionality depends on biaxial texturing, films can approach single-crystalline performance without having perfectly aligned biaxial texture. This has been demonstrated in the case of biaxially textured superconducting  $\text{YBa}_2\text{C}_3\text{O}_{7-x}$ , where the critical current density for biaxially textured films is comparable to critical current density in single-crystalline films<sup>25</sup>. It is also expected that biaxially textured ferroelectric films will exhibit domain switching characteristics similar to single-crystalline materials. Performance of perovskite ferroelectrics (e.g.  $\text{BaTiO}_3$  and  $\text{PbTiO}_3$ ) actuators is directly tied to its biaxial texture because piezoelectric actuation can only occur along the (001) crystal planes. Therefore the direction that these planes are oriented dictates the actuation directions. Geometrical considerations limit a randomly oriented polycrystalline film to less than half (47.5%) of the actuation of a single-crystal film, while a biaxially textured ferroelectric film, with out-of-plane and in-plane

orientation distributions of  $3^\circ$  and  $7^\circ$  full width at half maximum (FWHM), respectively, can produce over 90% of a single-crystal's actuation. For superconductors and ferroelectric materials, the extent to which the polycrystalline films mimic single-crystalline behavior will depend on the biaxial texture; the narrower it is, the more single-crystal-like the film.

Ferroelectric and superconducting films inherit their biaxial texture from the MgO heteroepitaxial template. By understanding the biaxial texture formation in MgO, we can learn to optimize biaxial texture and produce high-quality ferroelectric and superconducting films. The implementation of the reflection high-energy electron diffraction (RHEED) based method discussed in the previous chapter has provided insight into biaxial texture formation in IBAD MgO. We have been able to measure MgO biaxial texture both during the earliest nucleation stages and in real-time during growth. Equipped with unprecedented detailed measurements of biaxial texture development in MgO, we have provided new insight into the mechanisms promoting biaxial texture during IBAD.

### **3.1.1 Texture formation using IBAD**

Ion beam-assisted deposition combines one of the traditional vapor deposition techniques (electron beam evaporation, magnetron sputtering, ion sputtering, laser ablation) with surface bombardment from a collimated flux of ions in the 10 eV to 1 keV range. Figure 3.1 graphically shows a typical IBAD system. With a Kaufmann source, ions can either be inert species like  $\text{Ar}^+$  or can be reactive species like  $\text{N}^+$  for TiN deposition. The three main parameters affecting ion-surface interactions are the ion/atom

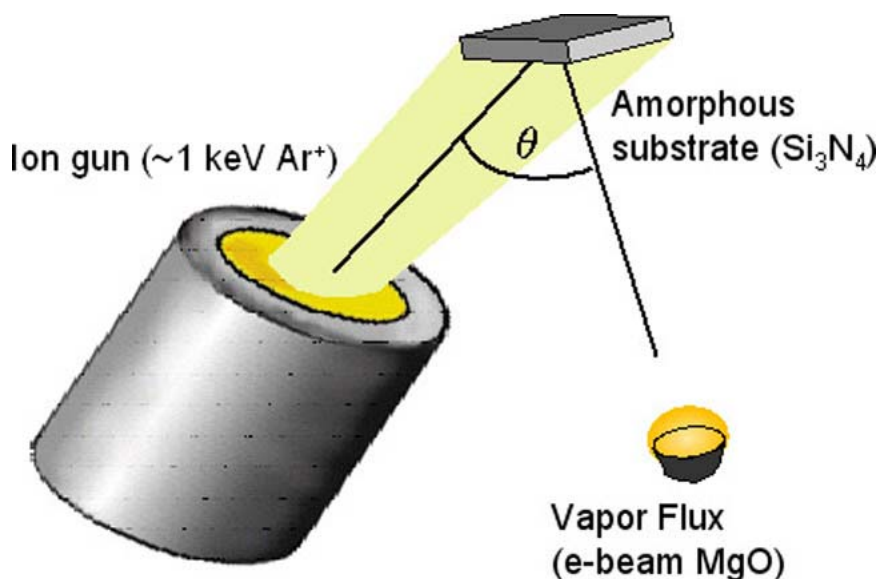


Figure 3.1 Schematic of an ion beam-assisted deposition (IBAD) apparatus. The ion source is typically a Kaufmann ion gun and the growth material is deposited using physical vapor deposition (PVD). The optimal incidence angle of the ion bombardment ( $\theta$ ) depends on the film,  $45^\circ$  is optimal for  $\text{MgO}$ <sup>33</sup> and  $55.4^\circ$  is optimal for yttrium stabilized zirconia<sup>38</sup>.

flux ratio, ion energy, and ion incident angle. By manipulating these parameters different growth regimes can be selected, effectively changing the final biaxial texture.

When deposited on amorphous substrates, many materials grow as polycrystalline films with a preferred out-of-plane orientation<sup>26,27,28</sup>. The film texture is characterized by the full width at half maximum (FWHM) of the (assumed to be Gaussian) grain orientation distribution from the c-axis. When biaxially textured, the films are characterized by the out-of-plane ( $\Delta\omega$ ) and in-plane ( $\Delta\phi$ ) orientation distributions. In 1985, the first experiment to use IBAD for growing biaxially textured thin films was reported<sup>28</sup>. Using pole figure analysis, Yu et al.<sup>28</sup> showed that ion sputter deposited Nb grew with a (110) fiber texture perpendicular to the substrate and a random in-plane orientation. When  $200 \text{ eV Ar}^+$  ions, at a  $20^\circ$  from glancing incident angle and a flux ratio

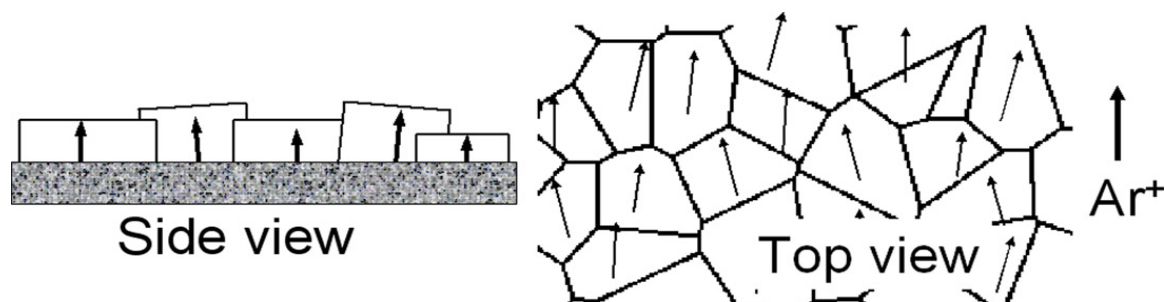


Figure 3.2 Biaxially textured film. The side view shows the MgO grains growing out of amorphous  $\text{Si}_3\text{N}_4$  with a preferred out-of-plane direction (the arrows indicate the (001) direction). On the right, the in-plane (001) planes, represented by the arrows, nominally align around the direction of the  $\text{Ar}^+$  bombardment.

of 1.3  $\text{Ar}^+$  per Nb atom, also impinged on the surface during growth an in-plane texture also formed around the direction of the incident ions. Biaxially textured (see Figure 3.2) films have also been grown by using a glancing angle vapor deposition technique<sup>29,30</sup>; however, IBAD grown films exhibit narrower out-of-plane ( $\Delta\omega$ ) and in-plane ( $\Delta\phi$ ) orientation distributions.

The strong ion/atom flux ratio and incident angle biaxial texture dependency was well illustrated by Rauschenbach et al. for IBAD TiN growth<sup>31</sup>. Using 2 keV  $\text{N}^+$  ions and electron beam evaporated Ti, TiN was grown on (111) Si with varying ion current densities and incident angles. While TiN grown in a reactive N atmosphere with no ion impingement grows with a (111) fiber texture, normal ion incident TiN films showed a (001) fiber texture (both techniques produce random in-plane orientations). A biaxially textured film, (111) out-of-plane and (001) in-plane (toward the incident ions), was grown using a  $54.7^\circ$  ion incidence angle from normal, which is the angle between the (001) and (111) planes. By increasing the ion current from  $12 \mu\text{A}/\text{cm}^2$  to  $70 \mu\text{A}/\text{cm}^2$ , the in-plane orientation distribution ( $\Delta\phi$ ) was reduced from  $18^\circ$  to  $13^\circ$  FWHM.

Further evidence of texture dependence on ion incident angle has been seen in  $\text{CeO}_2$ <sup>32</sup> and  $\text{MgO}$ <sup>33</sup>. While neither film showed a change in crystallographic texture for changing ion incidence angles at fixed ion flux and energy, the in-plane orientation distribution ( $\Delta\phi$ ) was a function of the ion incident angle. For  $\text{CeO}_2$  the highest quality film was grown using an ion incident angle of  $55^\circ$  from normal, the angle between (111) and (100)<sup>32</sup>. The narrowest in-plane orientation distributions for IBAD  $\text{MgO}$  were obtained with an ion incidence angle of  $45^\circ$ , the angle between the thermodynamically preferred out-of-plane (001) and the (110) channeling direction<sup>34</sup>.

### 3.1.2 Theories of IBAD biaxial texturing mechanisms

There are two opposing mechanisms purporting to explain IBAD biaxial texture development, anisotropy of sputtering rates and anisotropy of ion-induced surface damage for different grain orientations<sup>35</sup>. The first researchers to observe IBAD biaxial texturing attributed it to anisotropy of sputtering rates for different grain orientations<sup>28,36,37</sup>. This model supposes that faster growing grains eventually occlude slower growing grains. This is a reasonable picture for the biaxial texture development seen in IBAD YSZ, which exhibits a gradual decrease in the out-of-plane ( $\Delta\omega$ ) and in-plane orientation distribution ( $\Delta\phi$ ) as the film grows, not reaching a minimum until the film is about 600 nm thick<sup>38</sup>. Coupled with the increased sputtering yield experienced by misaligned grains, there is also a shadowing effect that aggravates the growth disparity between grains. Using a 2D molecular dynamics simulation, Ying et al.<sup>39</sup> showed that shadowing effects alone could cause grains to overgrow adjacent grains. Taller grains (less sputtered because of correct alignment with incoming ions) were observed to

incorporate border adatoms into their crystal structure, effectively growing laterally over the shorter grains.

More recent experiments and simulations have cast doubt on the selective sputtering mechanism. Ressler et al.<sup>35</sup> used a 150 eV and 300 eV Ar<sup>+</sup> ion beam to etch three samples of YSZ, half of each sample having the (111) and the other half having the (110) oriented to the ion beam. Using typical IBAD deposition conditions, the etch rates for the 150 eV Ar<sup>+</sup> ion beam were two orders of magnitude smaller ( $\sim .02$  A/s) than the typical deposition rates (1.2 or 2.4 A/s). The difference in etch rates for (111) and (110) surfaces using the 300 eV Ar<sup>+</sup> ion beam were only about 0.03A/s, with some samples having higher etch rates for the (111) oriented halves and the others having higher etch rates for the (110) oriented halves. A similar experiment by Iijima et al.<sup>40</sup> was performed by etching a single-crystal of YSZ with a 300 eV Ar<sup>+</sup> ion beam at a 55° from normal incident angle. They found no statistically different etch rate as they rotated the sample around the normal axis. A selective sputtering mechanism predicts that the etch rate will be lower when the (111) is lined up with the ion beam than when it is misaligned. However, no evidence of increased etch rate for the misaligned crystal was observed.

### **3.1.2.1 Anisotropic ion damage**

Anisotropic ion damage for different grain orientations has also been proposed as the dominant biaxial texturing mechanism<sup>27,41,35</sup>. This model proposes that biaxially textured films do not develop by having the aligned grains grow over the misaligned grains, but evolve via lateral grain growth. Grains with stable lattice planes oriented directly into the ion beam are assumed to sustain less damage than misaligned grains. After an ion impact there is local heating that allows for reordering of the local surface

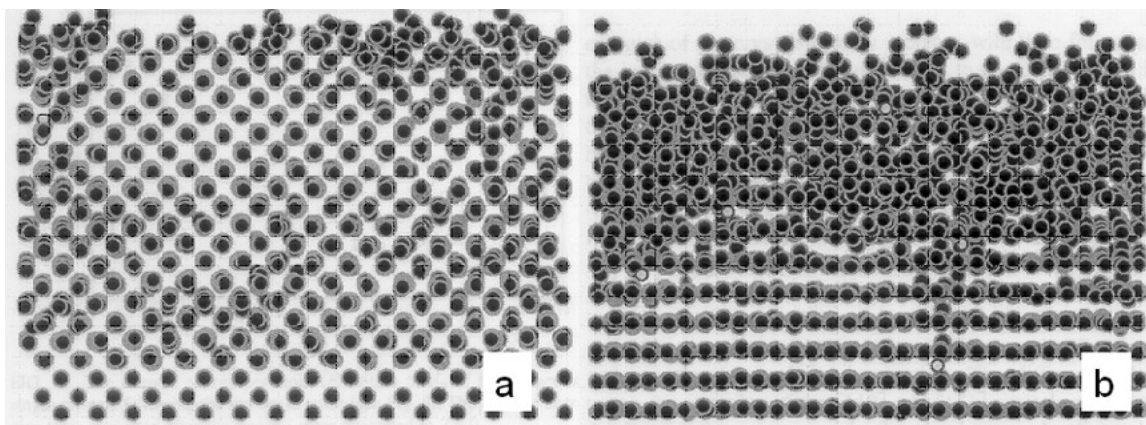


Figure 3.3 Molecular dynamics simulation of FCC crystals after twenty 100 eV, perpendicular Ar ion impacts. The top crystal has a (110) c-axis orientation and the bottom crystal has a (111) c-axis orientation<sup>27</sup>. Crystal damage depends on the crystal direction oriented toward the ion flux.

atoms. During this local thermal spike the grain with the least damage grows into the more highly damaged grain through a recrystallization process. The recrystallization driven grain boundary migration rate is proportional to the difference in energy density of adjacent grains. The grain boundary acts as a sink for surface defects as it migrates into the more damaged grain, leaving a more perfect crystal behind it. The recrystallized sections take on the orientation of the less damaged grain and increase the size of the well-aligned grain at the expense of the misaligned one<sup>27</sup>.

Recent 3-D molecular dynamics simulations by Dong and Srolovitz<sup>27,42</sup> support the anisotropic ion damage model. A simulated bi-crystal fcc film (nominally Al) was created with one fiber axis in the (111) and the other in the (110). The ion damage sustained by each crystal was examined by bombarding each crystal orientation with twenty 100 eV ions. Figure 3.3 shows that the (111) oriented crystal sustained significantly more damage than the (110) oriented crystal<sup>27</sup>. The classical boundary migration theory was validated by taking a damaged (111) oriented crystal, like in Figure 3.3, turning it 90°, attaching the damaged portion to the side of a perfect (110) oriented

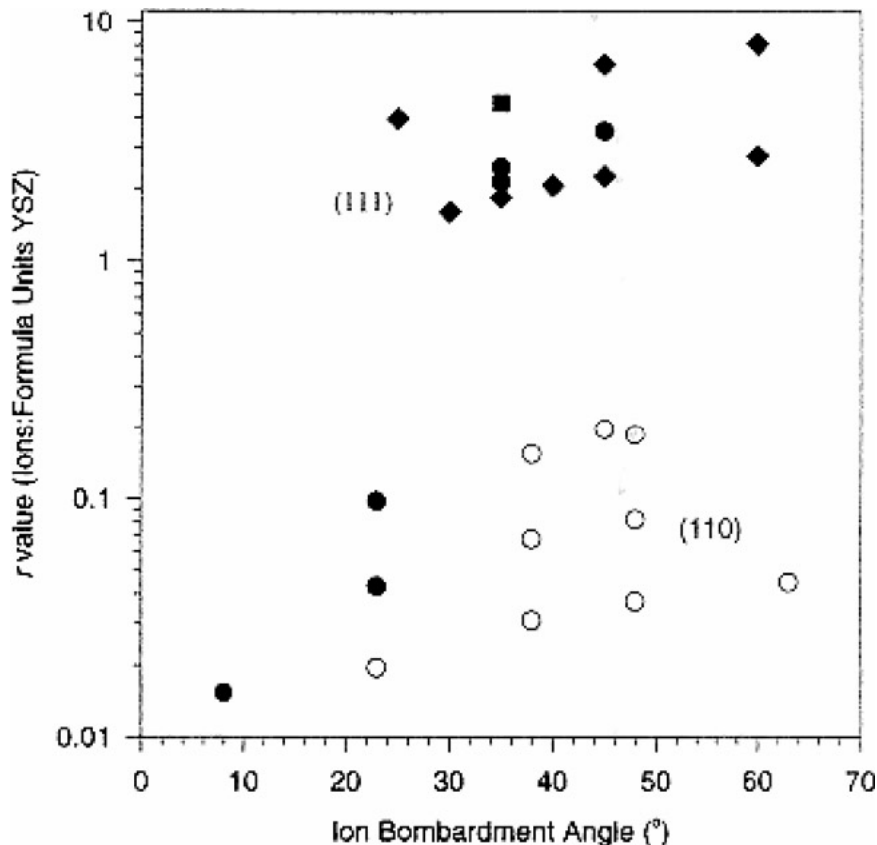


Figure 3.4 In-plane alignment direction for IBAD YSZ as a function of  $r$  (ion/atom flux ratio) and ion bombardment angle. The different symbols represent that the films were grown by different deposition methods, e.g., sputter deposition and e-beam evaporation, and substrate temperatures, e.g., room temperature to  $600^{\circ}\text{C}$ <sup>35</sup>.

crystal, and allowing the combined structure to equilibrate over time at a typical substrate temperature. The grain boundary was observed to grow into the (111) oriented crystal leaving relatively damage free (110) oriented crystal material behind it, just as predicted by classical boundary migration theory<sup>27</sup>. The final simulation evidence comes from IBAD growth simulations. The full IBAD simulation produced efficient occlusion of the (111) crystal by the (110) crystal. Turning off the selective sputtering during a second simulation produced no noticeable effect on the grain boundary migration rate into the (111) crystal. However, when the anisotropic ion damage was excluded from the simulation, leaving only the selective sputtering grain boundary migration mechanism,

the (110) boundary showed only slight migration into the more slowly growing (111) grain<sup>42</sup>. These simulations indicate that anisotropic ion damage dominates over selective sputtering in IBAD texture formation.

Recent experiments have also shown strong support for the anisotropic ion damage mechanism. The highest density lattice planes are typically most resistant to ion-induced damage. The lattice density, as seen by an ion, is a function of the ion energy. At 200 eV the CeO<sub>2</sub> (110) plane has a higher density than the (111) plane. At 300 eV the relative densities are reversed. Following this trend, the in-plane orientation for IBAD grown CeO<sub>2</sub> (using a 55° from normal ion incidence) switched from (110) to (111) when, under otherwise identical conditions, the ion energy was changed from 200 eV to 300 eV<sup>43</sup>. Taken as a whole, yttrium stabilized zirconia (YSZ) IBAD data also support the anisotropic ion damage mechanism<sup>35</sup>. YSZ IBAD films grown at high ion/atom ratios typically show (111) in-plane orientation, while low ion/atom ratios produce (110) in-plane orientations. Atomic binding calculations show that Zr<sup>4+</sup> ions on the (111) and (110) surfaces have very similar free energies, ~80 eV. However, the O<sup>2-</sup> ions on the (111) and (110) surfaces have been calculated to have -16 eV and -12 eV free energies, respectively<sup>35</sup>. At low ion/atom flux ratios the (110) surface is the most damage-resistant because it has a higher density than the (111) surface. However, the O<sup>2-</sup>/Zr<sup>4+</sup> ratio on the (110) surface is two, while the O<sup>2-</sup>/Zr<sup>4+</sup> ratio on the (111) surface is only one. At high ion/atom flux ratios the O<sup>2-</sup> is preferentially sputtered from the surface and can not be replaced due to a high ion flux. This leaves the (110) surface more susceptible to ion-induced damage than the (111) surface, effectively allowing the (111) in-plane orientation to develop.

Even among the anisotropic ion damage mechanism proponents there is disagreement about the cause of the damage anisotropy. One view is that ion damage is reduced by increased ion channeling for the selected grain orientation. Ensinger<sup>41</sup> argued for this mechanism based on experiments with IBAD TiN fiber texture development. He suggested that as ion energies increased, with ion/atom flux equal to one, the (100) fiber texture began to dominate the non IBAD preferred (111) fiber texture because the three fold more open (100) preferentially escaped damage by allowing more ions to channel. The other main view is that the ability of lattice planes to withstand damage is a function of its ability to disperse the energy of ion impacts, as opposed to its ability to avoid high-energy collisions. Ressler et al.<sup>35</sup> attempted to demonstrate this by showing that the (111) or (110) oriented toward the ion beam based on the ion flux and not the ion incident angle. They argued that if channeling was responsible for the in-plane orientation, then using a 45° ion beam incidence should produce a (110) oriented film, while using a 55° ion beam incidence should produce a (111) oriented film, these being the respective channeling angles for a (001) oriented film. Figure 3.4<sup>35</sup> shows that both (111) and (110) oriented films were grown at either ion beam incidence angle and the authors conclude that in-plane alignment can not be a result of ion channeling. Ressler et al. further supported their claim by growing (111) in-plane oriented LCMO, even though at the ion energy used channeling was calculated to be impossible for the (111), but possible for (100) and (110)<sup>35</sup>.

### **3.1.3 MgO texture development**

The rapid biaxial texture development of IBAD MgO makes it a promising material for use as a heteroepitaxial substrate for ferroelectric and superconducting

materials. In contrast to the gradual texture development observed for IBAD YSZ<sup>40</sup>, which continues to improve in-plane texture until film thickness reaches over half a micron, MgO has been observed to have narrow in-plane orientation in films as thin as 3 nm<sup>33</sup>. These same authors reported that they could produce films with  $\Delta\phi = 7^\circ$  and  $\Delta\omega = 3^\circ$  (in-plane and out-of-plane orientation distribution FWHM, respectively) in 10 nm thick films. Because they relied on laboratory based x-ray analysis, these measurements were not taken on the original IBAD films, but were taken on the films after 60 nm of homoepitaxial MgO was grown on them at 600° C. This required the assumption that the biaxial texture would not change during homoepitaxy. Later work by Groves et al. partially validated this assumption by demonstrating that for well-textured IBAD MgO films the in-plane orientation distribution ( $\Delta\phi$ ) changes by less than 1° FWHM during homoepitaxy at 500° C<sup>44</sup>, but there has been no such measurement for the out-of-plane distribution ( $\Delta\omega$ ). Measuring out-of-plane orientation distribution on 10 nm MgO films using XRD requires a x-ray source with synchrotron brightness.

It has been postulated that MgO biaxial texture develops quickly due to the synergy between the ion beam alignment and thermodynamics. High-temperature physical vapor deposition of MgO on amorphous SiO<sub>2</sub> exhibits a strong (001) fiber texture<sup>45</sup>, which is only enhanced by including a 45 degree incident Ar<sup>+</sup> ion beam (the angle for ion channeling along the <110> direction). By contrast, the slow texture development in YSZ is proposed to result from the fact that the ion beam has to overcome the thermodynamically favorable (111) c-axis orientation and realign the (111) with the ion beam, leaving the film in a less stable (001) orientation<sup>33</sup>.

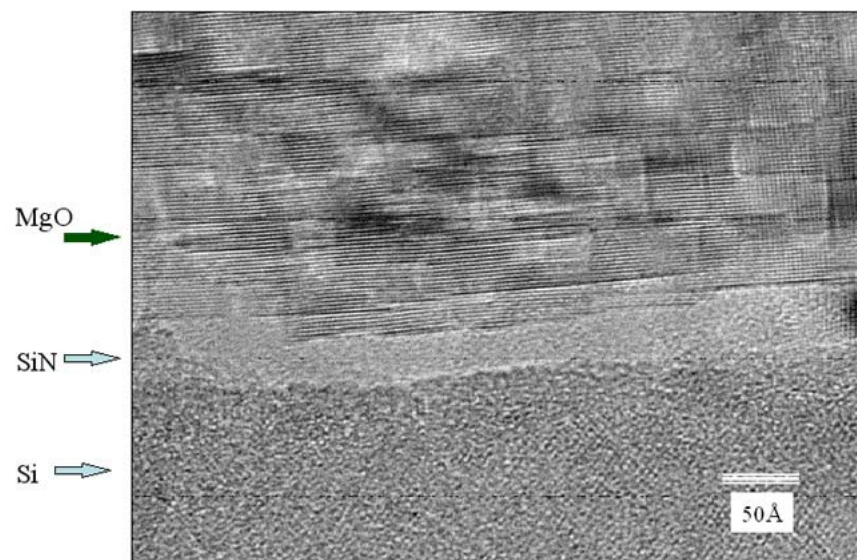


Figure 3.5 Cross section TEM of IBAD MgO (deposited at 300 C) in which the ion beam was incident at roughly 45 degrees with respect to the normal of the substrate and image planes<sup>33</sup>.

Another characteristic of IBAD MgO growth is the periodic renucleation of MgO grains during growth. Figure 3.5 is a TEM micrograph taken by Wang et al.<sup>33</sup> showing that the polycrystalline MgO grains appear as square blocks. Based on this image, IBAD MgO renucleation occurs every few nanometers of film growth.

For such thin films it seems unlikely that gradual texturing mechanisms like overshadowing by fast growing grains or grain boundary migration toward highly damaged grains could create such strongly biaxially textured films. Although ion channeling and selective ion erosion of misaligned grains has been the proposed mechanism<sup>33</sup>, the difficulty of analyzing biaxial texture of 10 nm thick MgO films has prevented quantitative conclusions about the texturing mechanisms. Previous studies have used TEM (tedious), synchrotron radiation (expensive), or homoepitaxial MgO layers (100 nm), hoping that the homoepitaxy does not change the texture, to measure the biaxial texture of IBAD MgO films. In this study we use RHEED for fast quantitative

texture measurement. Another advantage to using RHEED is that it gives the entire biaxial texture evolution because it is an *in situ* diagnostic. Close RHEED observations have also given us insight concerning the role of biaxially textured grain nucleation in the rapid biaxial texture development of IBAD MgO.

### 3.1.4 Chapter overview

Our RHEED-based biaxial texture analysis technique facilitates fast, *in situ* measurement of biaxial texture for very thin films that was not previously possible. With our new capabilities we have been able to study MgO biaxial texture formation during nucleation, as well as easily run many experiments to explore the biaxial texture formation during later stages of MgO growth. In this chapter I will discuss how we determined that early biaxial texture formation is dominated by selective ion damage and solid phase crystallization. Then I will report the evolution of IBAD MgO biaxial texture as a function of film thickness, as well as show how biaxial texture of MgO evolves during MgO homoepitaxy on thin IBAD films. For the first ~10 nm of growth the biaxial texture improves drastically from its value at nucleation. Our RHEED-based measurements provide the first practical method for measuring the out-of-plane orientation distribution ( $\Delta\omega$ ) for MgO films less than 4 nm thick. There are also indications that biaxial texture measurements on homoepitaxial films are not quantitatively the same as direct measurement of biaxial texture from a thin IBAD MgO sample. Finally, I will discuss the dependence of biaxial texture on growth parameters like the ion/MgO flux ratio, showing that the in-plane orientation distribution is limited by the out-of-plane orientation distribution. Our experiments suggest that the narrowest in-plane orientation distribution ( $\Delta\phi$ ) we can expect from IBAD is 2 degrees broader than

the out-of-plane orientation distribution ( $\Delta\omega$ ). This is consistent with an ion channeling mechanism, but is not proof of such.

### 3.2 IBAD MgO biaxial texture during nucleation

In contrast to materials like yttria stabilized zirconia (YSZ) where biaxial texture evolves slowly during one micron of IBAD growth<sup>46</sup>, the biaxial texture of IBAD MgO develops rapidly during the nucleation phase. Biaxial texturing mechanisms such as anisotropic sputtering, ion channeling, and anisotropic grain damage<sup>27</sup> have been proposed to explain biaxial texture evolution during growth of YSZ, but do not specifically address the nucleation-mediated biaxial texturing seen for MgO. It has been suggested that IBAD MgO grains nucleate with biaxial texture because surface energy is minimized with a (001) fiber texture, leaving in-plane alignment to be achieved by ion channeling along the [011] zone axis<sup>33</sup>. High-temperature physical vapor deposition of MgO on amorphous SiO<sub>2</sub> favors nucleation with a (001) fiber texture<sup>45</sup>, but our own experiments, as well as other's experiments<sup>47</sup>, show that kinetic limitations result in nucleation with random orientation at room temperature.

#### 3.2.1 Experiment

We have used transmission electron microscopy (TEM), electron dispersive x-ray analysis (EDAX), ellipsometry, and *in situ* reflection high-energy electron diffraction (RHEED) to investigate IBAD MgO biaxial texture during the first few nanometers of film growth. Using electron beam evaporation, films of MgO were deposited by room temperature ion beam-assisted deposition onto 30 nm thick Si<sub>3</sub>N<sub>4</sub> TEM windows at the rate of 0.17 nm/s with simultaneous ion bombardment of 750 eV Ar<sup>+</sup> ions from a

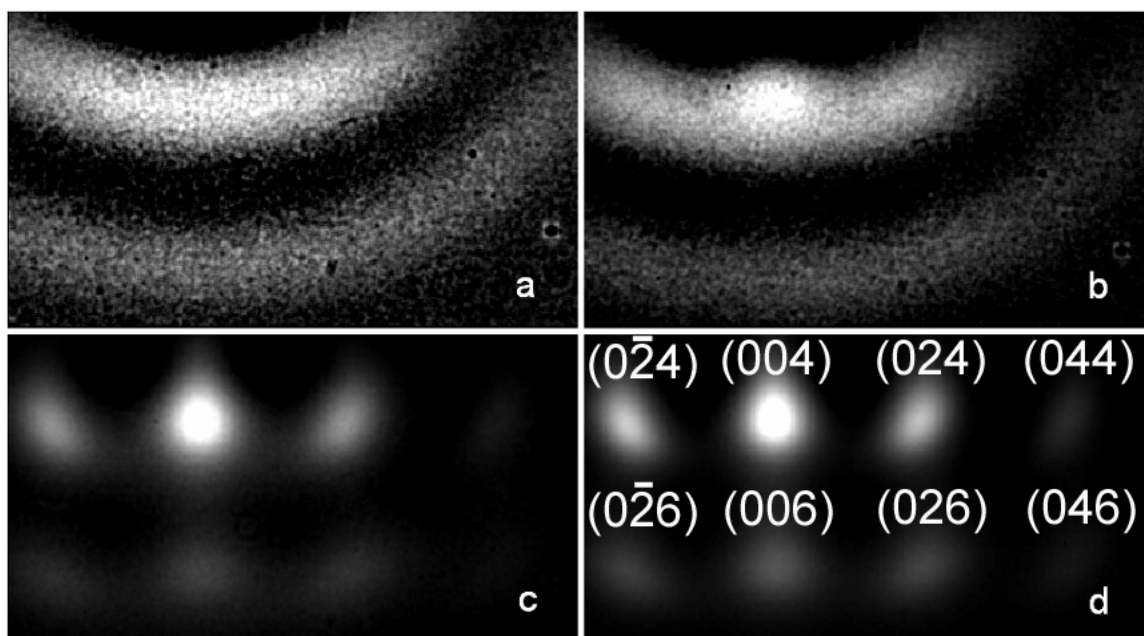


Figure 3.6 *In situ* RHEED images from a continuous IBAD MgO growth experiment where the film thickness is equal to: 2.5 nm (a), 3.1 nm (b), 3.6 nm (c), and 4.2 nm (d). The field of view contains diffraction spots from  $(0\bar{2}4)$ , in the upper left corner, to  $(046)$  in the lower right corner.

Kaufman ion gun. The ions impinged on the surface at a  $45^\circ$  incidence angle with an ion/MgO molecule flux ratio of 0.43.

The growth of each sample used for TEM observation was stopped when the RHEED image exhibited the desired relative contributions from diffraction rings and spots. RHEED was performed with 25 keV electrons at a  $2.6^\circ$  incidence angle and images were taken with a 16 bit dynamic range, 1024 x 1024 pixels, CCD camera. In order to increase the sensitivity to weak diffraction intensities, the diffuse RHEED background was removed by subtracting a RHEED image of the amorphous  $\text{Si}_3\text{N}_4$  substrate from all subsequent RHEED images.

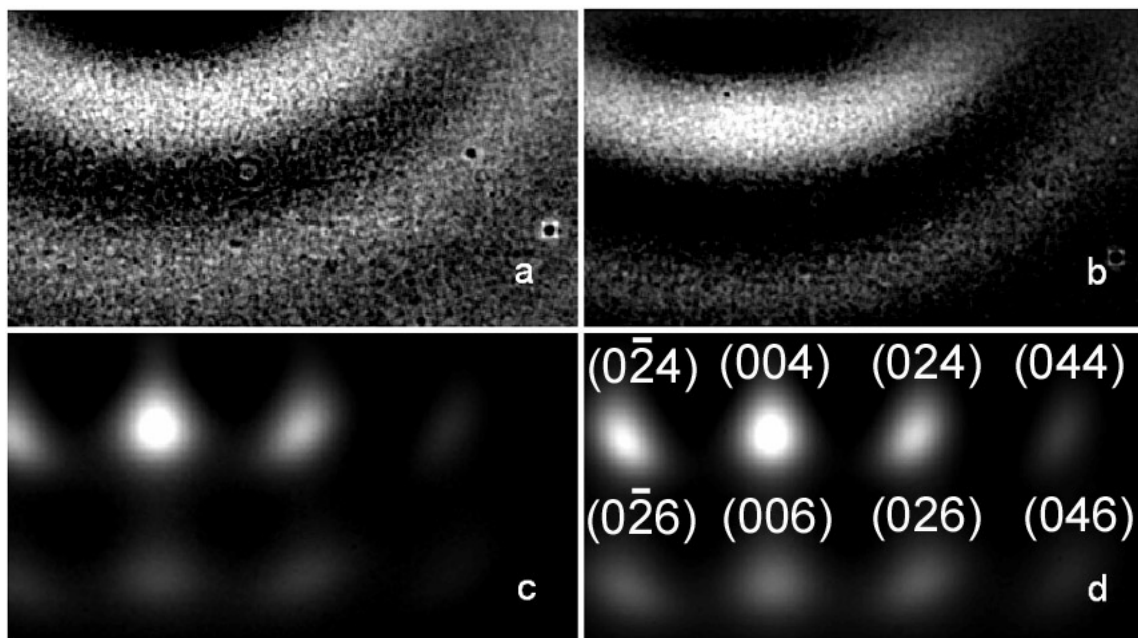


Figure 3.7 RHEED images from different IBAD MgO films grown to: 1.9 nm (a), 3.7 nm (b), 4.6 nm (c), and 4.8 nm (d). The field of view contains diffraction spots from  $(0\bar{2}4)$ , in the upper left corner, to  $(046)$  in the lower right corner.

### 3.2.2 Results

RHEED pattern development for IBAD MgO grown on amorphous  $\text{Si}_3\text{N}_4$  is shown in Figure 3.6. Film thicknesses were determined by measuring the final MgO film thickness by ellipsometry and then assuming a constant growth rate. The evolution from diffraction rings (Figure 3.6a) to diffraction spots (Figure 3.6d) has been observed for IBAD MgO film growths with ion energies varying from 500 to 1100 eV and ion/MgO flux ratios from 0.21 to 0.57. Observations of RHEED pattern development during ion bombardment of the  $\text{Si}_3\text{N}_4$  substrate without MgO deposition confirm that the broad diffraction rings do not originate from the ion beam modification of the substrate.

IBAD MgO films, grown to thicknesses of 1.9 nm, 3.7 nm, 4.6 nm, and 4.8 nm, were analyzed with RHEED and TEM in an effort to elucidate the development of biaxial texture during the nucleation phase. RHEED images from these samples (Figure 3.7)

show that the RHEED pattern development for these films follows the same evolution as observed for the single continuous growth (Figure 3.6). The transition from broad diffraction rings to diffraction spots begins at 3.7 nm (Figure 3.7b) and is finished by 4.8 nm (Figure 3.7d). RHEED diffraction rings typically indicate a random out-of-plane orientation distribution, but the RHEED image from 1.9 nm of IBAD MgO (Figure 3.7a) lacks rings that would be present in a randomly oriented polycrystalline film, suggesting that the film is amorphous MgO.

The transmission electron diffraction pattern of the thinnest film (1.9 nm) confirms that it is amorphous, as illustrated in Figure 3.8a. EDAX measures the amount of MgO on the surface in Figure 3.8a to be 34 percent of the amount present in Figure 3.8d, corroborating the relative film thicknesses measured by ellipsometry. Atomic force microscopy measured film roughness to be 0.24 and 0.23 nm rms for the 1.9 and 3.7 nm thick IBAD MgO films shown in Figure 3.8a and Figure 3.8b respectively.

These observations strongly suggest that the MgO films in Figure 3a and Figure 3b are continuous and amorphous. Only diffraction rings from (001) fiber textured grains were observed. However, the diffraction patterns show that the in-plane orientation distribution changes from random at 3.7 nm (Figure 3.8b) to highly aligned at 4.8 nm (Figure 3.8d). During the rapid development of biaxial texture, rapid crystal growth also occurs. Individual grains are not observed for the 1.9 nm thick film (Figure 3.8a); however, starting with the onset of fiber texture development, the dark field images show progressively larger grains as shown in Figure 3.8b- Figure 3.8 d. The area fraction of diffracting MgO crystalline material observed in dark field TEM and the in-plane orientation distribution, measured using RHEED analysis<sup>48</sup>, are plotted as a function of

film thickness in Figure 3.9. There is a clear correlation between lateral crystal growth and biaxial texture.

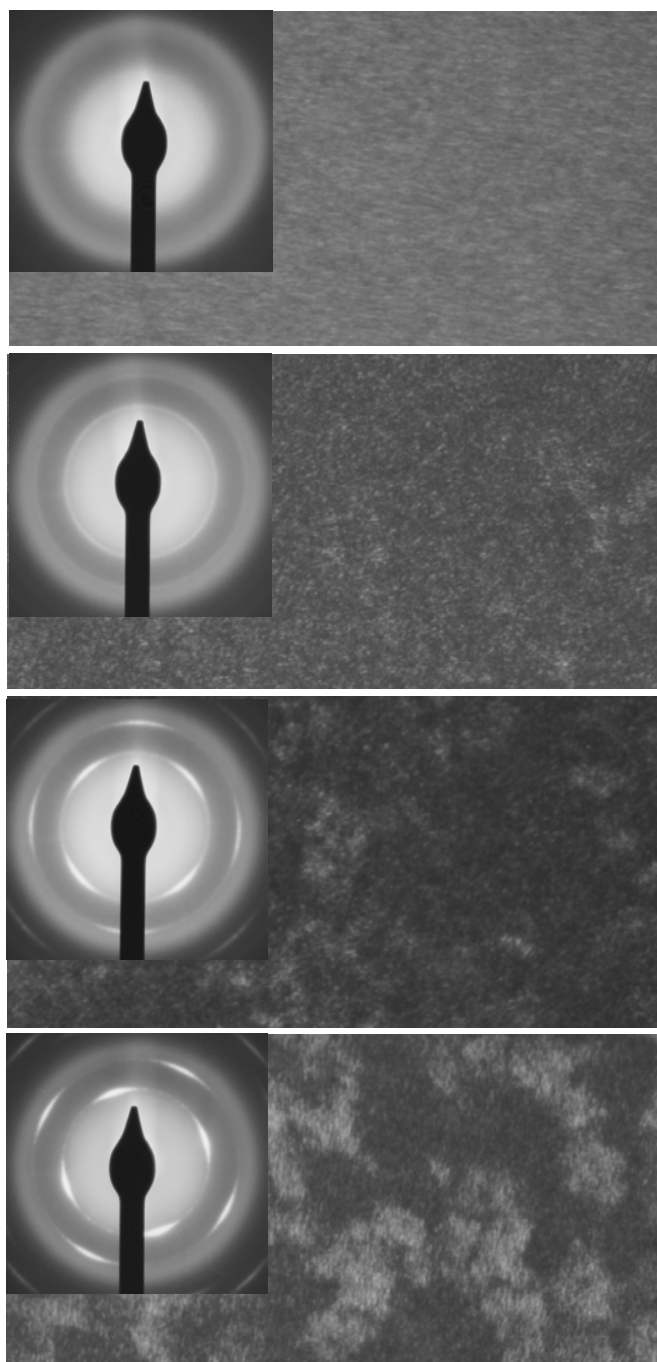


Figure 3.8 TEM dark field images and diffraction patterns for IBAD MgO films with thicknesses equal to: 1.9 nm (a) (top image), 3.7 nm (b) (second image), 4.6 nm (c) (third image), and 4.8 nm (d) (bottom image).

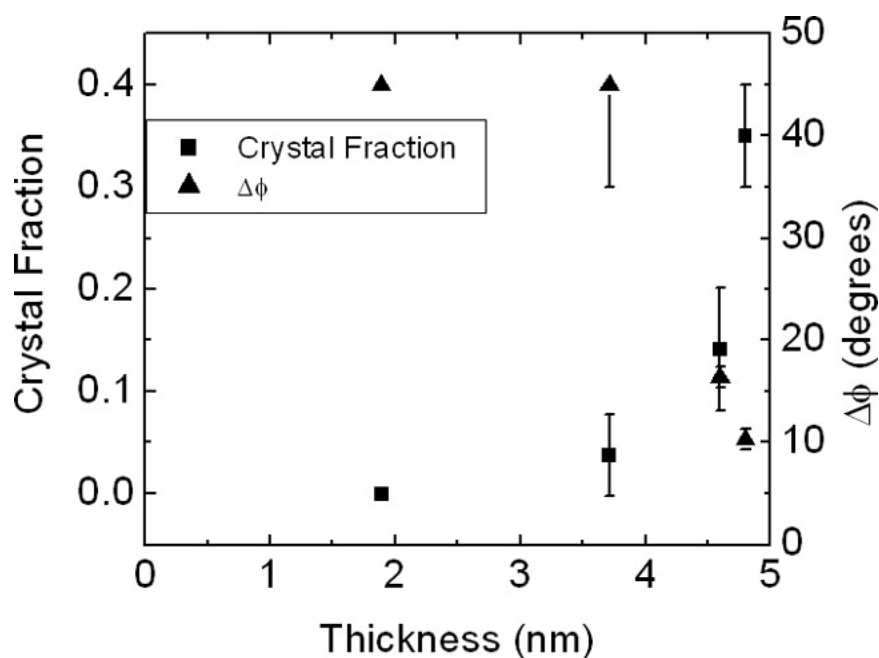


Figure 3.9 Fraction of crystalline material observed for IBAD MgO with dark field TEM as a function of film thickness. In-plane orientation distribution ( $\Delta\phi$ ) measured as a function of film thickness.

### 3.2.3 Biaxial texture nucleation mechanism

The observations reported here are consistent with a three-stage microstructural evolution during ion beam-assisted deposition: i) an initially amorphous MgO film is deposited which remains amorphous in the thickness range between 0-3.5 nm; ii) MgO crystals nucleate via solid phase crystallization<sup>49</sup> with restricted out-of-plane texture and nearly random in-plane texture at a thickness of approximately 3.5 nm; iii) in-plane texture evolves rapidly in the thickness range between 3.5 and 4.5 nm due to amorphization of grains with misaligned in-plane texture and preferential lateral solid phase growth of grains with [011] lattice planes aligned with the ion bombardment. Recent molecular dynamic simulations of Ar<sup>+</sup> ion collisions with small MgO crystals yield insights to nucleation-mediated IBAD biaxial texture development. Molecular

dynamics simulations by Zepeda-Ruiz and Srolovitz calculate that for a single  $\text{Ar}^+$  ion impact along the [011] channeling direction (a minimum damage direction), a  $1.3 \times 1.3 \times 1.3$  nm MgO crystal is amorphized, but a  $2.1 \times 2.1 \times 2.1$  nm MgO crystal sustains little permanent damage<sup>50</sup>. It is energetically favorable for MgO to form small crystallites, however, the ion bombardment amorphizes and laterally distributes the material from the first crystals, even those aligned along ion channeling directions. Once the film reaches a critical thickness, there is enough material for stable sized MgO crystals to form. We suggest that surface-free energy minimization, coupled with energy from ion collisions, drives the out-of-plane orientation toward a (001) fiber texture<sup>51</sup>. There is no energetically favorable in-plane orientation for nucleation on an amorphous substrate and so the MgO crystals nucleate in the amorphous MgO matrix with a random in-plane orientation distribution. Crystals which have the [011] zone axis aligned along the direction of the incoming  $\text{Ar}^+$  ions receive less damage than misaligned crystals, which can be locally amorphized by ion bombardment<sup>27,50</sup> and effectively prevented from growing. As a result, solid phase crystallization proceeds around grains which are oriented with a (001) fiber texture and an in-plane orientation that faces the [011] zone axis toward the incoming ions, creating a biaxially textured MgO thin film.

Sensitive RHEED experiments and subsequent TEM analysis revealed an abrupt, unexpected transition from an amorphous film to a biaxially textured film. These results clearly show that anisotropic ion damage, not anisotropic ion sputtering, is responsible for nucleating biaxially textured IBAD MgO films. The experimental observations are consistent with the appearance of biaxial texture from an initially amorphous layer of MgO through solid phase crystallization around biaxially textured seed grains<sup>52</sup>.

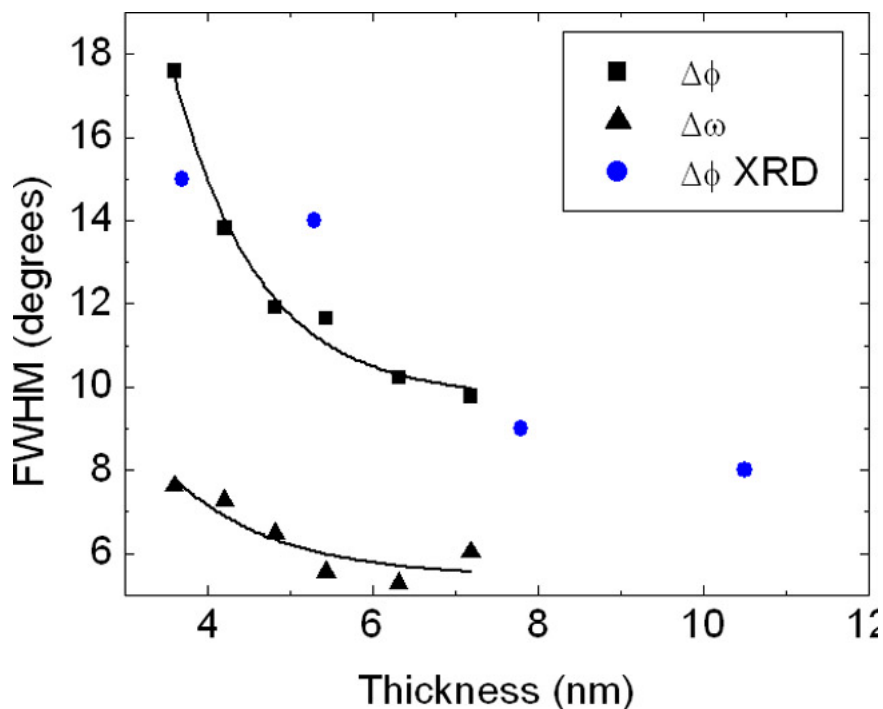


Figure 3.10 In-plane ( $\Delta\phi$ ) and out-of-plane ( $\Delta\omega$ ) orientation distribution for IBAD MgO growth as a function of film thickness measured using RHEED. The lines are a fit to the data. In-plane orientation distribution ( $\Delta\phi$ ) measured using grazing incidence x-ray diffraction by Groves et al. are included for comparison<sup>53</sup>

### 3.3 Biaxial texture improvement as a function of film thickness

Through biaxially textured solid phase nucleation, IBAD MgO forms a film with biaxial texture of narrow angular distribution within the first 4 nm of growth. Subsequent IBAD growth narrows this texture to an optimum within about 10 nm of growth, but further IBAD causes texture degradation. Figure 3.10 shows the progression of IBAD MgO biaxial texture as a function of film thickness. Included with our own RHEED-based measurements are in-plane orientation distributions measured by Groves et al. using x-ray diffraction (XRD)<sup>53</sup>. Even though our RHEED-based measurements are taken *in situ*, the growth had to be stopped to measure in-plane orientation distribution with a rocking curve. However, because these measurements are *in situ*, it allowed for a

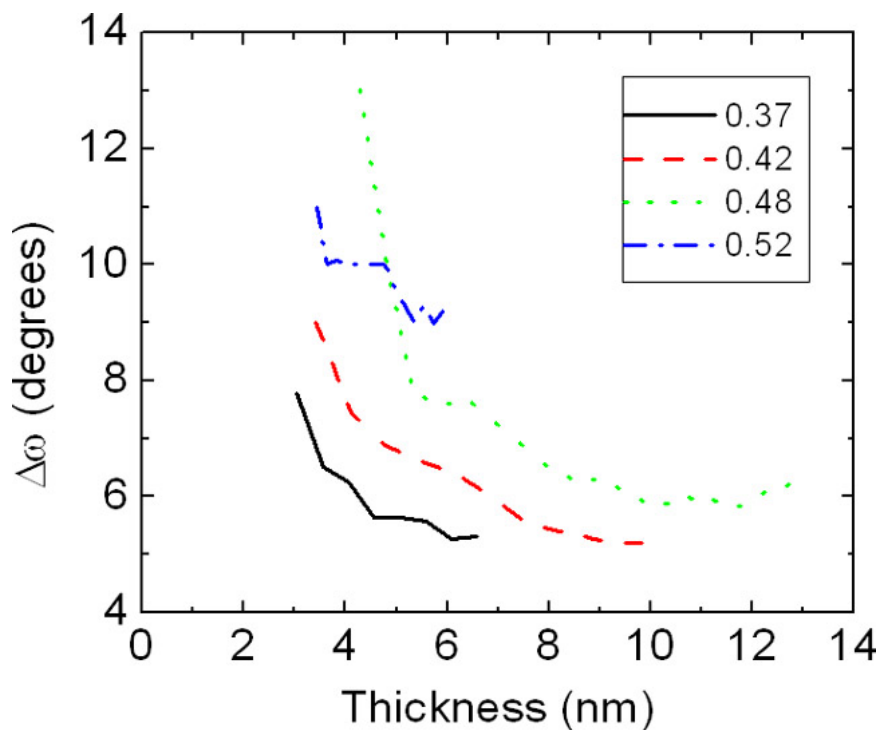


Figure 3.11 *In situ* RHEED measurements of out-of-plane orientation distribution ( $\Delta\omega$ ) as a function of film thickness for ion/MgO flux ratios from 0.37 to 0.52.

continuation of growth on the same sample after in-plane distribution measurement, which allowed for the first continuous observation of biaxial texture development in IBAD MgO.

The XRD measured samples listed in Figure 3.10 were measured by stopping IBAD growth at the specified thickness and then depositing a 100 nm homoepitaxial MgO layer at 500° C so that it could be measured using XRD<sup>53</sup>. This method makes the unlikely assumption that the biaxial texture of the < 10 nm thick film will not change during 100 nm of homoepitaxy, as well as being subject to run to run variations in the IBAD processing.

Despite these limitations, we see that the XRD measurements show a similar trend for the in-plane orientation distribution development as a function of film thickness.

The result is that from the first biaxially textured film (4 nm) to the optimal film characteristics (8 nm), the in-plane orientation distribution ( $\Delta\phi$ ) decreases from  $17^\circ$  to  $10^\circ$  FWHM and the out-of-plane orientation distribution ( $\Delta\omega$ ) decreases from  $8^\circ$  to  $6^\circ$  FWHM.

RHEED-based biaxial texture measurement method provides information not measurable via x-ray scattering and facilitates measurements of biaxial texture, providing insight into biaxial texture development. One of the powerful aspects of RHEED-based analysis is the real-time acquisition of out-of-plane orientation distribution ( $\Delta\omega$ ) measurements. Figure 3.11 shows the out-of-plane orientation distribution measured from IBAD MgO as a function of film thickness and ion/MgO flux ratio. As illustrated previously in Figure 3.10, during ion beam-assisted deposition the out-of-plane orientation distribution narrows as the film grows. At 0.52 ion/MgO flux ratio ( $\text{Ar}^+$  energy of 750 eV) the deposition condition is close to producing zero net growth because of ion sputtering and therefore results in increased ion damage to the MgO film. Decreasing the ion/MgO flux ratio from 0.52 to 0.37 reduces the ion damage, resulting in more rapid narrowing of the out-of-plane orientation distribution as the film grows. Each data point in Figure 3.11 was collected during IBAD MgO growth by taking a one second exposure time image of the RHEED pattern, the points being separated by 3 seconds of growth. The low point to point noise levels show that the measurement technique is stable and reproducible. Using x-ray scattering to obtain out-of-plane orientation distributions as a function of film thickness would require stopping the growth at each thickness interval and performing an out-of-plane rocking curve. Using the advanced photon source (APS) 33ID-D beam line with  $2.9 \times 10^5$  cps, the out-of-plane rocking curve

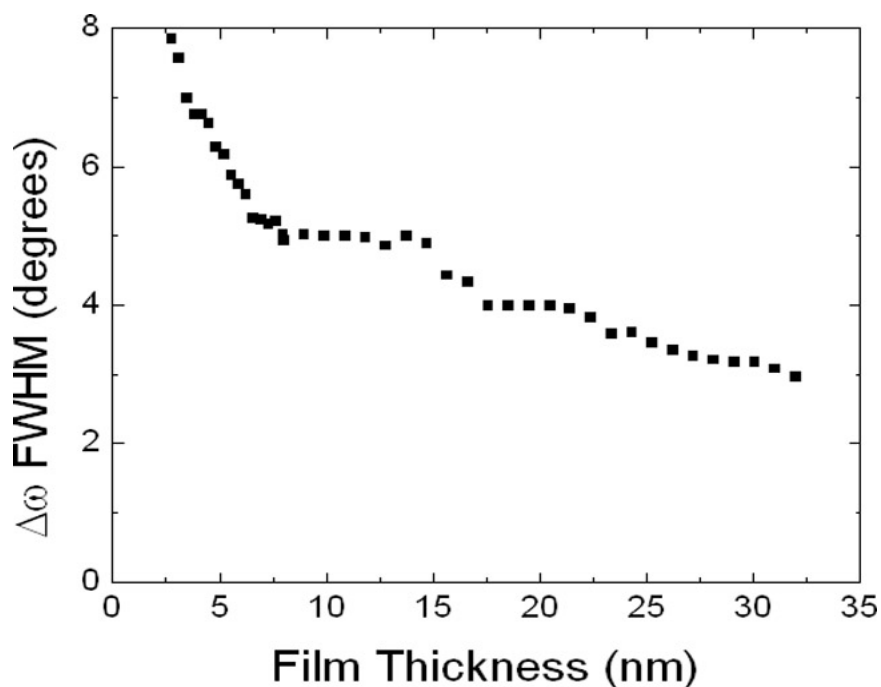


Figure 3.12 Out-of-plane orientation distribution ( $\Delta\omega$ ) for IBAD MgO growth and MgO homoepitaxy. From 0-8 nm the growth is performed by IBAD, while subsequent growth is done using homoepitaxy at 600° C.

for a 4 nm MgO film, with an out-of-plane FWHM of 7°, took over 30 minutes to resolve.

The real-time RHEED measurements have the added advantage of being more surface sensitive than x-ray diffraction, allowing for a more accurate picture of the out-of-plane texture evolution as a function of film thickness.

### 3.4 Biaxial texture development during homoepitaxy

Because IBAD MgO films are often less than 8 nm thick, the biaxial texture is not resolvable with lab-based (e.g. sealed tube or rotating anode) x-ray sources. To create an MgO film thick enough for biaxial texture measurement with lab-based x-rays, a common practice has been to grow thick homoepitaxial layers of MgO on top of the IBAD layer and assume that the biaxial texture does not change during homoepitaxy. Using our RHEED-based texture analysis method we have been able to monitor the

biaxial texture during homoepitaxy. A typical example of the out-of-plane ( $\Delta\omega$ ) development during MgO homoepitaxy is illustrated in Figure 3.12. The first 8 nm were grown using 1200 eV ion beam-assisted deposition and the subsequent 24 nm was a homoepitaxial deposition at 600° C, with an MgO flux rate of 0.3 angstroms/second. During both the IBAD growth and homoepitaxy the out-of-plane orientation distribution decreases with increasing film thickness. C.P. Wang and coworkers report out-of-plane orientation distributions approaching 3° FWHM, which is consistent with the results here. However, this value is significantly narrower, about 2° narrower, than the value for the out-of-plane orientation distribution of typical IBAD MgO films, as demonstrated in Figure 3.12.

### 3.5 Dependence of biaxial texture on growth conditions

Simultaneous RHEED-based measurements of both the in-plane and out-of-plane orientation distribution yield insights into the limitations of in-plane texturing through IBAD. Figure 3.13 shows the dependence of the optimal in-plane and out-of-plane orientation distributions as a function of ion/MgO flux ratio. The optimal in-plane orientation distribution as a function of ion/MgO flux ratio has been previously measured by C.P. Wang for 700 eV Ar<sup>+</sup> ion bombardment<sup>34</sup> and their results follow the same trend that we have observed for in-plane orientation distribution. However, the efficiency of the RHEED-based method allowed us to more finely resolve the dependency of the in-plane distribution on ion/MgO flux ratio and also measure the out-of-plane orientation distribution simultaneously.

We observe two regimes of biaxial texturing: at low ion/MgO flux ratio the out-of-plane orientation distribution is constant and the in-plane orientation distribution gets

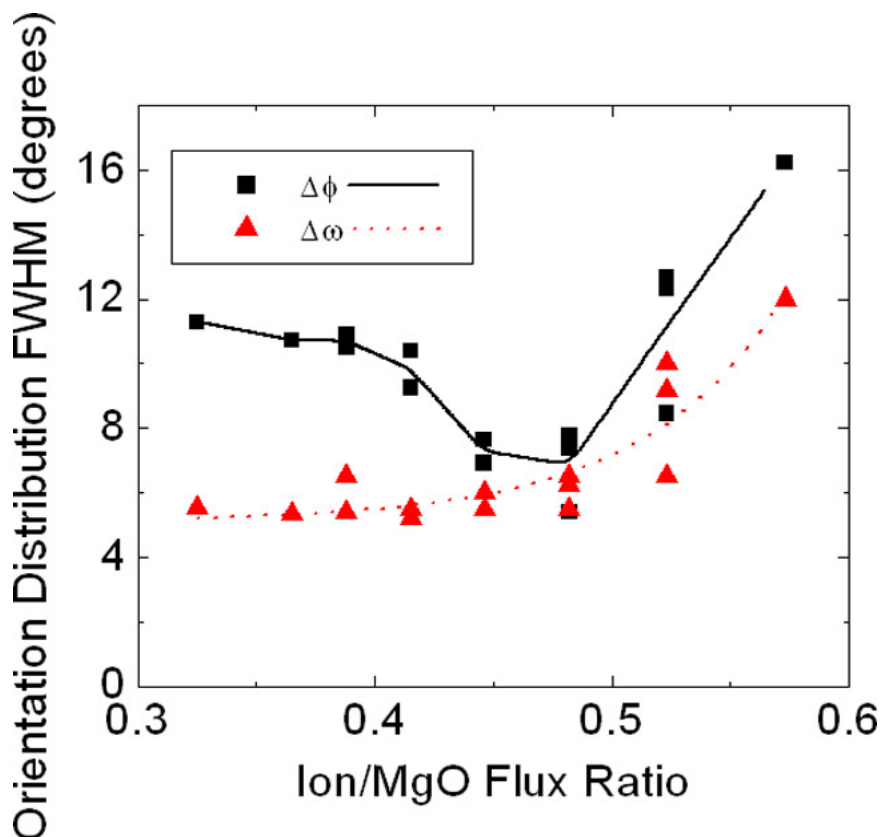


Figure 3.13 Optimal in-plane ( $\Delta\phi$ ) and out-of-plane ( $\Delta\omega$ ) orientation distributions for IBAD MgO growth with 750 eV Ar<sup>+</sup> ions as a function of ion/MgO molecule flux ratio. Measurements were performed using RHEED-based analysis and the lines are fits to the data.

narrower as the ion/MgO flux ratio increases, while at high ion/MgO flux ratios the out-of-plane orientation distribution broadens with increasing ion/MgO flux ratio and is accompanied by a broadening of the in-plane orientation distribution. High-temperature physical vapor deposition of MgO on amorphous SiO<sub>2</sub> favors nucleation with a (001) fiber texture<sup>45</sup>, however at room temperature we have not observed a strong out-of-plane texture without ion bombardment. The ion bombardment energy must be sufficient for MgO to grow in the preferred [001] out-of-plane orientation.

Ressler et al. proposed that ion-induced in-plane alignment results from anisotropic grain damage, where the grains with the most damage-resistant planes oriented toward the axis of the incoming ion flux are selected to grow and grains which

do not have damage-resistant planes oriented toward the incoming ions are damaged and do not grow<sup>35</sup>. For IBAD MgO, the (101) planes are found to orient toward the Ar<sup>+</sup> ion bombardment. At low ion/MgO flux ratios the film has enough energy to select the preferred (001) out-of-plane texture, but does not have enough ion bombardment to efficiently select the in-plane orientation of every crystal, resulting in a broad in-plane orientation distribution. As the ion/MgO flux ratio increases to the optimal ratio, between 0.45 and 0.48 for 750 eV Ar<sup>+</sup> ion bombardment, the out-of-plane orientation distribution stays constant, while the increase in ion bombardment more efficiently selects the crystals with the (101) plane oriented toward the ion bombardment until the in-plane orientation distribution is within 2° of the out-of-plane distribution. Once the ion/MgO flux ratio increases past the optimum condition, ion damage causes the out-of-plane texture to broaden. A MgO crystal that has been rotated out-of-plane about the x-axis (the x-axis is the direction of the ion bombardment projected onto the plane of the substrate) misorients the (101) plane away from the Ar<sup>+</sup> ions. However, a subsequent in-plane rotation, a rotation about the axis perpendicular to the substrate, can be used to restore the (101) plane to directly face the incident ions. As the out-of-plane distribution broadens, the distribution of in-plane rotations required to realign the (101) directions along the axis of the incoming ion bombardment also broadens. The in-plane orientation distribution achievable with IBAD is limited by the out-of-plane orientation distribution. These experiments indicate that the minimum in-plane orientation distribution achievable for IBAD MgO with 750 eV Ar<sup>+</sup> ion bombardment is 2 degrees, which could only be obtained if the out-of-plane orientation distribution approaches 0° FWHM.

It is not only the out-of-plane orientation distribution that would limit the in-plane orientation distribution. Assuming ion channeling is an important alignment mechanism, the open lattice planes have a finite acceptance angle that will allow ion channeling and the in-plane orientation distribution will not be narrower than the acceptance angle. The acceptance angle is a function of the ion energy because the scattering cross section of the ion decreases at higher energies. The MgO (110) planes are observed to align toward the incoming ion bombardment; however, the ion bombardment itself has an angular divergence. The Kaufmann source on our chamber is expected to have an angular divergence greater than  $15^\circ$  FWHM. To geometrically reduce the beam divergence we have moved the ion gun aperture 14 inches from the substrate so that the 3 cm source more closely approximates a point source and ions with an angular divergence of greater than  $2.5^\circ$  will not hit the center of the sample. The out-of-plane orientation distribution is driven by both thermodynamics (the (100) is the thermodynamically favorable out-of-plane orientation) and the ion beam alignment. However, it appears that the out-of-plane orientation distribution is already limited by the divergence of the ion beam. The minimum IBAD MgO out-of-plane orientation distribution that we have grown is  $\sim 5^\circ$  FWHM, which is on the same order as the total divergence of the ion beam ( $\pm 2.5^\circ$ ). The minimum in-plane orientation achievable is not the out-of-plane orientation distribution plus the divergence of the ion beam, because the ions which are aligning the out-of-plane orientation distribution are simultaneously aligning the in-plane orientation distribution. To reduce both the in-plane and out-of-plane orientation distribution requires a reduction in the ion divergence. The divergence of the ion beam can be reduced geometrically by moving the ion beam further away from the sample. This method is only limited by the

required flux of ions at the substrate which will decrease as the ion source moves farther away.

### 3.6 Conclusion

The application of RHEED-based biaxial texture analysis for *in situ* measurement of biaxial texture development in IBAD MgO has yielded new insights into biaxial texture development mechanisms. Sensitive RHEED experiments and subsequent TEM analysis revealed an abrupt, unexpected transition from an amorphous MgO film to a biaxially textured film. These results clearly show that anisotropic ion damage, not anisotropic ion sputtering, is responsible for nucleating biaxially textured IBAD MgO films. The experimental observations are consistent with the appearance of biaxial texture from an initially amorphous layer of MgO through solid phase crystallization around biaxially textured seed grains.

RHEED-based biaxial texture measurements provide a unique opportunity to measure the relationship between out-of-plane orientation and in-plane orientation development as a function of film thickness. We have been able to observe that both the out-of-plane and in-plane orientation distributions nucleate with a relatively broad distribution that improves as a function of film thickness until the optimal biaxial texture is reached at ~8 nm.

We have also observed the dependence of the in-plane orientation distribution on the out-of-plane orientation distribution for 750 eV IBAD MgO growth. At near zero net growth ion/MgO flux ratios, the slow growing film accumulates a lot of ion damage. Renucleation of the MgO crystals during growth of the highly damaged material provides the opportunity for the crystals to nucleate with the (001) rotated of the film normal

direction and thus degrades the out-of-plane texturing. Previous researchers have postulated that crystal directions with open lattice planes<sup>33</sup> or crystal directions which are resistant to ion damage are oriented toward the ion bombardment<sup>35</sup>. Therefore, because an out-of-plane axis rotation causes the (101) plane to rotate away from the incoming ions, the crystals must perform an in-plane rotation to reorient the (101) toward the ion bombardment, effectively coupling the in-plane orientation distribution to the out-of-plane orientation distribution. We have found that to achieve the minimum in-plane orientation distribution attainable using ion beam-assisted deposition requires the out-of-plane orientation distribution to approach 0° FWHM. Our experiments suggest that for 750 eV Ar+ IBAD MgO, the minimum in-plane orientation distribution achievable is approximately 2° FWHM. These dependencies have only been observable because of the *in situ* nature of RHEED and its ability to analyze the biaxial texture of films less than 4 nm thick. Traditionally, researchers have grown homoepitaxial layers on thin IBAD MgO templates to create a film thick enough to measure biaxial texture with lab-based x-ray sources. However, we have shown that the biaxial texture, especially the out-of-plane texture, changes with homoepitaxy of MgO on the IBAD template.

RHEED simulations of other biaxially textured cubic materials like BaTiO<sub>3</sub> exhibit similar dependence on biaxial texture as seen in MgO, indicating that this method should be generally applicable to cubic materials. Weak scattering of MgO and rapid biaxial texture development make investigation of IBAD biaxial texture development difficult with *ex situ* x-ray diffraction. The surface sensitivity and *in situ* nature of RHEED provides novel information about biaxial texture development and will continue

to facilitate rapid investigation of biaxial texturing mechanisms and biaxial texture optimization.

---

<sup>25</sup> X. D. Wu, S. R. Foltyn, P. N. Arendt, W. R. Blumenthal, I. H. Campbell, J. D. Cotton, J. Y. Coulter, W. L. Hulst, M. P. Maley, H. F. Safar, and J. L. Smith, *Appl. Phys. Lett.* **67**, 2397 (1995).

<sup>26</sup> J. M. E. Harper, K. P. Rodbell, E. G. Colgan, and R. H. Hammond, *J. Appl. Phys.* **82**, 4319 (1997).

<sup>27</sup> L. Dong and D. J. Srolovitz, *J. Appl. Phys.* **84**, 5261 (1998).

<sup>28</sup> L. S. Yu, J. M. E. Harper, J. J. Cuomo, and D. A. Smith, *Appl. Phys. Lett.* **47**, 932 (1985).

<sup>29</sup> J. F. Whitacre, Z. U. Rek, J. C. Bilello, and S. M. Yalisove, *J. Appl. Phys.* **84**, 1346 (1998).

<sup>30</sup> A. K. Malhotra, S. M. Yalisove, and J. C. Bilello, *Mater. Res. Soc. Symp. Proc.* **403**, 33 (1996).

<sup>31</sup> B. Raushenbach, M. Zeitler, J. W. Gerlach, and B. Stritzker, *Nucl. Instr. and Meth. In Phys. Res. B* **127/128**, 813 (1997).

<sup>32</sup> M. Q. Huang, J. Geerk, S. Massing, O. Meyer, H. Reiner, and G. Linker, *Nucl. Instr. and Meth. In Phys. Res. B* **148**, 793 (1999).

<sup>33</sup> C. P. Wang, K. B. Do, M. R. Beasley, T. H. Geballe, and R. H. Hammond, *Appl. Phys. Lett.* **71**, 2955 (1997).

<sup>34</sup> C. P. Wang, Ph.D. Thesis, Stanford University, (1999).

<sup>35</sup> K. G. Ressler, N. Sonnenberg, and M. J. Cima, *J. Am. Ceram. Soc.* **80**, 2637 (1997).

<sup>36</sup> R. M. Bradley, J. M. E. Harper, D. A. Smith, *J. Appl. Phys.* **60**, 4160 (1986).

- 
- <sup>37</sup> L. S. Yu, J. M. E. Harper, J. J. Cuomo, and D. A. Smith, *J. Vac. Sci. Technol. A* **4**, 443 (1986).
- <sup>38</sup> Y. Iijima, M. Hosaka, N. Tanabe, N. Sadakata, T. Saitoh, and O. Kohno, *J. Mater. Res.* **13**, 3106 (1998).
- <sup>39</sup> F. Ying, R. W. Smith, and D. J. Srolovitz, *Appl. Phys. Lett.* **69**, 3007 (1998).
- <sup>40</sup> Y. Iijima, K. Onabe, N. Futaki, N. Sadakata, O. Kohno, and Y. Ikeno, *J. Appl. Phys.* **74**, 1905 (1993).
- <sup>41</sup> W. Ensinger, *Nucl. Instr. and Meth. In Phys. Res. B.* **106**, 142 (1995).
- <sup>42</sup> L. Dong and D. J. Srolovitz, *Appl. Phys. Lett.* **75**, 584 (1999).
- <sup>43</sup> S. Gnanarajan and N. Savvides, *Thin Solid Films* **350**, 124 (1999).
- <sup>44</sup> J. R. Groves, P. C. Yashar, P. N. Arendt, R. F. DePaula, E. J. Peterson, and M. R. Fitzsimmons, *Physica C* **355**, 293 (2001).
- <sup>45</sup> J. S. Lee, B. G. Ryu, H. J. Kwon, Y. W. Jeong, and H. H. Kim, *Thin Solid Films* **354**, 82 (1999).
- <sup>46</sup> J. Wiesmann, J. Dzick, J. Hoffmann, K. Heinemann, and H. C. Freyhardt, *J. Mater. Res.* **13**, 3149 (1998).
- <sup>47</sup> M. O. Aboelfotoh, *Appl. Phys. Lett.* **24**, 347 (1974).
- <sup>48</sup> R. T. Brewer, H. A. Atwater, J. R. Groves, and P. N. Arendt, *J. Appl. Phys.* **93**, 205 (2003).
- <sup>49</sup> K. T. -Y. Kung, R. B. Iverson, and R. Reif, *Appl. Phys. Lett.* **46**, 683 (1985).
- <sup>50</sup> L. A. Zepeda-Ruiz and D. J. Srolovitz, *J. Appl Phys.* **91**, 10169 (2002).
- <sup>51</sup> J. -G. Yoon, H. K. Oh, and S. J. Lee, *Phys. Rev. B* **60**, 2839 (1999).
- <sup>52</sup> R. T. Brewer and H. A. Atwater, *Appl. Phys. Lett.* **80**, 3388 (2002).

---

<sup>53</sup> J. R. Groves, P. N. Arendt, H. Kung, S. R. Foltyn, R. F. DePaula, L. A. Emmert, and J. G. Storer, IEEE Trans. on Appl. Supercond. **11**, 2822 (2001).



## Chapter 4      Ferroelectric Properties of $\text{Ba}_x\text{Pb}_{1-x}\text{TiO}_3$ on Biaxially Textured MgO

### 4.1 Introduction

$\text{Ba}_x\text{Pb}_{1-x}\text{TiO}_3$  (PBT) has a tetragonal perovskite structure at room temperature (see Figure 1.1), where Ba and Pb interchangeably occupy the cube corner sites. The tetragonal distortion results in an electric dipole moment directed along the long crystal axis, also called the c-axis. The c-axis and dipole moment can orient along any of the six equivalent (001) directions. This material can act as an actuator because the direction of the c-axis can be rotated  $90^\circ$  using either an external electric field or a mechanical stress.

#### 4.1.1 Ferroelectric actuator

One can imagine linear actuator structures fabricated out of a ferroelectric membrane or bridge structure which uses a combination of electric fields and stress to accomplish linear actuation. Linear actuation from a stress/electric field actuator is depicted pictorially in Figure 4.1. The force applied normal to the ferroelectric thin film could be pressure from a trapped gas or it could be from a rod attached to the structure to be moved by the actuator. In Figure 4.1a, no electric field is applied across the ferroelectric membrane so the tensile stress causes the c-axes to rotate into the plane of the film. As a result the overall membrane lateral length is elongated and the center of the membrane sinks. In Figure 4.1b, an electric field is applied perpendicular to the membrane, inducing the electric dipoles to orient along the direction of the applied electric field. If the electric field imposed across the thin plane of the film exceeds a

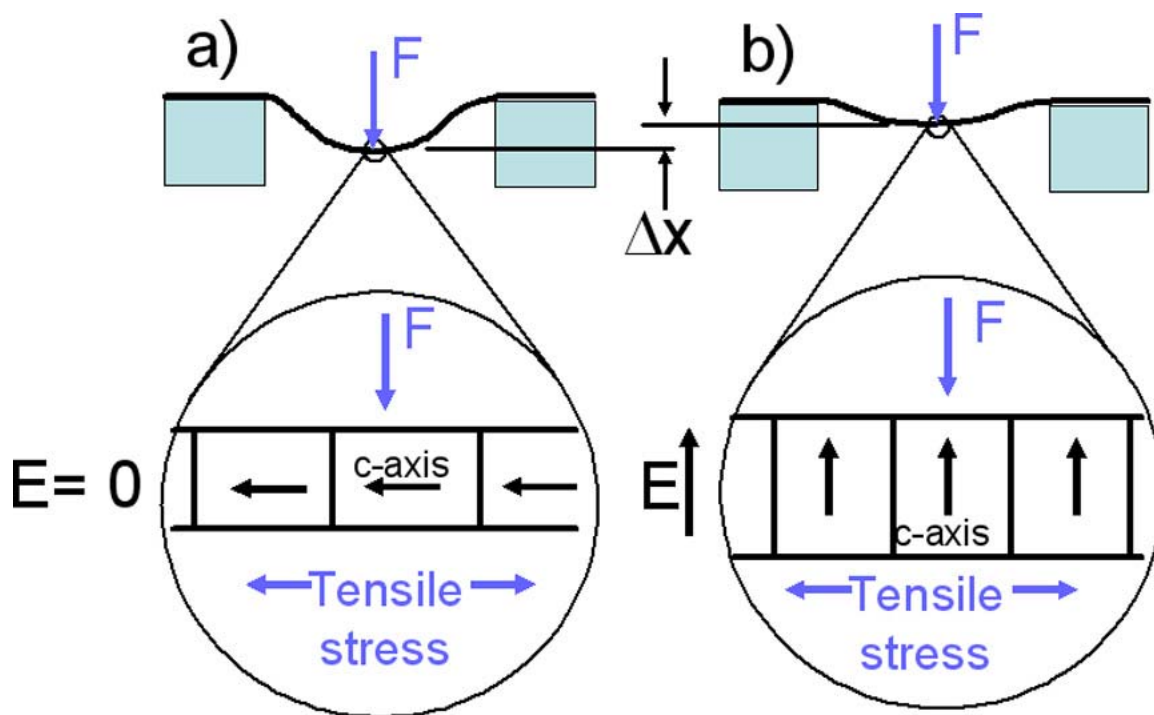


Figure 4.1 Schematic of a ferroelectric membrane linear actuator using stress and electrical fields. a) With zero electric field the stress orients the c-axis in plane, elongating the membrane, and causing the center of the membrane to sink. b) With the application of an electric field perpendicular to the membrane, the ferroelectric dipole moment aligns with the electric field and the shorter a-axes are aligned in-plane, shrinking the membrane and lifting the center up a distance  $\Delta x$ , which is the linear translation attainable from this structure.

minimum coercive field, then the electric dipole, and therefore the c-axis, is forced to orient in the direction of the electric field, despite the tensile stress which tends to orient the c-axis in the plane of the ferroelectric membrane. If all crystals have their c-axes oriented out-of-plane, the shorter a-axes are oriented in the plane of the ferroelectric membrane, making the ferroelectric membrane as short and flat as possible, lifting the center of the membrane. Releasing the electric field would allow the membrane to revert to the state shown in Figure 4.1a. The distance this linear actuator structure can translate,  $\Delta x$  in Figure 4.1, is proportional to the length of the membrane and the  $c/a$  ratio.

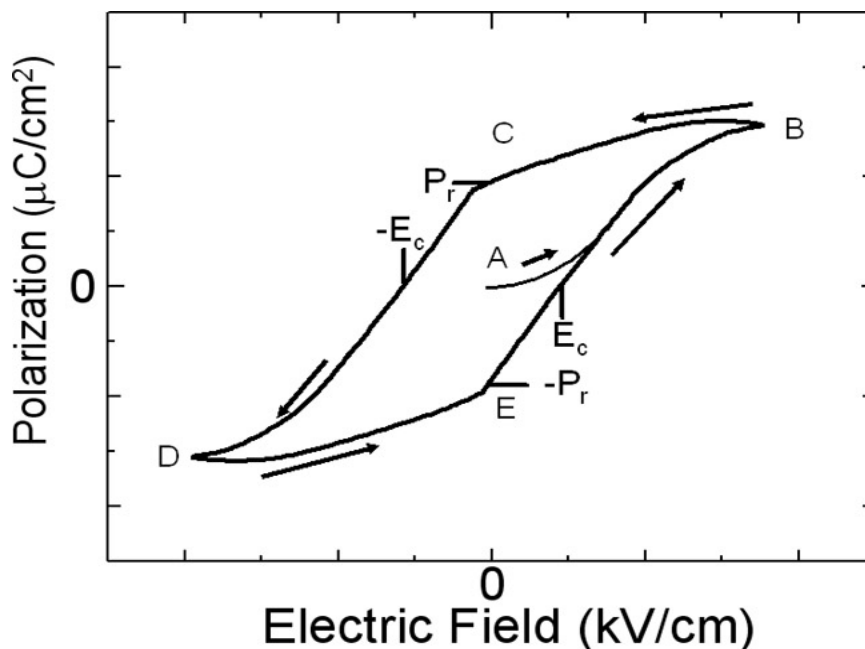


Figure 4.2 A polarization hysteresis loop plots the dielectric polarization as a function of applied voltage. Points C and E are the positive and negative remnant polarizations ( $P_r$ ), respectively. The coercive field ( $E_c$ ) must be calculated from the voltage drop across the ferroelectric material when the net polarization goes to zero.

For integration of ferroelectric actuators with silicon electronics we would like to grow ferroelectric films on amorphous layers. The resulting grain orientation distribution of the ferroelectric film will greatly affect actuator performance.

For randomly oriented polycrystalline ferroelectrics, geometric considerations limit the membrane actuation to less than half of the actuation achievable by a single-crystalline ferroelectric membrane. A biaxially textured ferroelectric film, however, would approach the full actuation of a single-crystalline film as the orientation distribution decreased toward zero.

#### 4.1.2 Ferroelectric thin film characterization

While ultimately we are interested in measuring actuator switching speed and work/volume (combining both actuation displacement and the force provided by the

actuator), measurements on thin ferroelectric films fully attached to the substrate can give insight into how the final actuator will perform without the extra difficulty of building complicated test structures.

### 4.1.3 Polarization hysteresis loops

One of the standard methods for characterizing ferroelectric properties is to make polarization field measurements. An example of a polarization hysteresis loop from this type of experiment is included as Figure 4.2. Even though regions of the ferroelectric film have a uniform polarization (these regions are called domains), a domain structure will form that reduces the net crystal dipole toward zero to minimize the total energy associated with the spontaneous ferroelectric polarization. Therefore, the hysteresis loop starts near the origin and with the application of an electric field the dipole moments will rotate to align along the direction of the electric field (segment A to B). If the electric field is decreased to zero (segment B to C), the crystal polarization will not return to zero, but will return to  $P_r$  [ $\mu\text{C}/\text{cm}^2$ ], which is called the remnant polarization. For a single domain crystal, this is a measurement of the intrinsic ferroelectric dipole moment. In real crystals, some ferroelectric domains are pinned and cannot rotate in an applied electric field, and the measured remnant polarization will give a measurement of the fraction of domains that cannot rotate. By applying a negative voltage (segment C to D), the ferroelectric domains can be switched, via domain nucleation and growth, into the opposite direction. The coercive field,  $E_c$ , is the field required to bring the crystal net polarization to zero by switching half of the ferroelectric domains. The coercive field is a measurement of the difficulty of dipole orientation switching. In thin film ferroelectrics, the coercive field will be affected by crystal defects, grain boundaries, and the

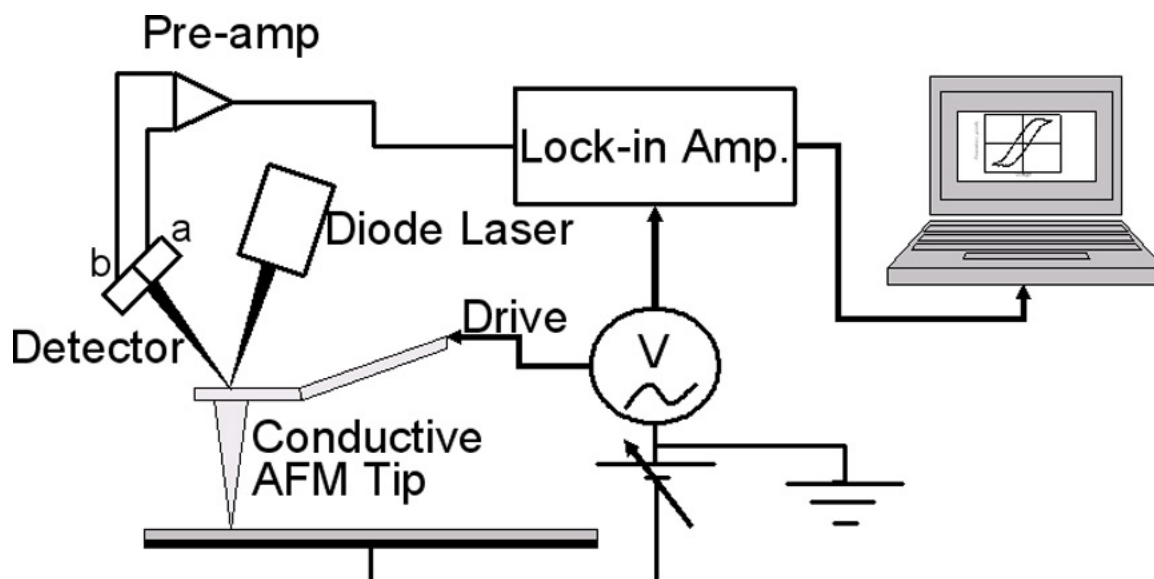


Figure 4.3 Schematic of a dynamic contact mode electrostatic force microscopy (DC-EFM) system.

mechanical stress applied to the film from the substrate. If the electric field again approaches zero (segment D to E) the polarization will not approach zero, but will approach the negative remnant polarization value.

#### 4.1.3.1 Dynamic contact mode electrostatic force microscopy

Ferroelectric film domain structures were mapped using dynamic contact mode electrostatic force microscopy (DC-EFM). Figure 4.3 shows a schematic of a DC-EFM instrument<sup>54</sup>. DC-EFM is performed by setting a conductive AFM tip into contact mode over the sample surface which is biased with respect to the AFM tip, applying an ac electric field, and measuring the tip deflection as a function of the applied voltage using a lock-in amplifier. The tip amplitude vibration dependence on the ac electric field is sensitive to the surface charge density from the local polarization<sup>54</sup>. Ferroelectric domains with the dipole oriented in the plane of the film will not contribute to the tip deflection associated with the applied ac voltage.

## 4.2 Chapter summary

Biaxially textured MgO was used as a heteroepitaxial template for  $\text{Ba}_x\text{Pb}_{1-x}\text{TiO}_3$  (PBT) grown using sol-gel and metal organic chemical vapor deposition (MOCVD). A ferroelectric film with a different composition was also grown on biaxially textured MgO by molecular beam epitaxy (MBE). Biaxial texture of the MgO templates and the ferroelectric films were measured using RHEED, showing that the ferroelectric biaxial texture is strongly correlated with the MgO biaxial texture. X-ray diffraction was used to examine phase purity, a/c axis ratio (relative fraction of the film with the a-axis oriented out-of-plane versus the fraction of the film with the c-axis oriented out-of-plane). The ferroelectric/ MgO interface, heterostructure defects, grain size and film orientations were examined with cross section transmission electron microscopy (TEM). Finally, the ferroelectric properties of biaxially textured PBT films were examined. The ferroelectric domain structure was mapped using DC-EFM and polarization hysteresis loops were taken at several points over the films to evaluate local ferroelectric domain switching.

## 4.3 Biaxially textured ferroelectrics on biaxially textured MgO

### 4.3.1 Growth methods

Several growth methods were investigated for heteroepitaxy of PBT on biaxially textured MgO templates to determine their suitability for making biaxially textured PBT. While the best possible ferroelectric properties are desirable, it is also important to develop a low temperature deposition process ( $< 500^\circ \text{C}$ ) so that is compatible with fabricated silicon electronics.

### 4.3.1.1 Sol-gel

Sol-gel deposition is a flexible thin film growth method that allows for easy composition tuning and can be performed without expensive high vacuum equipment. A solution is first made by dissolving metallorganic precursors in an organic solvent. The substrate is then spin coated with a metallorganic solution and annealed at a low temperature to drive off the organic components and any water present (either added on purpose or from ambient moisture), leaving a sparse amorphous matrix. Finally, the film is sintered at a high temperature to create a dense, crystalline film.

The sol-gel films examined in this experiment were grown on biaxially textured MgO by Stacey Boland using the solution system of Pb-acetate: Ba-acetate: Ti-isopropoxide dissolved in ethylene glycol, with acetylacetonate for Ti-isopropoxide chelation, in 1: 1: 2 ratios<sup>55</sup>. Water was added to the solution such that the molar ratio of H<sub>2</sub>O to Ti was 8. This solution was spin coated onto the biaxially textured MgO templates at 4000 rpm, pyrolyzed at 250° C for 3 minutes, then calcined at 600° C for 2 hours. Rutherford backscattering (RBS) measurements show that a single coating following this procedure results in a 47 nm thick film with a Ba<sub>0.55</sub>Pb<sub>0.45</sub>TiO<sub>3</sub> composition. This same deposition process was followed for deposition on a (001) single-crystal MgO substrate as well. On the single-crystal film, instead of only one layer, 3 layers were grown. Each additional layer was deposited after the full process of sintering at 600° C was completed for the previous layer.

The main advantages of using a sol-gel process are easy composition control, low equipment cost, and the potential for low temperature processing. Film composition is controlled by changing the ratio of metallorganic precursors, allowing in principle for the

deposition of all  $\text{Ba}_x\text{Pb}_{1-x}\text{TiO}_3$  solid solution compositions for  $x = 0$  to 1. Process parameters can be varied to achieve crystalline films at temperatures lower than  $450^\circ\text{C}$ <sup>56</sup>, making it a practical candidate for ferroelectric film deposition on silicon electronics wafers.

#### 4.3.1.2 MOCVD

Metallorganic chemical vapor deposition (MOCVD) was chosen as a second method for deposition of PBT. The MOCVD PBT films in this experiment were grown by David Boyd and Mohamed El-Naggar at Caltech<sup>57</sup>. The Ba, Pb, and Ti precursors are  $\text{Ba}(\text{tmhd})_2$ ,  $\text{Pb}(\text{tmhd})_2$ ,  $\text{Ti}(\text{OPri})_2(\text{tmhd})_2$ , where tmhd is 2,2,6,6-tetramethylheptane-3,5-dionate and OPri is di-isopropoxy. The source materials are kept in separate bubblers and combined in a gas line at  $250^\circ\text{C}$  before being introduced into a mixing chamber with oxygen. The well mixed gas is introduced into the deposition chamber through a shower head nozzle where it is deposited onto the MgO substrate at a total pressure of 15 mtorr and  $750^\circ\text{C}$ . MOCVD PBT was grown on both biaxially textured MgO substrates and (001) single-crystalline MgO.  $\text{Ba}_{0.03}\text{Pb}_{0.97}\text{TiO}_3$  and  $\text{Ba}_{0.2}\text{Pb}_{0.8}\text{TiO}_3$  was grown using this method.

One of the main reasons for using MOCVD to grow ferroelectric films is the relatively high (3.7 nm/min) growth rate, which makes it suitable for growing micron thick layers for actuator structures. It is also possible to perform infrared spectroscopy during growth for both composition and rate monitoring.

### 4.3.1.3 MBE

Molecular beam epitaxy (MBE) consists of evaporating film components in high vacuum and depositing them on a substrate where the evaporated material uses the order of the substrate to orient its own crystal directions. Composition control can be more difficult in MBE than in sol-gel or MOCVD and the difficulty increases with each additional element in a desired material. Careful flux monitoring and control of each individual component is essential to producing stoichiometric films, although sometimes differences in reactivity and elemental volatility can be exploited to ease the control requirements. One of the advantages of MBE is that the high vacuum environment provides the opportunity to perform *in situ* RHEED monitoring, which can aid in creating stoichiometric films<sup>58</sup>, yield real-time crystal structure information, and can monitor the biaxial texture development in real-time.

I designed and fabricated a high vacuum system capable of IBAD MgO, *in situ* biaxial texture RHEED analysis, and co-evaporation of lead, barium, and titanium with an oxygen atom source for the fabrication of biaxially textured MBE  $\text{Ba}_1\text{Pb}_{1-x}\text{TiO}_3$ . Images of the MBE chamber and a schematic of the main chamber components are included as Figure 4.4- Figure 4.7. IBAD MgO is grown using e-beam evaporation of MgO from a 4-pocket Temescal CV-10 source and concurrent ion bombardment from a 3 cm Ion Tech Inc. Kaufman ion gun. Because the divergence of the ion flux broadens the in-plane orientation distribution, the ion gun is placed 17 inches from the substrate to geometrically decrease the effective divergence of the ion gun at the substrate. The ion flux with divergence angle of greater than  $4^\circ$  from the ion gun normal will miss the

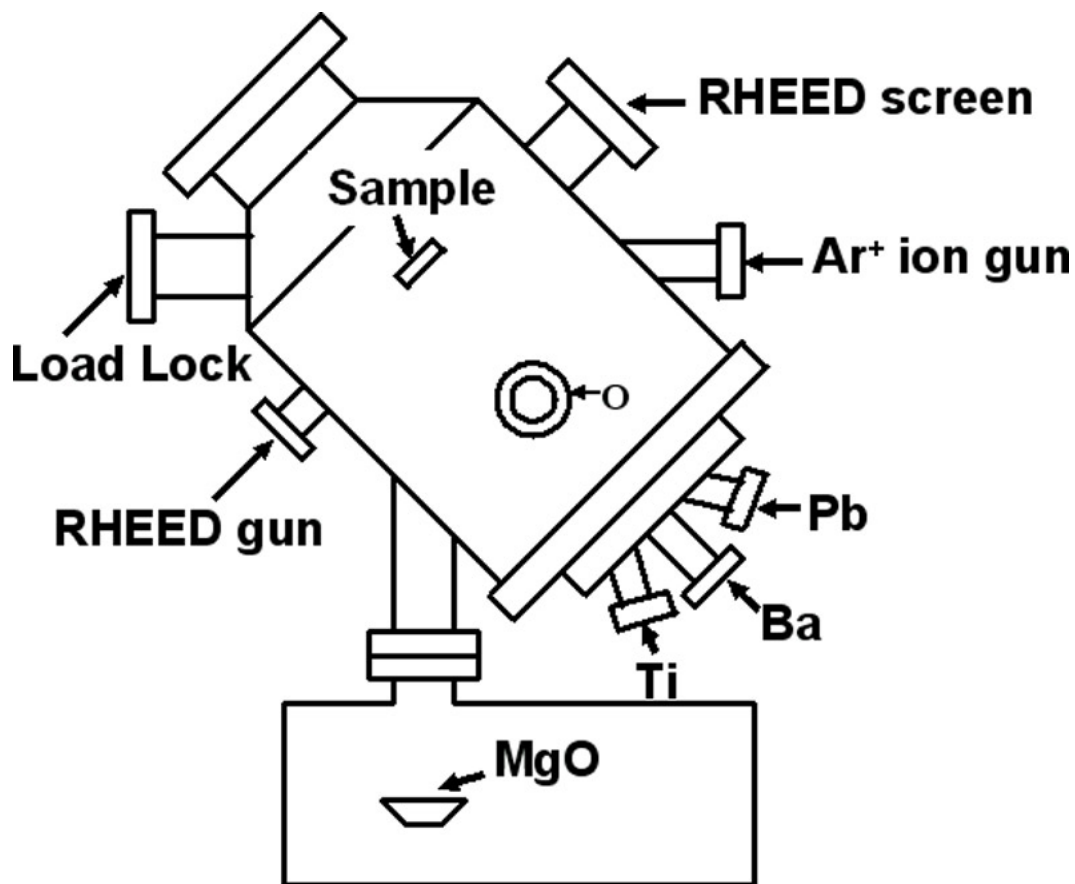


Figure 4.4 Schematic of the IBAF MgO and oxide molecular beam epitaxy chamber.

substrate and space charging in the beam should act to narrow the divergence angle further.

Before IBAF MgO growth, the ion source is allowed to warm up for at least 15 minutes and the ion flux is monitored by a translatable faraday cup to verify that the ion flux rate is stable. During growth, the MgO deposition rate is monitored by an Inficon quartz crystal monitor, located between the e-beam evaporator and the substrate, but out of the line of sight from the MgO to the sample. The quartz crystal monitor is also shielded from the ion bombardment. Shutters cover the elemental sources to protect them from sputtering caused by the ion gun during IBAF. The RHEED gun and screen were located so that RHEED patterns can be collected from the sample in the growth position

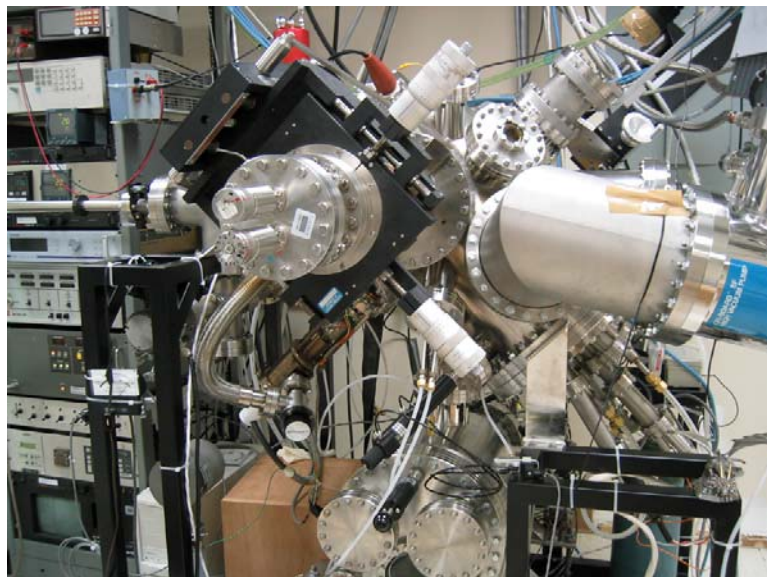


Figure 4.5 Side view of the IBAF MGO and oxide MBE chamber.

and the RHEED gun is differentially pumped through the load lock so that it can operate when the growth chamber is at  $1 \times 10^{-4}$  torr (this is the Ar partial pressure necessary to operate the ion gun).

The capability to grow  $\text{Ba}_x\text{Pb}_{1-x}\text{TiO}_3$  is provided by elemental sources of Ba, Pb, Ti, and oxygen. Ba and Pb are evaporated from separate effusion cells. Each cell is filled with high purity Pb (99.999%) or Ba (99%) and the deposition rate is controlled through temperature PID control, which relies on the vapor pressure of the element at a given temperature to provide the desired elemental flux.

Our titanium source is a Varian Ti-ball sublimation pump run by a stable HP 6673A power supply<sup>59</sup>. The titanium ball is heated by a tungsten wire coiled inside the titanium ball. The sublimation rate of the titanium is set by controlling the current running through the tungsten wire. Finally, because Pb is difficult to oxidize, we use an Oxford Applied Research RF oxygen atom source. Oxygen is injected into the source,

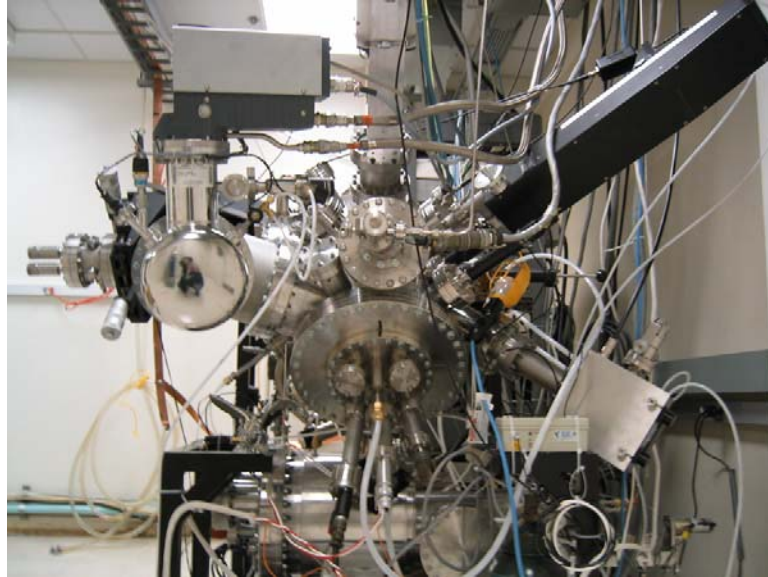


Figure 4.6 Front view of the IBAD MgO and oxide MBE chamber.

creating a background oxygen pressure of  $6 \times 10^{-5}$  torr, and 500 W of RF power is used to dissociate a fraction of the  $O_2$  to make oxygen atoms, which then drift to the substrate. Because of the high substrate temperatures needed ( $> 700^\circ$  C) and the oxidizing atmosphere, the substrate heating element is a single machined piece of SiC.

The two main challenges for successful  $Ba_xPb_{1-x}TiO_3$  MBE growth are to control the flux rates to achieve the desired stoichiometry and to oxidize the Pb so that it will incorporate into the ferroelectric film. Composition control can be simplified by the volatility of Pb. It has been shown that  $PbTiO_3$  growth is controlled entirely by the Ti flux, which has almost unity sticking fraction and oxidation rates. By applying a large excess of Pb, stoichiometric films are obtained because the excess Pb evaporates, leaving behind  $PbTiO_3$ <sup>60</sup>. To mitigate the flux control issues and to alleviate the oxidation requirements of  $PbTiO_3$  growth we decided to grow  $Ba_xPb_{1-x}TiO_3$ , where  $x = 0.9$ . By growing  $BaTiO_3$  slightly Ba poor with a large excess of Pb, we reduce the amount of Pb that requires oxidation by a factor of 10 with respect to  $PbTiO_3$ , while the composition

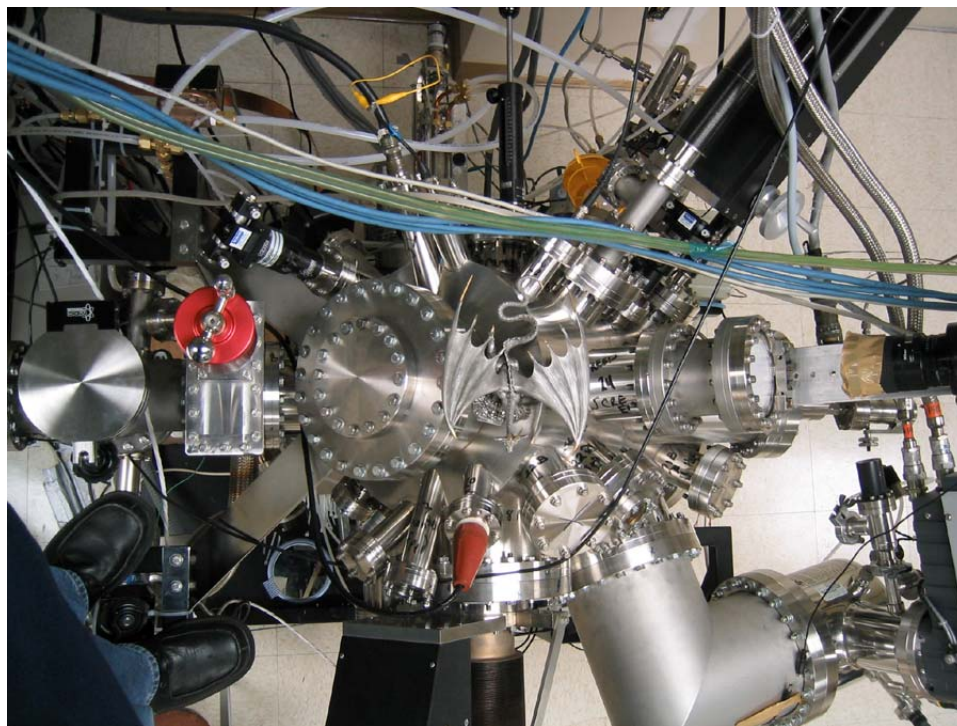


Figure 4.7 Top view of the IBAD MgO and oxide MBE chamber.

control is provided by the evaporation of excess Pb that could not be incorporated into the perovskite sites left vacant by the paucity of Ba.

MBE growth requires very stable deposition rates. Before deposition, the Ba, Pb, and Ti sources are taken to the expected deposition temperatures and allowed to stabilize for one hour before the fluxes are monitored. A quartz crystal monitor is then moved into a position about 1 inch in front of the shuttered substrate and each elemental flux is monitored one at a time by opening individual source shutters. The desired fluxes are lower than the real-time detection rate sensitivity limit of the quartz crystal monitor ( $<0.1$  nm/s), so an average deposition rate is measured over a 2 to 5 minute time span. The temperature or power of each source is then changed to more closely approach the desired deposition rate and then allowed to come to a steady state for another 15-30 minutes before monitoring the deposition rate again. The sources are relatively stable

from experiment to experiment, so the changes are minor and the sources can be stabilized in a few hours. Once the desired rates are obtained, the quartz crystal monitor is retracted, the oxygen source is turned on, and the substrate shutter is lifted to begin growth.

Growth of  $\text{Ba}_{0.9}\text{Pb}_{0.1}\text{TiO}_3$  was attempted by supplying the substrate with 0.9 Ba: 0.7 Pb: 1 Ti. The Pb flux was a factor of 7 larger than necessary to fill the Ba sites in a  $\text{BaTiO}_3$  crystal left by the deficiency of Ba supplied, but the excess Pb was expected to evaporate, leaving a stoichiometric film. The elemental deposition rates were measured at 1.08 nm/min Ba, 0.40 nm/min Pb, and 0.54 nm/min Ti before growth. The substrate was a biaxially textured MgO film grown by IBAD and a subsequent 50.0 nm of homoepitaxial MgO (as measured by the quartz crystal monitor) deposited at 600° C. For MBE the substrate was held at 700° C. With the titanium source on, the chamber base pressure is  $5.0 \times 10^{-8}$  torr. Oxygen was introduced through a leak valve to yield a background pressure of  $4.5 \times 10^{-5}$  torr and the RF atom source power was set at 500 W. The film was grown for 2500 seconds and the final film thickness was measured to be 60 nm by cross section TEM, making a total deposition rate of 1.44 nm/min.

The final composition of the MBE film, measured using RBS, was  $\text{Ba}_{0.67}\text{Sr}_{0.03}\text{Pb}_{0.002}\text{Ti}_{1.3}\text{O}_3$ . The Sr originates as a 0.5% impurity in the 99% pure Ba source material. This film has the correct metal/oxygen ratio for a perovskite structure, which could be achieved if Ti is present as both  $\text{Ti}^{2+}$  (substituting in the Ba cubic corner sites) and  $\text{Ti}^{4+}$  (in its normal body center perovskite position).

The MBE  $\text{Ba}_x\text{Pb}_{1-x}\text{TiO}_3$  was only the initial growth experiment and knowing the final stoichiometry indicates several ways to improve the stoichiometry of future films.

Even with 700% excess Pb the final film contained almost no Pb. Experiments growing MBE PbTiO<sub>3</sub> using Pb, Ti, and O<sub>3</sub> showed that for a constant Pb flux, by increasing the O<sub>3</sub> background pressure from  $5 \times 10^{-6}$  torr to  $5 \times 10^{-5}$  torr changed the resulting films from almost pure anatase TiO<sub>2</sub> to entirely perovskite PbTiO<sub>3</sub><sup>61</sup>. It is possible that operating under the oxygen pressure and RF power in this experiment the oxygen atom pressure was not sufficient to oxidize the Pb and resulted in negligible Pb incorporation in the film. The other result from this growth experiment is that even though the initial growth rate of Ba was sufficient to grow Ba<sub>0.9</sub>Ti<sub>1.1</sub>O<sub>3</sub>, the actual film had a significantly lower Ba content. Experiments using both quartz crystal monitors and atomic adsorption spectroscopy have seen that the Ba flux is significantly decreased with the addition of O<sub>3</sub> to the growth chamber<sup>61</sup>. A similar reduction in the Ba flux with the addition of oxygen would yield results consistent with our findings. To obtain the correct stoichiometric growth of BaTiO<sub>3</sub> will require either a careful calibration of the effect that oxygen has on the Ba evaporation rate, *in situ* atomic adsorption spectroscopy for real-time Ba flux monitoring, or reflection electron energy loss spectroscopy for real-time composition monitoring. The small amount of Pb in the MBE film and the significant amount of the Sr impurity (which will equivalently substitute for Ba in the perovskite cubic cell) prohibit referring to the MBE grown film as PBT. I will therefore designate it as BST for the remainder of this chapter.

### 4.3.2 Crystallographic orientation

Both BaTiO<sub>3</sub> and PbTiO<sub>3</sub> grow heteroepitaxially on (001) single-crystal MgO where the [001]<sub>Ferroelectric</sub> is parallel with the [001]<sub>MgO</sub> and the [100]<sub>Ferroelectric</sub> is parallel with the [100]<sub>MgO</sub><sup>62,63</sup> so the same heteroepitaxially relationship was expected from PBT

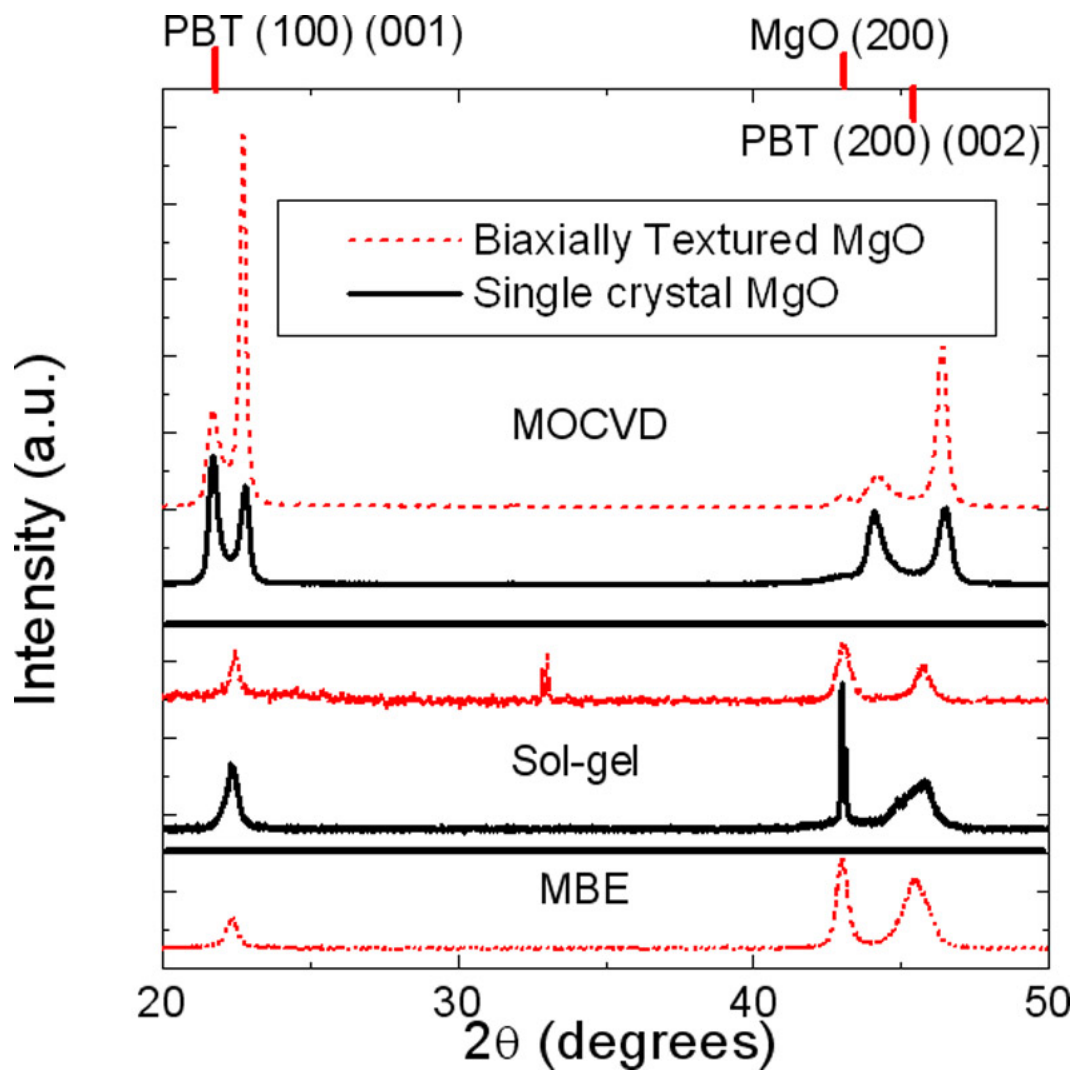


Figure 4.8 X-ray  $\theta$ - $2\theta$  curves from PBT deposited by MOCVD and sol-gel on single-crystal MgO (001) and biaxially textured MgO. An x-ray  $\theta$ - $2\theta$  curve from MBE BST is also included.

on MgO. The crystallographic orientation of PBT and BST deposited on biaxially textured MgO and PBT deposited on single-crystal MgO was measured using x-ray ( $\text{Cu } k_{\alpha}$ ) diffraction  $\theta$ - $2\theta$  curves (Figure 4.8). All films show (100) and (001) orientation (the extra sol-gel peak at  $2\theta = 32^{\circ}$  is attributed to the  $\text{Si}_3\text{N}_4/\text{Si}$  (001) substrate (002) Si peak). The relative amounts of a-axis and c-axis orientations (specifying whether the long crystal axis, also the electric dipole direction (the c-axis) or the short crystal axis (the a-axis) is oriented normal to the film surface) result from the stresses imposed on the PBT

thin films by the coefficient of thermal expansion mismatch between it and the substrate<sup>64,65</sup>. The thermal expansion of the substrate for biaxially textured MgO films is dominated by the silicon wafer. The coefficient of thermal expansion for silicon is  $2.59 \times 10^{-6}/\text{K}^{66}$ , while the coefficient of thermal expansion for MgO is  $14.8 \times 10^{-6}/\text{K}^{67}$ , for  $\text{PbTiO}_3$  it is  $12.6 \times 10^{-6}/\text{K}$  and for  $\text{BaTiO}_3$  it is  $9.8 \times 10^{-6}/\text{K}^{68}$ . PBT grown on MgO at high temperatures experience a compressive stress during cooling, which promotes c-axis formation. The c-axis component of the MOCVD film grown on single-crystal MgO is higher than for the sol-gel film because it was grown at a  $150^\circ \text{C}$  higher temperature and accumulated more compressive stress during cooling. All PBT and BST films grown on biaxially textured MgO substrates were predominately a-axis oriented, which is consistent with the low Si coefficient of thermal expansion causing a tensile stress to be imposed on the PBT and BST thin films during cooling.

#### 4.3.2.1 Composition and c/a ratio

The a-axis and c-axis coefficients were measured from the location of the (200) and (002) diffraction peaks. For MOCVD grown PBT films we measure  $a = 0.390 \text{ nm}$  and  $c = 0.411$  for a c/a ratio of 1.054. In the sol-gel  $\theta-2\theta$  no (002) and (200) peak separation is obvious, but a close examination of the peak shape belies the convolution of two separate peaks. Fitting two Gaussians to both the (001) and (100) PBT peak and the (002) and (200) PBT peak yields consistent measurements for the a-axis and c-axis spacing, which are  $a = 0.397 \text{ nm}$  and  $c = 0.403 \text{ nm}$  for a c/a ratio of 1.016. MBE BST was only deposited on biaxially textured MgO and did not display a c-axis orientation, therefore only the a-axis lattice constant could be measured ( $a = 0.398 \text{ nm}$ ). Despite

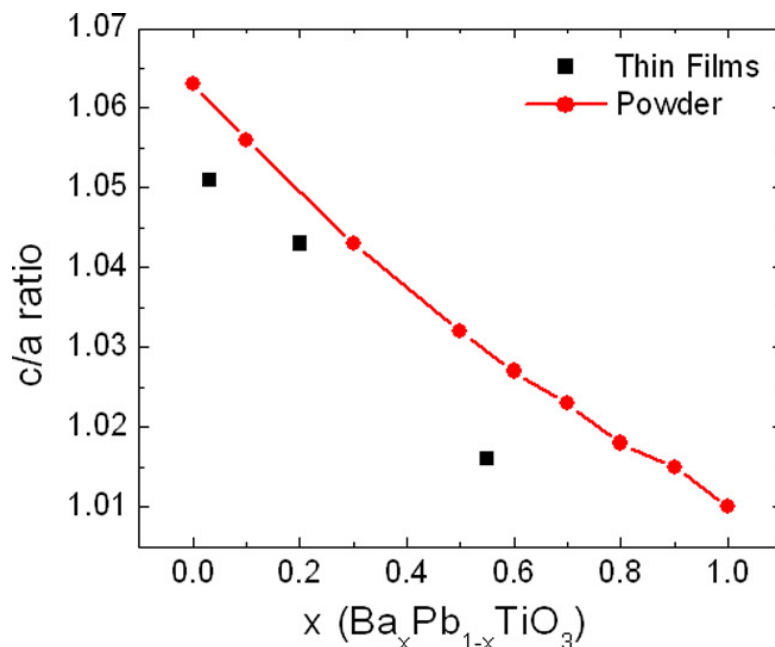


Figure 4.9 C/a ratio of  $\text{Ba}_x\text{Pb}_{1-x}\text{TiO}_3$  as a function of Ba composition ( $x$ ). Thin film data are the biaxially textured samples in this work and the powder samples are from the literature<sup>69</sup>.

extra Ti in the BST films, no extra diffraction peaks besides the perovskite (100) and (200) are observed.

The  $c/a$  ratio and lattice constants of  $\text{Ba}_x\text{Pb}_{1-x}\text{TiO}_3$  are expected to vary monotonically from the values for  $\text{BaTiO}_3$  to the values for  $\text{PbTiO}_3$  as  $x$  goes from 1 to 0 (for  $\text{BaTiO}_3$   $a = 0.3992$  nm,  $c = 0.4036$  nm,  $a/c$  ratio = 1.011 and for  $\text{PbTiO}_3$   $a = 0.3903$  nm,  $c = 0.4152$  nm,  $c/a$  ratio = 1.064)<sup>69</sup>. A linear interpolation between the  $c/a$  ratio for bulk  $\text{PbTiO}_3$  and  $\text{BaTiO}_3$  can not be expected for  $c/a$  ratio of  $\text{Ba}_x\text{Pb}_{1-x}\text{TiO}_3$  where  $0 < x < 1$  because of substrate clamping effects. The thickness required before heteroepitaxial  $\text{BaTiO}_3$  relaxes to its bulk value has been observed to range from just over 20 nm<sup>70</sup> to over 200 nm<sup>71</sup> depending on the substrate and deposition method. Figure 4.9 is a graph of the PBT  $c/a$  ratio as a function of the composition where  $x$  is defined as the fraction of Ba in the PBT film ( $\text{Ba}_x\text{Pb}_{1-x}\text{TiO}_3$ ). In all cases, the  $c/a$  ratio is smaller than the linear interpolation between  $\text{PbTiO}_3$  ( $x = 0$ ) and  $\text{BaTiO}_3$  ( $x = 1$ ).

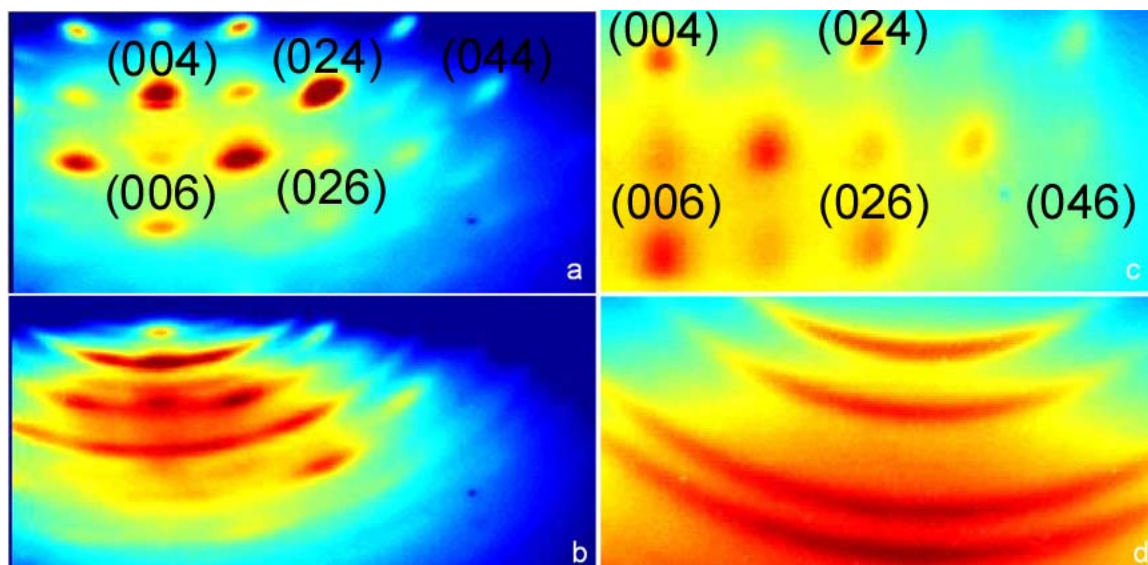


Figure 4.10 RHEED images of PBT grown on biaxially textured MgO. Sol-gel PBT (a) and MOCVD (c) PBT RHEED images from films deposited on MgO templates made from 8 nm of IBAD MgO and an additional 20 nm of homoepitaxial MgO grown at 600° C. Sol-gel (b) and MOCVD (d) PBT RHEED images from films deposited on MgO templates made from 8 nm of IBAD MgO.

#### 4.3.2.2 Biaxially textured MgO substrate effects

Heteroepitaxy of PBT was performed on two types of biaxially textured MgO templates. The first type of substrate was 8 nm IBAD MgO/ Si<sub>3</sub>N<sub>4</sub>/ Si (001). The second type of substrate was 20 nm homoepitaxial MgO grown at 600° C/ 8 nm IBAD MgO/ Si<sub>3</sub>N<sub>4</sub>/ Si (001). X-ray  $\theta$ -2 $\theta$  scans of PBT, grown by both sol-gel and MOCVD, exhibit much stronger diffraction when grown on homoepitaxial MgO surfaces than if they were grown on IBAD MgO surfaces. While the sol-gel on IBAD MgO only displays (001) diffraction peaks (albeit much weaker than for the films grown on homoepitaxial MgO surfaces), the MOCVD film grown on IBAD MgO displays diffraction peaks from (001), (110), and (111) orientations.

There are also striking differences in the RHEED patterns from PBT deposited directly on IBAD MgO surfaces and from films deposited on homoepitaxial MgO

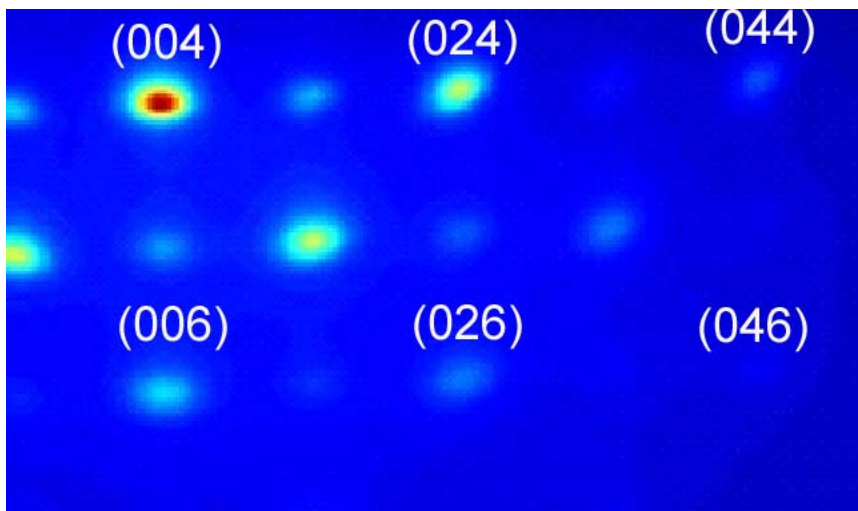


Figure 4.11 RHEED image of BST grown heteroepitaxially on biaxially textured MgO made from 8 nm of IBAD MgO and 20 nm of homoepitaxial MgO grown at 600° C.

surfaces. Figure 4.10 shows RHEED patterns from sol-gel and MOCVD PBT grown on IBAD MgO surfaces and IBAD MgO films with an additional 20 nm of homoepitaxial MgO grown at 600° C. The films grown on IBAD MgO surfaces exhibit broad out-of-plane orientation distributions, evident from the broad diffraction rings which appear instead of sharp diffraction spots. The out-of-plane orientation distribution cannot be measured for these films using our standard RHEED method because it is only valid for narrow orientation distributions. PBT films grown under the same conditions on biaxially textured MgO with a homoepitaxial layer show sharp diffraction spots characteristic of narrow out-of-plane orientation distributions ( $\Delta\omega = 3^\circ$  FWHM for MOCVD and  $\Delta\omega = 4^\circ$  FWHM for sol-gel). All diffraction patterns in Figure 4.10 have high broad background intensities. The broad background can come from scattering from a rough surface, grain boundaries, lattice defects, or amorphous regions in the film.

A RHEED image from MBE grown BST on biaxially textured MgO (with the homoepitaxial layer) is shown as Figure 4.11. The out-of-plane orientation distribution

for the MBE film is similar to the out-of-plane orientation distribution measured for the sol-gel and MOCVD film ( $\Delta\omega = 2.5^\circ$  FWHM), however, the diffuse background scattering is much weaker than for the sol-gel and MOCVD films.

IBAD MgO surfaces may not function as good heteroepitaxial templates for PBT because of the high defect density inherent in ion bombardment processes. Because the heteroepitaxy is *ex situ*, the IBAD MgO surface is exposed to moisture from the atmosphere. While water absorbs readily on the MgO (001) surface, experimental evidence and calculations suggest that the MgO (001) surface is stable under hydroxylation and MgO dissolution and pitting only occurs at surface defects<sup>72</sup>. IBAD MgO samples stored in the atmosphere (or even in a nitrogen purge box for extended periods) will change from a smooth mirror-like surface to a pitted, rough finish. The IBAD MgO samples were exposed to atmosphere for the minimum possible time before heteroepitaxy, but it may have been enough for moisture to degrade the crystallinity of the MgO surface. We speculate that the homoepitaxial layer grown on IBAD MgO reduces the defect density from ion bombardment and makes the substrate less susceptible to damage from water absorption. During one experiment, the homoepitaxial MgO film was left in room ambient overnight before the MOCVD PBT heteroepitaxial growth. The resulting PBT demonstrated biaxial texture commensurate with the MgO template, despite its exposure to the atmospheric moisture. Therefore, the homoepitaxial biaxially textured MgO templates are at least somewhat stable in atmospheric moisture.

### 4.3.3 Biaxial texture

Experiments to study the biaxial texturing of PBT on biaxially textured MgO used IBAD MgO films with an additional ~20 nm of homoepitaxially grown MgO at 600° C in

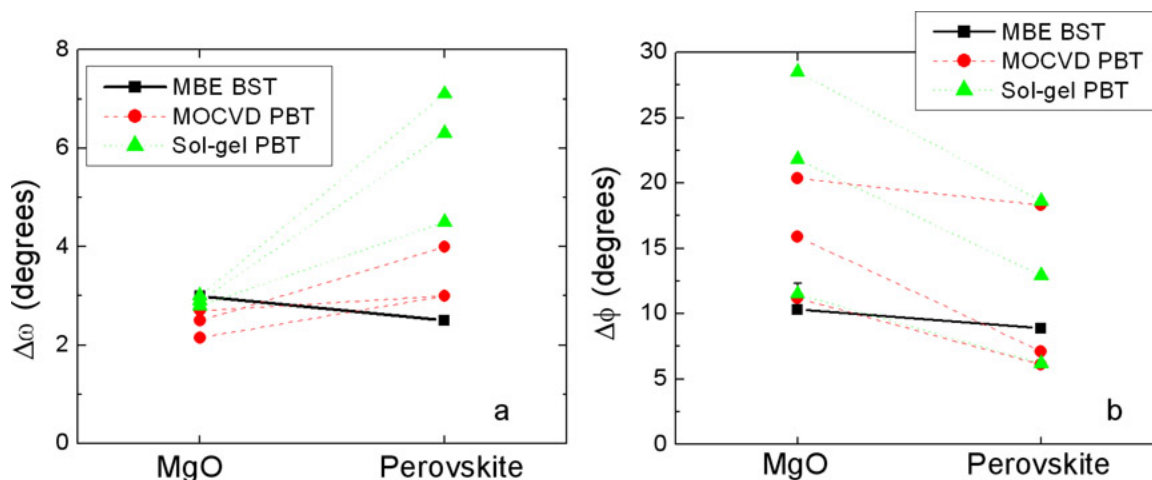


Figure 4.12 Out-of-plane ( $\Delta\omega$ ) and in-plane ( $\Delta\phi$ ) orientation distributions of biaxially textured MgO templates and the heteroepitaxial perovskite (BST or PBT) deposited by MBE, MOCVD, or sol-gel.

$3 \times 10^{-5}$  torr of  $O_2$ . The biaxial texture of the MgO template was controlled by changing the ion/MgO flux ratio during IBAD. Homoepitaxial MgO deposition rates varied from 0.15 nm/s to 0.03 nm/s (according to the quartz crystal monitor), but the deposition rate showed no significant effect on biaxial texture. I measured the sticking coefficient for MgO at 600° C to be 0.4, so the actual deposition rates varied between 0.06 nm/s and 0.012 nm/s.

A series of biaxially textured MgO templates were grown with various in-plane ( $\Delta\phi$ ) and out-of-plane ( $\Delta\omega$ ) orientation distributions. PBT was deposited on these MgO templates using sol-gel and MOCVD growth. BST was also deposited on biaxially textured MgO templates using MBE growth. The biaxial texture of the MgO templates and the heteroepitaxial PBT and BST were measured using RHEED and compared. A summary of these results is shown in Figure 4.12, where the in-plane ( $\Delta\phi$ ) and out-of-plane ( $\Delta\omega$ ) orientation distributions are plotted for each sample as a function of the film layer (homoepitaxial MgO and PBT/BST). The in-plane orientation distribution

measurement for the MBE MgO template is actually from the IBAD MgO surface (the in-plane distribution was not measured after homoepitaxial MgO growth and before the BST heteroepitaxy), but based on previous experiments the in-plane orientation distribution of the homoepitaxial MgO layer should be within  $2^\circ$  of the in-plane orientation distribution of the IBAD layer. We observe that the biaxial texture of the PBT is strongly dependent on the biaxial texture of the MgO template. The in-plane orientation distribution of the PBT is narrower than the MgO template. This has also been observed for heteroepitaxial  $\text{YBa}_2\text{Cu}_3\text{O}_{7-x}$  on  $\text{MgO}$ <sup>73</sup>. TEM images of MOCVD grown on biaxially textured MgO show grains which are 40 to 80 nm across compared with 27 nm grains observed in homoepitaxial MgO in TEM. This indicates that the PBT selectively nucleates on the well-aligned grains to create a more highly in-plane aligned film. The out-of-plane orientation degrades slightly, only by a few degrees, for PBT heteroepitaxy but this may result from the roughness of the homoepitaxial MgO template, which is typically measured at 0.8 nm rms in the AFM.

MBE grown films exhibited a closer correlation between the MgO template and heteroepitaxial BST in-plane orientation distributions. The strong dependence of the PBT and BST biaxial texture on the MgO template biaxial texture confirms that PBT and BST biaxial texture can be controlled through the MgO template. This provides incentive to optimize the IBAD MgO biaxial texture growth.

#### **4.3.4 TEM analysis**

We analyzed the ferroelectric film thickness and microstructure using cross section transmission electron microscopy (TEM). We also studied the effect of the different growth methods on the MgO biaxially texture template.

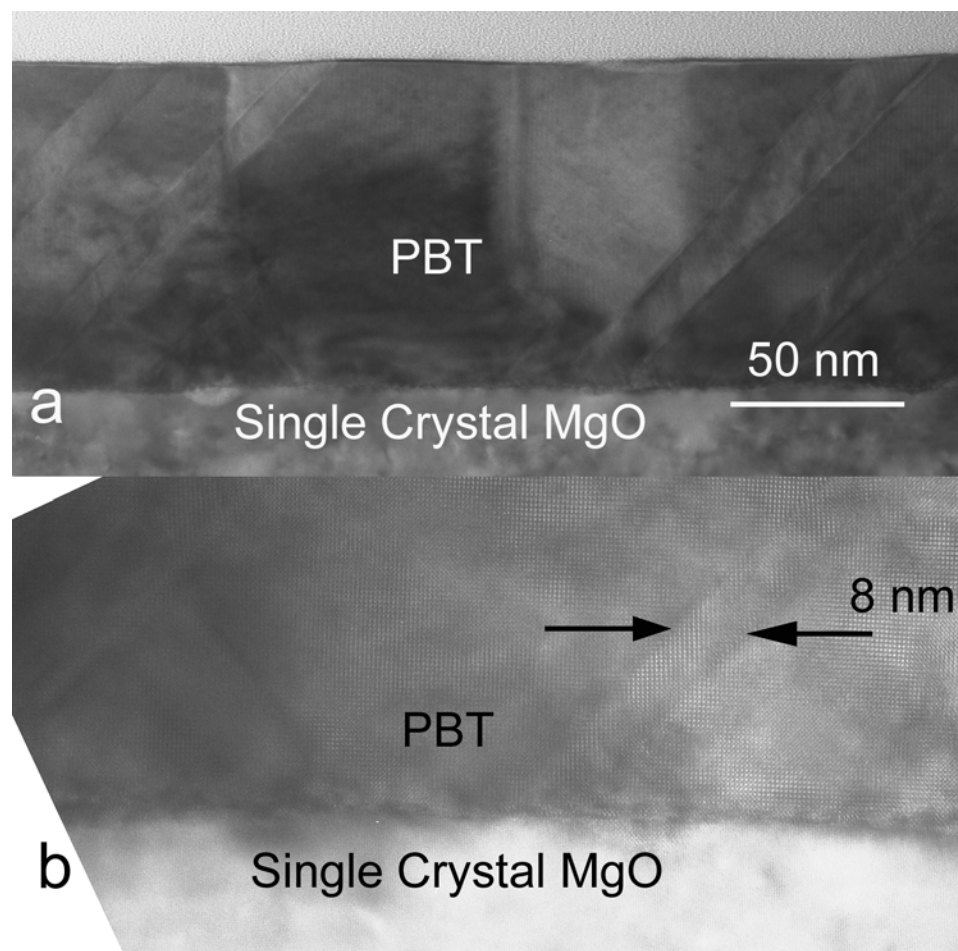


Figure 4.13 Cross section TEM images of MOCVD PBT grown on single-crystal MgO (001). b) is a high-resolution image of one of the  $45^\circ$  defects in (a).

#### 4.3.4.1 MOCVD PBT on MgO

MOCVD PBT grown on IBAD/homoepitaxial MgO shows significant differences from MOCVD PBT deposited on single-crystalline MgO. Figure 4.13a is a representative image of MOCVD PBT on single-crystal MgO. Semi-regularly spaced defects run at forty-five degrees to the surface normal. The penetration of one of these defects through a grain boundary suggests that these stacking faults formed following growth. The defect structure is very similar to the form predicted for a-axis/c-axis

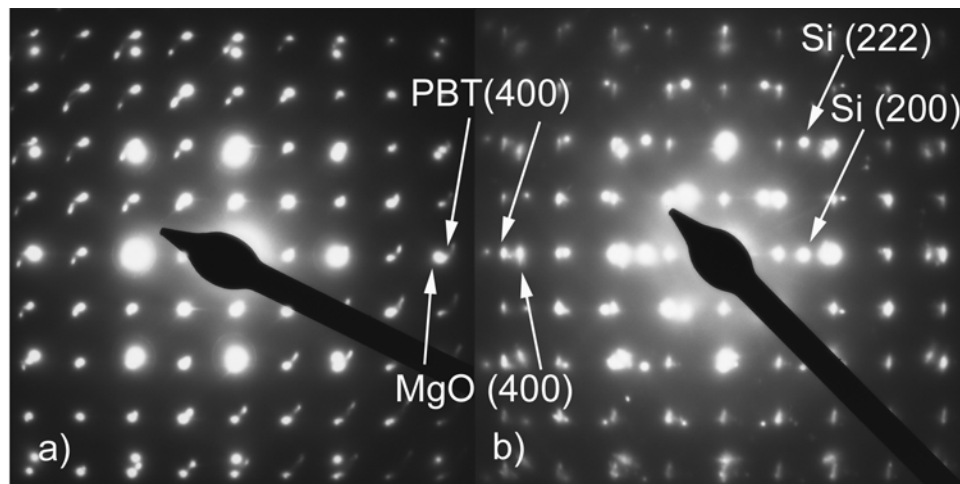


Figure 4.14 Diffraction patterns from MOCVD PBT grown on (a) single-crystal MgO (001) and (b) biaxially textured MgO.

ferroelectric domain boundaries. The forty-five degree boundary is predicted to form between a-axis and c-axis domains to minimize the ferroelectric dipole energy.

If these defects were formed to accommodate the lattice mismatch between MgO and the average of the measured a-axis and c-axis lattice constant (because the film is relatively equally mixed a-axis and c-axis according to x-ray diffraction), they would have to form every 8.2 nm. Looking at the defect density over a micron yielded one defect line every 22.4 nm. However, by looking at high-resolution TEM images of the MgO/PBT interface (Figure 4.13b), it is evident that each of the 45° lines is actually two separate defects separated by 7-8 nm. The actual defect density is one defect for every 11.2 nm, which is on the same order as the defect density expected to relieve the MgO/PBT lattice mismatch.

Figure 4.14a is a diffraction pattern from MOCVD PBT grown on single-crystal MgO. The large, sparse diffraction spots come from the MgO and the dense, small spots are characteristic of perovskite structure PBT. The double diffraction spots from the PBT film appears to be from out-of-plane rotated PBT crystals. The absence of diffraction

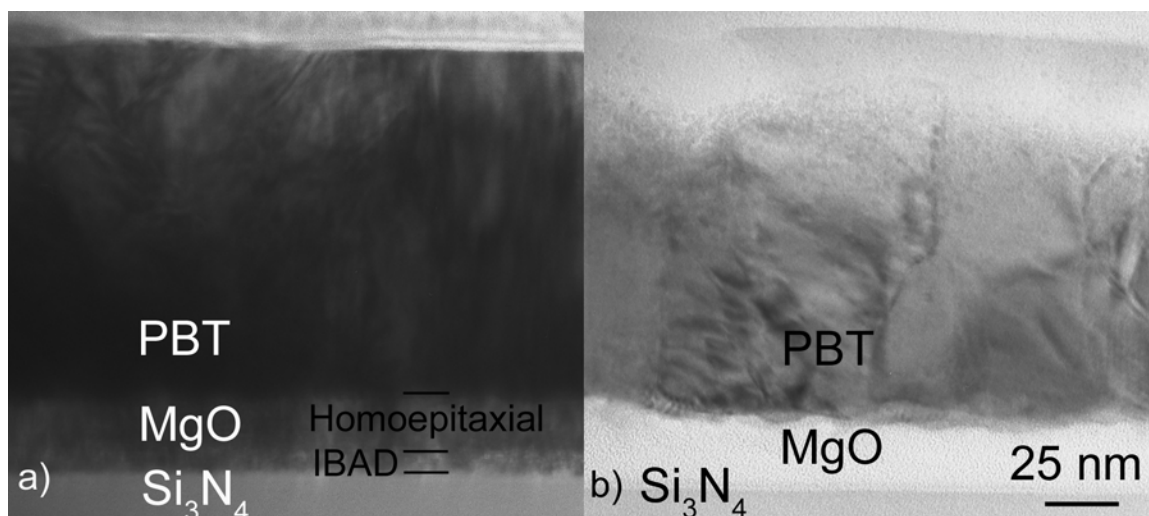


Figure 4.15 MOCVD PBT grown on biaxially textured MgO. In some areas the MgO layer appears crystalline (a), while in other areas it does not appear to be crystalline (b). rings confirms a very narrow out-of-plane orientation distribution ( $\Delta\omega$ ) and the MgO (001) and PBT (001) directions are aligned.

Figure 4.14b is a diffraction pattern from MOCVD PBT grown on biaxially textured MgO. This diffraction pattern is equivalent to the diffraction pattern taken from the PBT on single-crystalline MgO except that there are diffraction spots from the Si substrate. This diffraction pattern shows (001) and (100) peak splitting resulting from simultaneous diffraction from a-axis and c-axis domains. The measured  $c/a$  ratio measured from this diffraction pattern is 1.044 ( $c = 0.409$  nm,  $a = .392$  nm), which is consistent with the  $\theta-2\theta$  x-ray measurement ( $c = 0.410$  nm,  $a = .391$  nm, and  $c/a = 1.049$ ). The biaxially textured PBT diffraction pattern does not show appreciably more out-of-plane orientation distribution ( $\Delta\omega$ ) than PBT on single-crystal MgO (001). It also demonstrates the alignment of the (001) PBT and (001) MgO crystal directions.

The characteristics of the MgO biaxial textured template appeared very different in two different regions. Figure 4.15 shows TEM bright field images of the PBT/MgO/Si<sub>3</sub>N<sub>4</sub>/Si film stack at two different film locations. In Figure 4.15a, lattice

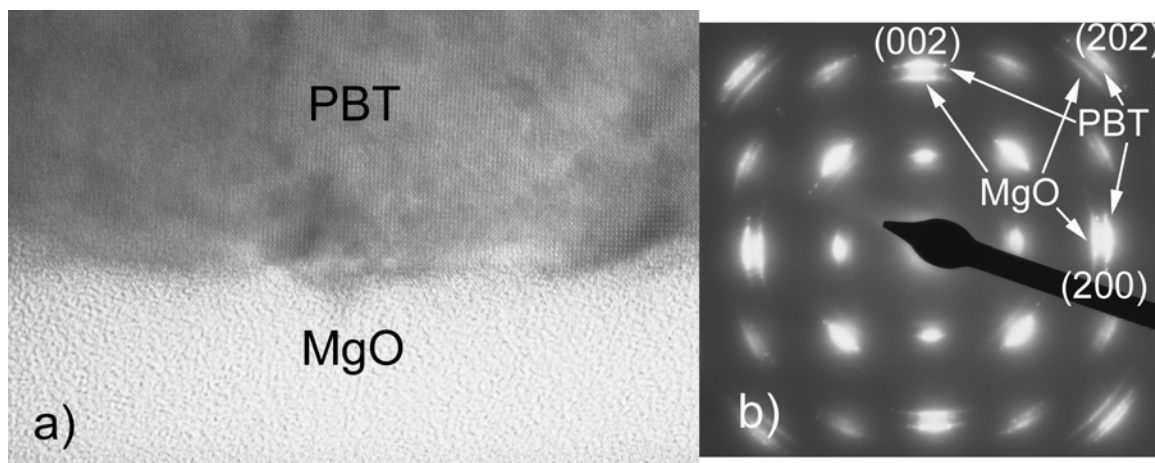


Figure 4.16 a) High-resolution TEM image of the interface between biaxially textured MgO and MOCVD PBT. b) Plan view diffraction pattern of MOCVD PBT on biaxially textured MgO.

planes are observable through out the MgO layer, proving its crystallinity. There is also a clear distinction between the highly damaged IBAD MgO layer (the first 7.8 nm) and the homoepitaxial layer (18 nm thick). However, in Figure 4.15b the MgO appears to be amorphous. It is questionable to conclude simply from the appearance of the MgO layer that it is actually amorphous. A high-resolution image of the amorphous-looking MgO template/ PBT interface clearly shows the crystalline PBT emerge from the disordered MgO (Figure 4.16a). The crystalline PBT on the MgO suggests that the template was crystalline. MOCVD PBT growth on  $\text{Si}_3\text{N}_4$  results in weak diffraction and peaks from (111), (110), and (001) orientations.

There is no appreciable difference between the PBT microstructure over the crystalline MgO and the apparently amorphous region. Strong (001) texturing and biaxial texturing of this film grown on biaxially textured MgO makes it unlikely that the MgO template was amorphous before film growth. At least some regions of the MgO layer must have been crystalline to seed the preferred (001) out-of-plane growth direction and then overgrow any amorphous MgO regions present.

One explanation for the apparently amorphous MgO regions is that these regions were amorphized by the ion milling when they became extremely thin. One TEM image shows a hole in the amorphous looking-MgO, demonstrating the films thinness.

The polycrystalline PBT on biaxially textured MgO looks qualitatively different than the PBT on single-crystal MgO. In the PBT on single-crystal MgO  $45^\circ$  defects were observed at frequent intervals running through the entire film surface. On biaxially textured MgO templates these defects are not present, but more grain boundaries are evident. Plan view TEM images reveal that the biaxially textured PBT average grains size is 60 nm.

A plan view diffraction pattern of the MOCVD PBT on biaxially textured MgO confirms the RHEED measurement of narrow in-plane orientation distribution (Figure 4.16b). The arcs of the IBAD MgO diffraction spots are marginally larger than the arcs from the PBT, signifying that the PBT has a narrower in-plane orientation distribution. The diffraction pattern also demonstrates that PBT (100) is oriented along the MgO (100).

#### **4.3.4.2 Sol-gel PBT on MgO**

Sample preparation for the sol-gel PBT on biaxially textured MgO was much more difficult than for the MBE or MOCVD biaxially textured films. Several times during ion milling, samples delaminated at the MgO/  $\text{Si}_3\text{N}_4$  interface before they were thin enough for cross section TEM. The failure of the MgO film indicates that it was less robust than the biaxially textured MgO under the MOCVD film and under the MBE film (which did not have any delamination issues during sample preparation). Despite the difficulties in preparing the TEM sample, one area was found that was suitable for TEM

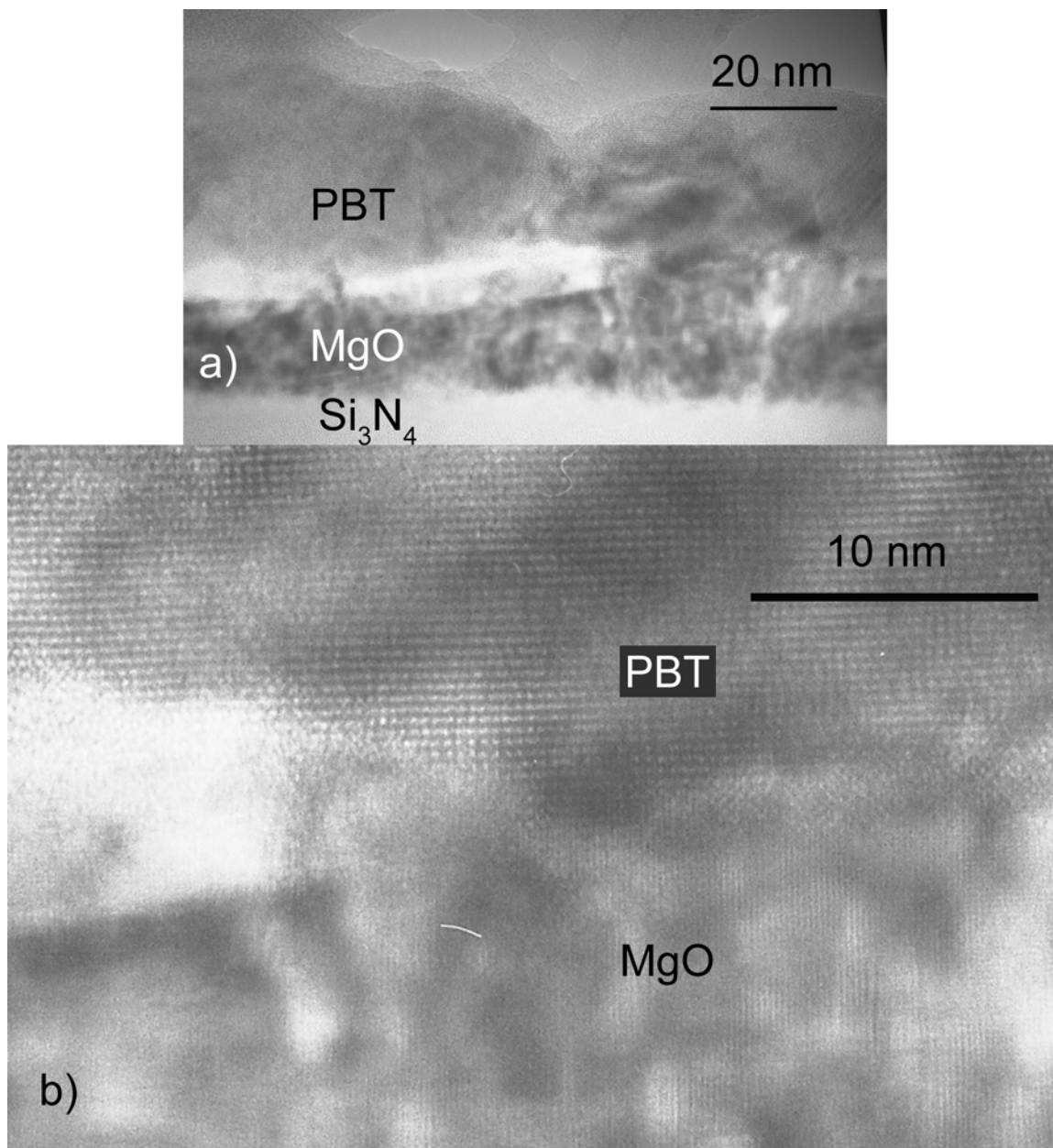


Figure 4.17 a) Cross section TEM high-resolution image of sol-gel PBT on biaxially textured MgO. b) Close up of a small interface region from image (a).

imaging.

Figure 4.17a is a high-resolution cross section TEM image of the sol-gel PBT/MgO biaxially textured interface. Sections of the PBT/ MgO interface appear sharp and others appear rough and broad. In the broad interface regions, the MgO layer appears thinner than at the sharp interface areas. Figure 4.17b is a close-up of a transition

between a sharp and broad interface region. On the right, the MgO and PBT lattice planes are visible and the sharp interface on this small scale appears rough. To the left in Figure 4.17b, the interface opens up with the addition of what appears to be amorphous material between crystalline MgO and PBT. Other biaxially textured MgO growth experiments result in uniformly thick MgO layers (see Figure 4.18), so the apparently amorphous material should be part of the biaxially textured MgO layer. These images are not conclusive evidence that amorphous material is present in the MgO/ PBT interface; however, they do demonstrate the inhomogeneity of the interface.

The measured PBT thickness is 47 nm and the MgO is 21 nm thick (where there is not an thick interface phase). PBT grain sizes are on the order of 20 to 30 nm, not much larger than the 20 to 25 nm grain sizes observed in other biaxially textured MgO layers.

#### **4.3.4.3 MBE BST on biaxially textured MgO**

The biaxially textured MgO layer in the MBE heterostructure appears very flat and crystalline everywhere. Figure 4.18a is a high-resolution TEM of the BST/ MgO/ Si<sub>3</sub>N<sub>4</sub>/ Si film stack. The high defect density IBAD layer is distinguishable from the homoepitaxial layer and the lattice planes are distinguishable throughout the entire MgO layer, demonstrating that the MgO can survive the TEM sample preparation without becoming amorphous.

A diffraction pattern taken from the film stack is included as Figure 4.18b. The diffraction pattern is a superposition of diffractions from the silicon substrate, the BST layer, and the IBAD MgO. The biaxially textured MgO and BST diffraction spots are small arcs, characteristic of contributions from many grains slightly rotated with respect

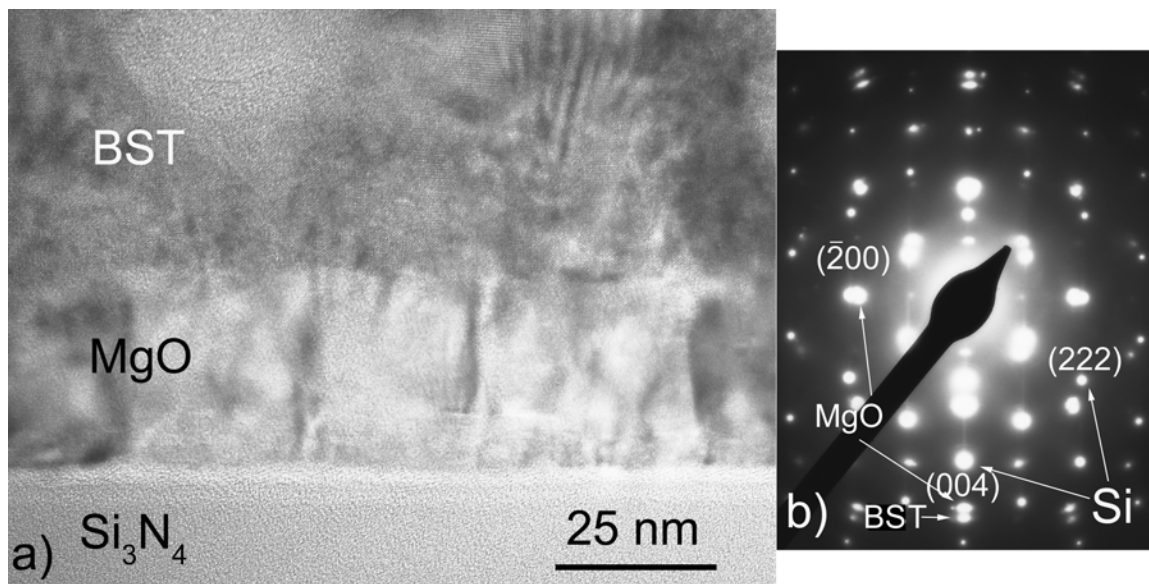


Figure 4.18 Cross section TEM high-resolution image of BST on biaxially textured MgO. (b) Diffraction pattern from image (a). The diffraction pattern is a superposition of diffraction spots from MgO, a BST perovskite structure, and Si.

to each other, demonstrating good out-of-plane orientation alignment. This diffraction pattern compares very closely to the biaxially textured MOCVD PBT diffraction pattern (Figure 4.14b). The main difference between these two patterns is that the weak perovskite diffraction spots are even weaker in the biaxially textured BST diffraction pattern. No extra spots are present in the BST diffraction pattern, even though there is only half as much Ba as Ti in the BST film.

A dark field TEM image takes the electrons from one of the electron diffraction spots and uses only those electrons to create an image of the sample. In the resulting image, only portions of the film that contribute to the selected diffraction spot are visible. Figure 4.19 is a dark field image taken from a diffraction pattern of the entire film stack thickness. The bright areas which run from the MgO substrate into the BST demonstrate that the BST very closely adopts the orientation of the MgO template grain. We can also observe that many of the BST grains are the same size as the MgO grains.

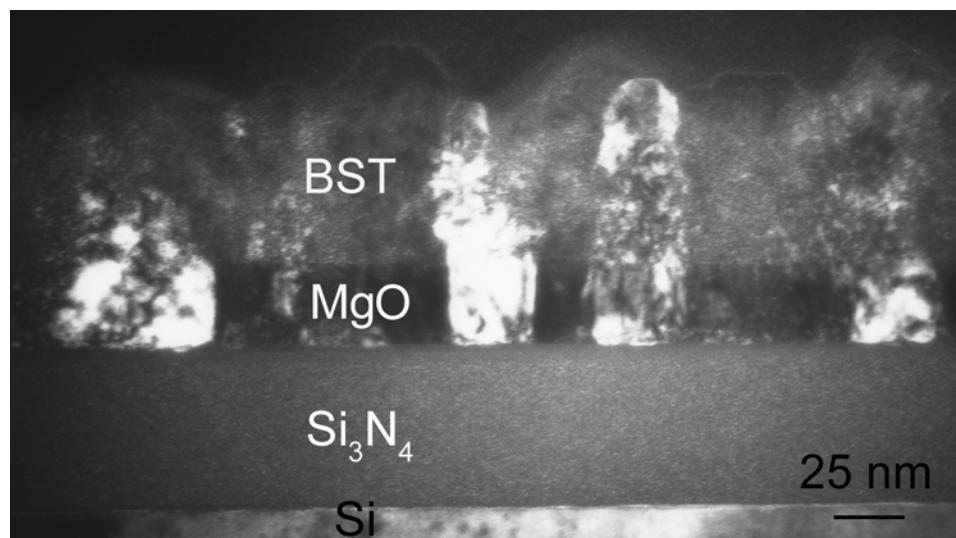


Figure 4.19 Dark field TEM image of the BST/ biaxially textured MgO/ amorphous Si<sub>3</sub>N<sub>4</sub> /Si film stack. MgO grain orientation propagates into the BST layer.

#### 4.3.5 Effect of deposition method on the biaxially textured MgO template

The TEM, x-ray diffraction, and RHEED measurements create a coherent picture for the biaxial texture inheritance of perovskite ferroelectrics on biaxially textured MgO. TEM images show that the IBAD MgO has a very high defect density which is reduced, but not eliminated in the homoepitaxial layer. We speculate that neither sol-gel nor MOCVD growth on IBAD MgO layers yields biaxially textured ferroelectric films because the defective IBAD layer is susceptible to damage by the moisture in the atmosphere at the crystal defects. The homoepitaxial layer makes the biaxially textured layer more stable in the atmosphere and so the layer is largely intact for heteroepitaxy.

Of the three deposition methods, the sol-gel method most aggressively attacks the biaxially textured MgO layer. Sol-gel solution contains water, which is known to dissolve and pit defective MgO films<sup>72</sup>. In addition to water, the sol-gel solution contains

acetylactone. We have observed that acetone vapors effectively degrade IBAD MgO films. We further suggest that TEM sample preparation was difficult for the biaxially textured sol-gel sample because the MgO layer was degraded during the sol-gel deposition. The high-resolution cross section TEM shows fully crystalline MgO layers right next to areas with amorphous-looking material at the MgO/ PBT interface. The biaxial texture of the sol-gel PBT improves over the biaxial texture of the MgO because the IBAD MgO biaxial texturing process produces the fewest number of defects in the most highly in-plane aligned grains. These grains are most likely to survive the sol-gel deposition and provide nucleation sites for biaxially textured PBT. We were unable to determine if there was a significant fraction of amorphous material in the sol-gel PBT film because it was too thin to obtain a diffraction pattern from the PBT film without including the MgO and amorphous  $\text{Si}_3\text{N}_4$  layer as well.

As for the sol-gel PBT heteroepitaxy on biaxially textured MgO, the MOCVD PBT in-plane orientation distribution improved over the in-plane orientation distribution of the MgO template. The biaxially textured MgO layer showed some weakness under ion milling, but was structurally superior to the MgO template layer in the sol-gel sample. These results suggest that hydroxylation at lattice defects also affected the biaxially textured MgO template for the MOCVD growth experiment. Because the MOCVD was performed in a separate chamber from the MgO growth, moisture in the atmosphere was able to degrade the most defective MgO regions enough to reduce the nucleation probability on heavily damaged, highly in-plane misaligned grains. With minimal atmosphere exposure and without solution to carry away dissolved MgO, the interface between the MOCVD and biaxially textured MgO stayed sharp. The MOCVD film was

crystalline everywhere because the crystals that nucleated on well-aligned grains overgrew several MgO grains.

Finally, the MBE BST deposition most closely reproduced the biaxial texture of the biaxially textured MgO template. Because MBE growth was performed *in situ*, the MgO template was preserved as-grown and the MBE BST faithfully adopted the texture and grain size from the substrate. The RHEED image from this film was the sharpest of the three ferroelectric films despite the surface roughness and the non-stoichiometric growth.

To protect the MgO template from degradation in the atmosphere or during ferroelectric deposition, the MgO could be capped by an inert layer before it is taken out of the high vacuum growth chamber. The 4-pocket electron beam evaporator could be used to cap the MgO with oxides like yttria stabilized zirconia (YSZ) and CeO<sub>2</sub>, which are appropriate heteroepitaxial templates for perovskite materials<sup>73</sup>.

#### 4.4 Ferroelectric properties

Ba<sub>x</sub>Pb<sub>1-x</sub>TiO<sub>3</sub> is interesting as an active actuator material because the 90° ferroelectric domain switching has potential to provide fast actuation and large strains. Ultimately these materials will be evaluated in MEMs structures for switching frequency and work response under applied electric fields and mechanical loading. Even before actuator structures are fabricated, indications of ferroelectric film actuation performance can be obtained by measuring the ferroelectric domain structure, remnant polarization, and coercive fields. The remnant polarization (see Figure 4.2) measures a combination of the film out-of-plane alignment (crystals rotated away from the surface normal will yield a smaller polarization field perpendicular to the sample), the fraction of the ferroelectric

film that is switchable under an applied electric field, and the intrinsic polarization of the material. The coercive field is the field required to produce a net zero polarization (see also Figure 4.2). This is a measurement of how difficult it is to induce ferroelectric domains to switch directions and is an indicator of the electric field or stress required to switch an actuator. Low coercive fields and high polarizations are desirable because the final actuator structures will experience less stress during switching (low coercive field) and also contain a maximum number of switchable ferroelectric domains (high polarization).

#### **4.4.1 DC-EFM and polarization hysteresis loops**

We have used a modified Park Scientific Instruments Autoprobe CP to obtain DC-EFM images of the biaxially textured PBT thin films. Figure 4.3 is a schematic of a DC-EMF. We float the substrate at +10 V or -10V and apply a 3.2 kHz, 5 V ac signal to the tip. Contact mode AFM and DC-EFM scans are taken simultaneously, enabling a direct comparison between the surface topology and the ferroelectric domain structure. Our DC-EFM has not been calibrated, so that the film polarization can not be quantitatively measured from the ac induced tip deflection so our DC-EFM images represent a qualitative measurement of the domain structure. Solid dark or bright areas indicate out-of-plane polarization (c-axis), while areas with a grainy mixture of dark, white, and gray are either a-axis oriented or have no or very little intrinsic electric dipole moment.

Polarization hysteresis loops were acquired using the DC-EFM for selected features of the DC-EFM or topographical images. A local polarization hysteresis loop was acquired by sweeping the substrate bias from 0 V to +10 V, down to -10 V, and

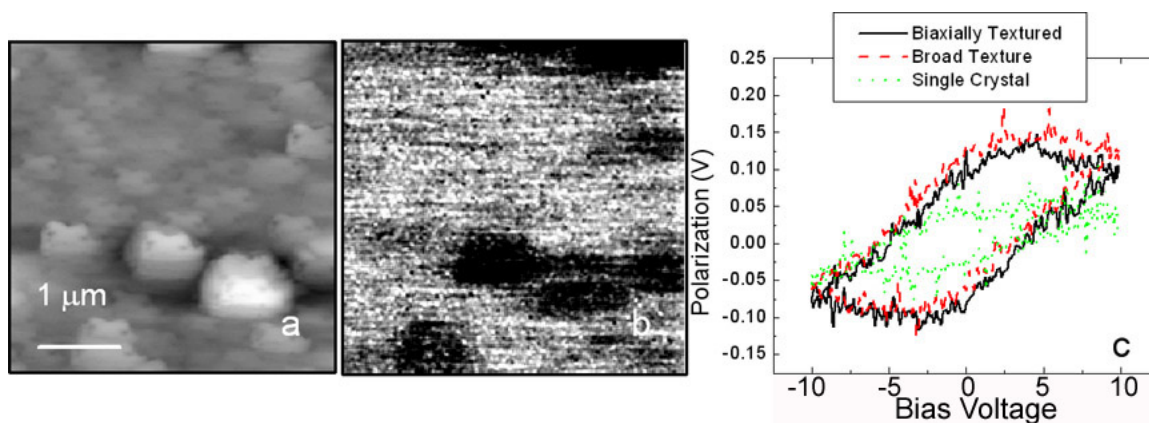


Figure 4.20 (a) Contact AFM topographic image of sol-gel PBT deposited on biaxially textured MgO. (b) Dynamic contact mode electrostatic force microscopy image of the film in (a). (c) Polarization hysteresis loops taken with the dynamic contact mode electrostatic force microscopy system from sol-gel PBT films deposited on different substrates. The biaxially textured and broad texture PBT films are 50 nm thick and the PBT on single-crystal MgO is 150 nm thick.

finally up to 0 V while applying a 3.2 kHz, 5 V ac signal to the AFM tip, and recording the induced tip deflection through the lock-in amplifier as a function of DC voltage. The hysteresis loop frequency was 5 Hz. In our experiments the film polarization is measured as the voltage difference between the a and b sides of the split photo diode detector. The measured voltage is related to the tip deflection caused by the electrostatic interaction of the AFM tip with the local film polarization [ $\mu\text{C}/\text{cm}^2$ ]. To calibrate the polarization as a function of tip deflection requires a well defined tip radius, as well as knowledge of all film dielectric constants and film thicknesses. Although the hysteresis loop demonstrates that the films are ferroelectric and switchable, the polarization loops cannot be directly compared because the films have different thicknesses.

#### 4.4.1.1 Sol-gel PBT

Figure 4.20 contains  $4 \times 4 \mu\text{m}$  topographic (a) and DC-EFM images (b), as well as a polarization hysteresis loop (c) from the biaxially textured sol-gel film characterized by x-ray diffraction, TEM, RBS, and RHEED earlier this chapter. Comparing the DC-

EFM to the topographic image shows that the c-axis regions (the dark regions) are attached to large grains, while the small grained areas show little DC-EFM contrast and are probably a-axis oriented. The polarization curve (Figure 4.20c) was taken from one of the large grains evident in the topographic image. This proves that the material is ferroelectric and that the domains are switchable by  $180^\circ$ . Polarization hysteresis loops taken from the small grained, non c-axis oriented regions also exhibit hysteresis, indicating that the a-axis regions are also switchable. A hysteresis loop was included from a sol-gel PBT film grown directly on IBAD MgO, which results in a weak diffraction and broad out-of-plane orientation distribution. The polarization hysteresis loop from the poorly textured film cannot be directly compared to the biaxially textured film because the biaxially textured PBT has an additional 20 nm MgO layer underneath it which will significantly affect the electric field in the PBT film. A polarization hysteresis is observed in the poorly textured film. This hysteresis loop is for a small region and it would be important to examine the polarization behavior of larger areas to study the long range effects on domain switching from biaxial texture.

A polarization hysteresis loop from sol-gel grown on single-crystal MgO is also included in Figure 4.20c. It is not appropriate to directly compare this hysteresis loop with the other two because the voltage drop across the PBT is much different than for the biaxially textured films because it is on a thick MgO substrate, instead of being stacked on MgO /Si<sub>3</sub>N<sub>4</sub> / Si. A 4x4  $\mu\text{m}$  DC-EFM scan of the sol-gel PBT on single-crystal MgO produced no discernible DC-EFM signal (see Figure 4.21b). Undoubtedly, the limited voltage range (+10 V to -10 V) of the DC-EFM limits the resolution of this technique on thick dielectric substrates (like MgO). However, by reducing the scan to 1x1  $\mu\text{m}$ , small



Figure 4.21 (a) Contact mode AFM topographical image of sol-gel PBT deposited on single-crystal MgO (001). (b) DC-EFM image of the film in (a). (c) A smaller DC-EFM scan of the image in (a). Decreasing the DC-EFM scan size increases sensitivity.

regions of dark, c-axis oriented domains become apparent (see Figure 4.21c). As with AFM, the resolution of DC-EFM depends on the scan size.

#### 4.4.1.2 MOCVD PBT

Topographical and DC-EFM images of well characterized biaxially textured MOCVD PBT are shown in Figure 4.22 and show similar structure to that observed in the sol-gel DC-EFM images where the c-axis polarized areas are correlated with large crystals. On single-crystal MgO, the DC-EFM image exhibits low contrast because most of the voltage drop is across the MgO substrate and does not create a very strong field in the thin (112 nm) layer of PBT. However, c-axis ferroelectric domains were observable in DC-EFM measurements from a 650 nm thick MOCVD PBT film grown on single-crystal MgO. The grain size apparent in the topographical image (Figure 4.22c) is reflected in the size of the c-axis domains in the DC-EFM image (Figure 4.22d).

Polarization hysteresis loops from MOCVD PBT films grown on biaxially textured MgO, single-crystal MgO, and a PBT film with a broad orientation distribution (grown on an IBAD MgO template without homoepitaxial MgO) are compared in Figure

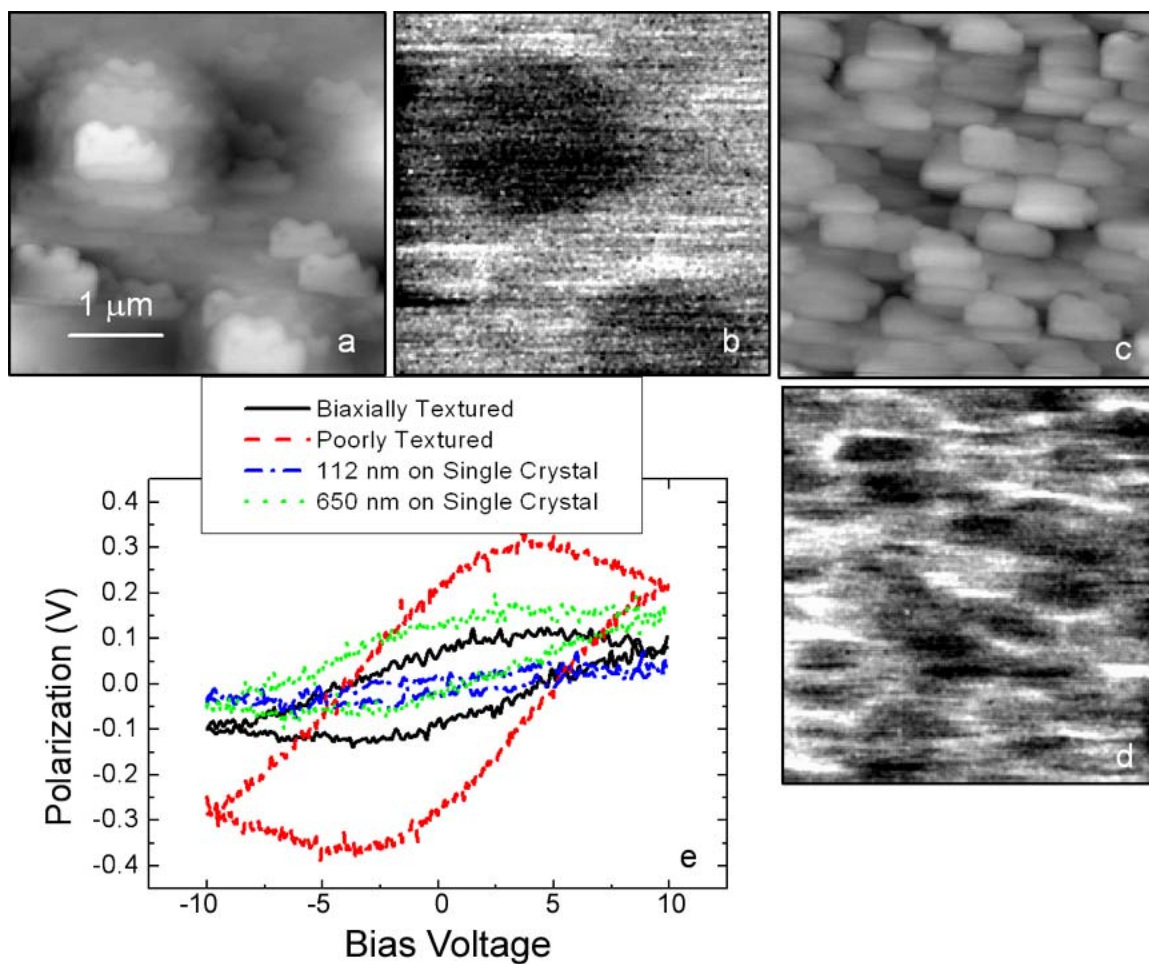


Figure 4.22 (a) Contact mode AFM image of MOCVD PBT deposited on biaxially textured MgO. (b) DC-EFM ferroelectric domain image of the topographical image (a). (c) Contact mode AFM image of MOCVD PBT deposited on single-crystal MgO (001). (d) DC-EFM ferroelectric domain image of the topographical image (c). (e) Polarization hysteresis loops of MOCVD deposited on different MgO substrates.

4.22e. The poorly textured PBT film had a larger remnant polarization than the biaxially textured film. The difference in the preparation of these samples was that the poorly textured PBT was grown on 8 nm of IBAD MgO instead of a 20 nm homoepitaxial MgO layer.

Because the poorly textured PBT has a thinner MgO layer, a higher field is induced in the PBT layer for the same applied substrate voltage, imposing a greater switching potential on the dipoles and resulting in a larger fraction of switching and the observed higher remnant polarization. For a direct comparison between these two polarization hysteresis loops the electric field in the PBT layer must be calculated.

The polarization loops of MOCVD PBT on single-crystalline MgO cannot be directly compared to the PBT on biaxially textured MgO because the electric field induced in the PBT at a given applied voltage is a function of the PBT film thickness, the PBT dielectric constant and the MgO film thickness. The polarization loop of the 112 nm MOCVD film is extremely weak, while the polarization hysteresis loop from the 650 nm MOCVD film is comparable to the loop observed on the biaxially textured thin film. Polarization loops were taken at multiple locations on each thin film and all locations produced polarization hysteresis loops, confirming ferroelectricity in the films at least on the length scale of the AFM tip area.

#### **4.4.1.3 MBE BST**

The topographical and DC-EFM images from the well characterized, biaxially textured MBE BST is shown in Figure 4.23. The relationship between the c-axis regions (the white spots in the lower and upper right hand corners, as well as the dark region in the lower middle part of the DC-EFM image) and surface topography are not as obvious in this film as it is in the MOCVD and sol-gel films. Hysteresis loops from this film also demonstrate that it is an active ferroelectric. The polarization hysteresis loops from biaxially textured MOCVD, sol-gel, and MBE films are all plotted in Figure 4.23c. The

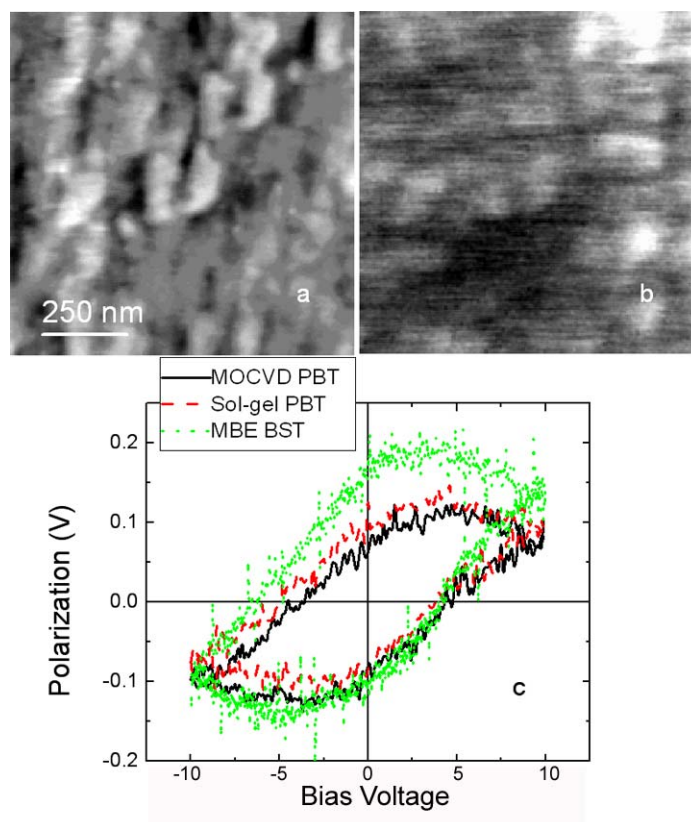


Figure 4.23 (a) Contact mode AFM topographical image of MBE BST deposited on biaxially texture MgO. (b) DC-EFM ferroelectric domain image of the BST in image (a). (c) Polarization hysteresis loops taken with the DC-EFM system from sol-gel and MOCVD PBT films deposited on biaxially textured MgO. A polarization hysteresis loop from MBE BST on biaxially textured MgO is also included.

thickness variation and composition variation (which affects the dielectric constant) prevent direct comparison of the remnant polarization and coercive field.

#### 4.4.1.4 Further ferroelectric characterization

The ferroelectric characterization demonstrates that c-axis domains are typically the same size as topographical features in the film. We also find that ferroelectric response is generated everywhere we probed on the film surfaces. However, to quantitatively compare the ferroelectric properties of the films grown by the different

methods, with different compositions, and with different biaxial textures we need to calculate coercive fields and remnant polarizations. Because we obtained accurate film thickness measurements from TEM, we can use capacitance voltage measurements to calculate the dielectric constant for the ferroelectric films (if we assume that literature values of the dielectric constant of MgO and Si<sub>3</sub>N<sub>4</sub> are valid). However, we would also have to model the voltage drop across the p-type Si substrate as it is only doped at  $5 \times 10^{15} \text{ cm}^{-2}$  and does not possess metallic conductive properties.

The most straightforward way to make quantitative measurements between biaxially textured ferroelectric films grown by different methods would be to grow ferroelectric films on identical substrates (equal biaxially textured MgO layers and Si<sub>3</sub>N<sub>4</sub> layers). By using degenerately doped Si wafers ( $10^{20} \text{ cm}^{-2}$ ) the need to model voltage drop across the silicon is eliminated. Even with the uncertainties inherent in the dielectric properties of highly defective MgO, the identical substrates would provide direct comparison between films as the biaxial texture was varied.

Another interesting measurement would be to probe polarization hysteresis at a macroscopic scale in a ferroelectric tester as a function of the ferroelectric biaxial texture. By probing the coercive field over a large ensemble of ferroelectric domains and across a large number of grain boundaries, if there are different barrier for domain migration across low-angle grain boundaries then across high-angle grain boundaries it would be reflected in the magnitude of the coercive field.

## 4.5 Conclusion

By growing biaxially textured ferroelectric films on amorphous substrates we made a significant step toward integrating ferroelectric actuators with Si based

electronics. The biaxial texture of the MgO template is adopted and even improved by the heteroepitaxial ferroelectric deposition process. Cross section TEM and RHEED biaxial texture measurements suggest that the *ex situ* (sol-gel and MOCVD) heteroepitaxial processes create more highly in-plane aligned ferroelectrics than the MgO template by selectively nucleating on MgO grains that are well-aligned because the defective misaligned grains are degraded by atmospheric moisture. All the PBT and BST ferroelectric films possessed ferroelectric properties and switchable dipole moments, as demonstrated through the DC-EFM polarization hysteresis loops.

---

<sup>54</sup> J. W. Hong, S. I. Park, Z. G. Khim, Rev. Sci. Instrum. **70**, 1753 (1999).

<sup>55</sup> W. D. Yang, S. C. Pillai, S. W. Boland, and Sossina M. Haile, Mat. Res. Soc. Symp. Proc. **748**, U12.21 (2001).

<sup>56</sup> U. Selvaraj, A. V. Prasadarao, and S. Komarneni, Mater. Lett. **20**, 71 (1994).

<sup>57</sup> Personal Communication

<sup>58</sup> J. H. Haeni, C. D. Theis, and D. G. Schlom, J. Electroceramics **4**, 385 (2000).

<sup>59</sup> C. D. Theis and D. G. Schlom, J. Vac. Sci. Technol. A **14**, 2677 (1996).

<sup>60</sup> D. G. Schlom, J. H. Haeni, J. Lettieri, C.D. Theis, W. Tian, J.C. Jiang, and X.Q. Pan, Mat. Sci. and Eng. B **87**, 282 (2001).

<sup>61</sup> C. D. Theis and D. G. Schlom, J. Cryst. Growth **174**, 473 (1997).

<sup>62</sup> Y. Yoneda, T. Okabe, K. Sakaue, and H. Terauchi, Surface Science **410**, 62 (1998).

<sup>63</sup> S. Kim and S. Baik, Thin Solid Film **266**, 205 (1995).

<sup>64</sup> W. K. Choi, S. K. Choi, and H. M. Lee, J. Mater. Res. **14**, 4677 (1999).

<sup>65</sup> V. Srikant, E. J. Tarsa, D. R. Clarke, and J. S. Speck, J. Appl. Phys. **77**, 1517 (1995).

<sup>66</sup> Properties of Crystalline Silicon, edited by Robert Hull (INSPEC, London, 1999).

- 
- <sup>67</sup> Thermal Expansion of Nonmetallic Solids, Vol. 13 of Thermophysical Properties of Matter, edited by Y. S. Touloukian, R. K. Kirby, R. E. Taylor, and T. Y. R. Lee (Plenum, New York, 1977).
- <sup>68</sup> B. Jaffe, W. R. Cook Jr., and H. Jaffe, Piezoelectric Ceramics; pp. 56-59. Academic Press, London, U.K., 1971.
- <sup>69</sup> G. Burns, Phys. Rev. B **10**, 1951 (1974).
- <sup>70</sup> Y. Yoned, T. Okabe, K. Sakaue, H. Terauchi, H. Kasatani, and K. Deguchi, J. Appl. Phys. **83**, 2458 (1998).
- <sup>71</sup> L. Beckers, J. Schubert, W. Zander, J. Ziesmann, A. Eckau, P. Leinenbach, and C. Buchal, J. Appl. Phys. **83**, 3305 (1998).
- <sup>72</sup> J. A. Mejias, A. J. Berry, K. Refson, and D. G. Fraser, Chem. Phys. Lett. **314**, 558 (1999).
- <sup>73</sup> J. R. Groves, P. N. Arendt, S. R. Foltyn, Q. X. Jia, T. G. Holesinger, H. Kung, E. J. Peterson, R. F. DePaula, P. C. Dowden, L. Stan, and L. A. Emmert, J. Mater. Res. **16**, 2175 (2001).

## Chapter 5 Conclusion

Throughout this thesis I have worked to understand and facilitate the fabrication of biaxially textured materials, which often possess electrical properties similar to those of single-crystals even when randomly oriented polycrystalline materials do not. The ability to fabricate biaxially textured films on amorphous substrates enables new materials integration opportunities with silicon-based electronics and provides a route for increasing single device functionality. We developed a path way to fabricate biaxially textured perovskite ferroelectric materials on amorphous substrates with the intent to facilitate integration of ferroelectric-based microactuators with silicon-based electronics.

To investigate the properties of biaxially textured materials requires a facile method to determine the degree of biaxial texturing. To this end, a reflection high-energy electron diffraction (RHEED) based technique was developed for *in situ*, fast biaxial texture analysis.

### 5.1 RHEED-based biaxial texture measurements

Chapter 2 detailed the development of RHEED as an *in situ* biaxial texture measurement technique. Using a kinematical electron scattering model, we show that the RHEED pattern from a biaxially textured polycrystalline film can be calculated from an analytic solution to the electron scattering probability. We found that diffraction spot shapes are sensitive to out-of-plane orientation distributions, but not to in-plane orientation distributions, requiring the use of in-plane RHEED rocking curves to fully experimentally determine biaxial texture. Using information from the simulation, a RHEED-based experimental technique was developed for *in situ* measurement of MgO

biaxial texture. The accuracy of this technique was confirmed by comparing RHEED measurements of in-plane and out-of-plane orientation distribution with synchrotron x-ray rocking curve measurements. An offset between the RHEED-based and x-ray measurements (the RHEED measured slightly narrower orientation distributions than x-ray analysis), coupled with evidence that the biaxial texture narrows during ion beam-assisted deposition, indicates that RHEED-based measurements are more appropriate for probing surface biaxial texture than x-ray measurements.

RHEED-based biaxial texture measurement was essential to our efforts to produce biaxially textured ferroelectrics. Biaxially textured MgO has been used as a heteroepitaxial template for other perovskites, so optimization of the MgO biaxial texture is essential to optimizing the biaxial texture of ferroelectrics. RHEED measurements allow for fast optimization of MgO biaxial texture, fast analysis of MgO biaxial texture to determine if it is suitable for ferroelectric heteroepitaxy, and fast measurement of ferroelectric biaxial texture.

## **5.2 Biaxial texture development in IBAD MgO**

Our efforts to understand biaxial texture formation in ion beam-assisted deposition (IBAD) of MgO were discussed in Chapter 3. We discovered that biaxial textured MgO emerges after about 3 nm of ion beam-assisted growth. TEM and RHEED measurements were used to discover the initial deposition of an amorphous MgO layer, followed by an ion bombardment-mediated solid phase crystallization of a biaxially textured film. RHEED measurements were also used to show that once the biaxial textured film crystallized, the out-of-plane and in-plane orientation distributions narrowed as the film thickness increases. Finally, we optimized the IBAD MgO biaxial

texture by measuring the biaxial texture for 750 eV Ar<sup>+</sup> ion bombardment as a function of the ion/MgO flux ratio. The most interesting result is that the in-plane orientation distribution is limited by the out-of-plane orientation distribution. Our experimental results suggest that the minimum in-plane orientation distribution attainable by ion beam-assisted deposition is 2° FWHM and can only be achieved if the (001) MgO planes can be uniformly oriented perpendicular to the substrate for all grains (i.e. the out-of-plane orientation distribution goes to 0° FWHM).

Understanding the biaxial texture development of IBAD MgO is essential to optimizing and controlling it for ferroelectric heteroepitaxy. The quality of the IBAD MgO template greatly influences the ferroelectric film microstructure.

### 5.3 Biaxially textured ferroelectric films

In Chapter 4 we investigated the growth of perovskite ferroelectrics on biaxially textured MgO templates. Sol-gel and metallorganic chemical vapor deposition (MOCVD) were used to grow Ba<sub>x</sub>Pb<sub>1-x</sub>TiO<sub>3</sub> (PBT) and molecular beam epitaxy (MBE) was used to grow Ba<sub>0.67</sub>Sr<sub>0.03</sub>Ti<sub>1.3</sub>O<sub>3</sub> (BST). PBT grown directly on IBAD MgO surfaces was not biaxially textured, whereas if the IBAD MgO layer was capped with an additional 25 nm of homoepitaxial MgO before heteroepitaxy, the PBT would inherit the biaxial texture from the MgO template. Through RHEED-based biaxial texture analysis we observed that the in-plane orientation distribution of PBT, deposited using *ex situ* techniques (not performed in the same high vacuum growth environment where the MgO was deposited), narrowed significantly with respect to the in-plane orientation distribution of its MgO template (from 11° to 6° FWHM). We also observed that the in-plane orientation distribution of *in situ* MBE BST on biaxially textured MgO resulted in a BST film whose

in-plane orientation distribution was within  $1^\circ$  FWHM of the MgO template in-plane orientation distribution. Cross section transmission electron microscopy (TEM) was used to investigate the microstructure of the heteroepitaxial ferroelectric films. Films deposited on biaxially textured MgO using *ex situ* growth techniques (sol-gel and MOCVD) were found to have degraded MgO templates.

We speculate that moisture from the atmosphere degrades the MgO template by attacking the defects in biaxially textured MgO substrate. PBT grown on IBAD MgO surfaces was not biaxially textured because the high defect density made the entire MgO template subject to hydroxylation and degradation from atmospheric moisture. By capping IBAD MgO with an MgO homoepitaxial layer, grown at  $600^\circ\text{C}$ , the MgO defect density was reduced and produced biaxially textured PBT on MgO using sol-gel synthesis and MOCVD. We also infer that PBT in-plane orientation distributions were narrower than the MgO template because misaligned MgO grains were more highly damaged during IBAD growth and were not fully healed by MgO homoepitaxy. These highly damaged, misaligned grains are preferentially degraded by atmospheric moisture, allowing PBT to preferentially nucleate on well-aligned MgO grains and to possess a narrower in-plane orientation distribution than the MgO template by over growing less well oriented MgO regions. The MBE BST more closely reflected the MgO template in-plane orientation distribution because the *in situ* BST growth did not subject the MgO to hydroxylation from the atmosphere, leaving all MgO grains crystalline and available for BST nucleation.

The ferroelectric domain structure of biaxially textured PBT (grown by sol-gel and MOCVD) and BST (grown by MBE) was mapped using dynamic contact mode

electrostatic force microscopy (DC-EFM). C-axis domains were observed to be associated with large grains. Polarization hysteresis loops obtained with the DC-EFM at several locations on each film indicate that the entire film is ferroelectric on the scale of the AFM tip size.

## **5.4 The next step**

The ability to fabricate biaxially textured ferroelectric materials on amorphous substrates enables the fabrication of biaxially textured ferroelectric actuator test structures. Microactuator performance can be evaluated as a function of biaxial texture and experimental measurements of ferroelectric domain motion dependence on biaxial texturing can be compared with computational models to understand ferroelectric domain wall motion across low-angle grain boundaries. These experiments will benefit from our understanding of biaxial texture formation in ion beam-assisted deposition of MgO and the ability to measure biaxial texture with reflection high-energy electron diffraction.

## Appendix A Derivation of Kinematic Electron Scattering Model for Biaxially Textured Polycrystalline Films

### A.1 Electron scattering from a periodic potential

The wave function for an electron that scatters off of a potential  $\mathbf{V}$  can be calculated using the time dependent Schrödinger equation

$$i \frac{\partial}{\partial t} |\psi(t)\rangle = (\mathbf{H} + \mathbf{V}) |\psi(t)\rangle. \quad (0.1)$$

If we define  $\psi(t)$  in the interaction representation we essentially wrap the Hamiltonian around the potential  $\mathbf{V}$ .

$$|\psi(t)\rangle = \exp(-it\mathbf{H}) * |\phi(t)\rangle \quad (0.2)$$

$$i \frac{\partial}{\partial t} \exp(-it\mathbf{H}) |\phi(t)\rangle = (\mathbf{H} + \mathbf{V}) \exp(-it\mathbf{H}) * |\phi(t)\rangle \quad (0.3)$$

$$\mathbf{H} \exp(-it\mathbf{H}) * |\phi(t)\rangle + \exp(-it\mathbf{H}) * i \frac{\partial}{\partial t} |\phi(t)\rangle = (\mathbf{H} + \mathbf{V}) \exp(-it\mathbf{H}) * |\phi(t)\rangle \quad (0.4)$$

$$\exp(-it\mathbf{H}) * i \frac{\partial}{\partial t} |\phi(t)\rangle = \exp(-it\mathbf{H}) \mathbf{V} \exp(-it\mathbf{H}) * |\phi(t)\rangle \quad (0.5)$$

By redefining  $\mathbf{V}$  in the interaction representation as  $\mathbf{V}(t) = \exp[it\mathbf{H}] \mathbf{V} \exp[-it\mathbf{H}]$ , and knowing that  $\mathbf{V}$  is on the order of 10 eV while the electron energy for reflection high-energy electron diffraction (RHEED) applications is on the order of 20 keV, we can solve the last equation using the Born approximation

$$|\phi(t)\rangle = \left(1 - i \int_0^t dt' \mathbf{V}(t')\right) |\phi(0)\rangle. \quad (0.6)$$

Physically, the Born approximation is equivalent to consideration of the single electron scattering approximation. The multiple scattering case, although more realistic,

is computationally more intensive. We are interested in measuring the electron intensities at long times compared to the interaction time of the electrons with the potential. Therefore,  $|\phi(t)\rangle \rightarrow |\phi\rangle$  and  $|\phi(0)\rangle \rightarrow |\phi_o\rangle$  for  $t \rightarrow \infty$

$$|\phi\rangle = |\phi_o\rangle - \int_0^\infty dt' \exp(it'\mathbf{H}) \mathbf{V} \exp(-it'\mathbf{H}) |\phi_o\rangle. \quad (0.7)$$

Operating in momentum space greatly simplifies calculations. We apply an eigenstate  $\langle k|$  of  $\mathbf{H}$  to Equation (0.7).

$$\langle k| \exp(it\mathbf{H}) = \langle k| \exp(it\varepsilon_k) \text{ where } \varepsilon_k = \frac{k^2\hbar}{2m} \quad (0.8)$$

$$\langle k|\phi\rangle = \phi(k) = \phi_o(k) - i \int_0^\infty dt' \exp(it'\varepsilon_k) \langle k| \mathbf{V} \exp(-it'\mathbf{H}) |\phi_o\rangle \quad (0.9)$$

$$\mathbf{1} = \int \frac{dp^3}{(2\pi)^3} |p\rangle \langle p| = \int dx^3 |x\rangle \langle x| \quad (0.10)$$

$$\phi(k) = \phi_o(k) - i \int_0^\infty dt' \exp(it'\varepsilon_k) \int \frac{dp^3}{(2\pi)^3} \langle k| \mathbf{V} \exp(-it'\mathbf{H}) |p\rangle \langle p|\phi_o\rangle \quad (0.11)$$

$$\int dx^3 dy^3 \langle k||x\rangle \langle x|\mathbf{V}|y\rangle \langle y||p\rangle \quad (0.12)$$

$$\int dx^3 dy^3 \exp(-ikx) \mathbf{V}(x) \delta(x-y) \exp(ipy) \quad (0.13)$$

$$\int dx^3 \exp(-ikx) \mathbf{V}(x) \exp(ipx) = \tilde{\mathbf{V}}(k-p) \quad (0.14)$$

$$\exp(-it\mathbf{H}) |p\rangle = |p\rangle \exp(-it\varepsilon_p) \quad (0.15)$$

$$\phi(k) = \phi_o(k) - i \int \frac{dp^3}{(2\pi)^3} \tilde{\mathbf{V}}(k-p) \phi_o(p) \int_0^\infty dt' \exp(it'(\varepsilon_k - \varepsilon_p)) \quad (0.16)$$

$$\phi(k) = \phi_o(k) - i \int \frac{dp^3}{(2\pi)^3} \tilde{\mathbf{V}}(k-p) \phi_o(p) \delta(\varepsilon_k - \varepsilon_p) \quad (0.17)$$

$$\delta(g(x)) = \frac{\delta(x-x_o)}{g'(x_o)} \quad (0.18)$$

$$\phi(k) = \phi_o(k) - i \frac{\partial k_o}{\partial \varepsilon} \int \frac{dp^3}{(2\pi)^3} \tilde{V}(k-p) \phi_o(p) \delta(p-k) \quad (0.19)$$

This equation would be difficult to evaluate except that for the RHEED experiment  $\tilde{V}(k-p)$  is a slowly varying function and can be pulled out of the integral and evaluated at  $p=k_o$ , which is the incident electron wave vector. We now define the incoming electron wave function in momentum space with a well defined momentum.

$$\phi_o(p) = (2\pi\sigma^2)^{\frac{3}{2}} \exp\left[-\sigma^2(k_o-p)^2\right] \quad (0.20)$$

The spread of the momentum is related to  $\sigma$ . We must also now pay close attention to the vector nature of  $k$ ,  $k_o$ , and  $p$ . We will decompose  $dp^3$  into spherical components and integrate.

$$\begin{aligned} \phi(k) &= \phi_o(k) - i \frac{\partial k_o}{\partial \varepsilon} (2\pi\sigma^2)^{\frac{3}{2}} \tilde{V}(k-k_o) \\ &\int_0^\pi d\theta \int_0^{2\pi} d\Phi \int_0^\infty dp \sin\theta \frac{p^2}{(2\pi)^3} \exp\left[-\sigma^2(k_o^2 - p^2 - 2pk_o \cos\theta)\right] \delta(p-k) \end{aligned} \quad (0.21)$$

$$x = \cos\theta \quad dx = -\sin\theta d\theta$$

$$\begin{aligned} \phi(k) &= \phi_o(k) + i \frac{\partial k_o}{\partial \varepsilon} (2\pi\sigma^2)^{\frac{3}{2}} \tilde{V}(k-k_o) \\ &\int_1^{-1} dx \int_0^{2\pi} d\Phi \int_0^\infty dp \frac{p^2}{(2\pi)^3} \exp\left[-\sigma^2(k_o^2 - p^2 - 2pk_o x)\right] \delta(p-k) \end{aligned} \quad (0.22)$$

$$\phi(k) = \phi_o(k) + i \frac{\partial k_o}{\partial \varepsilon} (2\pi\sigma^2)^{\frac{3}{2}} \tilde{V}(k-k_o) 2\pi \int_1^{-1} dx \frac{k^2}{(2\pi)^3} \exp\left[-\sigma^2(k_o^2 - k^2 - 2kk_o x)\right] \quad (0.23)$$

$$\int_1^{-1} dx \exp\left[2\sigma^2 kk_o x\right] = \frac{\exp\left[-2\sigma^2 kk_o\right] - \exp\left[2\sigma^2 kk_o\right]}{2\sigma^2 kk_o} \quad (0.24)$$

$$\phi(k) = \phi_o(k) + i \frac{\partial k_o}{\partial \varepsilon} \frac{\sigma}{(2\pi)^{\frac{1}{2}}} \tilde{\mathbf{V}}(k - k_o) \frac{k}{k_o} \exp[-\sigma^2(k_o^2 - k^2)] (\exp[-2\sigma^2 k k_o] - \exp[2\sigma^2 k k_o]) \quad (0.25)$$

Knowing that  $\exp[-2\sigma^2 k k_o] \ll 1$

$$\phi(\vec{k}) = \phi_o(\vec{k}) - i \frac{\partial k_o}{\partial \varepsilon} \frac{\sigma}{(2\pi)^{\frac{1}{2}}} \tilde{\mathbf{V}}(\vec{k} - \vec{k}_o) \frac{k}{k_o} \exp[-\sigma^2(k_o - k)^2]. \quad (0.26)$$

We have now separated the final wave function into an unscattered component,  $\phi_o(\vec{k})$ , and a scattered component. Vector arrows have now also been included to distinguish between vectors and scalars. In the RHEED experiment we measure the intensity of the electrons at the RHEED screen so we are interested in the probability density for the final wave function scattered into a solid angle  $d\Omega$ .

$$\frac{dP_s}{d\Omega} = \int dk \frac{k^2}{(2\pi)^2} \left| \phi_s(\vec{k}) \right|^2 \quad (0.27)$$

$$\phi_s(\vec{k}) = -i \frac{\partial k_o}{\partial \varepsilon} \frac{\sigma}{(2\pi)^{\frac{1}{2}}} \tilde{\mathbf{V}}(\vec{k} - \vec{k}_o) \frac{k}{k_o} \exp[-\sigma^2(k_o - k)^2] \quad (0.28)$$

Now we make the second kinematical approximation which is that we only allow electrons to scatter elastically, i.e.  $|\vec{k}| = |\vec{k}_o|$ . We can represent this mathematically by inserting a delta function. We redefine the vectors as scalars multiplied by unit vectors ( $\vec{k}_o = k_o \hat{e}$  and  $\vec{k} = k_o \hat{n}$ ).

$$\frac{dP_s}{d\Omega} = \int dk \frac{k^2}{(2\pi)^2} \left| \phi_s(\vec{k}) \right|^2 \delta(k - k_o) \quad (0.29)$$

$$\frac{dP_s}{d\Omega} = \int dk \frac{k^2}{(2\pi)^2} \delta(k - k_o) \left( \frac{\partial k_o}{\partial \varepsilon} \right)^2 \frac{\sigma^2}{2\pi} \left| \tilde{\mathbf{V}}(\vec{k} - \vec{k}_o) \right|^2 \left( \frac{k}{k_o} \right)^2 \exp[-2\sigma^2(k_o - k)^2] \quad (0.30)$$

$$\frac{dP_s}{d\Omega} = \frac{k_o^2}{(2\pi)^2} \left( \frac{\partial k_o}{\partial \varepsilon} \right)^2 \frac{\sigma^2}{2\pi} \left| \tilde{\mathbf{V}}(k_o \hat{n} - k_o \hat{e}) \right|^2 \left( \frac{k_o}{k_o} \right)^2 \exp \left[ -2\sigma^2 (k_o - k_o)^2 \right] \quad (0.31)$$

$$\frac{dP_s}{d\Omega} = \frac{k_o^2}{(2\pi)^2} \left( \frac{\partial k_o}{\partial \varepsilon} \right)^2 \frac{\sigma^2}{2\pi} \left| \tilde{\mathbf{V}}(k_o(\hat{n} - \hat{e})) \right|^2 \quad (0.32)$$

This is the standard result used in material science as the beginning point for calculating scattering probabilities. It is well-known that the scattering amplitude  $k_o \hat{e} \rightarrow k_o \hat{n}$  is

$$A(k\hat{e} \rightarrow k\hat{n}) \propto -i \int d\vec{r} \exp \left[ -ik(\hat{n} - \hat{e}) \cdot \vec{r} \right] \mathbf{V}(\vec{r}) \quad (0.33)$$

and that the probability density is

$$P(k\hat{e} \rightarrow k\hat{n}) = \left| A(k\hat{e} \rightarrow k\hat{n}) \right|^2 \propto \left| \int d\vec{r} \exp \left[ -ik(\hat{n} - \hat{e}) \cdot \vec{r} \right] \mathbf{V}(\vec{r}) \right|^2 = \left| \tilde{\mathbf{V}}(k_o(\hat{n} - \hat{e})) \right|^2, \quad (0.34)$$

which is exactly what we derived from the time-dependent Schrödinger Equation. What we finally see is that the probability that the electron will scatter into any particular direction ( $\hat{n}$ ) is just

$$\left| \langle k\hat{n} | \mathbf{V}(\vec{r}) | k\hat{e} \rangle \right|^2 = \left| \tilde{\mathbf{V}}(k_o(\hat{n} - \hat{e})) \right|^2. \quad (0.35)$$

So the potential  $\mathbf{V}(\vec{r})$  actually serves as an operator coupling the matrix elements of different wave vectors together.

Solving for the RHEED intensity is reduced to creating a physically accurate representation of the potential  $\mathbf{V}(\vec{r})$ . However, the representation must also allow for a computationally efficient solution to  $\int d\vec{r} \exp \left[ -ik(\hat{n} - \hat{e}) \cdot \vec{r} \right] \mathbf{V}(\vec{r})$ .

## A.2 Polycrystalline potential construction

We will begin the next section by constructing a potential that represents a polycrystalline film with narrow grain orientation distributions<sup>74</sup>. In real space,

$$\mathbf{V}(\vec{r}) = \sum_{\vec{R}} v(\vec{r} - \vec{R}) = \sum_{\vec{G}} V_{\vec{G}} \exp[i\vec{G} \cdot \vec{r}]. \quad (0.36)$$

Here,  $\vec{G}$  is an inverse lattice vector while  $\vec{R}$  is a real lattice vector. This represents the potential for a periodic lattice. For a polycrystalline film, each individual grain (which will be indexed by a  $g$ ) is a single-crystal and the film is a summation of these individual grains. Each grain is assigned a grain envelope function  $\Theta_g(\vec{r} - \vec{a}_g)$ , a central lattice location  $\vec{a}_g$ , and a rotation  $\mathbf{B}_g$  which is a rotation matrix that rotates the grain orientation around the x, y, and z axes. ( $\hat{x}$  is parallel to the crystal surface and in the direction of the incident electron beam,  $\hat{y}$  is parallel to the crystal surface and perpendicular to the direction of the incident electron beam,  $\hat{z}$  is perpendicular to the crystal surface.) The polycrystalline potential is then

$$\mathbf{V}(\vec{r}) = \sum_g \Theta_g(\vec{r} - \vec{a}_g) \sum_{\vec{G}} V_{\vec{G}} \exp[i\mathbf{B}_g \vec{G} \cdot (\vec{r} - \vec{a}_g)]. \quad (0.37)$$

$$\Theta_g(\vec{r} - \vec{a}_g) = \begin{cases} 1 & \text{if } \vec{r} \text{ is inside the grain } g \\ 0 & \text{if } \vec{r} \text{ is outside the grain } g \end{cases} \quad (0.38)$$

Substituting this in to get the scattering probability gives us

$$r \rightarrow r + a_g \quad \text{and} \quad r' \rightarrow r' + a_{g'}$$

$$P(k\hat{e} \rightarrow k\hat{n}) \propto \sum_{\vec{G},g} \sum_{\vec{G}',g'} V_{\vec{G}} V_{\vec{G}'}^* \int d\vec{r}^3 \exp[-ik(\hat{n}-\hat{e})\cdot(\vec{r}-a_g)] \int d\vec{r}'^3 \exp[-ik(\hat{n}-\hat{e})\cdot(\vec{r}'-a_{g'})] \cdot \Theta_g(\vec{r}) \Theta_{g'}^*(\vec{r}') \exp[i\mathbf{B}_g \vec{G} \cdot \vec{r}] \exp[-i\mathbf{B}_{g'} \vec{G}' \cdot \vec{r}'] \quad (0.39)$$

We want to rewrite this equation to emphasize that the exponential terms represent the phase relation between neighboring grains.

$$P(k\hat{e} \rightarrow k\hat{n}) \propto \sum_{\vec{G},g} \sum_{\vec{G}',g'} V_{\vec{G}} V_{\vec{G}'}^* \exp[i\phi_{\vec{G},g} - i\phi_{\vec{G}',g'}] \int d\vec{r}^3 \int d\vec{r}'^3 \Theta_g(\vec{r}) \Theta_{g'}^*(\vec{r}') \cdot \exp\left[i\left(\mathbf{B}_g \vec{G} - k(\hat{n}-\hat{e})\right) \cdot \vec{r}\right] \exp\left[-i\left(\mathbf{B}_{g'} \vec{G}' + k(\hat{n}-\hat{e})\right) \cdot \vec{r}'\right] \quad (0.40)$$

It is clear that if the phases  $\phi_{\vec{G},g}$  and  $\phi_{\vec{G}',g'}$  are random then the terms where  $g \neq g'$  and  $\vec{G} \neq \vec{G}'$  will sum to zero. This is called the random phase approximation.

This reduces our problem to the diagonal terms

$$P(k\hat{e} \rightarrow k\hat{n}) \propto \sum_{\vec{G},g} |V_{\vec{G}}|^2 \int d\vec{r}^3 \int d\vec{r}'^3 \Theta_g(\vec{r}) \Theta_g^*(\vec{r}') \cdot \exp\left[i\left(\mathbf{B}_g \vec{G} - k(\hat{n}-\hat{e})\right) \cdot \vec{r}\right] \exp\left[-i\left(\mathbf{B}_g \vec{G} + k(\hat{n}-\hat{e})\right) \cdot \vec{r}'\right] \quad (0.41)$$

$$r \rightarrow r' + r$$

$$P(k\hat{e} \rightarrow k\hat{n}) \propto \sum_{\vec{G},g} |V_{\vec{G}}|^2 \int d\vec{r}^3 \exp\left[i\left(\mathbf{B}_g \vec{G} - k(\hat{n}-\hat{e})\right) \cdot \vec{r}\right] \int d\vec{r}'^3 \Theta_g(\vec{r}') \Theta_g^*(\vec{r}' + r) \quad (0.42)$$

This result has also been suggested by Litvinov et al.<sup>75</sup>. The key to computationally efficient analysis of this equation is to “sum” over the grains (which for realistic scattering experiments can be  $>10^8$  individual grains) by integrating using probability distributions of the grain orientations. It is also necessary to decouple the size distribution (we assume that all grains are the same size anyway) from the orientation

distribution so that the grain size and orientation averaging can be done independently of each other

$$P(k\hat{e} \rightarrow k\hat{n}) \propto \sum_{\bar{G}} |V_{\bar{G}}|^2 \int dr^3 \exp \left[ i(\mathbf{B}\bar{G} - k(\hat{n} - \hat{e})) \cdot \vec{r} \right] \left\langle \exp \left[ i(\mathbf{B}_g - \mathbf{B})\bar{G} \cdot \vec{r} \right] \right\rangle_g \cdot \left\langle \int dr'^3 \Theta_g(\vec{r}') \Theta_g^*(\vec{r}' + r) \right\rangle_g \quad (0.43)$$

In (0.43),  $\mathbf{B}$  is a rotation matrix which specifies the rotational orientation of the entire sample. The rotation matrix used is an alternate rotational convention to the Eulerian Angle rotations. The rotation matrix  $\mathbf{B}$  is constructed by first rotating the crystal about the z-axis by the angle  $\phi$  (0.44), then rotating about the new y-axis by the angle  $\omega_y$  (0.45), and finally rotating around the new x-axis by the angle  $\omega_x$  (0.46).

$$R_z(\phi) = \begin{bmatrix} \cos \phi & \sin \phi & 0 \\ -\sin \phi & \cos \phi & 0 \\ 0 & 0 & 1 \end{bmatrix} \quad (0.44)$$

$$R_y(\omega_y) = \begin{bmatrix} \cos \omega_y & 0 & -\sin \omega_y \\ 0 & 1 & 0 \\ \sin \omega_y & 0 & \cos \omega_y \end{bmatrix} \quad (0.45)$$

$$R_x(\omega_x) = \begin{bmatrix} 1 & 0 & 0 \\ 0 & \cos \omega_x & \sin \omega_x \\ 0 & -\sin \omega_x & \cos \omega_x \end{bmatrix} \quad (0.46)$$

The final form of  $\mathbf{B}$  (0.47) is the product of the rotation matrices  $R_z(\phi)$ ,  $R_y(\omega_y)$ , and  $R_x(\omega_x)$ .<sup>76</sup>

$$\mathbf{B} = \begin{bmatrix} \cos \omega_y \cos \phi & \cos \omega_y \sin \phi & -\sin \omega_y \\ \sin \omega_x \sin \omega_y \cos \phi - \cos \omega_x \sin \phi & \sin \omega_x \sin \omega_y \sin \phi + \cos \omega_x \cos \phi & \cos \omega_y \sin \omega_x \\ \cos \omega_x \sin \omega_y \cos \phi + \sin \omega_x \sin \phi & \cos \omega_x \sin \omega_y \sin \phi - \sin \omega_x \cos \phi & \cos \omega_y \cos \omega_x \end{bmatrix} \quad (0.47)$$

First we will analyze the grain envelope portion of (0.43). We will chose the simplest envelope function possible, which is a square in the plane of the film (using the average grain size = L) and have a uniform height (h) across the sample

$$\Theta_g(\hat{x}, \hat{y}, \hat{z}) = \begin{cases} 1 & \text{if } \left| \frac{x}{L} \right|, \left| \frac{y}{L} \right|, \left| \frac{z}{h} \right| < 0.5 \\ 0 & \text{otherwise} \end{cases} \quad (0.48)$$

For this envelope function the self convolution is trivial

$$\int dr'^3 \Theta_g(\vec{r}') \Theta_g^*(\vec{r}' + r) = \begin{cases} L^2 h \left(1 - \left| \frac{x}{L} \right| \right) \left(1 - \left| \frac{y}{L} \right| \right) \left(1 - \left| \frac{z}{h} \right| \right) & \text{if } \left| \frac{x}{L} \right|, \left| \frac{y}{L} \right|, \left| \frac{z}{h} \right| < 1 \\ 0 & \text{otherwise} \end{cases} \quad (0.49)$$

For computational purposes, we want to approximate this function using a Gaussian

$$\left\langle \int dr'^3 \Theta_g(\vec{r}') \Theta_g^*(\vec{r}' + r) \right\rangle_g = \frac{L^2 h}{(2\pi\sigma_\theta^2)^{\frac{3}{2}}} \exp\left[-\frac{1}{2} \vec{r}^T \Sigma \vec{r}\right] \quad (0.50)$$

$$\Sigma = \begin{pmatrix} (1/\sigma_\theta L)^2 & 0 & 0 \\ 0 & (1/\sigma_\theta L)^2 & 0 \\ 0 & 0 & (1/\sigma_\theta h)^2 \end{pmatrix} \quad (0.51)$$

$$\sigma = 0.435$$

We also used a new form of notation which is

$$\vec{k}^T \vec{r} = k_x x + k_y y + k_z z \quad \text{and} \quad \vec{r} \vec{k}^T = \begin{pmatrix} xk_x & xk_y & xk_z \\ yk_x & yk_y & yk_z \\ zk_x & zk_y & zk_z \end{pmatrix}$$

Next we address the orientation distribution of the grains. First we define the rotation matrix

$$\mathbf{B}_g = (1 - \omega_x \mathbf{X}_x - \omega_y \mathbf{X}_y - \phi_z \mathbf{X}_z) \mathbf{B} \quad (0.52)$$

$$\mathbf{B}_g - \mathbf{B} = (-\omega_x \mathbf{X}_x - \omega_y \mathbf{X}_y - \phi_z \mathbf{X}_z) \mathbf{B} \quad (0.53)$$

$$\mathbf{X}_x = \begin{pmatrix} 0 & 0 & 0 \\ 0 & 0 & 1 \\ 0 & -1 & 0 \end{pmatrix}, \mathbf{X}_y = \begin{pmatrix} 0 & 0 & -1 \\ 0 & 0 & 0 \\ 1 & 0 & 0 \end{pmatrix}, \mathbf{X}_z = \begin{pmatrix} 0 & 1 & 0 \\ -1 & 0 & 0 \\ 0 & 0 & 0 \end{pmatrix}.$$

The matrix  $\mathbf{B}$  is still the average grain orientation (0.47),  $\mathbf{X}_x$ ,  $\mathbf{X}_y$ ,  $\mathbf{X}_z$  are defined as rotation matrices around the x, y, and z axis respectively, and  $\omega_x$ ,  $\omega_y$ ,  $\phi_z$  are defined as the rotation angles of the grain around each axis. We said in the beginning that we want to look at films with narrow rotation distributions and the representation for  $\mathbf{B}_g$  makes approximations that are only valid for small rotation angles. The approximation for  $\mathbf{B}_g$  can be obtained from the form for  $\mathbf{B}$  (0.47), which is the exact form of a rotation matrix, by making the following small rotation angle ( $\theta$ ) approximations:  $\sin(\theta)$  is replaced by  $\theta$ , all  $\sin^2(\theta)$  terms go to zero, and  $\cos(\theta)$  or  $\cos^2(\theta)$  terms all go to one. These approximations produce maximum errors in the rotation matrix elements of 3% for  $10^\circ$  rotation angles and 11% for  $20^\circ$  rotation angles.

We next assume that the grains have a Gaussian distribution, centered on the average orientation  $\mathbf{B}$ . To get the contributions from the ensemble of grains with different orientations we integrate over the rotation axis angles, weighting it by the distribution function

$$\left\langle \exp \left[ i (\mathbf{B}_g - \mathbf{B}) \vec{G}^T \vec{r} \right] \right\rangle_g = \iiint d\omega_x d\omega_y d\phi_z p(\omega_x, \omega_y, \phi_z) \exp \left[ -i\omega_x (\mathbf{X}_x \mathbf{B} \vec{G})^T \vec{r} - i\omega_y (\mathbf{X}_y \mathbf{B} \vec{G})^T \vec{r} - i\phi_z (\mathbf{X}_z \mathbf{B} \vec{G})^T \vec{r} \right] \quad (0.54)$$

$$p(\omega_x, \omega_y, \phi_z) = \frac{\exp\left[-\frac{\omega_x^2}{2(\Delta\omega_x)^2}\right]}{\sqrt{2\pi(\Delta\omega_x)^2}} \frac{\exp\left[-\frac{\omega_y^2}{2(\Delta\omega_y)^2}\right]}{\sqrt{2\pi(\Delta\omega_y)^2}} \frac{\exp\left[-\frac{\phi_z^2}{2(\Delta\phi_z)^2}\right]}{\sqrt{2\pi(\Delta\phi_z)^2}} \quad (0.55)$$

We see that the terms  $\Delta\omega_x$ ,  $\Delta\omega_y$ ,  $\Delta\phi_z$  represent the width of the Gaussian orientation distributions around the x, y, and z axis respectively. **These are the key parameters that we want to learn about.** The integration is performed for rotations around each axis independently. The integration for each axis is equivalent, so we will only demonstrate the solution to the integration around the z-axis.

$$\int d\phi_z \exp\left[-\frac{\phi_z^2}{2(\Delta\phi_z)^2} - i\phi_z (\mathbf{X}_z \mathbf{B} \bar{\mathbf{G}})^T \vec{r}\right] \quad (0.56)$$

$$x = \phi_z, a = \frac{1}{2(\Delta\phi_z)^2}, b = (\mathbf{X}_z \mathbf{B} \bar{\mathbf{G}})^T \vec{r}$$

$$\int dx \exp\left[-(ax^2 + ibx)\right]$$

$$\int dx \exp\left[-a\left(x^2 + i\frac{b}{a}x\right)\right]$$

$$\int dx \exp\left[-a\left(x + i\frac{b}{2a}\right)^2 - \frac{b^2}{4a}\right]$$

$$\exp\left[-\frac{b^2}{4a}\right] \int dx \exp\left[-a\left(x + i\frac{b}{a}\right)^2\right]$$

$$\sqrt{\frac{\pi}{a}} \exp\left[-\frac{b^2}{4a}\right]$$

Replacing a, b, x and integrating over  $\omega_x$ ,  $\omega_y$ ,  $\phi_z$  we get

$$\left\langle \exp \left[ i \left( \mathbf{B}_g - \mathbf{B} \right) \vec{G}^T \vec{r} \right] \right\rangle_g = \exp \left[ - \frac{(\Delta\omega_x)^2 \vec{r}^T (\mathbf{X}_x \mathbf{B} \vec{G}) (\mathbf{X}_x \mathbf{B} \vec{G})^T \vec{r} - (\Delta\omega_y)^2 \vec{r}^T (\mathbf{X}_y \mathbf{B} \vec{G}) (\mathbf{X}_y \mathbf{B} \vec{G})^T \vec{r} - (\Delta\phi_z)^2 \vec{r}^T (\mathbf{X}_z \mathbf{B} \vec{G}) (\mathbf{X}_z \mathbf{B} \vec{G})^T \vec{r}}{2} \right]. \quad (0.57)$$

To simplify the notation we define

$$\Delta_{\vec{G}} = (\Delta\omega_x)^2 (\mathbf{X}_x \mathbf{B} \vec{G}) (\mathbf{X}_x \mathbf{B} \vec{G})^T + (\Delta\omega_y)^2 (\mathbf{X}_y \mathbf{B} \vec{G}) (\mathbf{X}_y \mathbf{B} \vec{G})^T + (\Delta\phi_z)^2 (\mathbf{X}_z \mathbf{B} \vec{G}) (\mathbf{X}_z \mathbf{B} \vec{G})^T. \quad (0.58)$$

Written out in matrix notation (for no average rotation, i.e.  $\mathbf{B}$  is the identity matrix)

this is

$$\Delta_{\vec{G}} = \Delta\omega_x^2 \begin{pmatrix} 0 & 0 & 0 \\ 0 & G_z^2 & -G_y G_z \\ 0 & -G_y G_z & G_y^2 \end{pmatrix} + \Delta\omega_y^2 \begin{pmatrix} G_z^2 & 0 & -G_x G_z \\ 0 & 0 & 0 \\ -G_x G_z & 0 & G_x^2 \end{pmatrix} + \Delta\phi_z^2 \begin{pmatrix} G_y^2 & -G_x G_y & 0 \\ -G_x G_y & G_x^2 & 0 \\ 0 & 0 & 0 \end{pmatrix}. \quad (0.59)$$

So we have now "summed" over the  $10^8$  grains by making judicious approximations and evaluating the functions analytically. Rewriting the equation we started with, including the new grain averaged terms

$$P(k\hat{e} \rightarrow k\hat{n}) \propto \frac{L^2 h}{(2\pi\sigma_\theta^2)^2} \sum_{\vec{G}} |V_{\vec{G}}|^2 \int d\vec{r}^3 \exp \left[ i \left( \mathbf{B} \vec{G} - k(\hat{n} - \hat{e}) \right)^T \vec{r} \right] \exp \left[ - \frac{\vec{r}^T (\Delta_{\vec{G}} + \Sigma) \vec{r}}{2} \right]. \quad (0.60)$$

We define

$$\mathbf{A}_{\vec{G}}^{-1} = \Delta_{\vec{G}} + \Sigma \quad (0.61)$$

and integrate over  $d\vec{r}^3$  by completing the square so that we can use the following integration identity.

$$\int d\vec{r}^3 \exp \left[ - \frac{(\vec{r} - i\mathbf{A}\vec{b})^T \mathbf{A}^{-1} (\vec{r} - i\mathbf{A}\vec{b})}{2} \right] = (2\pi)^{\frac{3}{2}} \sqrt{\det \mathbf{A}} \quad (0.62)$$

We define  $\vec{b} = (\mathbf{B}\vec{G} - k(\hat{n} - \hat{e}))$  and determine the extra factor needed to convert the integral in equation (0.60) to the integral in equation (0.62).

$$(\vec{r} - i\mathbf{A}\vec{b})^T \mathbf{A}^{-1} (\vec{r} - i\mathbf{A}\vec{b}) \quad (0.63)$$

$$\left( \vec{r}^T \mathbf{A}^{-1} - i\vec{b}^T \mathbf{A}^T \mathbf{A}^{-1} \right) (\vec{r} - i\mathbf{A}\vec{b}) \quad (0.64)$$

$$\vec{r}^T \mathbf{A}^{-1} \vec{r} - i\vec{b}^T \mathbf{A}^T \mathbf{A}^{-1} \vec{r} - i\vec{r}^T \mathbf{A}^{-1} \mathbf{A}\vec{b} + i^2 \vec{b}^T \mathbf{A}^T \mathbf{A}^{-1} \mathbf{A}\vec{b} \quad (0.65)$$

$\mathbf{A}$  is symmetric so  $\mathbf{A}^T = \mathbf{A}$  and equation (0.65) reduces to

$$\vec{r}^T \mathbf{A}^{-1} \vec{r} - i\vec{b}^T \vec{r} - i\vec{r}^T \vec{b} - \vec{b}^T \mathbf{A}^T \vec{b} = -2i\vec{b}^T \vec{r} + \vec{r}^T \mathbf{A}^{-1} \vec{r} - \vec{b}^T \mathbf{A}^T \vec{b}. \quad (0.66)$$

Taking the integral of equation (0.60), we complete the square of the exponent so that it resembles (0.66) and use the integration identity to integrate equation (0.60).

$$\int dr^3 \exp \left[ -\frac{-2i(\mathbf{B}\vec{G} - k(\hat{n} - \hat{e}))^T \vec{r}}{2} \right] \exp \left[ -\frac{\vec{r}^T \mathbf{A}_G^{-1} \vec{r}}{2} \right] \quad (0.67)$$

$$\int dr^3 \exp \left[ -\frac{1}{2} \left( -2i\vec{b}^T \vec{r} + \vec{r}^T \mathbf{A}_G^{-1} \vec{r} \right) \right] \quad (0.68)$$

$$\exp \left[ \frac{-\vec{b}^T \mathbf{A}_G^T \vec{b}}{2} \right] \int dr^3 \exp \left[ -\frac{1}{2} \left( -2i\vec{b}^T \vec{r} + \vec{r}^T \mathbf{A}_G^{-1} \vec{r} - \vec{b}^T \mathbf{A}_G^T \vec{b} \right) \right] \quad (0.69)$$

$$\exp \left[ \frac{-\vec{b}^T \mathbf{A}_G^T \vec{b}}{2} \right] \int dr^3 \exp \left[ -\frac{(\vec{r} - i\mathbf{A}\vec{b})^T \mathbf{A}^{-1} (\vec{r} - i\mathbf{A}\vec{b})}{2} \right] = (2\pi)^{\frac{3}{2}} \sqrt{\det \mathbf{A}} \exp \left[ \frac{-\vec{b}^T \mathbf{A}_G^T \vec{b}}{2} \right]$$

$$(0.70)$$

Replacing the result from equation (0.70) into the integral of equation (0.60) and substituting back in  $\vec{b} = (\mathbf{B}\bar{G} - k(\hat{n} - \hat{e}))$ , we get the final analytical solution to the kinematic electron scattering model for polycrystalline films with biaxial texture

$$P(k\hat{e} \rightarrow k\hat{n}) \propto \sum_{\bar{G}} |V_{\bar{G}}|^2 \sqrt{\det \mathbf{A}_{\bar{G}}} \exp \left[ -\frac{(\mathbf{B}\bar{G} - k(\hat{n} - \hat{e}))^T \mathbf{A}_{\bar{G}} (\mathbf{B}\bar{G} - k(\hat{n} - \hat{e}))}{2} \right]. \quad (0.71)$$

To calculate a full RHEED pattern, the algorithm determines the direction of  $\hat{n}$  for each pixel on the RHEED screen and then calculates the  $P(k\hat{e} \rightarrow k\hat{n})$  for each relevant  $\hat{n}$ .

The most important variables that can be manipulated are: the width of the distribution of the grain orientations about each axis  $\Delta\omega_x$ ,  $\Delta\omega_y$ ,  $\Delta\phi_z$ , the electron energy  $k_o$ , lateral grains size  $L$ , and the incident electron angle  $\theta$ .

---

<sup>74</sup> J. W. Hartman, R. T. Brewer, and Harry A. Atwater, J. Appl. Phys. **92**, 5133 (2002).

<sup>75</sup> D. Litvinov, T. O'Donnell, and R. Clarke, J. Appl. Phys. **85**, 2151 (1999).

<sup>76</sup> H. Goldstein, Classical Mechanics, 2nd ed. (Addison-Wesley, Reading, 1980), pp. 146, 147, 608.

## Appendix B Directions for Using RHEED-Based Biaxial Texture Analysis Software

### B.1 Procedure outline

Over the course of my thesis work I have developed both software and experimental procedures for analyzing biaxial texture of MgO. This appendix will describe the experimental method and software operation for obtaining biaxial texture measurements from RHEED. This section will focus on work for MgO, however, I will also describe how to create lookup tables for other cubic materials, as well as mention important issues to consider when analyzing a new material.

The first section will describe general information concerning experimental procedures and software that are relevant for both single-image analysis (for layer-by-layer out-of-plane texture analysis) and in-plane RHEED rocking curves (for in-plane texture analysis). I will then describe how to take RHEED data and perform the individual RHEED image analysis for out-of-plane orientation distribution ( $\Delta\omega$ ), effective grain size ( $L$ ), and electron penetration depth ( $h$ ) measurements. The software function and operation is described by examining the input file for each program and describing the function and options available on each input line. A similar process is followed to describe the software for creating new lookup tables for different materials. Finally, I will describe how to take in-plane RHEED rocking curve data, how to measure the in-plane orientation distribution ( $\Delta\phi$ ) using the software, and how to create lookup tables for RHEED rocking curves.

### **B.1.1 RHEED settings**

MgO RHEED experiments were done at 25 keV and 2.6 degrees incidence angle. The angle was chosen such that the specular RHEED reflection would be in the middle between the (004) and the (006) diffraction spots. This position was chosen to minimize contributions from specular scattering to either of these spots and to allow for strong scattering from the (xx4) and (xx6) spots, where  $x$  = even numbers from 0 to 4. We also chose to operate the electron gun at 25 keV to avoid being too close to the maximum electron gun operation voltage (30 keV), as well as to push the electron scattering as close to kinematical scattering conditions as possible. Also, it was found that at 25 keV, the in-plane rocking curve experiments were more reliable than at 15 keV. It is possible that the higher energy allows the electrons to be better represented by the kinematical scattering limit.

### **B.1.2 Imaging settings**

Images were taken with a 16 bit dynamic range, 1024 x 1024 pixels Photometrics CCD camera. Long exposure times (1 second) are used to increase signal to noise ratios and to reduce picture to picture fluctuations. To save hard drive space, and allow the analysis code to run faster, we condense the 1024 x 1024 image to a 512 x 512 image by using the image software to condense the value of four adjacent pixels into the value of one pixel, the value being the average of the four pixels. I use Noesys Transform to change the images into an ascii format from the “.fit” format exported by the Photometrics camera. The final ascii images are 512 x 512 arrays of numbers which represent the intensity at the given pixel location. There is also a row that contains a

header listing the number of the columns and a number at the beginning of each row that specifies which number the row is. The RHEED code automatically strips the column and row numbers and creates a vector where the first number is the intensity of pixel (1,1), the 512<sup>th</sup> number is the intensity of pixel (1,512), and the 513<sup>th</sup> number is the intensity of pixel (2,1). Therefore, RHEED images from any program can be analyzed with this program, provided that the images are converted into this ascii format or a small section of code is included into the program to create the vector described above.

## **B.2 Layer by layer growth RHEED analysis**

While the full biaxial texture is not measurable from a single RHEED image using the kinematical electron scattering model (because of the intensity renormalization caused by dynamical scattering), the electron penetration depth, effective grain size, and out-of-plane orientation distribution ( $\Delta\omega$ ) can be determined. Single-image RHEED analysis yields measurements of the out-of-plane orientation distribution as a function of film thickness without interrupting film growth. Specifically, this method measures  $\Delta\omega_x$ , the orientation distribution of the film around the in-plane axis in the direction of the incoming RHEED beam. Synchrotron x-ray diffraction experiments indicate that IBAD produces MgO films with  $\Delta\omega_y$  (the out-of-plane orientation distribution in the direction orthogonal to  $\Delta\omega_x$ ) within plus or minus one degree of  $\Delta\omega_x$ . Therefore, it is sufficient to measure the out-of-plane orientation distribution in one direction to know both out-of-plane orientation distributions. As a result of the approximate equivalence of  $\Delta\omega_x$  and  $\Delta\omega_y$ , the out-of-plane orientation distribution is simply referred to as  $\Delta\omega$ .

## **B.2.1 Experimental procedure**

To obtain a measurement of the out-of-plane orientation distribution as a function of film thickness, RHEED images need to be taken during the growth experiment without interrupting the film growth. This requires that at the desired growth position, the film has an RHEED incident angle of  $2.6^\circ$  (for MgO).

### **B.2.1.1 Creating a background image**

RHEED images contain diffuse scattering from inelastic and multiple scattering processes that are not accounted for by the kinematical simulation. These effects skew the shapes of the RHEED spots that need to be analyzed and must therefore be subtracted out. The analysis code provides several options for subtracting out background effects. The most effective and reliable method is to use the electron scattering from an amorphous background to subtract out the diffuse scattering from IBAD MgO RHEED images. The optimal procedure is to take a RHEED image at the beginning of a growth experiment to subtract from RHEED images taken during deposition. This method has the advantage of exactly representing the experimental set up and automatically aligning the background image with the diffuse scattering from polycrystalline MgO. If it is not possible to take a pre-growth image of the amorphous substrate (for example when measuring biaxial texture of a material grown in another chamber), a RHEED image from an amorphous material at the equivalent setup can be taken before or after the growth experiment and used to subtract out the background. Care should be taken to ensure that the background image intensity scales appropriately with respect to the experimental

RHEED image and that the peak of the background image corresponds with the peak of the diffuse scattering in the x and y directions of the experimental RHEED image.

## B.2.2 Input file

The input file controls the operation of the computer code, the methods that it uses to subtract the background, and how it finds diffraction spots for analysis. In this section I will describe what each line of the input code is asking for and how the different options will change the code operation. I will also specify the settings that I have found to be the most robust for getting reliable out-of-plane orientation distribution measurements. An example of the input file, called `inautolayer.dat`, follows.

```
Input file for autolayer.c
134 3      spot separation guess (Spot from spot one used for
          separation)
512 512      Y pixel and Z pixel image size
0.10      Minimum relative spot size
1 101303.txt  Use background? (0=No, 1=Yes) if 1 specify file.
1          adjust? (0=No, 1=Yes) (Subtract Background)
1          Make the background file (1= yes, 0 = No)
0          Reduce array size by 2? (1= yes, 0 = No)
0 1 0      Print out intensity file, adjusted intensity file,
          zero adjusted intensity? (0=No,1=yes)
0 1 0      Make movie? - print files out (1=yes, 0=No), number
          of extra frames, mark spots?(0=No,1=yes)
0          shift background to match positions? (1=yes, 0 = No)
0 4 -35    Manual shift Z? (1=yes,0 = No) Manual Y then Z shift
          (exp-back) - doesn't override homoepishift
0          Taylor expand background?(1=yes, 0=No) - only for
          Simple Cubic [100]
0 136 153  Set (004) position (0=No, 1=Yes) y z (004 position)
          (auto find option)
0 -2      Thru spot location, rel to spot separation from Spot
          1 (Y Z)
0 1        Spot 2 position (Relative to Spot 1. Number is
          fraction of the spot)
1 0        Spot 3 position (separation between spot 1 and 2 in
          the Y and Z)
1 1        Spot 4 position (direction that the spot is expected
          to be found)
2 0        Spot 5 position
2 1        Spot 6 position
0.5 0.5    Spot 1 and 2 background location (y) as fraction of
          spot separation
```

```

0.5 0.5          Spot 3 and 4 ""
0.5 0.5          Spot 5 and 6 ""
0.5              Z extension of background +- (as fraction of spot
                  separation)
6 -0.5 -0.5      Spot number of background for background intensity
                  matching (y,z in spot separation units)
0                No spots? (0=No, 1=Yes) (If yes, set spots from spot
                  separation)
0                Low Coverage analysis (0=no, 1=Yes) - Only works for
                  Cubic Oxides
0                Number of low coverage files
.5               Fraction above (004) to fit Low Coverage
0 0 221.743      Calculate d-spacing?Recalibrate
                  Lambda*CameraLength?(0=No,1=Yes), Calibrated
                  Lambda*CameraL
1501303.txt      file used to calibrate spot positions (fully developed)
0                Look at calibrated file only, ie no layers (0=No, 1=Yes)
14 14            number of IBAD files, number of input files
4.12 60          Time perfile (During IBAD, After IBAD) (filenames)
101303.txt
301303.txt
501303.txt
601303.txt
701303.txt
801303.txt
901303.txt
1001303.txt
1101303.txt
1201303.txt
1301303.txt
1401303.txt
1501303.txt
1601303.txt
1701303.txt
1801303.txt
1901303.txt
2001303.txt
2101303.txt
2201303.txt
2301303.txt
2401303.txt
2501303.txt

```

The following sections discuss the operation of each line of the input file in approximately the order that it appears in the input file.

### **B.2.2.1 Header line**

This line is ignored by the code and can be changed to remind the user of anything desired. Generally it just states that this input file was created for the `autolayer.c` program.

### **B.2.2.2 Spot separation**

The computer program does not independently find the location of the diffraction spot, it requires input to guide the algorithm specifying where to search for the diffraction spots. The first number on this line is an estimate of the diffraction spot separation distance (in pixels) from the first diffraction spot to the diffraction spot number listed as the second number. It is important for the diffraction spot separation distance to be reasonably close (within 10% or so) because the program uses this specified diffraction spot separation distance to locate diffraction spots (with the help of input from further down in the input file). It is essential that the spot number used is consistent between the experimental files and the simulations. When diffraction spot widths are measured (experimentally or simulated), the widths are measured as a fraction of the spot separation. This allows for direct comparison between experiment and simulation without requiring careful calibration to ensure that the simulation pixels are the same size as the experimental camera pixels. For example, in MgO, the diffraction spot used as the spot separation calibration spot is typically number 3, where number 1 is (004), number 2 is (006), and number 3 is (024). When measuring diffraction spot widths, I can therefore directly compare an experimental diffraction spot width of 0.5 (half the pixel distance between the (004) and (024) spots) with a simulated spot width of 0.5 (which is also half

the pixel distance between the simulated (004) and (024) spots). It is typically convenient to choose the spot separation distance as the distance between two adjacent allowed reflections.

### **B.2.2.3 Image size (Pixels)**

These numbers specify the pixel size of the images in the across (Y, increasing numbers from left to right) and down (Z, increasing numbers from the top to bottom). Any image size can theoretically be used; however, large images linearly reduce computation speed. The y and z directions are consistent throughout the code and were chosen to mimic the RHEED geometry, reflecting the fact that the RHEED image is a two dimensional diffraction image containing only spots where the miller indices contain  $h = 0$ .

### **B.2.2.4 Threshold for Gaussian fit**

Because the code is used to analyze films as they are growing, some expected diffraction spots may not be present in RHEED images acquired from very thin films. The computer code locates diffraction spots by searching for local maxima. Unfortunately, when no diffraction spots are present the program mistakes camera noise for diffraction spots. The full width at half maximum (FWHM) of camera noise is very narrow compared to real diffraction spots and is therefore easily identified by its narrow FWHM. The number input on this line represents the minimum allowable size for a diffraction spot width. If a feature, originally assumed to be a diffraction spot by the program, has a FWHM narrower than the specified width, the program determines that the feature in question is not actually a diffraction spot (probably it was a local maximum

from camera noise) and ignores it in the lookup tables. This process releases the user from manually determining if an image has the requisite number of diffraction spots to be analyzed or if the program mistakenly interpreted noise as a diffraction spot location.

#### **B.2.2.5 Background subtraction method**

This line determines whether or not an image is used to subtract out the diffuse background. Throughout the program, 0s and 1s are substituted for no and yes, respectively. This line also requires the user to specify the name of the file to be used for background subtraction, which is typically diffuse electron scattering from an amorphous surface. The image is opened and converted to an array that is used by the computer program. This array is saved on the hard drive as “newback.dat”.

#### **B.2.2.6 Adjust**

There are occasions when the fitting routines may not work and all that is desired is for the program to run so that the RHEED image can be examined in matlab. If adjust is set to 0 then the program will not subtract out the background, try to find the spots or measure the FWHM. This is also useful for getting a first guess at spot locations and spot separations in pixels.

#### **B.2.2.7 Make the background file**

The actual background subtraction routine in the program uses “newback.dat” as the background subtraction file. This file could have been previously created during a previous simulation (in which case a zero would be entered on this line) or it can be

created in real-time using the file specified previously as the background file (in which case a one would be entered on this line).

### **B.2.2.8 Reduce the array size**

The computational analysis time scales linearly with the number of pixels. If the images are large, or there are a lot of images, then to reduce computation time the number of pixels can be reduced by a factor of 4. The program will take four adjacent pixels and collapse them into a single pixel containing the average value of the original 4 pixels.

### **B.2.2.9 Print out intensity file**

This option allows the user to choose which images are printed out into a format viewable in matlab or for transformation into a movie. The first number specifies if the raw image should be printed out without background subtraction. The images are named `intnxxx.dat`, where `intn` is short for “intensity” and `xxx` is the number specifying which image of the sequence it is. The first image, which is also typically the background image, is specified as `intn000.dat`. The second number specifies whether or not to print out the intensity of images which have had the background subtracted out of them. These images follow the same number convention described above; however, the image names are `aintnxxx.dat`, where “aintn” is short for adjusted intensity. When the background is subtracted from RHEED images, especially RHEED images without strong diffraction spots, strong negative intensities can result. These compress the color gradation in the region of interest making it difficult to see the RHEED pattern structure. In these cases the minimum allowable intensity can be set to one (by making the third number a 1) and the program will set all negative intensity values to one. This option should only be used

for viewing the data because it artificially masks problems which may exist with the background subtraction method.

### **B.2.2.10 Make movie**

This line controls functions that format the output image files so that they can easily be imported into Quicktime to make RHEED movies of IBAD MgO growth. The first number controls whether or not the files are reformatted so that they are importable into Quicktime. This algorithm rotates the pictures and rescales the intensity values so that they can be converted into .png files using matlab (which will then be imported into Quicktime). The second number indicates how many extra frames should be interpolated between the data points. The high dynamic range camera can only take images every 4 seconds, resulting in jumpy movies. For artistic effect, extra frames can be added by interpolating the value of each individual pixel between actual images to make smooth transitions from image to image. The number determines how many extra images are added. To visually verify that the program is finding the correct diffraction spots and accurately measuring the FWHM, the program draws lines across measured diffraction spots showing the FWHM of the spots in two directions. If these indicators are not desired in the movie, the last number can be set to 0 and these markings will be eliminated.

### **B.2.2.11 Shift background position**

For IBAD MgO experiments, a RHEED image of the amorphous layer can be taken before growth and then directly subtracted from subsequent RHEED images. However, if the substrate is heated up the sample position will change slightly, making

the background file not match up with the diffuse background from the RHEED experiments. Also, if a pre-growth image of amorphous background is not available, an image of an amorphous background for a separate experiment can be used, but it will not necessarily line up with the diffuse background of the RHEED images. Algorithms are available for shifting the position of the background file to better match the RHEED image. Because no shifting is necessary when the background file is just the first of the growth files, the position of the background file can be locked in by setting this number to 0. If position matching is allowed, the program matches the background with the experiment by matching the maximum intensities of the two files along the y direction and by matching the z position of the substrate shadow in both images. While the y matching is quite simple and reliable, it is difficult to reliably locate the shadow edge of the substrate. The algorithm used to locate the substrate shadow looks for a sharp increase in the second derivative as the program cuts a line from  $z = 0$  toward the diffraction spots. The large increase in the second derivative should correspond to the substrate edge where electrons can start to shine on the RHEED screen. However, noise and different image intensities make it difficult to reliably identify the edge of the substrate shadow.

### **B.2.2.12 Manual shift**

Whether or not automatic background matching has been successful can be determined by looking at the background subtracted images. If there is a large negative region around the top diffraction spots then the background is too high in the z direction (low in z pixel number because the top of the image is  $z = 0$ ). If there is a large positive intensity region around the top diffraction spots then the background is too low. This

issue can be resolved, albeit painstakingly, by manually setting the number of pixels the background shifts in the z direction. In this line a 0 directs the manual background shifting functions to be ignored and a 1 directs the program to perform the manual background shifting operation. If manual background shifting is specified, results from the automatic algorithm will be ignored and the background will be shifted in the y and z direction the number of pixels indicated by the last two numbers in this line.

### **B.2.2.13 Taylor expand background**

This process was developed specifically for MgO and should not be used unless the diffraction pattern resembles a simple cubic [100] structure. The background file shape never perfectly matches the shape of the RHEED image background. If this option is chosen, a Taylor expansion of the error between the background and the RHEED intensity is used to correct the background image. Lines are cut vertically across the RHEED image in the middle between Bragg rods where no diffraction should be occurring and should therefore be zero. At every pixel along this line, the difference between the background and the RHEED image is recorded (as the error – because the background should subtract this to zero). The error of the background at every other point is determined by horizontally taking a second order Taylor expansion of the error. The background is finally modified by subtracting the error from the background at every point before it is subtracted from the RHEED image. This method is attractive because it reliably subtracts the background between spots to zero, however, there is concern that it artificially truncates the width of the diffraction spots if they are wide compared to the spot separation and run into the area where this method assumes there is no diffraction.

This method has not been used in the experiments used to verify the validity of RHEED measurements; however, for narrow diffraction spots this method could be evaluated.

#### **B.2.2.14 Set (004) position**

As previously stated, the program attempts to find and verify the position of diffraction spots by seeking for local maxima. This effort is typically unsuccessful if for some reason the (006) diffraction spot is more intense than the (004) spot – this usually results from an error in the incidence angle. This option allows one to manually specify the position of the (004) diffraction spot (or spot number 1 for any other material). The program will assume that the first diffraction spot is located at the manually input y and z values (the second and third numbers respectively), but will also do a limited local search for the absolute maximum. After forcing the computer to choose a certain location for the (004) diffraction spot, it is easy to verify that this was in fact the local maximum by watching the output of the program for the final location chosen by the limited search for a local maximum. If this is not the same as the chosen value, the new value should be chosen until the next iteration produces no small change in the chosen location of the (004) maximum.

#### **B.2.2.15 Through spot location**

These numbers specify, in units of spot separation, the location of the non-diffracted electron beam with respect to the first spot (spot (004) for MgO). The first number is the offset in the y direction and the second number is the offset in the z direction. The location of the through spot is necessary because the program uses the location of the thru spot, with respect to the location of each diffraction spot, to determine

the direction to cut the spot perpendicular to the through spot (which is the direction most dependent on the out-of-plane orientation distribution).

### **B.2.2.16 Spot positions (2-6)**

The next five lines tell the computer where to look for local maxima to find the location of five more diffraction spots, spots two through six. The first numbers are the offset from the first diffraction spot, in units of spot separation, in the y direction and the second number is the same thing for the z direction.

### **B.2.2.17 Background locations**

The following four lines are used when a reliable background subtraction file is not available. The kinematical model predicts that, except for exceptionally small grains and large out-of-plane orientation distributions, the background should approach zero between the diffraction spots. This algorithm takes the locations chosen manually (as the distance in the y direction from the diffraction spots where the background should be zero), records the intensity of the image on both sides of the diffraction spot, and then assumes that the background intensity between those locations (and underneath the diffraction spots) is a linear interpolation of the side values. This same method is used to subtract background intensity from in-plane rocking curve images where diffraction spot shape is not important. Although this method potentially artificially narrows wide diffraction spots, experiments comparing results from a single RHEED image which had the background subtracted using both this method and the method which subtracts out the background using an amorphous RHEED image yield very similar measurements for out-of-plane orientation distribution.

### **B.2.2.18 Z extension of the background**

This number tells the program how far in the plus and minus z directions to perform the background subtraction method described in the previous section. This number (specified as a fraction of the spot separation distance), should be large enough to include most of the diffraction spot, but must not be large enough to cause it to intersect with other background subtraction areas or diffraction spots.

### **B.2.2.19 Spot number for background matching**

The RHEED gun intensity drifts slightly during growth and so the background intensity must be scaled to match the diffuse scattering from the RHEED image. Because we predict that there should be no diffraction between spots we chose a point where no diffraction should contribute to the intensity and compare the intensity of the RHEED image with the background image at that same location and then scale the background image to match the intensity of the experimental image at that point. The scaling factor usually changes the background absolute intensity by less than 5 %. This process is most important when a background file from a different experiment must be used for the current one. The first number indicates which spot will be the base for the background normalization location. The next two numbers specify an offset from the diffraction spot location, in units of spot separation, where the comparison between the background file and the RHEED experiment intensity will occur.

### **B.2.2.20 No spots**

Sometimes it is desirable to look at RHEED images which do not have sharp diffraction spots. If a 1 is entered here than the program does not look for diffraction spots and just uses the manually input locations as the locations of diffraction spots.

### **B.2.2.21 Low coverage analysis**

Early growth analysis is specifically for IBAD MgO growth and refers to methods used to analyze the RHEED pattern before sharp diffraction spots are visible. During this growth regime the RHEED pattern has diffraction rings characteristic of either randomly oriented nanocrystalline films or amorphous films. Low coverage analysis deals with the spacing of these rings and tries to determine the atomic spacing for the spacing of the rings.

### **B.2.2.22 Number of low coverage files**

This number tells how many files should be looked at for diffraction rings instead of diffraction spots.

### **B.2.2.23 Fraction above (004)**

One can analyze not only the location of the rings, but also the FWHM of the rings if they have one. If this is a nanocrystalline film then there maybe some preferred out-of-plane orientation that would be reflected in the angular FWHM of the arc. The ring is cut off by the substrate shadow and so it is necessary to tell the program where to stop looking to fit the ring. The number here specifies, in spot separation units, how far above the (004) diffraction spot to stop looking for the ring. Although attempts have

been made to correlate the angular FWHM of the diffraction ring with an out-of-plane orientation distribution ( $\Delta\omega$ ), these attempts have not been successful.

#### **B.2.2.24 Calculate d-spacing**

With a known camera length, the atomic spacing can be calculated from the Camera Equation and the spacing of the diffraction rings. The first number specifies whether or not the program should attempt to calculate d-spacing from the rings. The recalibration option takes an image of diffraction spots, assumes that the diffraction spot spacing results from a d-spacing of perfect MgO single-crystals (4.2 angstroms) and then uses it to find the product of the wavelength and camera length. The last number is the calibrated product of wavelength and camera length. This number is used in the Camera Equation to get the d-spacing from subsequent measurements.

#### **B.2.2.25 Calibration file**

This should be an image of a fully developed RHEED pattern. The program will use this image to determine where the diffraction spots should be. Once found on a well developed pattern, the program will use these spot positions for finding the diffraction spots in subsequent RHEED images.

#### **B.2.2.26 Look at calibrated file only**

Unless otherwise specified in this line with a 1, the program will examine all files indicated below. When a growth experiment is first being examined it is necessary to verify that the program accurately finds the diffraction spot locations and is properly subtracting out the background. If a 1 is entered on this line, the program will only look

at the calibration file (listed above). It is then possible to view the RHEED pattern with the background subtracted out and verify that the chosen locations for the diffraction spots correspond to the actual locations of the desired diffraction spots.

#### **B.2.2.27 Number of IBAD files**

This line breaks the spot location algorithm up into two sections. The first number tells the program how many RHEED images there will be in the first section and the second number tells how many total files the program needs to analyze. This is useful because if a homoepitaxial layer is grown on top of the IBAD film, the high temperature tends to shift the location of the RHEED spots and the program needs to know that it needs to look for the RHEED spots in a new location and shift the background accordingly. If the second number is the same as the first, the program does not look for new diffraction spot locations or shift the background; however, if the second number is larger than the first, once it has analyzed as many images as the first number indicated, it will look for new diffraction spot locations, appropriately shift the background subtraction image and also use that new location for all subsequent analysis.

#### **B.2.2.28 Time per file**

These numbers specify the growth time between RHEED images. These times are used to track the film microstructure as a function of time (film thickness). The first number is used for the number of films specified above as the number of films for IBAD growth. The second number is used for any image taken after the number of IBAD films has been exhausted. During IBAD growth it is desirable to take images as fast as possible (every 1 to 5 seconds) because the biaxial texture is changing rapidly. During

homoeptaxy this is not the case and taking an image every minute or so easily captures the dynamics of texture development.

### **B.2.2.29 File names**

The following list of file names specifies the files that will be analyzed sequentially by the program. This is also the order that will be used to print out the results. During my experiments, the file names have been given a number, followed by the date in the format of month, day, and year (only one digit, because if I am still doing the same work in 10 years then I deserve to be confused). Any file names past the previously specified total number of files will be ignored. If a file is specified in this list that does not exist, then the program will crash.

This is the end of the explanation of the input file inautolayer.dat.

### **B.2.3 Output files**

As previously described, the program outputs several files to verify that the program is properly subtracting out background and finding the diffraction spot locations. These are the aintnxxx.dat and intnxxx.dat (xxx are numbers from 000 to 999). The final measurements and characterization of the RHEED pattern are contained in the files named ingausslookupxxx.dat (where xxx is again a number that specifies which of the series of analyzed images is being referenced) and are the input files for the lookup tables. A sample ingausslookup.dat file is included below.

```
File: 1601303.txt
inten  angle  fwhmy   fwhmz   fwhms   fwhml   fwhmp
0       0       1       1       1       1       1
2642.29 90.0   0.25844 0.35822 0.36186 0.25935 0.36186
1107.94 89.6   0.38139 0.41396 0.39387 0.38235 0.39387
2399.36 63.1   0.24957 0.33473 0.27693 0.29544 0.27693
```

```

1049.62 71.1 0.37835 0.38880 0.36039 0.42079 0.36039
 949.33 44.4 0.24898 0.39013 0.25918 0.37668 0.25918
 572.10 55.2 0.37654 0.19741 0.36036 0.50411 0.36036

```

The first line is a header telling the name of the file that was analyzed to find these results. The second line labels what the columns contain. Inten stands for the spot intensity, angle indicates the long axis angle cut across the spots (this is the direction perpendicular to the line between the non-diffracted electron beam and the diffraction spot), fwhm represents full width at half maximum of a Gaussian fit to the diffraction spot cut through the middle of the spot in the y (fwhmy), z (fwhmz), short axis (fwhms – perpendicular to the long axis), long axis (fwhml), and a random direction (fwhmp – set to coincide with the short axis, this is a superfluous remnant of the program development – it is not hurting anyone, so like non-destructive religious philosophies it has the right to exist). The following line tells the lookup table whether or not to consider the information in that column. A 0 instructs the lookup table to ignore information from that column and a 1 tells the lookup table to consider that column. Finally, the last six rows are the actual data, each row corresponding to a diffraction spot, spot numbers 1 through 6 in order. The numbers in each column contain the information for that spot as described above, with the additional specification that the fwhm are measured in units of spot separation. It is therefore necessary to be consistent with which two spots are chosen for the spot separation between the experiment and the simulation. This solves the pixel for pixel conversion problem between experiment and simulation.

## B.2.4 Look up table comparisons

In order to compare the ingausslookupxxx.dat files with the lookup tables, a separate directory containing the following files must be created: ingausslookuplist.dat,

gausslookup.c, grock004.dat, grock006.dat, grock024.dat, grock026.dat, grock044.dat, grock046.dat, and relintn.dat. Ingausslookuplist.dat contains the number of files to be analyzed by the lookup table and a list of the file names. The first line is the number of files to analyze. The next line, and every subsequent line, contains first a number, which represents the growth time at which the image was taken, and then the name of the ingausslookupxxx.dat to be analyzed. Gausslookup.c is the program that performs the comparison between the ingausslookupxxx.dat files and the values in the lookup tables. It compares the measurements contained in ingausslookupxxx.dat with the values from every lookup table entry and keeps a list of the 20 best matches, ranked by the accuracy of the match, and then uses a weighted average of these results (weighted by the accuracy of the match) to determine the out-of-plane orientation distribution ( $\Delta\omega$ ). The weighted averaging effectively interpolates between the table entries and provides a more accurate measurement than the discrete table entries allow (entries in the table for  $\Delta\omega$  are typically made for every 0.5 degrees). The lookup tables themselves are the grockxxx.dat files and how to create them will be described in great detail in the following section. A small section of grock024.dat is included below to demonstrate the general structure of the lookup tables.

```

h L   dw  dphi y   z   sep int   angle y       z       s       l       p       z/y  l/s  error
...
5.0 50  4.0 10.0 328 137 179 1362.87 63.43 0.1422 0.3831 0.2396 0.1616 0.2396 2.695 0.674 1.304
5.0 70  4.0 10.0 328 137 179 1397.49 63.43 0.1396 0.3828 0.2366 0.1588 0.2366 2.742 0.671 1.361
5.0 5  5.0 10.0 328 137 179 228.32 63.43 0.4197 0.3919 0.3870 0.4332 0.3870 0.934 1.119 0.107
5.0 6  5.0 10.0 328 137 179 298.79 63.43 0.3612 0.3904 0.3696 0.3835 0.3696 1.081 1.038 0.063
5.0 7  5.0 10.0 328 137 179 367.37 63.43 0.3216 0.3898 0.3560 0.3480 0.3560 1.212 0.978 0.093
5.0 8  5.0 10.0 328 137 179 431.93 63.43 0.2931 0.3892 0.3442 0.3214 0.3442 1.328 0.934 0.130
5.0 9  5.0 10.0 328 137 179 491.33 63.43 0.2719 0.3886 0.3340 0.3009 0.3340 1.430 0.901 0.168
5.0 10 5.0 10.0 328 137 179 545.16 63.43 0.2556 0.3881 0.3251 0.2848 0.3251 1.519 0.876 0.211
5.0 11 5.0 10.0 328 137 179 593.43 63.43 0.2428 0.3877 0.3176 0.2720 0.3176 1.596 0.857 0.246
5.0 12 5.0 10.0 328 137 179 636.44 63.43 0.2327 0.3872 0.3111 0.2617 0.3111 1.664 0.841 0.295
5.0 13 5.0 10.0 328 137 179 674.62 63.43 0.2245 0.3868 0.3055 0.2532 0.3055 1.723 0.829 0.328
5.0 14 5.0 10.0 328 137 179 708.45 63.43 0.2177 0.3865 0.3007 0.2462 0.3007 1.775 0.819 0.368
5.0 15 5.0 10.0 328 137 179 738.40 63.43 0.2121 0.3862 0.2966 0.2404 0.2966 1.821 0.810 0.397
5.0 16 5.0 10.0 328 137 179 764.93 63.43 0.2074 0.3859 0.2930 0.2354 0.2930 1.860 0.804 0.422
5.0 17 5.0 10.0 328 137 179 788.47 63.43 0.2035 0.3856 0.2898 0.2312 0.2898 1.895 0.798 0.445
5.0 18 5.0 10.0 328 137 179 809.39 63.43 0.2001 0.3854 0.2871 0.2276 0.2871 1.926 0.793 0.466
5.0 19 5.0 10.0 328 137 179 828.02 63.43 0.1972 0.3852 0.2847 0.2245 0.2847 1.954 0.789 0.506
5.0 20 5.0 10.0 328 137 179 844.65 63.43 0.1946 0.3850 0.2826 0.2219 0.2826 1.978 0.785 0.524
5.0 21 5.0 10.0 328 137 179 859.53 63.43 0.1924 0.3848 0.2808 0.2195 0.2808 2.000 0.782 0.540

```

```

5.0 22 5.0 10.0 328 137 179 872.87 63.43 0.1905 0.3847 0.2792 0.2174 0.2792 2.019 0.779 0.573
5.0 23 5.0 10.0 328 137 179 884.88 63.43 0.1888 0.3846 0.2777 0.2156 0.2777 2.037 0.777 0.587
5.0 24 5.0 10.0 328 137 179 895.70 63.43 0.1873 0.3844 0.2764 0.2140 0.2764 2.052 0.774 0.599
5.0 25 5.0 10.0 328 137 179 905.48 63.43 0.1860 0.3843 0.2752 0.2126 0.2752 2.066 0.773 0.611
5.0 27 5.0 10.0 328 137 179 922.40 63.43 0.1837 0.3841 0.2732 0.2102 0.2732 2.091 0.769 0.631
5.0 29 5.0 10.0 328 137 179 936.43 63.43 0.1819 0.3839 0.2715 0.2082 0.2715 2.111 0.767 0.648
5.0 31 5.0 10.0 328 137 179 948.17 63.43 0.1804 0.3838 0.2701 0.2066 0.2701 2.127 0.765 0.662
5.0 33 5.0 10.0 328 137 179 958.07 63.43 0.1792 0.3837 0.2690 0.2052 0.2690 2.142 0.763 0.674
5.0 35 5.0 10.0 328 137 179 966.50 63.43 0.1781 0.3836 0.2680 0.2041 0.2680 2.154 0.762 0.685
5.0 40 5.0 10.0 328 137 179 982.74 63.43 0.1761 0.3834 0.2661 0.2019 0.2661 2.177 0.759 0.705
5.0 45 5.0 10.0 328 137 179 994.21 63.43 0.1748 0.3833 0.2648 0.2005 0.2648 2.193 0.757 0.719
5.0 50 5.0 10.0 328 137 179 1002.59 63.43 0.1738 0.3832 0.2639 0.1994 0.2639 2.205 0.756 0.730
5.0 70 5.0 10.0 328 137 179 1020.58 63.43 0.1717 0.3829 0.2619 0.1971 0.2619 2.230 0.753 0.753
5.0 5 6.0 10.0 328 137 179 211.94 63.43 0.4342 0.3952 0.3881 0.4542 0.3881 0.910 1.171 0.129
5.0 6 6.0 10.0 328 137 179 272.12 63.43 0.3773 0.3929 0.3702 0.4054 0.3702 1.041 1.095 0.060
...

```

The relintn.dat file is somewhat of a relic from the process development; however, it may eventually become useful and so has not been eliminated. This is the lookup table for the relative spot intensities, meaning that it contains entries for the intensities of spots off of the (00) Bragg rod divided by the intensities of spots along the (00) Bragg rod. Early simulation results indicated that these relative intensities should be a function of the in-plane orientation distribution ( $\Delta\phi$ ). However, kinematical simulations are known to inaccurately calculate diffraction spot intensities so this measurement is inherently inaccurate. With future calibration between measurements from the relintn.dat lookup tables and rocking curves, it may make the values measured by relintn.dat usable for qualitative measurement of in-plane orientation distribution.

The results from gausslookup.c are printed in the file gausslayerout.dat. A sample of this file is included below.

```

time      h      L      dw  num  dwerror  dphi  dphierror
0.000    nan    nan    nan   0  0.0000   0.31   0.4408
4.120    nan    nan    nan   0  0.0000   9.49   0.6632
8.240   10.00   5.00  16.76  4  0.2591    nan  1000000000.0000
12.360   6.68   6.63   5.04  11  1.0133   8.69   0.6359
16.480   4.50  47.97  12.00  8  0.0482    nan  1000000000.0000
20.600   4.50  11.75   8.43  11  0.0692  19.00   0.0898
24.720   5.18  10.29   7.63  8  0.7208  18.58   0.0817
28.840   4.53  10.21   7.46  8  0.1356  16.95   0.0930
32.960   5.00  14.38   8.00  4  0.1484  16.11   0.0734
37.080   5.22   9.96   6.85  12  0.2578  13.36   0.0784
41.200   5.11  11.50   6.79  6  0.0187  12.26   0.0683
45.320   5.50   9.79   6.26  7  0.4683  10.48   0.0627

```

49.440	5.43	10.11	6.28	8	0.3904	10.00	0.0632
53.560	5.50	10.06	6.24	10	0.4193	9.61	0.0633
53.560	5.33	10.18	6.14	11	0.0432	10.00	0.0483

The first row labels all of the columns and each subsequent row is the measurement from an individual RHEED image. The first column, time, records the growth time of that image, the columns h, L, and dw are the measured effective electron penetration depth (nm), effective grain size (nm), and out-of-plane orientation distribution (FWHM degrees), respectively. Num indicates how many of the best matched entries from the look up table were used to determine the final microstructure parameters. The next column (dwerror) is an indication of how closely the experiment matched the best measured value in the lookup tables. The last two columns result from measurements from the relintn.dat lookup tables. The dphi column is the measurement for the in-plane orientation distribution ( $\Delta\phi$ ) and the dphierror indicates how well the experiment was represented by the best value in the lookup table. If the dwerror or the dphierror are much larger than normal then the accuracy of that measurement is in doubt because the measurement was not well represented by any explored simulation.

This example also shows the characteristic transition between images without clear diffraction spots during early growth and those with well defined diffraction spots. Before well defined spots appear, the simulation will report either that it found no solution at all (nan) with an error of  $10^9$  (the preset maximum error) or sequential images will produce randomly changing measurements – this results from analysis of very weak spots, where some are correctly analyzed and some are not. Images after the sixth image show stable trends in the development of h, L, dw and dphi. This corresponds with the regime where the diffraction spots are clearly visible and accurately measured by the program.

## B.2.5 Making new lookup tables

The previously described procedures require that lookup tables had already been created for the range of parameters that you are interested in. It is easy to recognize when the lookup tables do not cover the parameters needed because the list of lookup table matches will contain a large number of fits where the value is the extreme edge of a lookup table parameter. I have made a program which will create lookup tables for any cubic material. It is necessary to pick the two spots which will be used for the spot separation normalization (and to use the same spot separation for the experiments) as well as chose which spots to analyze and what order the spots will be analyzed in. This process must stay consistent throughout the analysis. The program can not recognize which spot is which, it must be specified. For MgO I have always used spots (004), (006), (024), (026), (044), and (046) as spots 1 through 6, in that particular order. The current code labels all spots using this convention, meaning that spot 1 is label (004), spot 2 is labeled (006), etc. This is also true for the names of lookup table files (grock004.dat, rockfwhm024.dat, etc.). When applying this program to other materials these may not be the diffraction spots that you are interested in analyzing. Unfortunately, the labels are well imbedded in the program so it is left to the user to label the diffraction spots as (004), (006), etc. and to remember what the actual diffraction spot index is for the each analyzed diffraction spot. The lookup table creation code is called `makegausslookup.c` (this code requires `nutil.h` to run). The input file, `inmakegausslookup.dat`, is included below.

```

12          lateral grain size
6           mean free path
0          0    phi and deltaphi
0          0    omegax and deltaomegax

```

```

0      0    omegay and deltaomegay
1.      overall normalization
180     distance between peaks (delta z)
1.75 0    angle of incidence(theta and phi)
25      energy in keV (lambda = 0.3877/(E^.5*(1+.9788e-3E)^.5)) (E
in keV) in A k=82.02 A^-1)
0.2     placement of y-center
0.15    placement of z-center
0        print to file?
.5      Step size
0        run one simulation, print result for testing (1=yes 0=no)
0        Start at specified values? (1=yes 0=no)
2.5 15  4    h (Low and high range for lookup table) and start value
5 50    10   L (Low and high range for lookup table) and start value
0 12    10   dw (Low and high range for lookup table) and start value
5 5     5    dphi (Low and high range for lookup table) and start value
8       Range of one side
4       Choose spot for spot separation calculations
0  -1     Y, Z thru spot location, fraction of spot sep from 1st spot
120 101   y,z first spot
120 289   y,z second spot
213 195   y,z third spot
307 101   y,z fourth spot
307 289   y,z fifth spot
401 195   y,z sixth spot
5 3.993 3.993 3.993    natombasis, simple cubic parameters (a,b,c)
0 0       inverse lattice reflections x
0 6       inverse lattice reflections y
-1 -5     inverse lattice reflections z
56 2 0 0 0  Z oxidation state, x,y,z
22 4 .5 .5 .5    Z oxidation state, x,y,z
8 -2 .5 .5 0     Z oxidation state, x,y,z
8 -2 .5 0 .5     Z oxidation state, x,y,z
8 -2 0 .5 .5     Z oxidation state, x,y,z

```

The following sections discuss the operation of each line of the input file in approximately the order that it appears in the input file.

### B.2.5.1 Unused inputs

The following lines are no longer used and originate in the code development: lateral grain size, mean free path, overall normalization, print to file, step size, range of one side.

### **B.2.5.2 Nominal orientation**

Biaxially textured films have a nominal orientation in the out-of-plane and in-plane directions around which the orientation distributions are centered. The three numbers for phi, omegax, and omegay specify the rotation of the nominal zone axis (in degrees) around the normal (z), x, and y axis respectively. The default is to have the [100] face in the x-direction (this is changed by a rotation around z by an angle phi) and to have the [001] direction face out-of-plane. The numbers for deltaphi, deltaomegax, and deltaomegay are superseded later and are irrelevant

### **B.2.5.3 Distance between peaks**

This number specifies, in pixels, the approximate distance desired between diffraction peaks in the simulation. In an experiment this is a function of the RHEED energy and distance between the substrate and the RHEED screen. This number was calibrated using MgO, such that it would produce the desired peak separation between the (004) and (024) spot at 25 keV (with a lattice constant of 4.2). This number will determine how many spots you can fit onto the simulated RHEED screen for analysis.

### **B.2.5.4 Angle of incidence**

This specifies the glancing angle between the incoming RHEED beam and the substrate surface. Typically this angle should be such that the specular reflection is between two rows of spots to minimize the contribution of the specular spot to diffraction spot intensities and ensure that there is strong diffraction from two rows of spots. The number for phi is redundant with the phi specifying the nominal crystal rotation and should not be used.

### **B.2.5.5 Energy**

This is the RHEED beam energy in keV. It is better to stay at high energies to minimize dynamical scattering. Experiments indicate that this method is more reliable at 25 keV than at 15 keV.

### **B.2.5.6 Placement**

The y-center and z-center numbers move the RHEED spots around on the screen. Y numbers will move the pattern laterally and the z number will move it vertically. This essentially changes which part of the pattern you are looking at, whether it is the center spots or more outlying spots. These numbers should be chosen such that the diffraction spots of interest are fully on the simulated RHEED screen. These numbers are typically between plus or minus one.

### **B.2.5.7 Test run**

Before running a loop of 10,000 plus RHEED images, it is necessary to verify that the program is creating and measuring the correct diffraction spots. By entering a 1 in this line it instructs the program to run only one simulation and print out the image to a file (intensity.dat). This allows the user to visually verify that the code is performing as expected. Normally the program will not print out the RHEED image to save computation time.

### **B.2.5.8 Parameter space settings**

The following five lines specify the range of the film microstructure characteristics that the RHEED code will generate lookup tables for. The program will

cycle through all possible permutations for effective electron penetration depth ( $h$ ), grain size ( $L$ ), out-of-plane orientation distribution ( $\Delta\omega$ ), and in-plane orientation distribution ( $\Delta\phi$ ). The range of each parameter is specified by the first two numbers on the corresponding line. The step size, the size between sequential iterations of a single parameter, varies from parameter to parameter. For  $h$ , the step size is 0.5 nm from 2.5 to 8.0 nm and 1.0 nm from 8.0 to 14.0 nm. For  $L$ , the step size is 0.5 nm from 5 to 15 nm, 1.0 nm from 15 to 25 nm, and 5 nm for grain sizes larger than 25 nm. The step size gradations were chosen to minimize computation time, while creating high-resolution in the look up tables in regions where the RHEED pattern changes rapidly as a function of  $h$  and  $L$  (small values of each). The step sizes for the out-of-plane ( $\Delta\omega$ ) and in-plane distributions ( $\Delta\phi$ ) are 0.5 degrees. The value of  $d\phi$  ( $\Delta\phi$ ) is set to 5 degrees in this file because diffraction spot shape is independent of the in-plane orientation distribution. To create a meaningful `relintn.dat` file it would be necessary to include a range for  $d\phi$  as well.

Before the settings for the parameter ranges there is a line requesting that the user specify if they would like to use a particular starting value in the ranges indicated. If this line is zero, then the program will run the simulation over the specified ranges. However, if a one is entered here, the program will initialize each parameter as the third number in each of the four lines. This is useful if the program was interrupted and it is desired to restart the lookup up tables at a certain point.

### **B.2.5.9 Specifying spot locations**

The first line indicates which spot is to be used to calibrate the spot separation distance. This program calculates the distance, in pixels, between the first diffraction

spot and the diffraction spot specified here. This is used to normalize the diffraction spot shapes and sizes with experimental results.

The program also requires the location of the non-diffracted, through spot so that it can decide what angles to cut the spots at. This is specified in the “Y and Z thru spot location” line in units of spot separation from the location of the first spot.

The next six lines are the pixel locations of spots 1 through 6. It is up to the user to determine (knowing the RHEED incidence angle, energy, and spot separation – previously specified) which spots are being shown on the screen, and subsequently which spots to call 1, 2, 3, etc.

#### **B.2.5.10 Building the crystal potential**

The remaining lines of the input file are reserved for constructing the crystal potential. These parameters are structured to create any cubic lattice using a simple cubic lattice with a basis. The first line contains the number of atoms in the basis, followed by the simple cubic lattice constant in the x, y, and z directions.

The next three lines specify the range of inverse lattice reflections which are to be included in the calculation. By changing the range and examining the RHEED pattern it is possible to verify which diffraction spots are present in the simulation. Only the required reflections should be calculated because extra reflections substantially increase the computation time.

The last five lines in this input file specify the atomic scattering factors for each atom and its basis location (in units of the simple cubic lattice parameters). The number of lines used here is equal to the number of atoms in the basis. The first number is the atoms atomic number and the second number is the oxidation state of the atom in the

lattice. These numbers are used to choose the correct atomic scattering factors from tables that must be provided with the code. The tables used with the code are from Table 2.2 B in the “International Tables for X-ray Crystallography”<sup>77</sup>. These tables contain numbers for a four Gaussian fit, as shown in Eq.(0.1), which will calculate the x-ray atomic scattering factor as a function of wave length ( $\lambda$ ) and scattering angle ( $\theta$ ).

$$f(\lambda^{-1} \sin \theta) = \sum_{i=1}^4 a_i \exp(-b_i \lambda^{-2} \sin^2 \theta) + c \quad (0.1)$$

The tables give  $a_i$ ,  $b_i$ , and  $c$  as a function of atomic number and oxidation state. The program has five different tables named ASF0.dat, ASF1.dat, ASF2.dat, ASF3.dat, ASF4.dat, which contain the  $a_i$ ,  $b_i$ , and  $c$  for different oxidation states (ASF $X$  stands for Atomic Scattering Factor and the oxidation state number). An example of one of these tables (ASF2.dat) is given below.

Z	a1	b1	a2	b2	a3	b3	a4	b4	c
12	3.49	2.16	3.83	4.75	1.32	0.18	0.84	10.14	0.485
8	3.28	20.46	3.21	7.18	1.89	96.0	-13.07	-.02	14.69
56	20.18	3.21	19.11	0.28	10.90	20.05	0.77	51.74	3.02
82	21.78	1.33	19.56	.488	19.14	6.77	7.01	23.81	12.47
-1	0	0	0	0	0	0	0	0	0

In this example the significant digits were truncated so that they will fit on the page, but in the program six significant digits are used for each parameter. The negative one, in the last line, signifies to the program that it is at the end of the table. Currently the tables contain very few entries; however, any material contained in the table can easily be added when needed. Oxygen, in the -2 oxidation state, was not present in Table 2.2 B<sup>77</sup>, so the oxygen parameters were obtained by fitting atomic scattering factors in Cullity<sup>78</sup>. The calculated atomic scattering factors are for x-rays. These are transformed to atomic scattering factors for electrons using the Mott Formula.

### **B.2.5.11 Lookup table making conclusion**

The input file provides an easy way to set up the creation of lookup tables for any cubic crystal where the x-ray atomic scattering factors are available. The program also offers the user the choice of the range of grain sizes, electron penetration depths, and out-of-plane orientations to consider. A typical lookup table contains about ten thousand entries and takes two to three days to create on a 700 MHz Pentium III. This time is greatly reduced by the ability to ignore effects of in-plane orientation distributions which show no large effect on the RHEED pattern diffraction spot shapes.

## **B.3 In-plane RHEED rocking curves**

While the single-image analysis method accurately determines the out-of-plane orientation distribution ( $\Delta\omega$ ), the in-plane orientation distribution ( $\Delta\phi$ ) is determined by in-plane RHEED rocking curves.

### **B.3.1 Experimental setup and procedure**

The growth position settings and the camera setup are identical to the specifications for the single-image analysis. The main difference between the single-image analysis and the in-plane RHEED rocking curve measurement is that a series of images at different  $\phi$  angles (the angle between the projection of the incoming electron beam in the plane of the substrate and the nominal [100] zone axis) must be taken for analysis. This is most easily accomplished by rotating the substrate around its normal axis, but could also be accomplished by rocking the RHEED beam back and forth electrostatically.

The method for obtaining in-plane orientation distribution is similar to the method used to get the out-of-plane orientation distribution. First the experimental images are analyzed by a program which creates an output file (in this case it contains the full width at half maximum – FWHM – of the rocking curves). This output file is run through lookup tables which determine the in-plane orientation distribution.

Performing an in-plane RHEED rocking curve analysis requires that all the RHEED images, already in the proper ascii text format (as described in the general procedures section), are contained in a directory with the following files: autorock.c (the c program), inautorock.dat (the input file that controls the program function), and nrutil.h (a standard c library file). The function of the program will be described by explaining how each line of the input file modifies the program's operation.

### B.3.2 Input file

The input file for the in-plane rocking curve analysis is very similar to the input file for the single-image analysis. An example of the input file inautorock.dat, set up for analyzing MgO, is included below.

```
Input file for autorock.c
110 3      spot separation guess (Spot from spot one used for
          separation)
512 512    Y pixel and Z pixel image size
0 005062.txt Use background? (0=No, 1=Yes) if 1 specify file.
1          adjust? (0=No, 1=Yes) (Subtract Background)
1          Make the background file (1= yes, 0 = No)
1          Shift background YZ? (1= yes, 0 = No)
1 4 -35    Manual shift Z? (1=yes,0=No) Manual Y,Z shift (exp-back)
0          Taylorfit background? (1=yes,0=No) only simple cubic
0          Reduce array size by 2? (1=yes, 0=No)
0 123 199  Set (004) position (0=No,1=Yes) y,z (004 position)
0 -2      Thru spot location, from Spot 1 (Y Z)
0 1        Spot 2 position (Relative to Spot 1)
1 0        Spot 3 position (Y,Z)
1 1        Spot 4 position (Y,Z)
2 0        Spot 5 position (Y,Z)
```

```

2      1      Spot 6 position (Y,Z)
0.5 0.5      Spot 1 and 2 background location (y)
0.5 0.5      Spot 3 and 4 as fraction of spot separation
0.5 0.5      Spot 5 and 6 ""
0.5          Z extension of background +-
6 -0.5 -0.5      Spot number of background for background intensity
                  matching (y,z in spot separation units)
2405062.txt file used to calibrate spot positions
0          Look at calibrated file only, ie no rock (0=No, 1=Yes)
0      1      Make movie(0=No, 1 = Yes), number of interpolated files
-25 30      range to use for (02x) rocking fit
-13 15      range to use for (04x) rocking fit
54          number of input files (list angle then file name)
-18.400    105062.txt
-16.356    205062.txt
-14.311    305062.txt
-12.267    405062.txt
-11.244    505062.txt
-10.222    605062.txt
-9.200     705062.txt
-8.178     805062.txt
-7.667     905062.txt
-7.156     1005062.txt
-6.644     1105062.txt
-6.133     1205062.txt
-5.622     1305062.txt
-5.111     1405062.txt
-4.600     1505062.txt
-4.089     1605062.txt
-3.578     1705062.txt
-3.067     1805062.txt
-2.556     1905062.txt
-2.044     2005062.txt
-1.533     2105062.txt
-1.022     2205062.txt
-0.511     2305062.txt
0.0000     2405062.txt
0.511      2505062.txt
1.022      2605062.txt
1.533      2705062.txt
2.044      2805062.txt
2.556      2905062.txt
3.067      3005062.txt
3.578      3105062.txt
4.089      3205062.txt
4.600      3305062.txt
5.111      3405062.txt
5.622      3505062.txt
6.133      3605062.txt
6.644      3705062.txt
7.156      3805062.txt
7.667      3905062.txt
8.178      4005062.txt
9.200      4105062.txt
10.222     4205062.txt
11.244     4305062.txt
12.267     4405062.txt

```

13.289	4505062.txt
14.311	4605062.txt
15.333	4705062.txt
16.356	4805062.txt
17.378	4905062.txt
18.400	5005062.txt
20.444	5105062.txt
22.489	5205062.txt
24.533	5305062.txt
26.578	5405062.txt

The following sections discuss the operation of each line of the input file in approximately the order that it appears in the input file.

### **B.3.2.1 Spot separation guess**

This is identical to the functionality for the single-image analysis program. (The comments from the single-image analysis will be repeated for continuity so that each section is independent). The computer program does not independently find the location of the diffraction spot, it requires input to guide the algorithm specifying where to search for the diffraction spots. The first number is an estimate of the diffraction spot separation distance (in pixels) from the first diffraction spot to the diffraction spot number listed as the second number. It is important for the diffraction spot separation distance to be reasonably close (within 10% or so) because the program uses this number to locate diffraction spots (with the help of input from further down in the input file). It is essential that the spot number used is consistent between the experimental files and the simulations. When diffraction spot widths are measured (experimentally or simulated), the widths are measured as a fraction of the spot separation. This allows for direct comparison between experiment and simulation without requiring careful calibration to ensure that the simulation pixels are the same size as the experimental camera pixels. For example, in MgO, the diffraction spot used is typically number 3, where number 1 is

(004), number 2 is (006), and number 3 is (024). When measuring diffraction spot widths, experiments can be directly compared to simulated spot widths because, for example, a diffraction spot width of 0.5 is half the distance, in pixels, between the (004) and (024) diffraction spots for both the simulation and experiments. Because the program was made for cubic materials, the distance between two adjacent, allowed reflection on the simple cubic lattice is a natural choice for a normalized distance.

### **B.3.2.2 Image size (pixels)**

These numbers specify the pixel size of the images in the horizontal direction ( $y$ , increasing from left to right) and the vertical direction ( $z$ , increasing from top to bottom). Any image size can theoretically be used; however, large images linearly reduce computation speed. The  $y$  and  $z$  directions are consistent throughout the code and were chosen to mimic the RHEED geometry, reflecting the fact that the RHEED image is a two dimensional diffraction image containing only spots where the miller indices contain  $h = 0$ .

### **B.3.2.3 Background subtraction settings**

The only crucial parameter for RHEED in-plane rocking curve measurements are the diffraction spot intensities. The background subtraction method for in-plane rocking curve analysis does not require the use of a diffuse RHEED image to preserve diffraction spot shapes. Background is subtracted by specifying the distance, in units of spot separation, in the  $y$  direction from each spot where there should be no crystal diffraction, taking the intensity of each side, and linearly interpolating between them to determine

what the background intensity should be underneath the diffraction spot. This method has the advantage of being fast and robust, while not requiring the difficult task of aligning a background image with the RHEED picture for each file. If extremely diffuse diffraction spots are present, or if the diffraction spots are closely spaced, then the diffraction intensity may not approach zero between diffraction spots, making this background subtraction method inaccurate. Fortunately this is not usually an issue; however, care should be taken to ensure that the diffraction intensity does approach zero at the specified background locations.

The background subtraction settings specified in the input file only determines the method for background subtracting of the RHEED image where  $\phi$  (the angle between the nominal [100] zone axis and the incoming electron beam) is zero. This file is used to perform a spot shape fitting algorithm identical to the one used for the layer by layer growth measurements. This avoids the need to use two programs to get the full biaxial texture. The output file (ingausslookup.dat) contains all the information necessary to run it through the lookup tables in the gausslookup.c program for a measurement of grain size (L), effective electron penetration depth (h), and out-of-plane orientation distribution ( $\Delta\omega$ ).

If the background is not used for subtraction, then the program will use the background subtraction method used for every other file, which is to draw a line between the diffraction spots, take the intensity of the RHEED images at those lines and linearly interpolate to estimate the background underneath the diffraction spots. The location of the background line is specified in the input file line labeled “background location y” and the following two lines. The numbers specify the displacement in the y axis, in both the

positive and negative y directions, from each diffraction spot, in units of diffraction spot separation, where the “background” should be zero. The following line specifies how far above and below the center of each spot this background subtraction should be executed (in units of spot separation).

If the background file is to be used, this is indicated on the line labeled “Use background?” and the file to be used is also specified. Several other lines are used to control the treatment of the background. The actual file used in the program for background subtraction is called “newback.dat”, regardless of what is specified above. The line labeled “Make the background file”, controls whether a new background file is made from the file specified above (enter a 1) or whether a previously created “newback.dat” file will be used and the file above be ignored (enter a 0).

Once the background file is chosen, it is necessary to align the background file with the RHEED image. If position matching is allowed (enter a 1 in the “Shift background YZ” line), the program matches the background with the experiment by matching the maximum intensities of the two files along the y direction and by matching the z position of the substrate shadow in both images. While the y matching is quite simple and reliable, it is difficult to reliably locate the shadow edge of the substrate. Entering a 0 on this line will force the program to subtract the background without attempting to align the two files.

Another option for aligning the background file with the RHEED image is to do it manually. Whether or not automatic background matching has been successful can be determined by looking at the background subtracted images. If there is a large negative region around the top diffraction spots then the background position is too high in the z

direction (high visually, but the center is shifted too far toward the zero z pixel). If there is a large positive intensity region around the top diffraction spots then the background position is too low in the z direction (low visually, the center is shifted too far toward the z maximum pixel). This issue can be resolved, albeit painstakingly, by manually setting the number of pixels the background shifts in the z direction. In the “Manual shift Z?” line a 0 directs the manual background shifting functions to be ignored and a 1 directs the program to perform the manual background shifting operation. If manual background shifting is specified, results from the automatic algorithm will be ignored and the background will be shifted in the y and z direction the number of pixels indicated by the last two numbers in this line.

Once the background is aligned with the RHEED image file, it must be scaled so that the diffuse intensity of the background file matches the diffuse intensity of the RHEED image. The line labeled “Spot number of background...” determines the location where the intensity of the background file is scaled to match the intensity of the RHEED image. This should be a location between diffraction spots where only diffuse background is present. The first number indicates which spot will be the base for the background normalization location. The next two numbers specify an offset from the diffraction spot location, in units of spot separation, where the comparison between the background file and the RHEED experiment intensity will occur.

A final choice for modifying the background subtraction is presented in the line labeled “Taylor fit background?” This process was developed specifically for MgO and should not be used unless the diffraction pattern resembles a simple cubic [100] structure. The background file shape never perfectly matches the shape of the RHEED image

background. If this option is chosen, a Taylor expansion of the error between the background and the RHEED intensity is used to correct the background image. Lines are cut vertically across the RHEED image in the middle between Bragg rods where no diffraction should be occurring and should therefore be zero. At every pixel along this line the difference between the background and the RHEED image is recorded (as the error – because the background should subtract this to zero). The error of the background at every other point is determined by horizontally taking a second order Taylor expansion of the error. The background is finally modified by subtracting the error from the background at every point before it is subtracted from the RHEED image. This method is attractive because it reliably subtracts the background between spots to zero; however, there is concern that it artificially truncates the width of the diffraction spots if they are wide compared to the spot separation and run into the area where this method assumes there is no diffraction. This method has not been used in the experiments used to verify the validity of RHEED measurements; however, for narrow diffraction spots this method is stable and could still prove to be reliable. In this circumstance it should still be evaluated.

If a 0 is entered in the “adjust?” line, then no background subtraction of any kind or analysis of diffraction spot shape would be performed. Entering a 0 in the “adjust?” line is desirable when one wants to get a first order approximation of where the diffraction spots are and the program has not successfully found diffraction spot locations automatically.

### **B.3.2.4 Reduce array size by 2**

The computational analysis time scales linearly with the number of pixels. If the images are large, or there are a lot of images, then to reduce computation time the number of pixels can be reduced by a factor of 4. The program will take four adjacent pixels and collapse them into a single pixel containing the average value of the original 4 pixels.

### **B.3.2.5 Diffraction spot locations**

As previously stated, the program attempts to find and verify the position of diffraction spots by seeking for local maxima. This effort is typically unsuccessful if for some reason the (006) diffraction spot is more intense than the (004) spot – this usually results from an error in the RHEED incidence angle or if the [001] axis is tilted. In the line “Set (004) position ..”, one can manually specify the position of the (004) diffraction spot (or spot number 1 for any material besides MgO). The program will assume that the first diffraction spot is located at the manually input y and z values (the second and third numbers respectively), but will also do a limited local search for the absolute maximum. After forcing the computer to choose a certain location for the (004) diffraction spot, it is easy to verify that this was in fact the local maximum by watching the output of the program for the final location chosen by the limited search for a local maximum. If this is not the same as the chosen value, the new value should be chosen until the next iteration produces no small change in the chosen location of the (004) maximum.

The numbers in the “Thru spot location...” line specify, in units of spot separation, the location of the non-diffracted electron beam with respect to the first spot (spot (004) for MgO). The first number is the offset in the y direction and the second

number is the offset in the z direction. The location of the through spot is necessary because the program uses the location of the through spot, with respect to the location of each diffraction spot, to determine the direction to cut the spot perpendicular to the through spot (which is the direction most dependent on the out-of-plane orientation distribution). This is only done on the file with a specified  $\phi$  angle equal to zero.

The next five lines tell the computer where to look for local maxima to find the location of five more diffraction spots, spots 2 through 6. The first numbers are the offset from the first diffraction spot, in units of spot separation, in the y direction and the second numbers are the offset from the first diffraction spot in the z direction.

### **B.3.2.6 Calibration file**

This should be a RHEED image where  $\phi$  is zero because diffraction spots will move slightly and disappear during the in-plane rocking curve. The program will use this image to determine where the diffraction spots should be and will look for them in this location even when they are not present at large  $\phi$  angles.

The line labeled “Look at calibrated ...” can be used to avoid performing a rocking curve and allow the user an opportunity to verify that the program properly located the diffraction spots. A 1 on this line will instruct the program to only look at the calibration file and print out the image as “aintn.dat” (this is the file with the background subtracted out).

### **B.3.2.7 Make movie?**

This line controls functions that format the output image files so that they can easily be imported into Quicktime to make movies of RHEED during IBAD growth. The

first number controls whether or not the files are reformatted so that they are importable into Quicktime. This algorithm rotates the pictures and rescales the intensity values so that they can be converted into .png files using matlab (which will then be imported into Quicktime). The second number indicates how many extra frames should be interpolated between the data points. In our setup, RHEED images are taken every 0.5 to 1 degree. Extra images can help a movie to look smoother. For artistic effect, extra frames can be added by interpolating the value of each individual pixel between actual images to make smooth transitions from image to image. The second number determines how many extra images are added.

### **B.3.2.8 Rocking curve range**

Once the in-plane angle  $\phi$  gets large ( $>12$  degrees), the original diffraction spots present at  $\phi$  equal to zero can start to disappear and be replaced by diffraction spots outside of the zeroth order Laue zone. These diffraction spots often appear in approximately the same place as the original diffraction spots and the computer can not tell the difference. Sometimes the in-plane rocking curve will reach a minimum at some angle  $\phi$ , and then start to increase again because of contributions from a diffraction spot that we are not trying to measure. This is particularly true for the (04) Bragg rod reflections. For broad in-plane textured MgO, the (244) diffraction spot can dominate the (044) rocking curve when  $\phi$  is greater than 15 degrees (or less than -15 degrees). The lines labeled “range to use for (02x)/(04x) rocking fit” are the limits for the angle  $\phi$  used by the computer when measuring the FWHM of the rocking curve. A RHEED image taken with the  $\phi$  angle outside of the specified range will not be included in the rocking

curve for the respective (02) or (04) Bragg rods. The interference from higher order Laue zones happens earlier for the (04) Bragg rods than for the (02) Bragg rods so the included angles for the rocking curve are typically narrower.

### **B.3.2.9 Input files**

The rocking curve RHEED images are specified in the list at the end of the input file. To the left of each file name is the in-plane rotation angle  $\phi$  at which that particular file was taken. To cover a wide range of angles  $\phi$ , save hard drive space, and resolve narrow in-plane rocking curves, it is generally desirable to use different step sizes for the in-plane rotation angle  $\phi$ , depending on how close or far the files are from  $\phi$  equal to zero. For the rocking curve tails it is sufficient to record images for every 2 degrees of  $\phi$ , while near the center,  $\phi$  step sizes of 0.5 degrees are more appropriate. This has the added advantage of giving larger weighted value to the center of the curve in a fitting routine than to the tails.

The number above the list of rocking curve images, in the line labeled “number of input files”, specifies how many input files the program should look for.

### **B.3.3 Output files**

The program creates files for the in-plane rocking curve lookup tables, verification that the program is working, and RHEED image files that will show the change in the RHEED images as a function of the rocking angle  $\phi$ .

### B.3.3.1 Rocking curve verification

There are several files that the RHEED code creates to allow the user to visually verify that the rocking curve program functioned properly. The most basic files are the `intn.dat` and `aintn.dat` files which are respectively the original and background subtracted image files of the RHEED pattern for the  $\phi$  equal to zero case. These are viewed in matlab by typing: `load aintn.dat <enter> mesh(aintn) <enter> view(90,90) <enter>`. This provides a 2 dimensional, color map display of the background subtracted RHEED intensity.

The program outputs files designed to be plotted in matlab to verify the accuracy of the rocking curve analysis. These files contain space delineated lists of numbers, each number coming from a different RHEED image, in the order that the images were examined. There is one file for each diffraction spot. For MgO, which is the example used here, the diffraction spots are (024), (026), (044), and (046). For other materials, using different diffraction spots, these can just be interpreted as spots 3, 4, 5, and 6. The first two diffraction spots are the spots along the (00) Bragg rod and do not yield information about the in-plane orientation distribution. The file names (where 000 represents where the 024, 026, 044, or 046 should specify which diffraction spot the file is for) are as follows, containing the information described: `x000.dat` – a list of the angle  $\phi$ , `y000.dat` - the y-pixel location of the diffraction spot, `z000.dat` – the z-pixel location of the diffraction spot, `intn000.dat` – the maximum intensity of the diffraction spot, `fit000.dat` – the intensity of the Gaussian fit to the spot intensity, `mback000.dat` – the intensity of the background on the negative y side of the diffraction spot, and `pback000.dat` – the intensity of the background on the positive y side of the diffraction

spot. These files can be graphed intelligibly using the matlab meta file included below called “plotrock.m”.

```
%Plotting matlab results to rocking curves
load x024.dat
load fit024.dat
load intn024.dat
load mback024.dat
load pback024.dat
load y024.dat
load z024.dat
load x026.dat
load fit026.dat
load intn026.dat
load mback026.dat
load pback026.dat
load y026.dat
load z026.dat
load x044.dat
load fit044.dat
load intn044.dat
load mback044.dat
load pback044.dat
load y044.dat
load z044.dat
load x046.dat
load fit046.dat
load intn046.dat
load mback046.dat
load pback046.dat
load y046.dat
load z046.dat

figure(1)
plot(x024,fit024,x024,intn024,x026,fit026,x026,intn026)
legend('fit024','intn024','fit026','intn026')
figure(2)
plot(x044,fit044,x044,intn044,x046,fit046,x046,intn046)
legend('fit044','intn044','fit046','intn046')
figure(3)
plot(x024,z024,x044,z044)
legend('z024','z044')
figure(4)
plot(x026,z026,x046,z046)
legend('z026','z046')
figure(5)
plot(x024,y024,x044,y044)
legend('y024','y044')
figure(6)
plot(x026,y026,x046,y046)
legend('y026','y046')
figure(7)
plot(x024,mback024+pback024,x026,mback026+pback026,x044,mback044+pback044,x046,mback046+pback046)
```

```

legend('024','026','044','046')
figure(8)
load cspot.dat
mesh(cspot)
view(90,90)

```

Plotrock.m creates 8 figures, most important of which are Figures 8, 3, 2, and 1. Figure 8, included here as Figure B.1, prints out the background subtracted RHEED image with spots indicating where the program believes the center of the diffraction spots are located. Looking at this figure verifies that the program chose the correct diffraction spots and successfully found the maximum intensity. Figure 3, included here as Figure B.2, is a plot of the z-pixel location of diffraction spots (024) and (044) as a function of the angle  $\phi$  (in degrees). Notice that the (024) z-location migrates slowly as the sample is

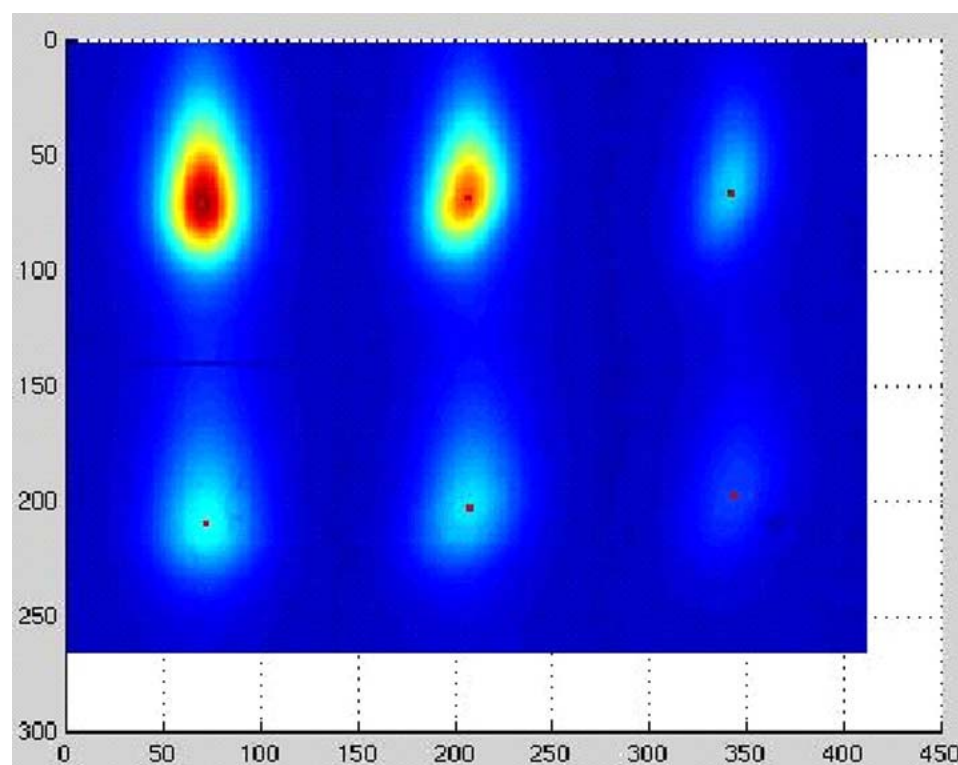


Figure B.1 Plotrock.m Figure 8. Color map output of the diffraction spots, with an additional spot (red) indicating where the program has determined the center of the diffraction spots to be located. This figure is used to assure that the program has successfully identified the desired RHEED spots.

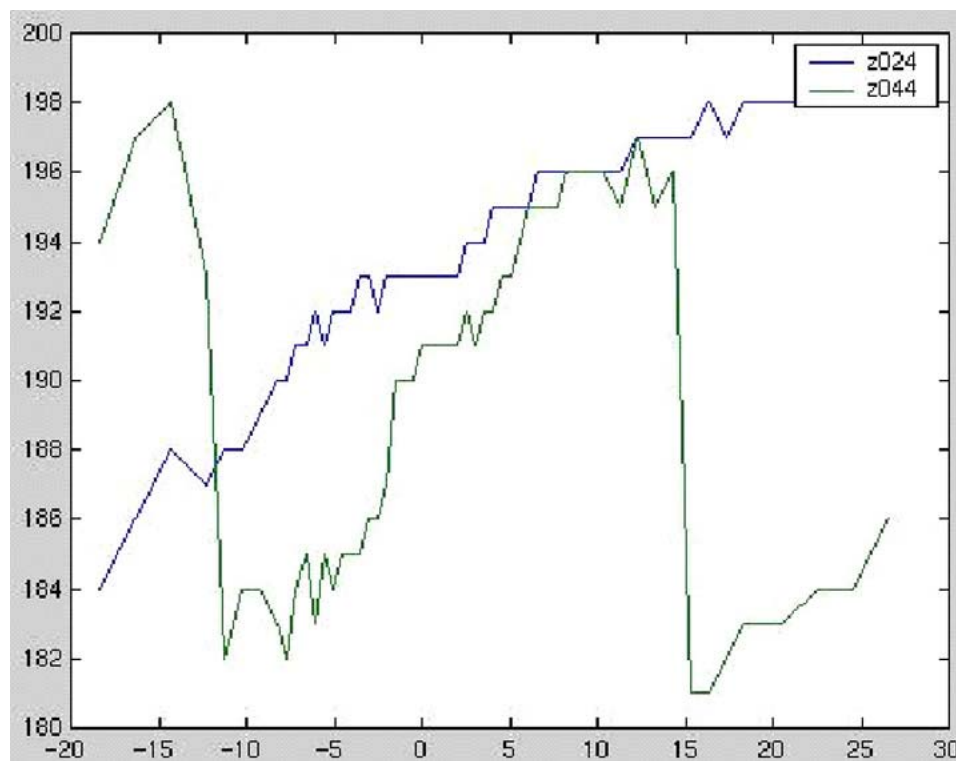


Figure B.2 Plotrock.m Figure 3. The  $z$  pixel locations (ordinate) of the MgO (024) and (044) diffraction spots are plotted as a function of the sample rotation angle  $\phi$  (abscissa). rotated, while there are abrupt jumps in the location of the (044) spot at  $\phi = -12^\circ$  and  $13^\circ$ . The discontinuities in the (044)  $z$ -location correspond to transitions between the RHEED intensity in this area being dominated by the (044) and the (244) diffraction spots.

The in-plane rocking curve for the (044), as well as the (046), diffraction spot is included as Figure B.3 (this is figure 2 in the plotrock.m file). At the point where the  $z$ -pixel location shifts in Figure B.2, the rocking curve intensity increases instead of decreasing as the (044) diffraction spot is rotated away from the diffraction condition. This is additional evidence that the (244) diffraction spot is contributing to the intensity of the rocking curve. Therefore, to get an accurate fit to the (044) diffraction spot rocking curve, the user should instruct the program to ignore rocking curve data for angles  $\phi$  where the (244) diffraction spot contributes to the rocking curve intensity. This

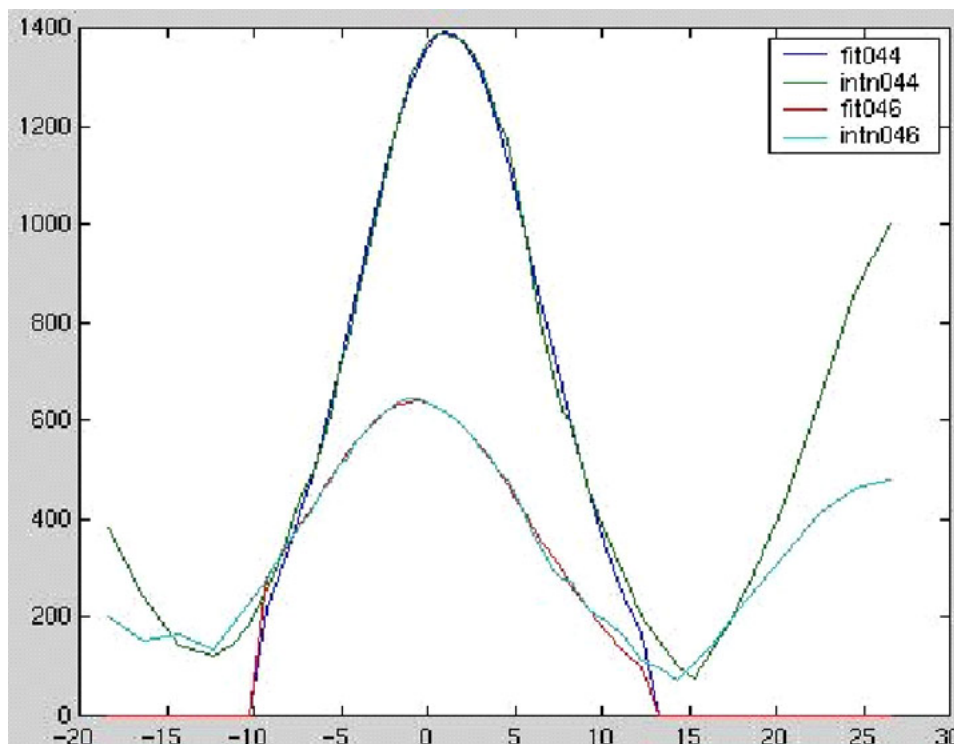


Figure B.3 Plotrock.m Figure 2. In-plane RHEED rocking curve for diffraction spots (044) and (046). The ordinate is the diffraction spot intensity and the abscissa is the rotation angle  $\phi$  (degrees). Gaussian fits to the rocking curves are also plotted.

is done by specifying the rocking curve range in the input file (inautorock.dat). Figure B.3 also contains the Gaussian fit to the in-plane rocking curves so that the user can visually verify that a good fit has been obtained. The fit cuts off abruptly at the specified rocking curve range limits, showing that only data which was dominated by intensity contributions from the (044), and not the (244) diffraction spot, was considered.

Figure B.4 shows the in-plane rocking curves for the (024) and (026) diffraction spots, as well as the Gaussian fits to the rocking curves. The (024) rocking curve is well fit by a Gaussian, however, the rocking curve for the (026) diffraction spot often exhibits the bimodal shape shown in Figure B.4. This does not allow for a good fit to the rocking curve making it necessary to ignore the FWHM from this curve in the lookup tables. A bimodal shape would originate from a film with two preferred out-of-plane orientations,

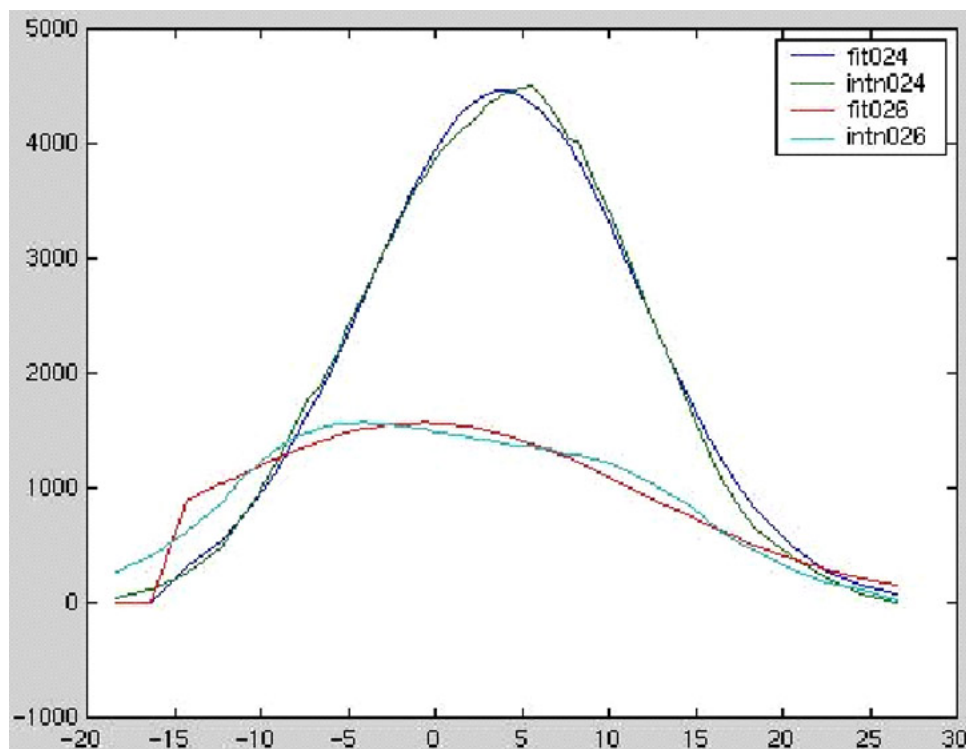


Figure B.4 Plotrock.m Figure 1. In-plane RHEED rocking curve for diffraction spots (024) and (026). The ordinate is the diffraction spot intensity and the abscissa is the rotation angle  $\phi$  (degrees). Gaussian fits to the rocking curves are also plotted.

but this would be reflected in rocking curves from all diffraction spots, which is not observed. The poor Gaussian fit to the (026) in-plane rocking curve indicates that it should not be considered in the lookup tables.

### B.3.3.2 Inlookup.dat – the lookup table file

The main function of the program is to create “inlookup.dat”. This is the input file for the RHEED in-plane rocking curve lookup tables. An example of this file is included below.

```
Rocking curve from:
18.57751 29.81274 12.70861 15.69326
0.06655 0.28850 0.03583 0.02357
1 1 1 1
Llow Lhigh Dwlow Dwhigh
```

```
0      50      0      20
5.51  10.41  4.61  11.71
```

The first line of numbers are the FWHM of the Gaussian fits to the rocking curves from the diffraction spot numbers 3, 4, 5, and 6, respectively (the (024), (026), (044), and (046) diffraction spots in the case of MgO). Below each number is a normalized chi squared error of the rocking curve fit. Note that the error for the (026) rocking curve is much larger than for the others. This indicates that the (026) rocking curve was not well represented by a Gaussian. These are actually the results from the rocking curves and fits printed in Figure B.3 and Figure B.4. The next line is a series of four 1s which tell the lookup table program whether or not (1 or 0 respectively) to use the corresponding FWHM to determine in-plane orientation distribution. In this case the (026) rocking curve is not well fit by a Gaussian, so if the user decided to ignore the (026) FWHM in the lookup tables this would be done by changing the second 1 to a 0.

Before comparing the experimental rocking curves with the lookup tables, the single-image analysis method should be performed to determine the grain size ( $L$ ) and out-of-plane orientation distribution ( $\Delta\omega$ ). The `autorock.c` program creates the “`ingausslookup.dat`” file for comparison with the single-image analysis lookup tables to measure grain size ( $L$ ) and out-of-plane orientation distribution ( $\Delta\omega$ ). The measured grain size and out-of-plane orientation distribution are then used to narrow the search for the in-plane orientation distribution in the lookup tables by excluding from comparison with “`inlookup.dat`” any entries with grain size or out-of-plane orientation distribution not close to the measured values. The range of grain sizes and out-of-plane orientation distributions that will be included in the search for the in-plane orientation distribution are entered in the corresponding locations labeled “`Llow`” (value that grain size  $L$  must be

greater than – *not* equal to – to be considered), “Lhigh” (value that grain size  $L$  must be smaller than – *not* equal to – to be considered), “Dwlow” (value that out-of-plane orientation distribution  $\Delta\omega$  must be greater than – *not* equal to – to be considered), and “Dwhigh” (value that out-of-plane orientation distribution  $\Delta\omega$  must be smaller than – *not* equal to – to be considered).

The last line read by the in-plane rocking curve lookup table program is the line containing the limits for grain size and out-of-plane orientation distribution; however, it is useful to include the measurements from the single-image analysis at the end of the file, as they are in the example. These numbers represent the electron penetration depth ( $h$ ), grain size ( $L$ ), out-of-plane orientation distribution ( $\Delta\omega$ ), and in-plane orientation distribution ( $\Delta\phi$  - measured using the relintn.dat lookup table), respectively. These numbers are then easily accessible when choosing the allowed range of grain size ( $L$ ) and out-of-plane orientation distribution ( $\Delta\omega$ ).

### **B.3.4 Look up table comparisons**

In-plane orientation distribution is determined by comparing the FWHM of the four rocking curves of inlookup.dat with the FWHM of simulated rocking curves in the lookup tables. Running inlookup.dat through the lookup tables requires that a directory be created containing the following files: inlookup.dat, rocklookup.c, rockfwhm024.dat, rockfwhm026.dat, rockfwhm044.dat, and rockfwhm046.dat. Rocklookup.c is the program that controls the lookup table search by limiting the search to the grain size and out-of-plane orientation distribution specified in inlookup.dat and by recording the lookup table entries that best fit the input file FWHMs. The lookup tables for diffraction

spots (024), (026), (044), and (046) are contained in the files rockfwhm000.dat (where 000 is 024, 026, 044, and 046 respectively). These files list the FWHM of the respective diffraction spot rocking curve as a function of grain size, out-of-plane orientation distribution, and in-plane orientation distribution. An example from a section of rockfwhm024.dat is included as an example of the structure of the lookup table.

FWHM Lookup table for the 024 spot, 25 keV, 2.6 degrees incident angle

```
L h Domega Dphi fwhm error
...
50.0 5.0 5.5 27.0 28.8250 879.9478
50.0 5.0 5.5 27.5 29.2744 841.4863
50.0 5.0 5.5 28.0 29.7248 805.2410
50.0 5.0 5.5 28.5 30.1760 771.0790
50.0 5.0 5.5 29.0 30.6283 740.3630
50.0 5.0 5.5 29.5 31.0815 712.0455
50.0 5.0 5.5 30.0 31.5358 685.5978
5.0 5.0 6.0 0.0 25.2809 155.8602
5.0 5.0 6.0 0.5 25.2857 155.3968
5.0 5.0 6.0 1.0 25.3000 154.0123
5.0 5.0 6.0 1.5 25.3239 151.7245
5.0 5.0 6.0 2.0 25.3573 148.7619
5.0 5.0 6.0 2.5 25.4002 145.1249
5.0 5.0 6.0 3.0 25.4526 140.8058
5.0 5.0 6.0 3.5 25.5143 135.9273
5.0 5.0 6.0 4.0 25.5854 130.6485
5.0 5.0 6.0 4.5 25.6657 124.7025
5.0 5.0 6.0 5.0 25.7552 118.2132
5.0 5.0 6.0 5.5 25.8536 111.3949
5.0 5.0 6.0 6.0 25.9611 104.1039
5.0 5.0 6.0 6.5 26.0774 96.5857
5.0 5.0 6.0 7.0 26.2022 88.9319
5.0 5.0 6.0 7.5 26.3356 81.2582
...
```

Rocklookup.c keeps a list of the twenty best simulated matches to the experimental data and ranks them according to the error between the simulation and the experimental rocking curves. In order to try and interpolate between the finite step sizes of the lookup tables (in-plane orientation distribution entries exist for every 0.5 degree FWHM step) an average of the best fits, weighted by the error between the simulated and the experimental rocking curves, is taken to refine the in-plane orientation distribution

measurement. The program also prints to the screen the list of the twenty best matches, along with the contribution to the matching error from each diffraction spot. Sometimes the (026) diffraction spot accounts for 90 percent of the total fitting error. This often results from the bimodality of the (026) rocking curve, which creates an artificially broad FWHM rocking curve measurement. In these situations the (026) rocking curve should be ignored and the results from a best fit to the three other rocking curves should be accepted.

### **B.3.5 Making new lookup tables**

Creating lookup tables for in-plane rocking curves follows much the same procedure as creating lookup tables for single-image analysis. The process begins with creating a directory with the lookup table fabrication program `rockfast.c`, the input file `inrockfast.dat`, atomic scattering factor files `ASF0.dat`, `ASF1.dat`, `ASF2.dat`, `ASF3.dat`, `ASF4.dat`, the c programming library file `nutil.h`, and `rockout.c` ( a file which modifies the output of `rockfast.c` to make the actual in-plane rocking curve tables. The functionality of `rockfast.c` is best explained by describing the operation and control of its operation afforded the user through the input file `infastrock.dat`. Because creating in-plane simulated RHEED rocking curve lookup tables is similar to creating lookup tables for single-image analysis, the rocking curve program requires much of the same set up as the single-image analysis program. Therefore, much of the information concerning setting up the input file will be similar to previous information about the single-image analysis lookup table input file. This information has been included again here so that this section will be autonomous.

### B.3.5.1 Input file infastrock.dat

The input file for rockfast.c is included below.

```

12          lateral grain size
6           mean free path
0          0    phi and deltaphi
0          0    omegax and deltaomegax
0          0    omegay and deltaomegay
1.         overall normalization
180        distance between peaks (delta z)
1.75 0     angle of incidence (theta and phi)
25         energy in keV
.2         placement of y-center
0.15      placement of z-center
15        Range of one side
1         Step size
0 0       Only run one simulation and print result for testing (1=yes
0=no) (Angle Phi to print)
0         Start at specified values (using specified ranges)? (1=yes
0=no)
5 5       5    h (Low and high range for lookup table) and start value
5 50     25    L (Low and high range for lookup table) and start value
0 11.5   5    dw (Low and high range for lookup table) and start value
0 20     5    dphi (Low and high range for lookup table) and start value
5 20     Spot Size - calculated area around spots(even) (Min and Max
allowable)
5 0      ZSpotSize + let z size expand with ysize?(1=yes, 0=no)
120 101   y,z first spot
120 289   y,z second spot
213 195   y,z third spot
307 101   y,z fourth spot
307 288   y,z fifth spot
401 195   y,z sixth spot
5 3.993 3.993 3.993    natombasis, simple cubic parameters (a,b,c)
0 -0      inverse lattice reflections x
0 6       inverse lattice reflections y
-1 -5     inverse lattice reflections z
56 2 0 0 0  Z oxidationstate, x,y,z
22 4 .5 .5 .5    Z oxidation state, x,y,z
8 -2 .5 .5 0    Z oxidation state, x,y,z
8 -2 .5 0 .5    Z oxidation state, x,y,z
8 -2 0 .5 .5    Z oxidation state, x,y,z

```

### B.3.5.2 Unused inputs

The following lines are no longer used and originate in the code development:

lateral grain size, mean free path, overall normalization.

### **B.3.5.3 Nominal orientation**

Biaxially textured films have a nominal orientation in the out-of-plane and in-plane directions around which the orientation distributions are centered. The three numbers for phi, omegax, and omegay specify the rotation of the nominal zone axis (in degrees) around the normal (z), x, and y axes, respectively. The default is to have the [100] face in the x-direction (this is changed by a rotation around the z axis by an angle  $\phi$ ) and to have the [001] direction face out-of-plane. The numbers for deltaphi, deltaomegax, and deltaomegay are superseded by later entries in the input file and are irrelevant

### **B.3.5.4 Distance between peaks**

This number specifies in pixels the approximate distance desired between diffraction peaks in the simulation. In an experiment this is a function of the RHEED energy and distance between the substrate and the RHEED screen. This number was calibrated using MgO, such that it would produce the desired peak separation between the (004) and (024) spot at 25 keV (with a lattice constant of 4.2). This number will determine how many spots fit onto the simulated RHEED screen for analysis.

### **B.3.5.5 Angle of incidence**

This specifies the glancing angle between the incoming RHEED beam and the substrate surface. Typically this angle should be such that the specular reflection is between two rows of spots so that the specular spot does not contribute to the experimental intensity of any spots and so that there is strong diffraction from two rows

of spots. The number for phi is redundant with the phi specifying the nominal crystal rotation and should not be used.

### **B.3.5.6 Energy**

This is the RHEED beam energy in keV. It is better to stay at high energies to minimize dynamical scattering. Experiments indicate that this method is more reliable at 25 keV than at 15 keV.

### **B.3.5.7 Placement**

The y-center and z-center numbers move the RHEED spots around on the simulated RHEED screen. Y numbers will move the pattern laterally and the z number will move it vertically. This essentially changes which part of the pattern is included on the screen, whether it is the center spots or more outlying spots. These numbers should be chosen such that the diffraction spots of interest are fully on the screen. Typical numbers are between plus and minus one.

### **B.3.5.8 Rocking curve settings**

The maximum angle  $\phi$  used in the simulated rocking curve is specified by the number in “Range of one side”. This number dictates how many degrees, in  $\phi$ , the simulation rocks the sample in both the positive and negative direction. The change in  $\phi$  (degrees) from simulation to simulation is specified by the number in the “Step size” line. The rocking curve starts at  $\phi$  equal to the negative “Range of one side” and the program records diffraction spot intensities for every “Step size” increment of the angle  $\phi$  until positive  $\phi$  is equal to or exceeds the “Range of one side”.

### **B.3.5.9 Test run**

Before running a loop of 10,000 plus RHEED images, it is necessary to verify that the program is creating and measuring the correct diffraction spots. By entering a 1 in this line it instructs the program to run only one simulated rocking curve. The additional number on this line instructs the program for which angle  $\phi$  of the rocking curve it should print out the image. This allows the user to visually verify that the code is performing as expected. Normally the program will not print out any RHEED images to save computation time.

### **B.3.5.10 Parameter space settings**

The following five lines specify the range of the film microstructure characteristics that the RHEED code will generate lookup tables for. The program will cycle through all possible permutations for effective electron penetration depth ( $h$ ), grain size ( $L$ ), out-of-plane orientation distribution ( $\Delta\omega$ ), and in-plane orientation distribution ( $\Delta\phi$ ). We have shown that the effective electron penetration depth ( $h$ ) has little or no effect on the in-plane rocking curves and so this parameter is typically set to 5 nm, which is a common  $h$  measurement for IBAD MgO from single-image analysis. The range over which each parameter is varied is specified by the first two numbers on the corresponding lines. The step size, the size between sequential iterations of a single parameter, varies from parameter to parameter. For  $L$ , the step size is 0.5 nm from 5 to 15 nm, 1.0 nm from 15 to 25 nm, and 5 nm for grain size larger than 25 nm. The step size gradations were chosen to minimize computation time, while creating high-resolution in the look up tables in regions where the RHEED pattern changes rapidly as a function of  $L$  (small

values of grain size). The step sizes for the out-of-plane and in-plane distributions are 0.5 degrees.

Before the settings for the parameter ranges there is a line requesting that the user specify if they would like to use a particular starting value in the ranges indicated. If this line is 0, then the program will run the simulation over the specified ranges. However, if a 1 is entered here, the program will initialize each parameter as the third number in each of the four lines. This is useful if the program was interrupted and it is desired to restart the lookup up tables at a certain point.

### **B.3.5.11 Diffraction spot size**

The computational time scales directly with the number of pixels included in each RHEED simulation. Lookup tables for single-image analysis include ~10,000 entries; but these same 10,000 entries require 31 calculated RHEED patterns per entry for in-plane rocking curves (this assumes a rocking curve range of  $\pm 15^\circ$  and  $\phi$  step size of  $1^\circ$ ). The time required to calculate a comprehensive in-plane rocking curve lookup table can become prohibitive. The only important data in the simulated RHEED pattern is the maximum intensity of the six diffraction spots. Therefore computation time can be greatly reduced by instructing the program to only calculate the RHEED intensity for a small region around each relevant diffraction spot.

The input lines labeled “Spot size ...” and “ZspotSize ...” control how much area around the diffraction spot locations are calculated. In “Spot size” the numbers indicate how large (in pixels) in the plus and minus direction the calculated area should be in the y direction. The program begins by setting the lateral spot size to the smallest number (5 in the example input file), and then after calculating a RHEED pattern it checks to see if the

maximum intensity is on the edge of the calculated area. If the maximum intensity is at the edge of the calculated area it increases the lateral spot size by 5 pixels (in the positive and negative direction) and checks again to see if the maximum spot intensity is at the edge of the calculated area. If the maximum intensity is still at the edge it will continue this process until the calculated spot area is equal to the maximum allowable size (which is 20 pixels in the positive and negative direction in this example). This algorithm was developed because diffraction spots change location – in the y direction – as the sample is rotated in-plane. This allows the program to calculate a minimum number of pixels and increase computational efficiency.

The “ZSpotsize” line controls the extent of the calculated diffraction spot area in the z direction. This can be set to a constant value (5 pixels in the positive and negative direction in this example) because for perfectly flat in-plane rotations the spot position only changes in the y-direction. The second number in this line either sets this value to be constant (entering a 0) or allows the z-value to change with the y-value (entering a 1) if for some reason the diffraction spot location does change in the z direction.

The increase in efficiency produced by this algorithm can be directly estimated by comparing the number of pixels calculated using this method to the number of pixels calculated for a full RHEED image. The full RHEED image is 600 x 412 pixels, this algorithm only calculates between 11 x 11 pixels per spot and 41 x 11 pixel per spot. The increase in efficiency therefore ranges between a factor of 100 and 340. To calculate a 30,000 entry in-plane rocking curve table requires a few days using the most efficient method. If full RHEED patterns were calculated it would take at least one year.

### **B.3.5.12 Specifying spot locations**

The input lines labeled “y,z first spot”, through “y,z sixth spot” are the pixel locations of spots 1 through 6. It is up to the user to determine (knowing the RHEED incidence angle, energy, and spot separation – previously specified) which spots are being shown on the screen, and subsequently which diffraction spot corresponds to which location.

### **B.3.5.13 Building the crystal potential**

The remaining lines of the input file are reserved for constructing the crystal potential. These parameters are structured to create any cubic lattice using a simple cubic lattice with a basis. The first line contains the number of atoms in the basis, followed by the simple cubic lattice constant in the x, y, and z directions.

The next three lines specify the range of inverse lattice reflections which are to be included in the calculation. By changing the range and examining the RHEED pattern it is possible to verify which diffraction spots are present in the simulation. Only the required reflections should be calculated because the simulation time scales as the number of diffraction spots squared.

The last five lines in this input file specify the atomic scattering factors for each atom and its basis location (in units of the simple cubic lattice parameters). The first number is the atom’s atomic number and the second number is the oxidation state of the atom in the lattice. These numbers are used to choose the correct atomic scattering factors from tables that must be provided with the code. The tables used with the code are from Table 2.2 B in the “International Tables for X-ray Crystallography”<sup>77</sup>. These

tables contain numbers for a four Gaussian fit, as shown in Eq.(0.2), which will calculate the x-ray atomic scattering factor as a function of wave length ( $\lambda$ ) and scattering angle ( $\theta$ ).

$$f(\lambda^{-1} \sin \theta) = \sum_{i=1}^4 a_i \exp(-b_i \lambda^{-2} \sin^2 \theta) + c \quad (0.2)$$

The tables give  $a_i$ ,  $b_i$ , and  $c$  as a function of atomic number and oxidation state.

The program has five different tables named ASF0.dat, ASF1.dat, ASF2.dat, ASF3.dat, ASF4.dat, which contain the  $a_i$ ,  $b_i$ , and  $c$  for different oxidation states (ASF $X$  stands for Atomic Scattering Factor and the oxidation state number). An example of one of these tables (ASF2.dat) is given below.

Z	a1	b1	a2	b2	a3	b3	a4	b4	c
12	3.49	2.16	3.83	4.75	1.32	0.18	0.84	10.14	0.485
8	3.28	20.46	3.21	7.18	1.89	96.0	-13.07	-.02	14.69
56	20.18	3.21	19.11	0.28	10.90	20.05	0.77	51.74	3.02
82	21.78	1.33	19.56	.488	19.14	6.77	7.01	23.81	12.47
-1	0	0	0	0	0	0	0	0	0

In this example the significant digits were truncated so that they will fit on the page, but in the program all six significant digits are used. The negative one, in the last line, signifies to the program that it is at the end of the table. Currently the tables contain very few entries; however, any material contained in the table can easily be added when needed. Oxygen, in the -2 oxidation state, was not present in Table 2.2 B<sup>77</sup>, so the oxygen parameters were obtained by fitting atomic scattering factors in Cullity<sup>78</sup>. The calculated atomic scattering factors are for x-rays. These are transformed to atomic scattering factors for electrons using the Mott Formula<sup>79</sup>.

### **B.3.5.14 Rockfast.c output files**

The output files from rockfast.c are called rock024.dat, rock026.dat, rock044.dat, and rock046.dat for the (024), (026), (044), and (046) MgO diffraction spots respectively. For other materials the 024, 026, 044, and 046 markers would correspond to spot numbers 3, 4, 5, and 6, respectively. These files contain the diffraction spot intensity as a function of effective electron penetration depth ( $h$ ), grain size ( $L$ ), out-of-plane orientation distribution ( $\Delta\omega$ ), in-plane orientation distribution ( $\Delta\phi$ ), and  $\phi$  (the rocking angle). At the end of each file is a line of -1's. These files are not the lookup tables for in-plane rocking curves because those files need to contain the FWHM of the rocking curves. These files are used by rockout.c to create the actual lookup tables.

### **B.3.5.15 Rockout.c – making the file lookup tables**

Rockout.c reads in the information from the rock000.dat (the 000 represents the diffraction spot location – 024, etc.) files to create the in-plane rocking curve lookup tables. Rockout.c records diffraction spot intensities as a function of  $\phi$  for each unique setting of  $h$ ,  $L$ ,  $\Delta\omega$ , and  $\Delta\phi$ , fits a Gaussian to the curve and measures the FWHM. The program knows that it has reached the end of the rock000.dat file when it reads in the line of -1's. It then creates a new file for each diffraction spot called rockfwhm000.dat (again, the 000 represents the diffraction spot location – 024, etc.). The rockfwhm000.dat files are the lookup tables for RHEED in-plane rocking curves.

## **B.4 Final results**

Using a combination of single-image analysis and RHEED in-plane rocking curves it is possible to measure the biaxial texture of MgO. This process is not unique to

MgO and should be viable for all cubic materials following the procedures outlined above. The accuracy of these measurements is better than  $\pm 1^\circ$  for either out-of-plane ( $\Delta\omega$ ) or in-plane orientation distributions ( $\Delta\phi$ ). This *in situ* biaxial texture measurement technique is a powerful way to quickly examine biaxial texture and gain insight into the mechanisms producing biaxial texture.

The c programs mentioned in this appendix are autolayer.c, autogausslookup.c, makegausslookup.c, autorock.c, rocklookup.c, rockfast.c, and rockout.c. For space considerations (300 pages of code), they are not included here. Contact the Atwater group at Caltech for copies.

---

<sup>77</sup> International Tables for X-Ray Crystallography, edited by James A. Ibers and Walter C. Hamilton (Kynoch Press, Birmingham, 1974) Vol. IV, Ch. 2 pp. 71-102.

<sup>78</sup> B. D. Cullity, Elements of X-Ray Diffraction, 2<sup>nd</sup> ed. (Addison-Wesley Publishing Company, Inc., Reading, 1978) pp. 520-521.

<sup>79</sup> D. Rez, P. Rez, and I. Grant, *Acta. Cryst.* **A50**, 481 (1994).

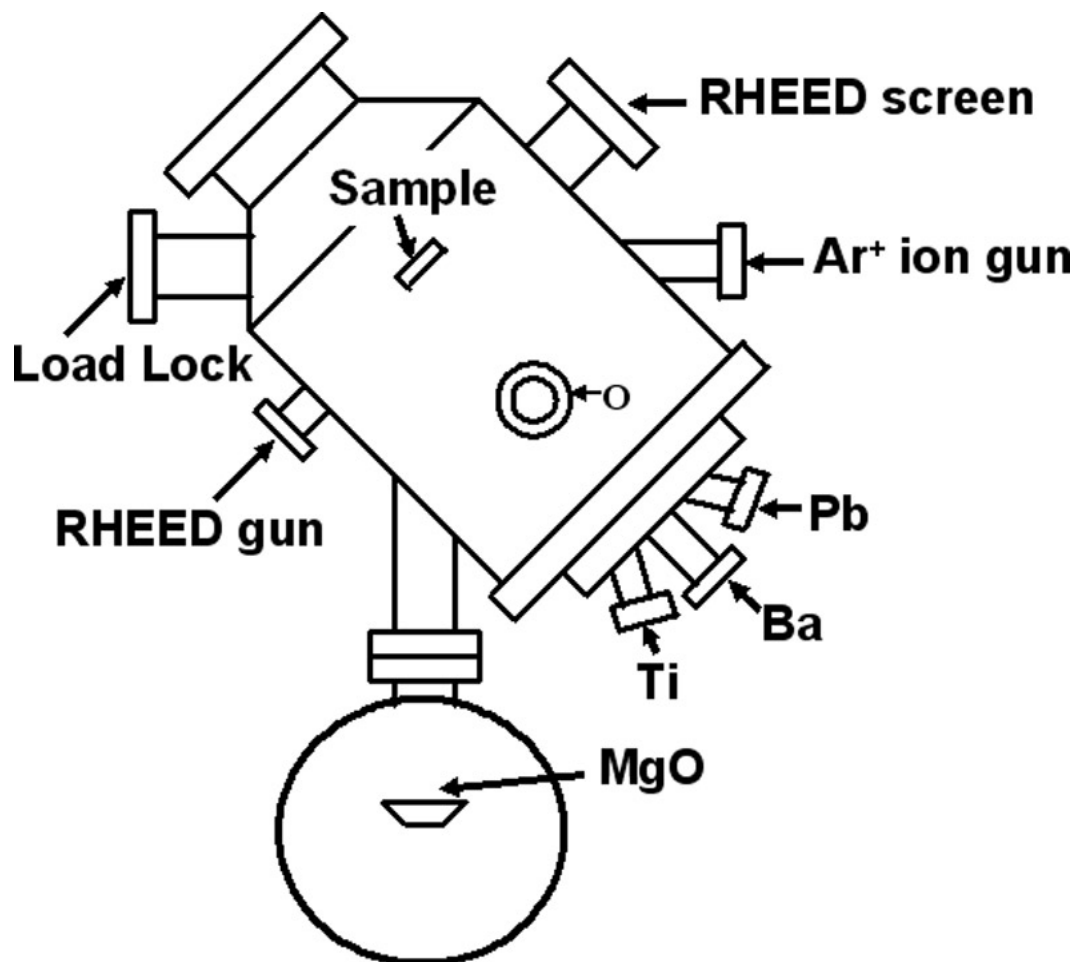


Figure C.1 Schematic of the IBAD MgO and oxide MBE high vacuum chamber.

## Appendix C Oxide MBE Growth Chamber

### Overview

For ion beam-assisted deposition (IBAD) of MgO and molecular beam epitaxy (MBE) of  $\text{Ba}_x\text{Pb}_{1-x}\text{TiO}_3$  I designed and fabricated a high vacuum growth chamber. Figure C.1 is a schematic of the growth chamber and Figures C.2 and C.3 are images of the growth chamber with important components labeled.

IBAD MgO is performed by evaporating MgO from a Temescal CV-10 four pocket e-beam evaporator source, with a simultaneous  $\text{Ar}^+$  ion bombardment from an Ion Tech Inc. 3 cm Kaufmann Ion Gun. The ion flux is verified before growth using a

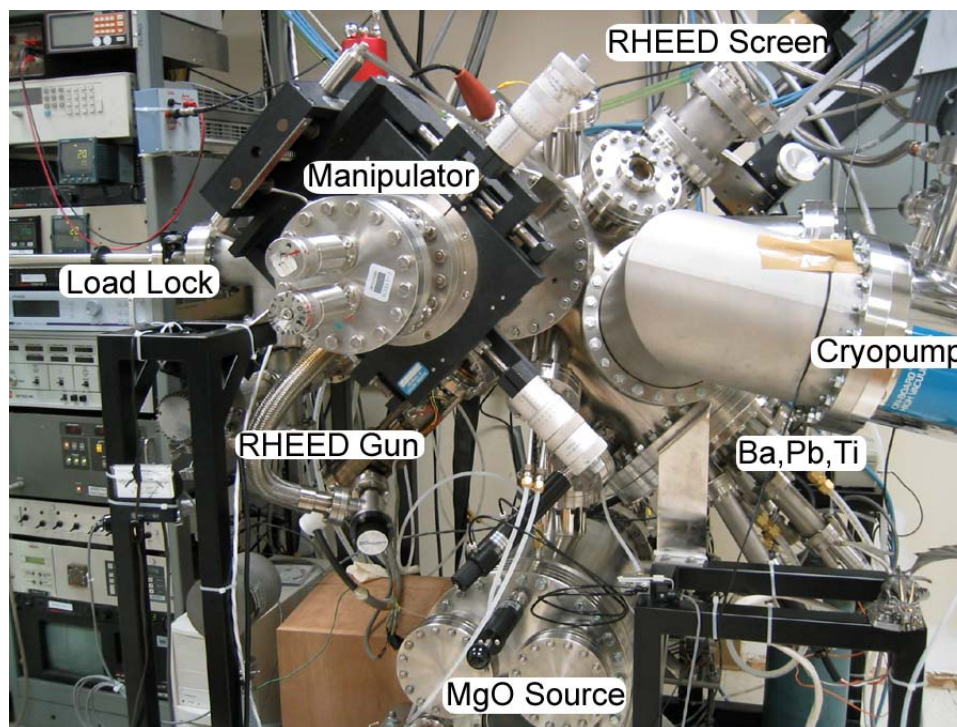


Figure C.2 Side view of the IBAF MgO and oxide MBE high vacuum chamber faraday cup. The faraday cup is constructed from a high vacuum BNC cable, where the collector is floated at  $-90\text{ V}$  to repel electrons in the ion beam. The collector is also surrounded by a grounded cylinder with a  $0.078\text{ cm}^2$  aperture to collect the  $\text{Ar}^+$  flux. The  $\text{Ar}^+$  current is measured with a Keithley 195A Digital Multimeter. The MgO flux rate is monitored with an Inficon quartz crystal monitor (QCM) during deposition (the tooling factor is 39%) and the deposition rate control must be provided manually by adjusting the beam current during growth. Real-time reflection high-energy electron diffraction (RHEED) monitoring is provided by an 8-bit video camera run using k-space software and a 16-bit CCD camera controlled with PMIS software. The k-space software gives a real-time plot of the maximum RHEED spot intensity (the growth is stopped when the RHEED spot intensity stops increasing) and the PMIS software controls a high dynamic

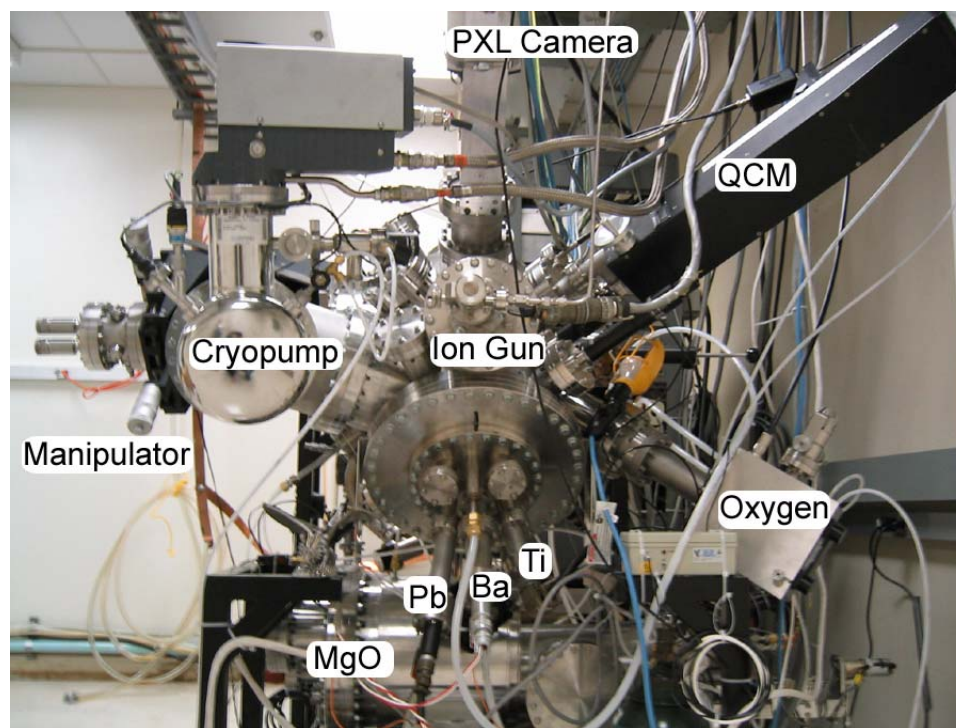


Figure C.3 Front view of IBAF MgO and oxide MBE high vacuum chamber range Photometrics PXL camera, which is used to take high-resolution, high dynamic range images of the RHEED pattern for quantitative biaxial texture analysis.

The capability to grow  $\text{Ba}_x\text{Pb}_{1-x}\text{TiO}_3$  is provided by elemental sources of Ba, Pb, Ti, and oxygen. Ba and Pb are evaporated from separate effusion cells. Each cell is filled with high purity Pb (99.999%) or Ba (99%) and the deposition rate is controlled through temperature PID control, which relies on the vapor pressure of the element at a given temperature to provide the desired elemental flux. DC power to each cell comes from a Sorensen DCS 60-18E power supply and a Eurotherm 2404 controller maintains the desired power output or crucible temperature.

Our titanium source is a Varian Ti-ball sublimation pump run by a stable Hewlett Packard 6673A power supply<sup>80</sup>. The titanium ball is heated by a tungsten wire coiled inside the titanium ball. The sublimation rate of the titanium is set by controlling the

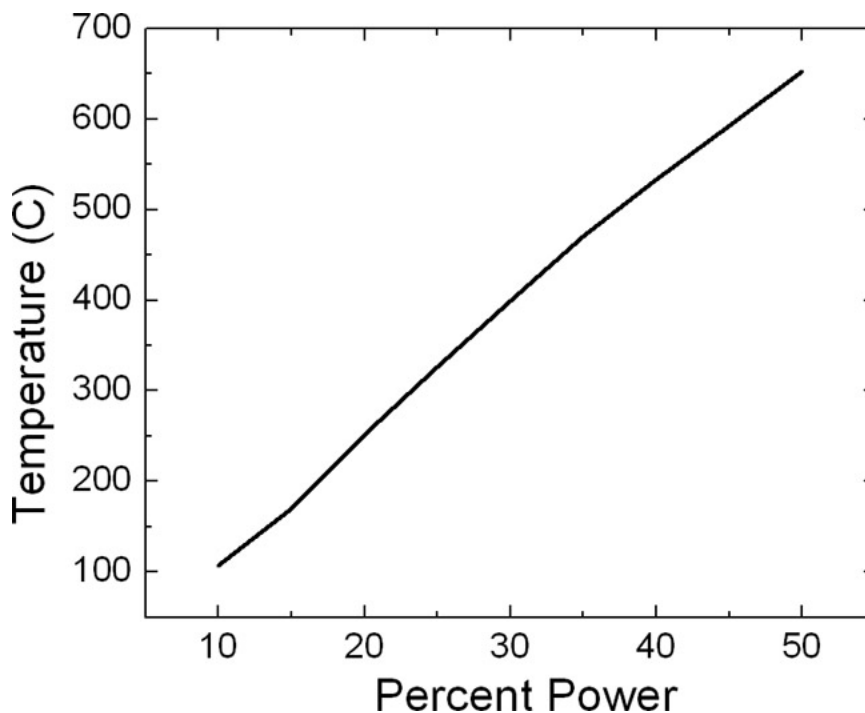


Figure C.4 Calibrated substrate temperature as a function of power percentage output by the Sorensen DCS 60-18E.

current through the tungsten wire. Finally, because Pb is difficult to oxidize, we use an Oxford Applied Research RF oxygen atom source. Oxygen is injected into the source (with a leak valve) creating a background oxygen pressure of  $6 \times 10^{-5}$  torr and 500 W of RF power is used to dissociate a fraction of the  $O_2$  to make oxygen atoms, which then drift to the substrate.

Because of the high substrate temperatures needed ( $> 700^\circ C$ ) and the oxidizing atmosphere, the substrate heating element is a single machined piece of SiC. The heater power supply is a Sorenson DCS 60-18E and power output is regulated by a Eurotherm 818 controller.

The oxide MBE process is computer controlled through LabView. Either temperatures or power percentages are used to control the power supplied to the Ba and Pb effusion cells. The Ti-ball source power is controlled by setting the Hewlett Packard

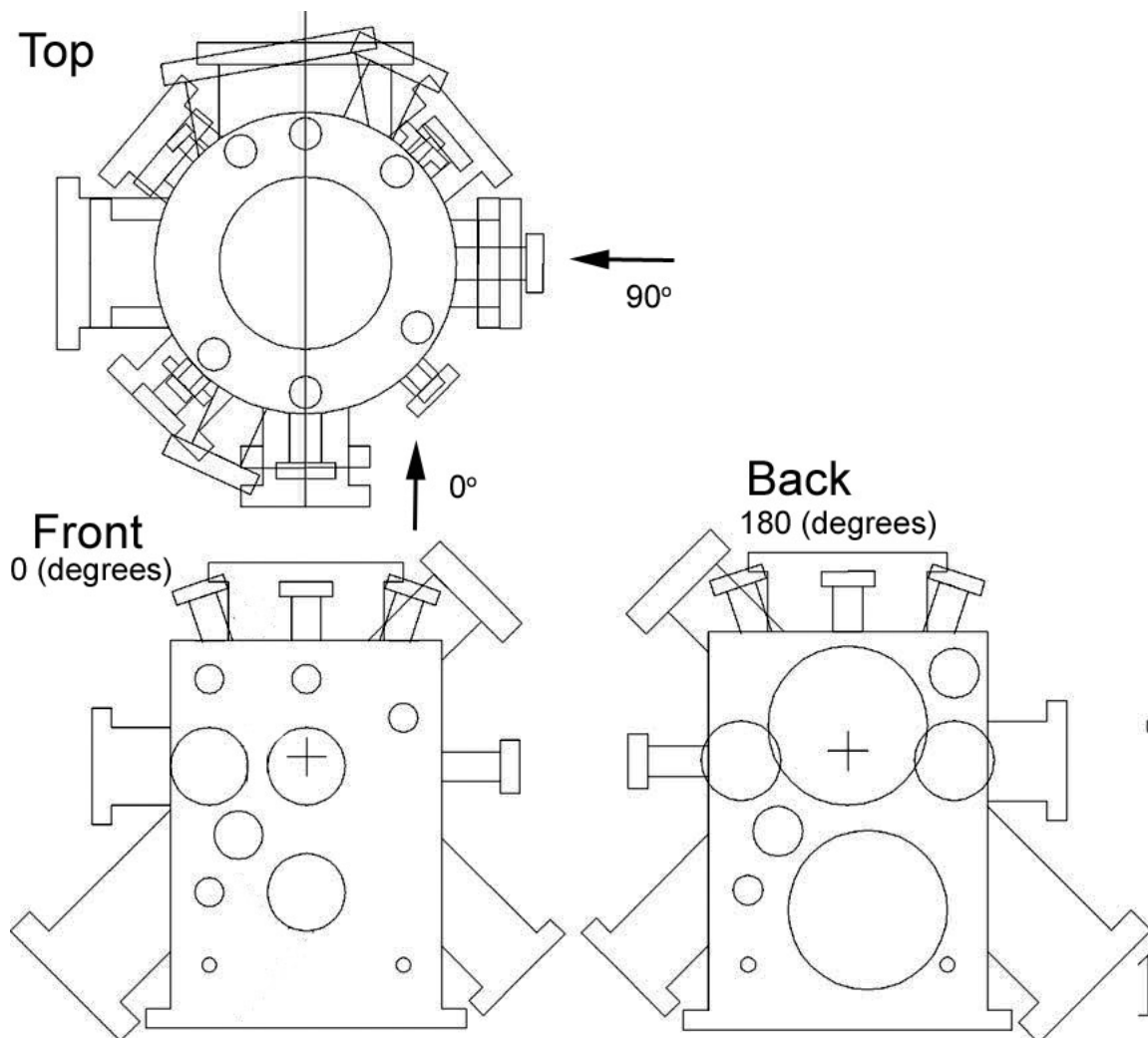


Figure C.5 Schematic of the main vacuum chamber design. The crosses specify the substrate position during growth. The top view is from  $0^\circ$  polar angle, the front view is from  $0^\circ$  azimuthal angle and  $90^\circ$  polar angle, and the back view is from  $180^\circ$  azimuthal angle and  $0^\circ$  polar angle.

6673A current output. Substrate temperature is maintained by specifying the power percentage output to the SiC element from the DC power supply. The substrate temperature was calibrated as a function of the power supply percent power output using a SensArray Corporation thermocouple wafer. Figure C.4 is the calibration curve for the molybdenum substrate block.

Shutters cover the substrate block and the individual elemental sources. The shutters are pneumatically actuated and can also be controlled by the computer.

## C.1 Parts List

Effusion Cells: EPI Knudsen cells, Sorensen DCS 60-18E power supplies, Eurotherm 2404 temperature controllers.

Titanium Source: Varian Ti-ball source, HP 6673A power supply.

Oxygen Source: Oxford Applied Research HD25, oxygen leak valve.

Substrate Heater: Johnsen Ultravac Inc., SiC heating element from Morgan Advanced Ceramics, Sorensen DCS 60-18E power supply, Eurotherm 818 controller.

MgO Evaporator: Temescal CV-10 4-pocket e-beam evaporator with a Thermionics beam sweep.

Ion gun: Ion Tech Inc. 3 cm DC Kaufmann ion gun.

RHEED system: Veetech VP-052S 30 keV RHEED gun and power supply, k-space associates P43 RHEED screen, Photometrics PXL 1024x1024, 16-bit CCD camera (PMIS software). The Photometrics camera must be run on an Intel Pentium I motherboard.

Quartz Crystal Monitors: Inficon XTC controller.

Mass Spectrometer: Ametek Dycor quadrupole gas analyzer.

Vacuum pumps: Main Chamber - CTI-Cryogenics 8F On Board cryopump. Load lock – Varian Turbo V-70D with Edwards RV3 mechanical pump.

## C.2 Chamber Design

The following chamber schematics and spreadsheet were used by Huntington to build the main oxide MBE vacuum chamber. The chamber is a 14 inch tube with a 16.5” conflat flange at the base.

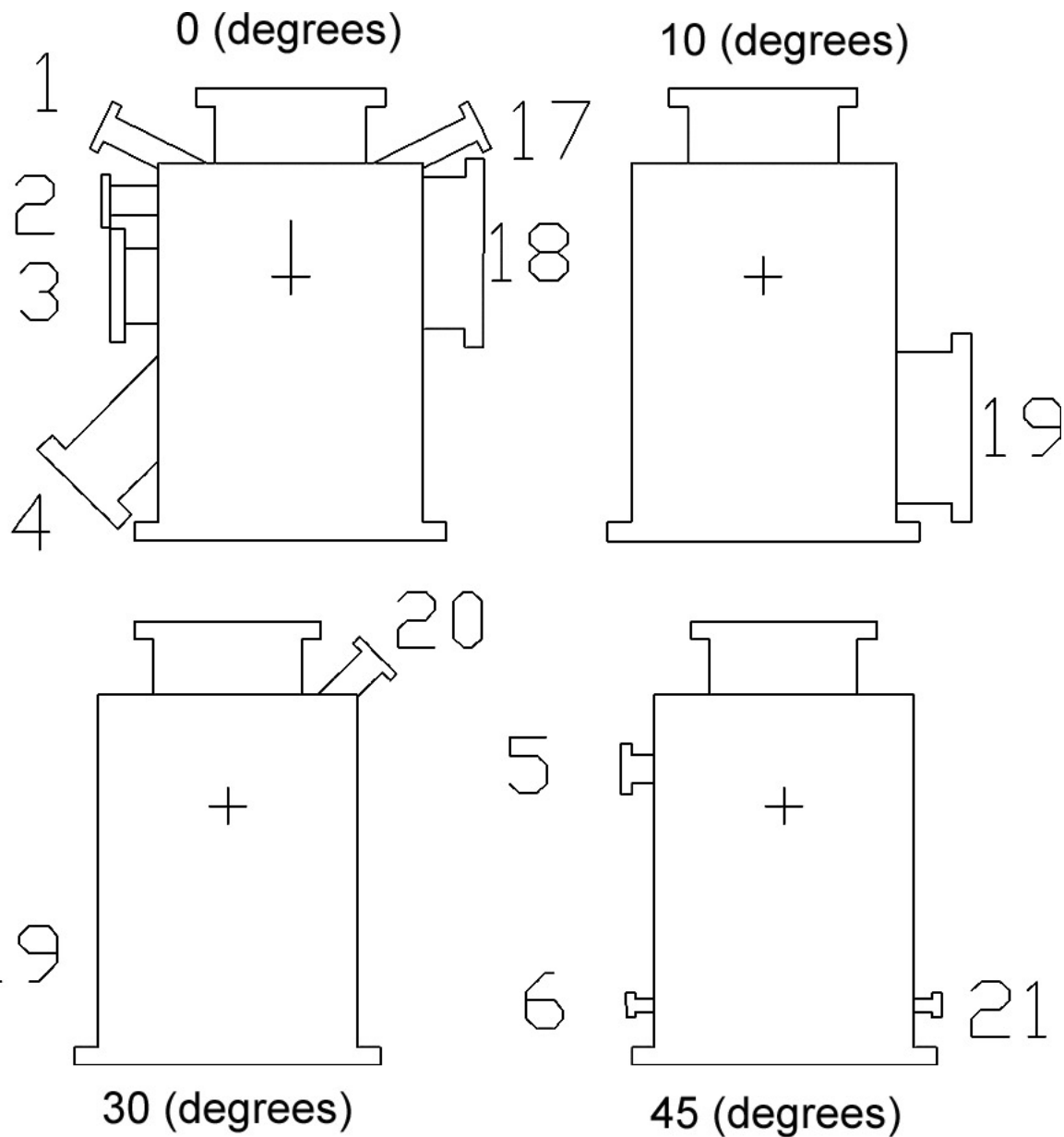


Figure C.6 Cross section views of the main vacuum chamber cut at different azimuthal angles (0, 10, 30, and 45 degrees). The specified azimuthal angle is the azimuthal angle of the ports on the left of each schematic. The ports are labeled with a number that corresponds with the specifications in Table C.1.

Table C.1 contains the necessary specifications for adding ports to the main chamber body. Each port in Figures C.6 to C.8 is identified with a number for comparison with the specifications in Table C.1.

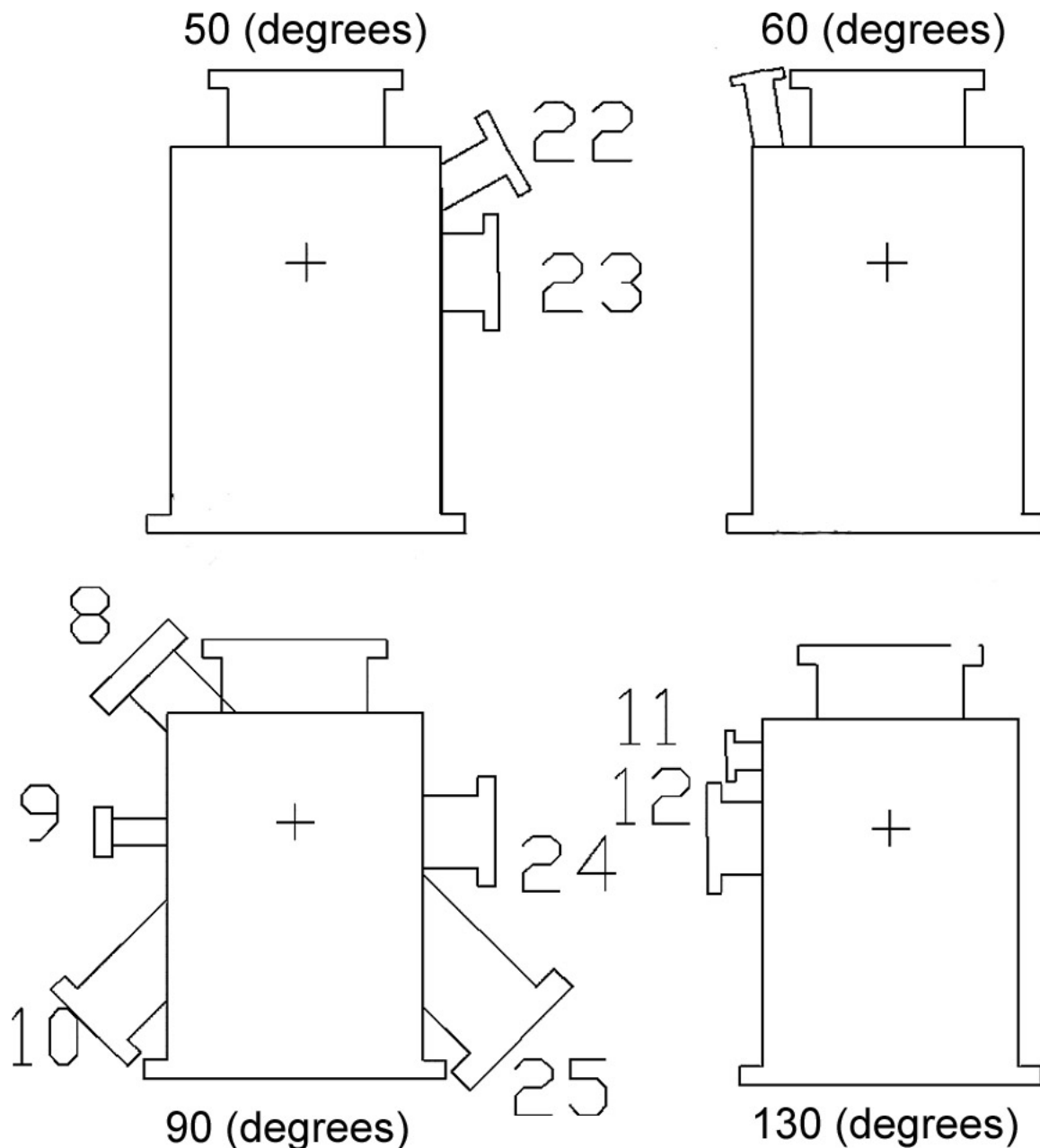


Figure C.7 Cross section views of the main vacuum chamber cut at different azimuthal angles (50, 60, 90, and 130 degrees). The specified azimuthal angle is the azimuthal angle of the ports on the left of each schematic. The ports are labeled with a number that corresponds with the specifications in Table C.1.

Each port is characterized by its flange size, focal point, focal length, azimuthal angle, and polar angle. All length and location dimensions are in inches. The flange size is the standard outer diameter of the conflat flange (t after the number means that it is a tapped flange). All tube sizes are standard tube sizes used with the appropriate conflat

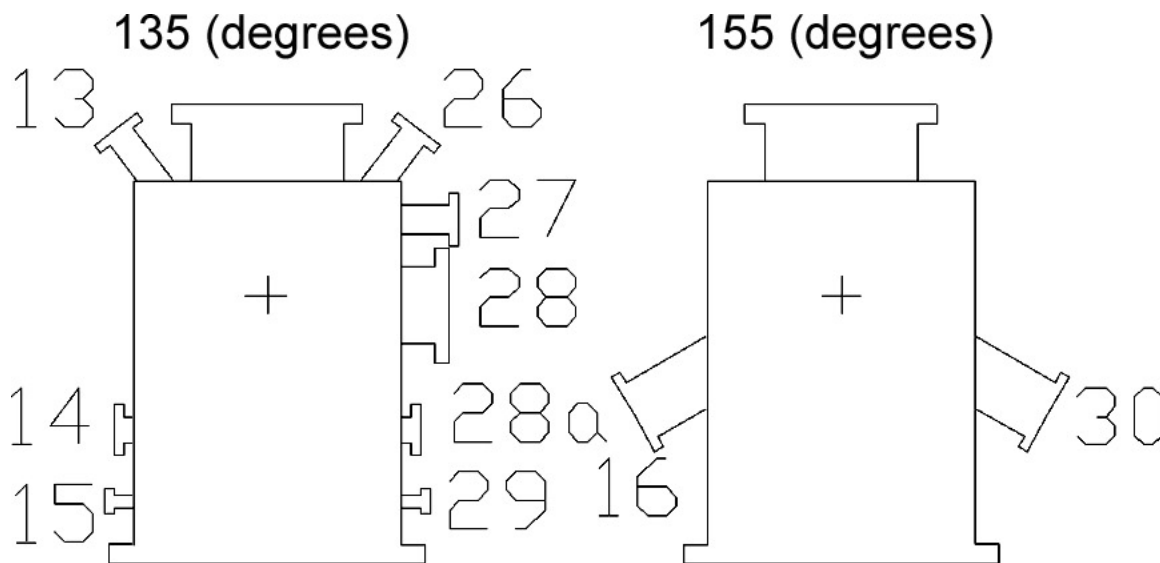


Figure C.8 Cross section views of the main vacuum chamber cut at different azimuthal angles (50, 60, 90, and 130 degrees). The specified azimuthal angle is the azimuthal angle of the ports on the left of each schematic. The ports are labeled with a number that corresponds with the specifications in Table C.1.

flange.

There are several focal points (the location pointed at by a port) used throughout the chamber design, each is specified by a letter. The x, y, and z coordinates associated with each letter are included at the end of Table C.1.

The origin (0,0,0) is located at the center of the 14 inch chamber tube at the bottom of the 16.5 inch flange. Positive x and y go from the center of the tube toward 0° and 90°, respectively. Positive z is from the base of the 16.5 inch chamber toward the other end of the chamber. Focal length specifies the distance from the focal point to the outside edge of the port

conflat flange. The azimuthal angle is the rotation angle of the port, centered at the focal point, around an axis parallel to the center axis of the chamber tube. Zero degrees azimuthal is marked in Figure C.5. The polar angle specifies the port rotation, centered at the focal point, around the axis perpendicular to the azimuthal rotation axis. For

example,  $0^\circ$  polar angle is parallel with the center axis of the main chamber tube and faces from the top of the chamber toward the 16.5 inch flange base, while  $90^\circ$  polar angle faces the port perpendicular to the tube side wall. Table C.1 also contains a column to specify which piece of equipment is attached to each of the ports.

The ports listed in Table C.1. correspond to the ports numbered in the autoCAD drawings in Figures C.5 to C.8. Figure C.5 shows chamber drawings from the top ( $0^\circ$  polar angle), front ( $0^\circ$  azimuthal angle,  $90^\circ$  polar angle), and side view ( $90^\circ$  azimuthal angle,  $90^\circ$  polar angle). Figures C.6 to C.8 are cross section views of the main vacuum chamber cut at the specified azimuthal angles to show individual ports. On the left of the chamber cross sections are the ports from the cut at the specified angle, while the ports drawn on the right hand side are the ports at the specified angle plus  $180^\circ$ . The port numbers identify each port with specifications listed in Table C.1. By assembling the series of drawings from cuts at all azimuthal angles containing ports, the full 3-D chamber design is ascertained.

Table C.1: List of ports on the main vacuum chamber, the flange size, port focal point location, focal length, azimuthal rotation angle, polar rotation angle, and the equipment attached to the port.

Port Number	Flange Size	Focal Point	Focal Length	Azimuthal Angle	Polar Angle	Equipment
1	2.75	A	11.2	0	63.5	Heater power feed-thru
2	2.75	B	10	0	90	Ion gauge
3	6	C	9.5	0	90	Faraday cup
4	6	D	16	0	135	Oxygen source
5	2.75	E	8.75	45	90	Mass spectrometer
6	4.5	F	10	45	90	Shutter
7	2.75	G	11	60	9	Shutter
8	6	D	12.75	90	45	Load lock
9	2.75	C	11	90	90	RHEED gun
10	6	D	16	90	135	MgO evaporator
11	2.75	B	9	130	90	Blank
12	6	C	10	130	90	View port

13	2.75	H	11	157.7	37.4	View port
14	2.75t	I	8	135	90	Shutter
15	4.5	F	10	135	90	Shutter
16	4.5	D	12.5	155	120	Quartz crystal monitor
17	2.75	A	11.2	180	63.5	View port
18	10	J	10.25	180	90	Manipulator
19	10	K	11	190	90	Cryopump
20	2.75	D	11.5	210	45	Ion gauge
21	4.5	F	10	225	90	Shutter
22	4.5	D	12	230	61	Blank
23	6	C	10	230	90	Blank
24	6	C	11	270	90	RHEED screen
25	8	D	17	270	135	Ion gun
26	2.75	L	11	337.7	37.4	Substrate ground
27	2.75	B	10	315	90	Faraday cup feed-thru
28	6	C	9.5	315	90	Quartz crystal monitor
28a	2.75t	I	8	315	90	Shutter
29	4.5	F	10	315	90	Shutter
30	4.5	D	12.5	335	120	Viewport
Focal Point	X	Y	Z			
A	0	0	17			
B	0	0	18			
C	0	0	13.5			
D	0	0	14			
E	0	0	16			
F	0	0	3.5			
G	2.5	4.33	13			
H	0	2.5	14			
I	0	0	7			
J	0	0	15.25			
K	0	0	6			
L	0	-2.5	14			

<sup>80</sup> C. D. Theis and D. G. Schlom, J. Vac. Sci. Technol. A **14**, 2677 (1996).

